



A University of Sussex PhD thesis

Available online via Sussex Research Online:

<http://sro.sussex.ac.uk/>

This thesis is protected by copyright which belongs to the author.

This thesis cannot be reproduced or quoted extensively from without first obtaining permission in writing from the Author

The content must not be changed in any way or sold commercially in any format or medium without the formal permission of the Author

When referring to this work, full bibliographic details including the author, title, awarding institution and date of the thesis must be given

Please visit Sussex Research Online for more information and further details



Magnetic Properties of Dysprosium and Uranium
Sandwich Complexes Based on Cyclopentadienyl and
Fulvalenyl Ligands

A thesis submitted to the University of Sussex for the degree of
Doctor of Philosophy

2021

Mian He

Department of Chemistry
School of Life Sciences

The work detailed in this thesis was finished under the supervision of Professor Richard A. Layfield at the University of Sussex from June 2018 to February 2021 and at the University of Manchester from May 2017 to May 2018. All the work is my own, unless stated to the contrary, and has not been previously submitted for any other degree at the University of Sussex or any other university.

Mian He

February 2021

Table of Contents

List of Abbreviations and Equations	1
Abstract.....	3
Acknowledgements	4
Chapter 1. General Introduction to Single-Molecule Magnets	5
1.1. Introduction to Lanthanide Ions	7
1.1.1. Lanthanide Electron Configurations	7
1.1.2 Lanthanide Ions	8
1.1.3 The Lanthanide Contraction	8
1.1.4 Magnetism of Free Ln ³⁺ Ions.....	9
1.1.5 Anisotropy of Ln ³⁺ Ions	10
1.1.6 Crystal-field to Lanthanide Ions.....	11
1.2 Magnetism in Single-molecule Magnet	13
1.2.1 The First SMM in 1993.....	13
1.2.2 Basic Properties of SMMs.....	14
1.2.3 The Effective Energy Barrier (U_{eff}) and the Blocking Temperature (T_{B}).....	15
1.2.4 Magnetic Relaxation and Quantum Tunnelling of the Magnetization (QTM).....	16
1.2.5 Magnetic Property Characterization	17
1.3 A Brief Overview of SMMs	23
1.3.1 The Early Years of SMMs: Manganese Polynuclear Clusters.....	23
1.3.2 Other 3d Transition Metal SMMs	24
1.3.2.1 Iron single-ion SMMs.....	25
1.3.2.2 Cobalt SMMs	25
1.3.3 Lanthanide single-ion SMMs	26
1.3.3.1 Terbium Single-ion SMMs	27
1.3.3.2 Erbium Single-ion SMMs	28
1.3.3.3 Dysprosium SMMs.....	30

1.3.3.4 SMMs Based on Less Common Lanthanides	33
1.3.4 Actinide SMMs	33
1.4 Synthetic Strategies for High-Temperature Dysprosium SMMs	35
1.4.1 High-Symmetry Dysprosium Single-ion SMMs	35
1.4.2 High-Performance Dysprosium Metallocene SMMs	38
1.5 Summary	42
Chapter 2. Dimetallic Dysprosocenium Single-Molecule Magnets Based on Fulvalene Ligands	43
2.1 Introduction to Fulvalenyl Complexes	44
2.2 Synthesis of Fulvalenyl Ligand and Bridged Complexes.....	47
2.2.1 Synthesis of the Fv ^{tttt} Ligand	47
2.2.2 Synthesis of [Fv ^{tttt} YCl ₂ Li(THF) ₂] ₂	48
2.2.3 Synthesis of Heterobimetallic Fulvalene-Bridged Double Metallocene.....	49
2.2.4 Synthesis of [DyFv ^{tttt}] ₂ [B(C ₆ F ₅) ₄] ₂	50
2.2.5 Synthesis of [{Ln(Cp*)(BH ₄) ₂ (Fv ^{tttt})].....	52
2.3 X-Ray Diffraction Studies.....	53
2.3.1 Crystal Structure of [Fv ^{tttt} Ln ₂ (BH ₄) ₂ THF].....	53
2.3.2 Crystal Structure of [(BH ₄)DyFv ^{tttt}] ₂	55
2.3.3 Crystal Structure of [{Ln(η ⁵ -Cp*)(μ-BH ₄) ₂ (η ⁵ :η ⁵ -Fv ^{tttt})].....	57
2.3.4 Crystal Structure of [{Dy(η ⁵ -Cp*)(μ-BH ₄)(η ⁵ :η ⁵ -Fv ^{tttt})] ₂ [B(C ₆ F ₅) ₄] ₂	59
2.4 Magnetic Property Characterization.....	61
2.4.1 DC Magnetic Measurements	61
2.4.2 AC Magnetic Measurement.....	63
2.4.3 Magnetic Property Measurements on Diluted Samples	73
2.4.4 Theoretical Calculations.....	76
2.5 Conclusions and Perspectives	82
Chapter 3. Fulvalene-Bridged Trimetallic Dysprosocenium SMMs.....	84
3.1 Introduction	85

3.2 Synthesis of Fulvalenyl-Bridged Trimetallic Dysprosocenium Complexes.....	86
3.3 X-Ray Diffraction Study	88
3.3.1 Crystal Structure of Compound 3.1	88
3.3.2 Crystal Structure of the Cation 3.2	91
3.4 Magnetic Property Measurements	93
3.4.1 DC Magnetic Measurements	93
3.4.2 AC Magnetic Measurements	94
3.4.3 Theoretical Calculations.....	100
3.5 Conclusions	103
Chapter 4. A Phosphole-Ligated Dysprosocenium Single-Molecule Magnet.....	104
4.1 Introduction	105
4.2 Synthesis of Phospholyl Ligands and Phosphole-Ligated SMMs.....	107
4.2.1 Synthesis of Mono-Phospholyl Ligands and Phospholide Compounds	107
4.2.2 Synthesis of a Bis(monophospholyl) Dysprosium Complex.....	108
4.2.3 Synthesis of $[(\text{Cp}^{\text{iPr}_5})\text{Dy}(\text{Cp}^{\text{Et}_4\text{P}})][\text{B}(\text{C}_6\text{F}_5)_4]$	108
4.3 X-Ray Diffraction Studies of Dysprosium-Phospholyl Complexes.....	110
4.3.1 Crystal Structure of Compound 4.4	110
4.3.2 Crystal Structure of Compound 4.6	111
4.3.3 Crystal Structure of $[(\text{Cp}^{\text{iPr}_5})\text{Dy}(\text{Cp}^{\text{Et}_4\text{P}})][\text{B}(\text{C}_6\text{F}_5)_4]$	113
4.3.4 Crystal Structure of $[(\text{Cp}^{\text{iPr}_5})\text{Dy}(\text{Cp}^{\text{Et}_4\text{P}})(\text{BH}_3)][\text{B}(\text{C}_6\text{F}_5)_4]$	116
4.4 Magnetic Property Measurements	118
4.4.1 DC Magnetic Susceptibility	118
4.4.2 AC Magnetic Measurements	121
4.4.3 Theoretical Calculations on $[(\text{Cp}^{\text{iPr}_5})\text{Dy}(\text{Cp}^{\text{Et}_4\text{P}})]^+$	126
4.5 Discussion and Conclusions.....	128
Chapter 5. Fulvalene-Bridged Dimetallic Uranocenium Cations.....	129
5.1 Introduction	130
5.2 Synthesis of Fulvalenyl Bridged Di-Uranocenium Complexes.....	133

5.3 X-Ray Diffraction Studies of Dinuclear Uranium Compounds.....	135
5.3.1 Structure of $[\{U^{III}(\eta^5-Cp^*)(\mu-I)\}_2(\eta^5:\eta^5-Fv^{tttt})]$ (5.1)	135
5.3.2 Crystal Structure of $[\{U^{III/IV}(\eta^5-Cp^*)(\mu-I)\}_2(\eta^5:\eta^5-Fv^{tttt})][B(C_6F_5)_4]$ (5.2)	137
5.4 Conclusions and Future Work.....	139
Chapter 6. General Conclusions.....	140
Chapter 7. Experimental Section	144
7.1 Chemical Synthesis.....	145
7.1.1 General Synthetic Procedures	145
7.1.2 Synthesis for Chapter 2.....	145
7.1.3 Synthesis for Chapter 3.....	162
7.1.4 Synthesis for Chapter 4.....	166
7.1.5 Synthesis for Chapter 5.....	174
7.2 X-Ray Crystallography	179
7.3 Magnetic property measurements	187
7.3.1 Additional Magnetic Information for Chapter 2.....	187
7.3.2 Additional Magnetic Information for Chapter 3.....	189
7.3.3 Additional Magnetic Information for Chapter 4.....	192
Reference	207

List of Abbreviations and Equations

AC	alternating current
Ac	acetate
Cb	cyclobutadienyl dianion
COT	cyclo-octatetraenyl dianion
Cp	cyclopentadienyl
Cp ^{iPr5}	penta-isopropylcyclopentadienyl
Cp ^{Et4P}	tetraethyl-phospholide
Cp*	pentamethylcyclopentadienyl
Cp'	(trimethylsilyl)cyclopentadienyl
DC	direct current
DCM	dichloromethane
DFT	density functional theory
Fv ^{tttt}	1,1',3,3'-tetra- <i>tert</i> -butylfulvalene
H _{dc}	induced DC field
KC ₈	potassium graphite
KD	Kramers doublet
Ln	lanthanide
M _J	secondary total angular momentum quantum number
Pc	phthalocyanine
QTM	Quantum tunnelling of the magnetization
IR	infrared
SMM	single-molecule magnet
SQUID	Superconducting Quantum Interference Device
T	temperature
T _B	maximum hysteresis temperature / magnetic blocking temperature
TBA	tetrabutylammonium cation!
THF	tetrahydrofuran

XRD	X-ray diffraction
U_{eff}	effective energy barrier
τ	magnetic relaxation time
τ_0	pre-exponential factor or attempt time
χ'	in-phase magnetic susceptibility (real component)
χ''	out-of-phase magnetic susceptibility (imaginary component)

Equation 1	on Page 15
Equation 2 and 3	on Page 16
Equation 4	on Page 21
Equation 5	on Page 82
Equation 6	on Page 103

Abstract

The PhD thesis describes a research project that focuses primarily on a series of dysprosium metallocenium single-molecule magnets containing cyclopentadienyl and fulvalenyl ligands. The project aims to discover the influence of the various ligand types on the magnetic properties, including the exchange coupling.

An introduction to SMMs is described in the first chapter, which mainly shows a historical perspective, current theoretical models and synthesis strategies. Inspired with the previous achievement of cyclopentadienyl sandwich SMMs in the Layfield group, I have successfully synthesized several dimetallic and trimetallic dysprosium metallocene SMMs containing the bulky pentafulvalenyl ligand $[(C_5^tBu_2H_2)_2]^{2-}$, with the complexes also containing bridging borohydride ligands, as described in Chapters 2 and 3, respectively. The bridged polynuclear structures show a periodic improvement in the SMM properties, such as an increase in the effective energy barrier to reversal of the magnetization, which is thought to be a consequence of the gradually diminishing influence of the borohydride ligands. The magnetic measurements and theoretical calculations also indicate that the quantum tunnelling of the magnetization (QTM) process is suppressed in the polynuclear system due to magnetic exchange.

In Chapter 4, I describe a dysprosocenium-based single-ion magnet, which is sandwiched by a mono-phospholyl ligand and a Cp* ligand. The near-linear metallocenium compound displays an excellent blocking temperature of 70 K and two separate energy barriers of 1410 cm^{-1} and 747 cm^{-1} due to two distinct Orbach processes. According to the AC magnetic susceptibility measurements, the compound unexpectedly gives two range of maxima in magnetic susceptibility (χ'_M and χ''_M), which is not observed in other reported phospholide samples.

In Chapter 5, two dimetallic uranocenium compounds are reported based on the fulvalenyl ligand, with additional iodide bridges. The dimetallic U(III)-U(III) sandwich structure gives distinct chemical reactivity as the iodide ligand cannot be removed, but resulting in a mixed-valence U(III)-U(IV) cation.

Acknowledgements

I would like to express my sincere thanks and regards to Prof. Richard A. Layfield, whose guidance, intelligence, kindness and input has been extremely valuable and an immeasurable benefit. His inspiration and support have been a driving force throughout this project. I am also grateful for the opportunity offered by Prof. Richard A. Layfield as well as the ERC for providing the funding, which allowed me to not only pursue my Ph.D. degree, but also cooperate with people in top universities and institutions: an experience which I will always treasure.

I would also like to give thanks to Prof. F. Geoffrey N. Cloke (FRS). As my co-supervisor before retirement, he has always been kind in supplying his glass-blowing skill and been very generous in sharing his knowledge. Thanks to all the previous and present members of Richard's group. Dr Benjamin Day gave much wonderful advice and ideas at the beginning of my research; Dr Fu-Sheng Guo shared lots of his own experience in experimental operation and magnetic data analysis; Dr Nikolaos Tsoureas, for his support within crystallography and kindly sharing his practical advice in organometallic synthesis. Thanks to Dr Arun Kumar Bar, Dr Anindita Chakraborty, Dr Maria Heras-Ojea, Dr Lewis Maddock, Dr Ollie Hemming, Mr Richard Collins, Mr James Durrant, Mr Chris Price and Ms Siobhan Temple for all their contributions and creating a great environment for doing research. Thanks should also be given to our close neighbours in L14: Dr Ian Crossley, Dr Samantha Furfari, Mr Kyle Pearce and Dr Madeleine Levis for creating a great environment for doing research.

Special thanks to Prof. Jinkui Tang, who helped measure so many complexes for magnetic property by himself and afforded me a research stint at the *State Key Laboratory* in Changchun. Special thanks to Dr Akseli Mansikkamäki, for all the complicated theoretical calculation.

Finally, on a personal note, I will always be grateful to my parents for their love and endless support. Last but absolutely not least, many, many thanks to my wife, Dr Min Feng, who is always patient with me, understands me, and gives me her selfless help not only in life but also in research.

Chapter 1

General Introduction to Single-Molecule Magnets

General Introduction to Single-Molecule Magnets

Research of SMMs (single-molecule magnets) has evolved into an advanced and popular field of study, continuing to attract a lot of attention from researchers in chemistry, physics and materials science. Because of their unique magnetic properties on the molecular-scale and their potential multifunctional behaviour (conductivity, redox properties, optics, chirality),¹⁻³ SMMs have the potential to revolutionise application in the next generation quantum materials, especially in the field such as data storage, molecular spintronic, sensors, and logic devices.⁴

Currently, most SMMs only show magnetic relaxation when cooled with liquid-helium cooling circumstance. Indeed, until now, only one SMM is known to function above liquid nitrogen temperatures (i.e., 80 Kelvin)⁵, which limits their potential applications. In order to achieve high-quality SMMs, current research is focused on improving key characteristics underpinning SMM behaviour such as the *effective energy barrier* (U_{eff}) and the *magnetic blocking temperature* (T_{B}) by using chemical or physical approaches.⁶

In this chapter, the basic principles of SMMs will be explained, focusing primarily on lanthanide magnetism and current strategies used to obtain high-quality SMMs with excellent effective energy barrier and blocking temperature. In that respect, some key examples to demonstrate the qualifiers of a 'good' SMM are also presented below.

1.1. Introduction to Lanthanide Ions

1.1.1. Lanthanide Electron Configurations

The lanthanide series covers 15 elements, whose atomic numbers are $Z = 57-71$ (Table 1.1). Scandium ($Z = 21$) (also referred to as a pseudo-lanthanide), yttrium ($Z = 39$), lanthanum and the other 14 lanthanide (Ce–Lu) elements are also referred to as the *rare-earth elements*, partly because of their similar chemical and physical properties. Lanthanides are the first elements in the periodic table with populated 4f orbitals, which has a crucial impact on their chemical and physical properties. The core-like nature of the 4f orbitals stems from them being buried within the lanthanide 5s and 5p shells, which are fully occupied. Based on the lowest energy principle, their electron configurations of atoms is either $[\text{Xe}]4f^n6s^2$ or $[\text{Xe}]4f^{n-1}5d^16s^2$ (Table 1.1).^{6, 7}

Table 1.1 The electronic configurations of lanthanide elements.

Element	Z	Electron configuration of neutral atoms	Electronic configurations of trivalent ions
La	57	$[\text{Xe}]4f^0 5d^1 6s^2$	$[\text{Xe}]4f^0$
Ce	58	$[\text{Xe}]4f^1 5d^1 6s^2$	$[\text{Xe}]4f^1$
Pr	59	$[\text{Xe}]4f^3 6s^2$	$[\text{Xe}]4f^2$
Nd	60	$[\text{Xe}]4f^4 6s^2$	$[\text{Xe}]4f^3$
Pm	61	$[\text{Xe}]4f^5 6s^2$	$[\text{Xe}]4f^4$
Sm	62	$[\text{Xe}]4f^6 6s^2$	$[\text{Xe}]4f^5$
Eu	63	$[\text{Xe}]4f^7 6s^2$	$[\text{Xe}]4f^6$
Gd	64	$[\text{Xe}]4f^7 5d^1 6s^2$	$[\text{Xe}]4f^7$
Tb	65	$[\text{Xe}]4f^9 6s^2$	$[\text{Xe}]4f^8$
Dy	66	$[\text{Xe}]4f^{10} 6s^2$	$[\text{Xe}]4f^9$
Ho	67	$[\text{Xe}]4f^{11} 6s^2$	$[\text{Xe}]4f^{10}$
Er	68	$[\text{Xe}]4f^{12} 6s^2$	$[\text{Xe}]4f^{11}$
Tm	69	$[\text{Xe}]4f^{13} 6s^2$	$[\text{Xe}]4f^{12}$
Yb	70	$[\text{Xe}]4f^{14} 6s^2$	$[\text{Xe}]4f^{13}$
Lu	71	$[\text{Xe}]4f^{14} 5d^1 6s^2$	$[\text{Xe}]4f^{14}$
Sc	21	$[\text{Ar}]3d^1 4s^2$	$[\text{Ar}]$
Y	39	$[\text{Kr}]4d^1 5s^2$	$[\text{Kr}]$

1.1.2 Lanthanide Ions

In the majority of lanthanide complexes, the trivalent Ln^{3+} oxidation state is the most common and has the general electronic configurations of trivalent Ln^{3+} ions are $[\text{Xe}]4f^n$. Nevertheless, the stability engendered by an empty ($4f^0$, Ce^{4+}), half-filled ($4f^7$, Eu^{2+} and Tb^{4+}) or fully occupied ($4f^{14}$, Yb^{2+} and Lu^{2+}) f-shell makes these electronic configurations common (or at least accessible), whilst divalent Sm^{2+} ($4f^6$) is also very common, featuring an electronic configuration same to Eu^{3+} . In the last decade, examples of divalent Ln^{2+} complexes across the series (except radioactive promethium) have been synthesised and studied.⁷ The work in this thesis focuses entirely on complexes of trivalent lanthanides.

1.1.3 The Lanthanide Contraction

Figure 1.1 illustrates the radial distribution functions for selected orbitals of a cerium atom, which shows an overlap area between the 4f and 5s/5p orbitals.⁸ The presence of three angular nodes in 4f orbitals results in reduced screening of the nuclear charge, resulting in an increased attraction between the nucleus and outer electrons. Hence, the lanthanide ionic or atomic radii shrink across the series from left to right, termed as *lanthanide contraction*.⁷

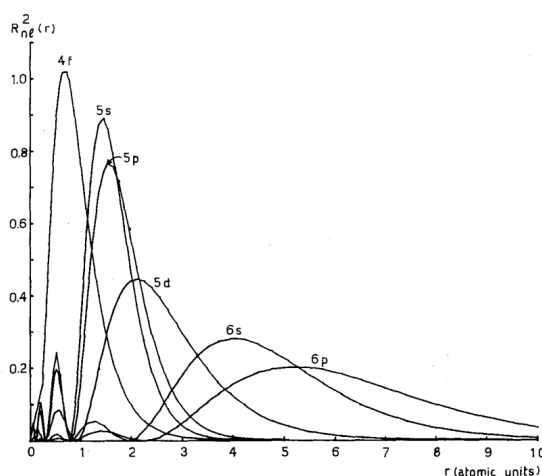


Figure 1.1 Radial distribution functions of 4f, 5s and 5p electrons for cerium, the figure reprinted from Ref. 8, with permission from Elsevier B.V.⁸

1.1.4 Magnetism of Free Ln^{3+} Ions

The electron configuration of lanthanide ions can be represented as $[\text{Xe}]4f^n$ (Table 1.1). The electron energy levels are based on three factors: electron repulsion, spin-orbit coupling and crystal-field effects. The 4f orbitals have a strong angular dependence (Figure 1.2),⁹ and in theory, the electronic ground state should mostly contribute to the magnetic properties based on the strong spin-orbit coupling according to the Russell-Saunders approximation. Furthermore, since the 4f electrons do not effectively shield 5s and 5p electrons from the nucleus and, conversely, the 5s and 5p orbitals effectively shield the 4f electrons from the external (chemical) environment. Because of this special ‘shielding’ structure in lanthanides, the degeneracy of the atomic 4f orbitals is not lifted to an appreciable extent by crystal field effects and electrons can have large angular momentum and strong spin-orbit coupling (SOC), which is much stronger than found in complexes of 3d metal ions.⁶

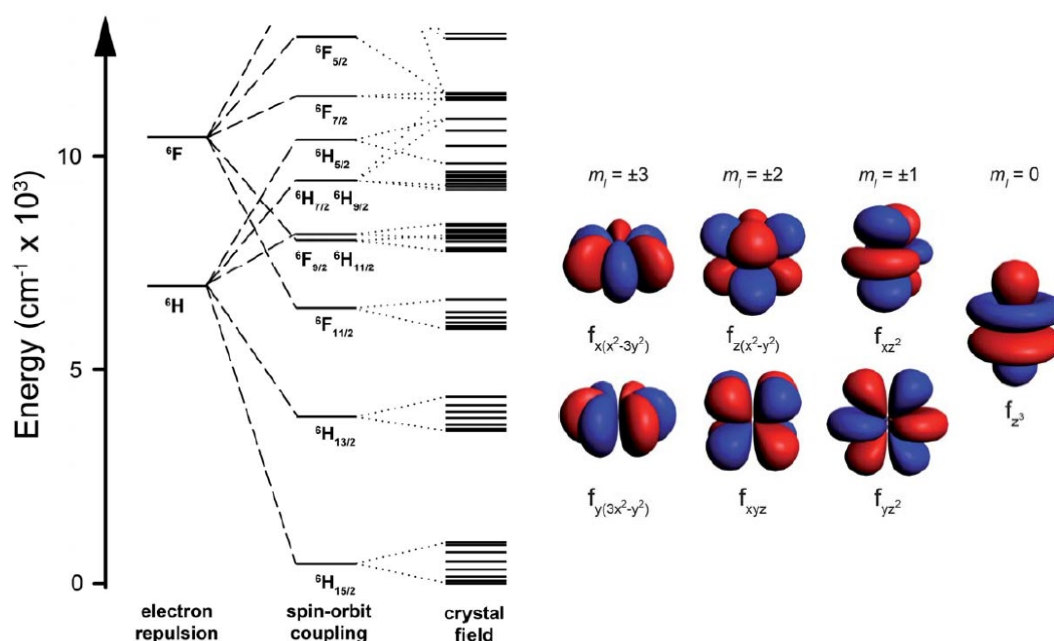


Figure 1.2 *Left.* Energy of electronic structure of the Dy^{3+} ion and *Right.* 4f orbitals from $m = 0$ to $m = \pm 3$, reprinted from Ref. 9, with permission from Royal Society of Chemistry.⁹

1.1.5 Anisotropy of Ln^{3+} Ions

Magnetic anisotropy – which refers to the non-spherical distribution of unpaired electron spin density – is an important consequence of SOC and plays an important role in SMMs. According to quadrupole moment calculations, the distribution of the 4f electron density in Ln^{3+} can be divided, qualitatively, into three types (Figure 1.3): Pm^{3+} , Sm^{3+} , Er^{3+} , Tm^{3+} , Yb^{3+} ions have anisotropic, prolate electron density (stretched along the z-axis); Ce^{3+} , Pr^{3+} , Nd^{3+} , Tb^{3+} , Dy^{3+} , Ho^{3+} ions have anisotropic, oblate electron density (extending in the xy-plane); and Gd^{3+} , Lu^{3+} ions are isotropic.^{6, 9, 10}

Two factors will affect the anisotropy of lanthanide ions: spin-orbit coupling and crystal-field splitting. Because the 4f electrons are shielded by the 5s and 5p orbitals, the lanthanide ions experience weak crystal-field splitting and have large unquenched orbital angular momentum, which leads to strong spin-orbit coupling. However, the contribution from the crystal-field is critical for understanding their SMM properties, a factor which is developed further in this thesis.

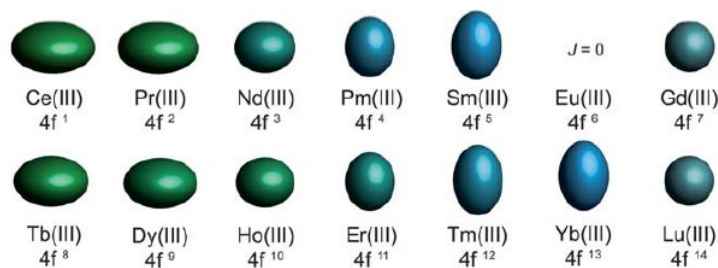


Figure 1.3 Anisotropy of trivalent lanthanide ions 4f electron distribution by quadrupole approximations, reprinted from Ref. 9, with permission from Royal Society of Chemistry.⁹

1.1.6 Crystal-field to Lanthanide Ions

Several theoretical models have been used to explain the distinct magnetic behaviour of many different types of SMMs. For lanthanide complexes, two factors are important for high-quality SMMs: (1) double degeneracy (bistability) in the magnetic ground state with a high magnetic moment; (2) strong SOC, combined with strong single-ion anisotropy and, as recently discovered, a strong crystal field which possibility enhances the oblate or prolate nature of the electron density distribution for the various Ln^{3+} ions. The first factor is associated with the natural property of the specific ions, with Dy^{3+} usually thought of as an ideal for SMM applications, because it is a Kramers ion and maintains the necessary degenerate ground state. The second factor is associated with the strength and symmetry of the crystal field, which is reflected by the coordination environment. A simple model to illustrate the relationship between $4f^n$ electron density and crystal field was published by Long *et al.* in 2011.⁹ The different shapes of 4f electron distribution were used to explain the effect of the crystal field (Figure 1.4): the crystal-field position should complement the shape of the electron density in order to obtain large anisotropy.

For the oblate ions Ce^{3+} , Pr^{3+} , Nd^{3+} , Tb^{3+} , Dy^{3+} and Ho^{3+} , the crystal-field should be placed along the z-axis direction. Conversely, if the crystal-field is set in the xy-plane for these lanthanides, the energy separation between ground and excited state(s) will decrease and magnetic relaxation will be subject to a low barrier (Figure 1.4 *left*). This model has been involved to explain the excellent magnetic property of dysprosium complexes in sandwich structures, such as $[(\text{Cp}^{\text{IPr5}})\text{Dy}(\text{Cp}^*)]^+$.^{5, 11, 12} For prolate ions, Pm^{3+} , Sm^{3+} , Er^{3+} , Tm^{3+} and Yb^{3+} , coordination in the equatorial xy-plane is preferred, (Figure 1.4 *right*). Some reported Er^{3+} samples fit with this rule of thumb, such as $\text{Er}[\text{N}(\text{SiMe}_3)_2]_3$.¹³ Although this model is very simple¹⁴, it is a helpful tool to predict the potential magnetic property for lanthanide SMMs, especially in the case of lanthanide metallocenes.⁹ Further detail about the role of the crystal field in lanthanide SMMs will be discussed in the following sections.

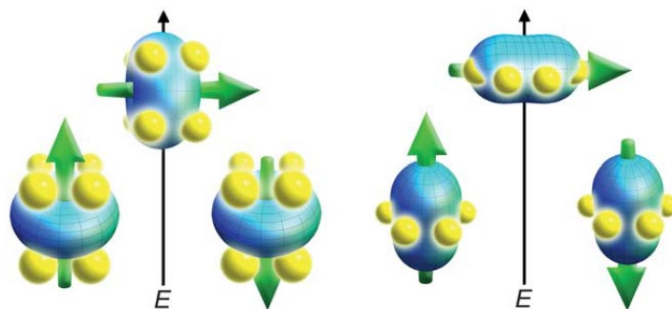


Figure 1.4 Low- and high-energy level of the 4f orbital electron density with respect to the crystal-field for oblate (*left*) and prolate (*right*) ions. The green arrow represents the orientation of the spin angular momentum coupled to the orbital moment. Reprinted from Ref. 9, with permission from Royal Society of Chemistry.⁹

1.2 Magnetism in Single-molecule Magnet

1.2.1 The First SMM in 1993

The discovery of SMMs can be tracked back to the early 1990s. Technically, the first characterization of a molecule displaying magnetic hysteresis was reported in several papers by Sessoli *et al.* in 1993,¹⁵⁻¹⁷ focusing on the now famous cluster $[\text{Mn}_{12}\text{O}_{12}(\text{CH}_3\text{COO})_{16}(\text{H}_2\text{O})_4]$ (Mn_{12}Ac). Although this manganese cluster was first synthesized in 1980 by Lis (Figure 1.5),^{18, 19} its magnetic properties were not investigated until the 1990s. In the paper, the authors indicated its potential to become an information storage material. As a result, Mn_{12}Ac became the first SMM and heralded the start of a new research field, which has grown substantially in the following decades. According to a theoretical calculation^{20, 21}, the relaxation time of Mn_{12}Ac is two months at 2 K or even 50 years at 1.5 K, which is longer than found in bulk magnetic materials. However, the hysteresis loop in Mn_{12}Ac can only be observed below 2.8 K.

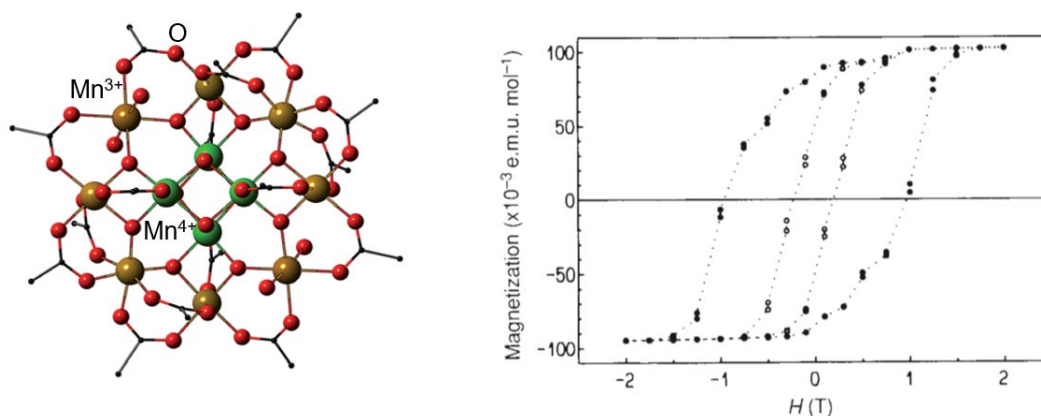


Figure 1.5 *Left:* molecular structure of the Mn_{12}Ac cluster, Reprinted from Ref. 19, with permission from Royal Society of Chemistry.¹⁹ *Right:* The hysteresis loops of Mn_{12}Ac at 2.2 K (black dots) and 2.8 K (white dots). Reprinted from Ref. 15, with permission from Springer Nature.¹⁵

1.2.2 Basic Properties of SMMs

Single-molecule magnets are bistable magnetic molecules. Generally, an SMM should display hysteresis based on the properties of individual molecules rather than relying on interactions across magnetic domains, as in traditional bulk magnets.²² In that respect, the nanoscale dimensions of SMMs have been proposed as the basis of information storage devices.

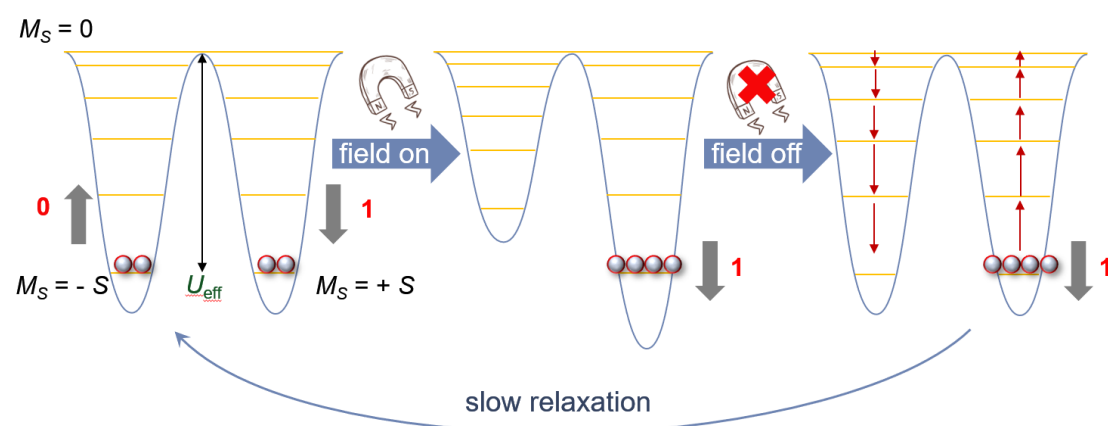


Figure 1.6 The double-well model of magnetic bistability in SMMs.

SMMs display the bistability, which can be described in terms of a simplified double potential energy well (Figure 1.6).²³ As mentioned previously, the energies of the unpaired electrons are subject to three factors: electron repulsion, spin-orbital coupling and crystal-field effects, which jointly induces the effective energy barrier gap between ground state ($M_S = \pm S$) and the excited states. In Figure 1.6 (left), the two wells on the bottom with spins of opposite orientations (up and down, or $M_S = \pm S$) refer to the two components of the bistable ground state (magnetic bistability), which can represent binary information 0 and 1 in storage devices. Originally, both sides of the potential are equally populated, so there is no net magnetization. However, if an external magnetic field is applied, the potential wells lose their degeneracy. One well goes to a lower energy state and the other one will increase in energy, which leads to a change of spin distribution and all the spins will settle in the new ground state and as a result the magnetic moment is trapped in one of the wells (Figure 1.6 middle).

After removing the magnetic field, anisotropy generates an effective energy barrier (U_{eff}) to repopulation of the two M_S states below a blocking temperature (T_B). Therefore, the digital signal '1' in this depiction is saved in the SMM (Figure 1.6 *right*). Although the spins will eventually relax to their equilibrium populations, the process could take a long time (e.g. even several years).²⁰

1.2.3 The Effective Energy Barrier (U_{eff}) and the Blocking Temperature (T_B)

As most reported SMMs show this magnetic bistability at extremely low temperatures (typically liquid-helium), one of the present challenges is to discover or develop higher quality SMMs such function at higher temperatures. In that respect, two physical parameters, *the effective energy barrier and the blocking temperature*, are widely used to determine and evaluate the 'quality' of such candidates for SMMs.

(1) The Effective Energy Barrier (U_{eff})

The effective energy barrier can be considered as the 'wall' between the two spin wells (Figure 1.6), which refers to the energy gap between the ground state and the highest excited magnetic state. SMMs with higher effective energy barrier normally have better performance. In theory, the effective energy barrier value refers to the anisotropy energy barrier ΔE (energy to reorientate the magnetization).

In a strongly exchange-coupled system, such as one containing 3d transition ions, it can determine by the largest possible spin of ground state value (S) and zero-field splitting parameter (D) according to Equation 1:

$$\Delta E = DS^2 \text{ or } D(S^2 - 1/4) \quad (1)$$

However, because the exchange interactions between ions in lanthanide complexes are weaker, Equation 1 is not suitable. Instead, the thermal energy barrier can be determined using an Arrhenius-type equation (Equation 2):

$$\tau = \tau_0 \exp(U_{\text{eff}}/K_B T) \text{ or } \tau = \tau_0 \exp(\Delta E/K_B T) \quad (2)$$

In Equation 2, τ represents the relaxation time, τ_0 is the pre-exponential factor, K_B is the Boltzmann's constant and T refers to temperature.⁶

(2) The Magnetic Blocking Temperature (T_B)

The blocking temperature can be considered as the 'proper' temperature at which an SMM can act as a magnet. It has to be mentioned that three definition of blocking temperature can be used: (a) the temperature at which the magnetic relaxation time is 100s; (b) the highest temperature at which a hysteresis loop can be observed, or (c) the temperature at which the field-cooled and zero-field cooled (FC-ZFC) magnetization diverge.⁹ Generally, the definition of (b) is widely accepted, which is also the standard definition in this thesis. Even though, caution should be used when comparing blocking temperatures in different SMMs.

1.2.4 Magnetic Relaxation and Quantum Tunnelling of the Magnetization (QTM)

The record SMM energy barrier is currently 1541 cm^{-1} (2219 K), while the record of blocking temperature is 80 K.⁵ Up to four different types of process can contribute to the magnetic relaxation in SMMs: Orbach processes, Raman processes, direct processes (Figure 1.7 *left*) and QTM (Figure 1.7 *right*), according to the following equation (Equation 3):

$$\tau^{-1} = \tau_0^{-1} \exp(-U_{\text{eff}}/K_B T) + CT^n + AT + \tau_{\text{QTM}}^{-1} \quad (3)$$

Orbach + Raman + Direct + QTM

(a) The direct process is a single-phonon process (Figure 1.7a), in which the phonon is excited to an energy of $\Delta = h\nu$, and is then emitted to the ground state. In Equation 3, the constant A is associated to the Kramers and non-Kramers doublets.

(b) The Raman process is a two-phonon process (Figure 1.7b), in which the phonon is excited to a virtual state with the absorption energy of $\Delta = h\nu_1$ and then transferred to its ground state with the emission energy of $\Delta = h\nu_2$. In Equation 3 (on page 16), the Raman exponent n depends on the exact energies of ground doublets.

(c) Compared to Raman process, the Orbach process has a similar two-phonon process (Figure 1.7c), but through a real state with the energy of $\Delta = h(\nu_1 - \nu_2)$, which is described by the Arrhenius in Equation 2 and 3 (on page 16).

(d) The QTM process corresponds to a spin inversion through the potential energy barrier. QTM does not only happen in the ground state but also in excited energy states (thermally assisted QTM). Different from the other three thermal relaxation processes, the quick spin-transfer of QTM leads to the reduction of relaxation time and results in a lower blocking temperature. Hence, in order to achieve high performing SMMs, strategies should be applied to suppress QTM.^{6, 24}

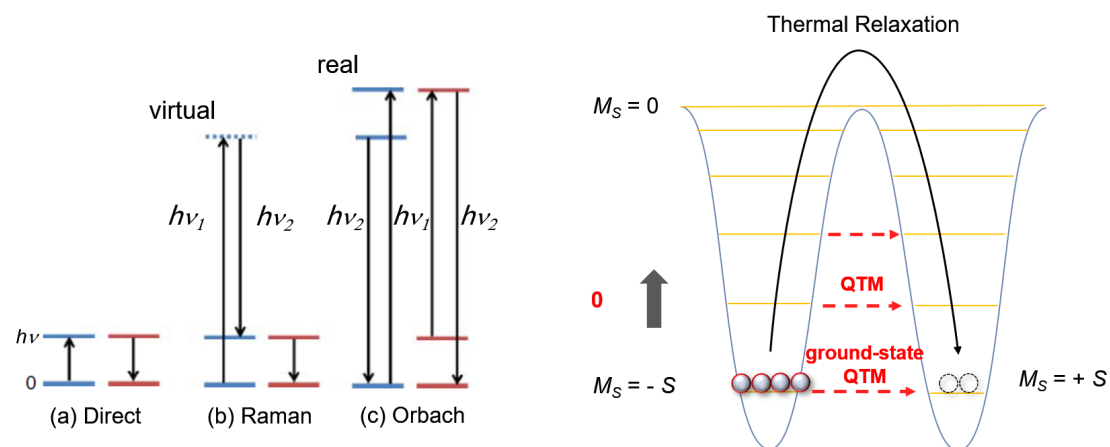


Figure 1.7 Left: Description of direct (a), Raman (b) and Orbach (c) processes, reproduced from Ref. 24, with permission from John Wiley & Sons.²⁴ Right: a double-well model represents the process quantum tunnelling (red dotted lines).

1.2.5 Magnetic Property Characterization

The common instrument used to study the magnetic properties of SMMs is SQUID (superconducting quantum interference device). The SQUID measurements allow the determination of to the DC and AC magnetic susceptibility, the magnetization and the

magnetic hysteresis behaviour of a potential SMM. As an example, the sandwich complex $[(\text{Cp}^{\text{ttt}})_2\text{Dy}][\text{B}(\text{C}_6\text{F}_5)_4]$ is used to introduce some of the common magnetic measurements by SQUID on SMMs.¹¹

(1) DC Magnetic Measurement

Generally, the DC measurement gives information of the thermal and field dependence of the magnetic properties for a SMM. For example, in Figure 1.8, the $\chi_M T$ vs. T plots of $[(\text{Cp}^{\text{ttt}})_2\text{Dy}][\text{B}(\text{C}_6\text{F}_5)_4]$ (2_{Dy}) and its precursor $[(\text{Cp}^{\text{ttt}})_2\text{DyCl}]$ (1_{Dy}) show a gradual reduction of $\chi_M T$ with the decrease of temperature from 300 to 80 K. Below 80 K, the $\chi_M T$ of $[(\text{Cp}^{\text{ttt}})_2\text{Dy}][\text{B}(\text{C}_6\text{F}_5)_4]$ drops dramatically, which illustrates its stronger thermal dependence at lower temperature, compared to the slight decrease of $\chi_M T$ for compound $[(\text{Cp}^{\text{ttt}})_2\text{DyCl}]$.¹¹

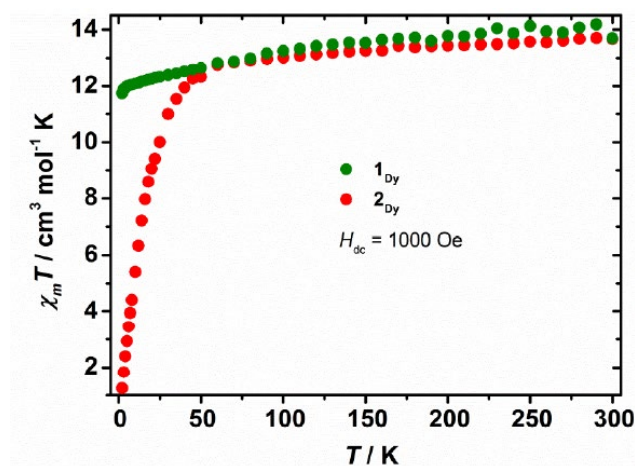


Figure 1.8. Plots of $\chi_M T$ vs. temperature for $[(\text{Cp}^{\text{ttt}})_2\text{DyCl}]$ (1_{Dy}) and $[(\text{Cp}^{\text{ttt}})_2\text{Dy}][\text{B}(\text{C}_6\text{F}_5)_4]$ (2_{Dy}), reproduced from Ref. 11, with permission from John Wiley and Sons.¹¹

A dynamic DC field can also be applied in forward and reverse directions to observe the hysteresis loops at different temperatures, in which the maximum temperature will be defined as the blocking temperature. For instance, the $[(\text{Cp}^{\text{ttt}})_2\text{Dy}][\text{B}(\text{C}_6\text{F}_5)_4]$ gives obvious opened hysteresis loops up to 60 K using an average sweep rate of 3.9 mT s^{-1} , which defines its blocking temperature ($T_B = 60 \text{ K}$) (Figure 1.9).¹¹

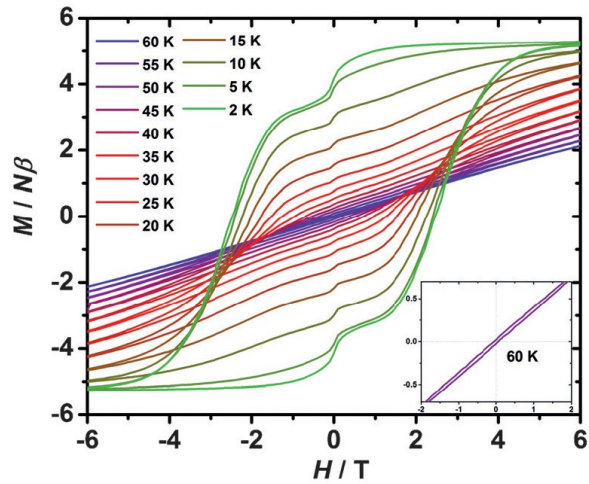


Figure 1.9 Thermal hysteresis loops in a changing DC field for $[(\text{Cp}^{\text{ttt}})_2\text{Dy}][\text{B}(\text{C}_6\text{F}_5)_4]$. Reproduced from Ref. 11, with permission from John Wiley and Sons.¹¹

Meanwhile, for a high-quality SMM with longer relaxation time than that measured in AC magnetic field, the relaxation time can be directly measured in a DC field (magnetic decay experiments): a DC field will be applied and the temperature will be cooled down to the required value, then remove the DC field and measure the function of magnetization moment changing with the time (M / t).

(2) AC Magnetic Susceptibility

The AC susceptibility measurement is specifically utilized to study the dynamic magnetism in SMMs. A small oscillating magnetic field is applied to measure the susceptibility in zero DC field or sometimes in an applied DC field. With the slow relaxation processes under blocking temperature, the magnetic susceptibility will be divided into two components: in-phase (χ') and out-of-phase (χ''), with a high-frequency AC field. The susceptibility plots can be represented in χ' / χ'' versus temperature (T) or versus frequency (ν).

As mentioned previously, the maximum temperature at which a peak can be observed in an out-of-phase (χ'') susceptibility is regarded as the 'blocking temperature' in some publications, although the acknowledged T_B refers to the highest temperature at which hysteresis loops can be observed (which depends on the sweep rate of the

magnetic field). However, its value is usually not equal to the defined blocking temperature (T_B) and we normally call it the temperature maxima in this thesis. In addition, if a supplementary DC field is applied in the original AC field, it will change the temperature dependence of the ac susceptibility. For $[(\text{Cp}^{\text{ttt}})_2\text{Dy}][\text{B}(\text{C}_6\text{F}_5)_4]$, the out-of-phase susceptibility are shown in Figure 1.10, in which a maxima can be observed at 111 K in the χ'' plot. Compared to its defined blocking temperature of $T_B = 60$ K, the value of maxima is clearly much higher.¹¹

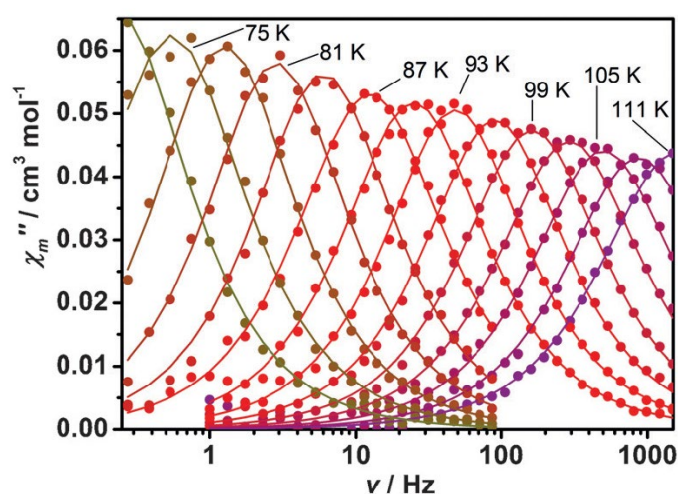


Figure 1.10 Temperature dependence of the out of phase (χ'') for $[(\text{Cp}^{\text{ttt}})_2\text{Dy}][\text{B}(\text{C}_6\text{F}_5)_4]$ at indicated frequencies under zero DC field at AC frequencies of $\nu = 0.1$ –1488 Hz from 75–111 K. Reproduced from Ref. 11, with permission from John Wiley and Sons.¹¹

The AC susceptibility data is analysed using equations arising from the Debye model (Equation 4):

$$\chi'(v_{ac}) = \chi_{\infty} + \frac{(\chi_s - \chi_{\infty})[1 + (2\pi v_{ac}\tau)^{1-\alpha} \sin(\alpha\pi/2)]}{1 + 2(2\pi v_{ac}\tau)^{1-\alpha} \sin(\alpha\pi/2) + (2\pi v_{ac}\tau)^{2(1-\alpha)}}$$

$$\chi''(v_{ac}) = \frac{(\chi_s - \chi_{\infty})(2\pi v_{ac}\tau)^{1-\alpha} \cos(\alpha\pi/2)}{1 + 2(2\pi v_{ac}\tau)^{1-\alpha} \sin(\alpha\pi/2) + (2\pi v_{ac}\tau)^{2(1-\alpha)}}$$

With Equation 4 (also known as Cole-Cole fitting), a series of variable (χ_s , χ_{∞} , α and τ) can be extracted and the plot of relaxation time versus inverse temperature is obtained. Further, after obtaining the best fit of the data with Equation 3 (on page 16), the parameters U_{eff} , τ_0 , C and n are obtained. Thus, we can find which relaxation processes happen in the SMM and their relative importance at a given temperature. For $[(\text{Cp}^{\text{ttt}})_2\text{Dy}][\text{B}(\text{C}_6\text{F}_5)_4]$, the plot of τ vs. T^{-1} of AC susceptibility is shown in Figure 1.11a. With a further fitting with the formula of $\tau^{-1} = \tau_0^{-1}e^{-U_{\text{eff}}/k_{\text{B}}T} + CT^n$, it indicates that the whole relaxation includes the Orbach and Raman processes, with an effective energy barrier of 1277 cm^{-1} .¹¹

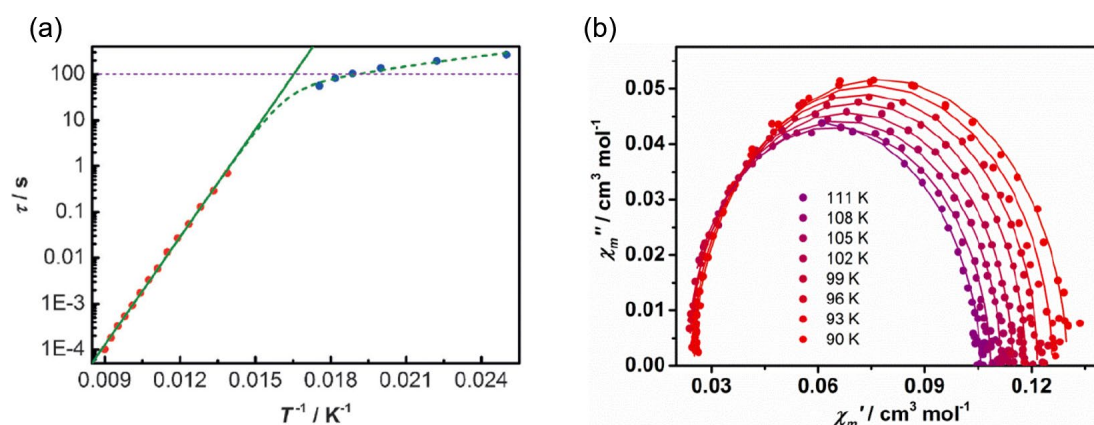


Figure 1.11 Temperature dependence of the relaxation time (a) and Cole-Cole plots for the AC susceptibilities in zero DC field (b) for $[(\text{Cp}^{\text{ttt}})_2\text{Dy}][\text{B}(\text{C}_6\text{F}_5)_4]$. Reproduced from Ref. 11, with permission from John Wiley and Sons.¹¹

If we make a plot of in-phase (χ') versus out-of-phase (χ''), an approximate semi-circular curve for $[(\text{Cp}^{\text{ttt}})_2\text{Dy}][\text{B}(\text{C}_6\text{F}_5)_4]$ is given (Figure 1.11b), which is called a Cole-Cole plot. In SMMs, there may be several pathways and this is reflected in asymmetry in the curve. In Figure 1.11, the data points and solid lines represent the experimental data and the fitting data, respectively, which also shows the quality of the fitting operation.

(3) Theoretical Calculation of Electronic Structure

At present, *ab initio* multireference theoretical calculations are widely used in SMMs, which simulate the energy states based on the non-optimized molecular structures.²⁵ The comparison of the experimental data and calculation results help us better understand the relaxation processes and overall magnetic property. Calculations in the Layfield group are carried out through a collaboration with Dr Akseli Manksikkamäki at the University of Oulu, Finland. For example, the *ab initio* calculation of $[(\text{Cp}^{\text{ttt}})_2\text{Dy}]^+$ cation illustrates its first non-negligible transition occurs around KD6 (KD refers to Kramers doublet) with the energy of 1156 cm^{-1} (Figure 1.12), which matches very well with the experimental effective energy barrier of 1277 cm^{-1} .¹¹

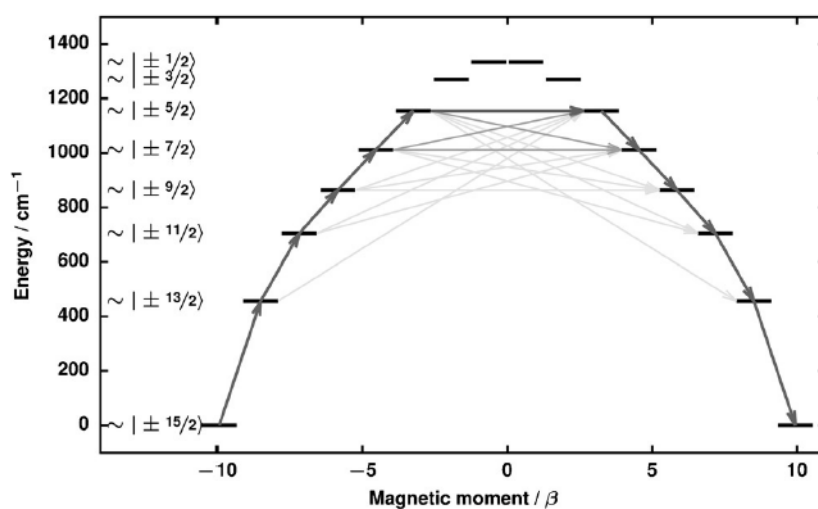


Figure 1.12 The *ab initio* calculated barriers for the local relaxation of magnetization for $[(\text{Cp}^{\text{ttt}})_2\text{Dy}][\text{B}(\text{C}_6\text{F}_5)_4]$. Reproduced from Ref. 11, with permission from John Wiley and Sons.¹¹

1.3 A Brief Overview of SMMs

Nowadays hundreds of SMMs are reported each year, occasionally with dramatic improvements of the magnetic properties. In this part, several typical samples are presented in order to briefly introduce the development of SMMs and also the synthetic strategies to access them. To closely associate with the topic of my project, the discussion will mainly focus on the lanthanide SMMs with sandwich structures, especially dysprosium metallocene SMMs.

1.3.1 The Early Years of SMMs: Manganese Polynuclear Clusters

Since the first SMM (Mn_{12}Ac) was published in 1993, a golden age of manganese coordination chemistry began (Figure 1.13).²⁶

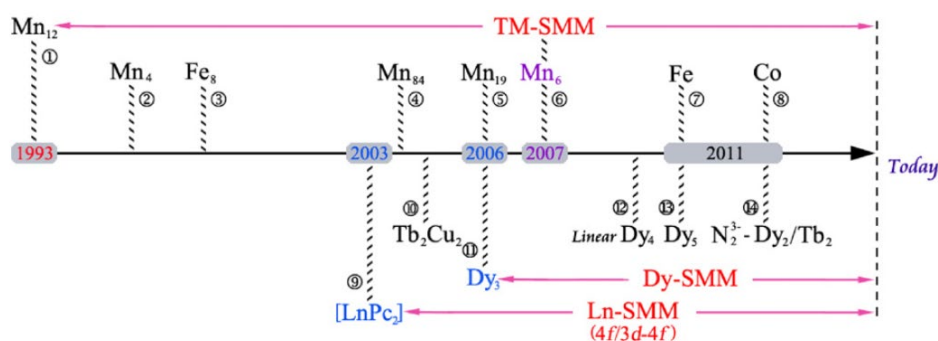


Figure 1.13 Timeline of SMM development. Reprinted from Ref. 26, with permission from Elsevier.²⁶

Several derivatives of the original Mn_{12}Ac cluster have been synthesized to study the effect of changing the crystal-field on the magnetic properties. Accordingly, the acetate group ($[\text{CH}_3\text{CO}_2]^-$) has been replaced by other acetate groups, i.e., $[\text{PhCO}_2]^-$,¹⁶ $[\text{BrCH}_2\text{CO}_2]^-$,^{28, 29} and $[\text{ClCH}_2\text{CO}_2]^-$.³⁰ While, larger clusters including more manganese

ions^{31, 32} or smaller structures with fewer Mn^{n+} centres ions have also been synthesised.³³ Even though, the highest effective energy barrier in such kind of compounds ($[Mn_6O_2(Et-sao)_6(O_2CPh)_2(EtOH)_4(H_2O)_2]$, $saoH_2 = \text{salicylaldoxime}$) is only slightly increased to 60 cm^{-1} (86 K) and the blocking temperature is normally below 5 K.³⁴ The magnetic properties of polynuclear manganese clusters are possibly due to their complicated chemical environments, which can be different for different manganese ions. The heterogeneous crystal-field creates distortion of axial anisotropies for different manganese ions and, finally, the overall anisotropy decreases. In recent years, as the importance of the symmetry strategy has become better understood in SMMs, several single-ion magnetic Mn^{3+} complexes have been reported.³⁵⁻⁴¹ The highest effective energy barrier to date is only 18.5 cm^{-1} (26.6 K), even with a better symmetry of the crystal-field and in an applied DC field, which indicates that complexes of this type may not be ideal as SMMs.

1.3.2 Other 3d Transition Metal SMMs

In 1997, the first non-manganese SMM was reported, i.e., the Fe_8 cluster $[(tacn)_6Fe_8OH_{12}]^{8+}$, with an energy barrier of 17 cm^{-1} (24.5 K, $tacn = \text{triazacyclononane}$).⁴² However, similar to the manganese SMMs, polynuclear 3d-cluster based on other transition metals cannot meet the requirements of higher magnetic performance.

In theory, for 3d transition metal ions, the spin-orbit coupling can provide anisotropy, which gives a large value of zero-field splitting (Equation 1 on page 15). However, it is found that the magnitude of D will decrease if the crystal-field has lower geometrical symmetry. In order to improve the crystal-field symmetry and easily control the structure through chemical synthesis, the study of single-ion or monometallic SMMs has become a hot topic. The reported 3d- or 5d-based single-ion SMMs mainly includes metals like Fe, Co, Ni and Cr.^{43, 44} According to their magnetic data, SMMs based on iron and cobalt display better magnetic properties.

1.3.2.1 Iron single-ion SMMs

A well-known Fe-based single-ion SMM $K[Fe\{C(SiMe_3)_3\}_2]$ was reported by Long *et al.*⁴⁵ In the molecular structure, the anion $[Fe\{C(SiMe_3)_3\}_2]^-$ (Figure 1.14) has an approximately linear structure ($C-Fe-C = 179.2^\circ$). The effective energy barrier of 226 cm^{-1} was relatively large (for the time), and the blocking temperature was determined to be 6.5 K. Long *et al.* also made other linear examples, like $[Fe(I)(N(SiMe_3)_3)_2]^-$ and $[Fe(II)(C(TMS)_3)_2]$, however, the energy barriers of these latter two iron complexes are not as good as for the one in $[Fe\{C(SiMe_3)_3\}_2]^-$.^{46, 47}

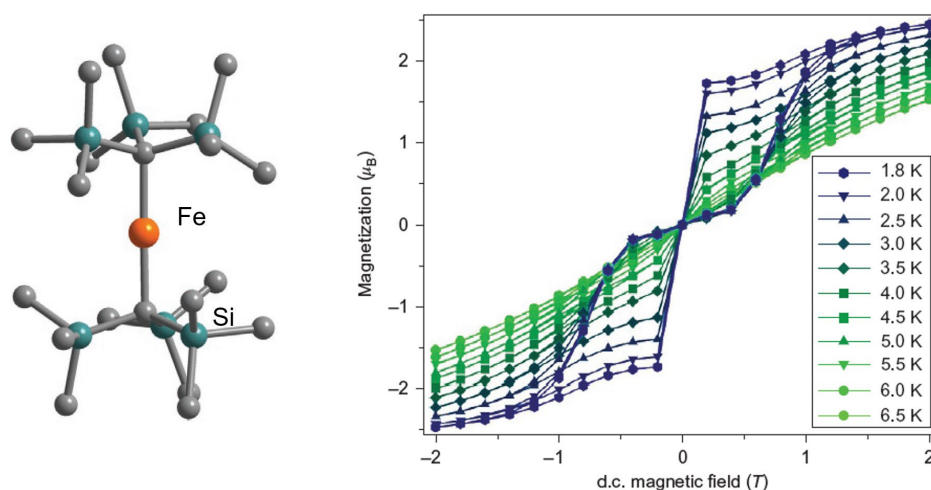


Figure 1.14 Structure of the $[Fe\{C(SiMe_3)_3\}_2]^-$ anion, and hysteresis loops (1.8 K–6.5 K) under induced DC field. Reprinted from Ref. 45, with permission from Springer Nature.⁴⁵

1.3.2.2 Cobalt SMMs

In 2002, the first cobalt SMM was described, i.e., the $[Co_4(hmp)_4(MeOH)_4Cl_4]$ (hmp^- = the anion of hydroxymethylpyridine) cluster was found to display SMM behaviour,^{48, 49} In 2011, the first Co-based single-ion SMM ($[Co(SPh)_4]^{2-}$) was reported and is also the first transition metal single-ion SMM to show magnetic relaxation in zero DC-field.⁵⁰ The properties of the Co^{2+} single-ion SMM quickly attracted attention, leading to many more cobalt single-ion complexes. The highest effective energy barrier in a cobalt single-ion SMM is currently 413 cm^{-1} (594 K), which is reported by Gao *et al.* in

2016.⁵¹ The $[(s\text{IPr})\text{Co}(\text{II})(\text{NDmp})]$ complex (Figure 1.15, NDmp = 2,6-dimesitylphenyl) has a near linear structure ($s\text{IPr}-\text{Co}-\text{NDmp} = 175.7^\circ$). In the same paper, other two linear Co^{2+} SMMs, $[(\text{IPr})\text{Co}(\text{NDmp})]$ ($\text{IPr}-\text{Co}-\text{NDmp} = 173.0^\circ$) and $[(\text{cyIPr})\text{Co}(\text{NDmp})]$ ($\text{cyIPr}-\text{Co}-\text{NDmp} = 177.5^\circ$) are reported to have lower effective barrier of 297 cm^{-1} and 288 cm^{-1} respectively.

Comparing all the 3d single-ion SMMs,³⁰ the high symmetry strategy seemingly helps to improve the energy barrier, especially compared to the early polynuclear clusters. However, the symmetry is obviously not the only factor that affects the magnetism, typically, some of high symmetric linear SMMs have even weaker barriers. Actually, the choice of ligands (crystal-field properties) and d^n configuration will also significantly influence the relaxation process. On the other hand, it can be noticed that, along with the increases in energy barrier, the blocking temperature is rarely mentioned because the value is usually under 10 K, even with the induced DC field and with fast hysteresis scan rates.

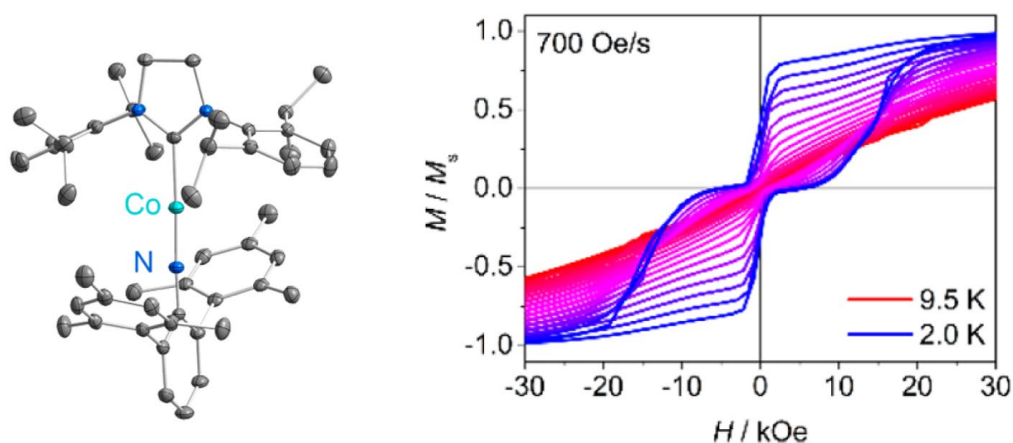


Figure 1.15 Structure of $[(s\text{IPr})\text{CoNDmp}]$, and hysteresis loops (2.0 K–9.5 K). Reprinted from Ref. 51, with permission from American Chemical Society.⁵¹

1.3.3 Lanthanide single-ion SMMs

The blocking temperature and effective energy barrier are the descriptors driving the development of SMMs. Initially, lanthanide complexes were not regarded as a

promising SMM candidate due to the weak exchange coupling and weaker crystal-field effects. However, some research has shown that lanthanide mononuclear complex with low coordination numbers can easily take advantage of the strong spin-orbit coupling and enhance the anisotropy.^{5, 11}

1.3.3.1 Terbium Single-ion SMMs

In 2003, the first Ln-SMM complexes, $[\text{NBu}_4][\text{LnPc}_2]$ (Pc = dianion of phthalocyanine; Ln = Tb^{3+} , Dy^{3+} , Ho^{3+} , Er^{3+} , Tm^{3+} , Yb^{3+}), were described by Ishikawa *et al.*, in which the lanthanide ions are coordinated by the $[\text{Pc}]^{2-}$ ligand in a sandwich-like structure (Figure 1.16 *left*).^{52, 53} The D_{4d} symmetry of crystal field matches with the crystal-field requirement of oblate $4f^8$ electron density of Tb^{3+} model in Long's paper.⁹ However, only the $[\text{Pc}_2\text{Tb}]^-$ anion has a good effective energy barrier of 230 cm^{-1} (331 K), while the $[\text{Pc}_2\text{Dy}]^-$ one has a distinct effective barrier of 28 cm^{-1} (40 K). Other $[\text{LnPc}_2]^-$ (Ln = Ho^{3+} , Er^{3+} , Tm^{3+} , and Yb^{3+}) did not show any slow magnetic relaxation. A cursory explanation of this phenomenon is that the $M_J = \pm 6$ state of Tb^{3+} has an oblate shape of electron density. Despite the difference between the Tb^{3+} and Dy^{3+} Pc-SMMs, a series of modified-structures was published in the following years, including versions with different oxidation levels, *e.g.* $[\text{Pc}_2\text{Tb}]^0$ ($U_{\text{eff}} = 410 \text{ cm}^{-1}$)⁵⁴ and $[\{\text{Pc}(\text{OEt})_8\}_2\text{Tb}][\text{SbCl}_6]$ ($U_{\text{eff}} = 550 \text{ cm}^{-1}$).^{55, 56} Another example, $[\text{Tb}\{(\text{O}-(\text{C}_6\text{H}_4)-p\text{-}^t\text{Bu})_8\text{Pc}\}(\text{Pc}')]$, was reported by Coronado *et al.* in 2013. This sandwich structure (Figure 1.16 *right*) is coordinated by two different ligands, Pc and $\text{Pc}(\text{O}-(\text{C}_6\text{H}_4)-p\text{-}^t\text{Bu})_8$, with an effective barrier of 652 cm^{-1} (939 K).⁵⁷

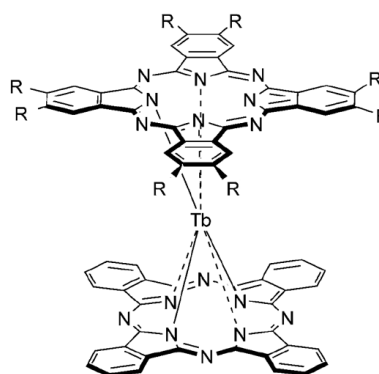
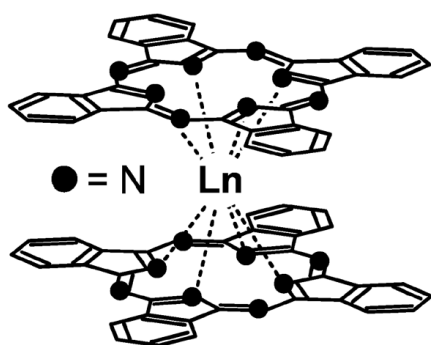


Figure 1.16 *Left:* structure of $[\text{Pc}_2\text{Tb}]^-$ anion, reprinted from Ref. 52, with permission from American Chemical Society.⁵² *Right:* structure of $[\text{Tb}(\text{O}(\text{C}_6\text{H}_4)\text{-}p\text{-}^t\text{Bu})_8\text{Pc}(\text{Pc})]$, reprinted from Ref. 57, with permission from John Wiley & Sons.⁵⁷

1.3.3.2 Erbium Single-ion SMMs

The first Er-SMM was the polyoxometalate sandwich complex $[\text{ErW}_{10}\text{O}_{36}]^{9-}$ (Figure 1.17) by Coronado *et al.* in 2008, in which an Er^{3+} ion is coordinated in a D_{4d} crystal-field by POMs (polyoxometalates).⁵⁸ The U_{eff} value is 38 cm^{-1} (55 K), however, the Tb^{3+} , Dy^{3+} , Tm^{3+} , and Yb^{3+} versions do not have any slow relaxation behaviour except those containing Ho^{3+} (3.47 cm^{-1}) and Nd^{3+} (51.4 cm^{-1} , $H_{\text{dc}} = 1 \text{ kOe}$)⁵⁹. Notably, the $\text{Er}^{3+} 4f^{10}$ ion has a prolate shape, which should prefer a transverse crystal-field from the xy -plane. Furthermore, it is difficult to explain the distinct properties of other $[\text{LnW}_{10}\text{O}_{36}]^{9-}$ sandwich complexes. Here, the ‘prolate and oblate electron’ model of Ln^{3+} displays its limitations.

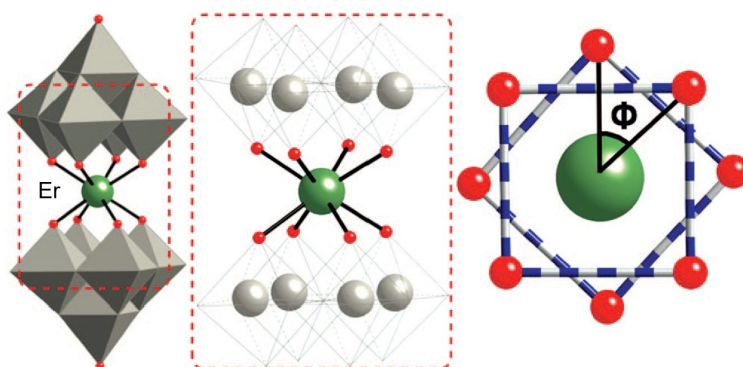


Figure 1.17 Structure of the $[\text{ErW}_{10}\text{O}_{36}]^{9-}$ and the coordination environment. Reprinted from Ref. 58, with permission from American Chemical Society.⁵⁸

Gao *et al.* were the first to introduce the COT^{2-} ligand (cyclo-octatetraenide, $\text{C}_8\text{H}_8^{2-}$) into Er^{3+} single-ion SMMs in 2011.⁶⁰ The combination of Cp^* and COT ligand gives complex $[(\text{Cp}^*)\text{Er}(\text{COT})]$ (Figure 1.18 *left*), which has two thermal relaxation paths with effective energy barrier of 224 cm^{-1} (323 K) and 137 cm^{-1} (197 K), respectively. Subsequently, a series of COT -based SMMs were reported, i.e., $[\text{Er}(\text{COT})_2]^-$ ($U_{\text{eff}} = 147$

cm^{-1} and 199 cm^{-1})^{61, 62} and $[\text{Li}(\text{DME})_3][\text{Er}(\text{COT}'')_2]$ ($U_{\text{eff}} = 130 \text{ cm}^{-1}$, $\text{COT}'' = 1,4$ -bistrimethylsilyl-cyclooctatetraenyl dianion).¹⁴ Using the isoelectronic to $(\text{Cp}^*)^-$, boron ligand $(\text{C}_5\text{H}_5\text{BNEt}_2)^-$, the effective energy barrier in the Er^{3+} complex $[(\text{C}_5\text{H}_5\text{BNEt}_2)\text{Er}(\text{COT})]$ (Figure 1.18 right) was measured to be 300 cm^{-1} (421 K).⁶³

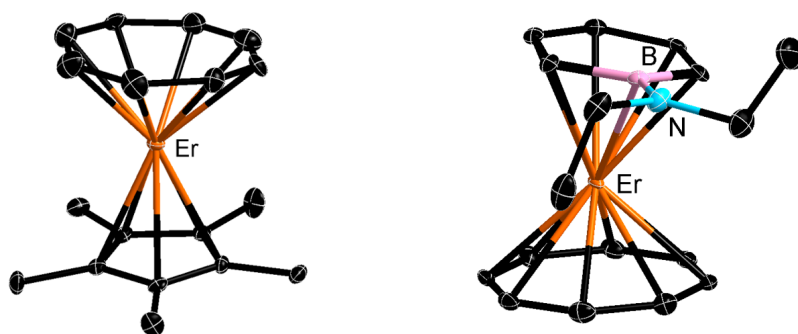
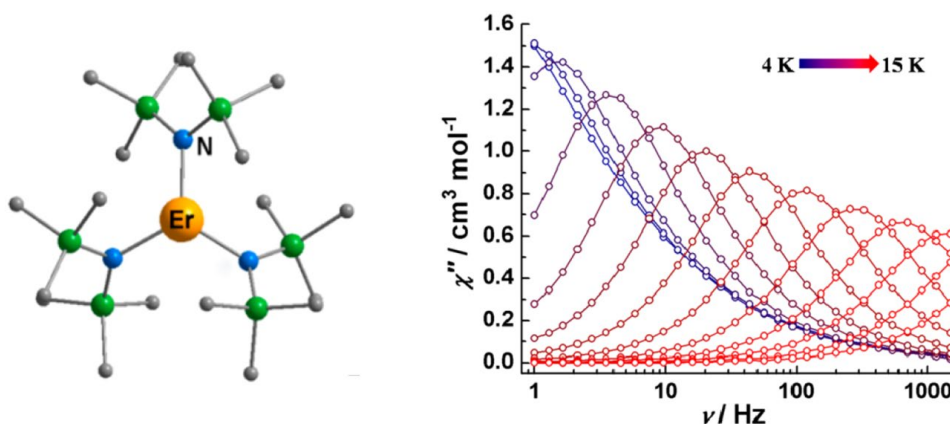


Figure 1.18 Structures of $[(\text{Cp}^*)\text{Er}(\text{COT})]$ (left) and $[(\text{C}_5\text{H}_5\text{BNEt}_2)\text{Er}(\text{COT})]$ (right). The structures are reproduced based on the cif files from the Ref. 60 and 63.^{60, 63}

For Er^{3+} SMMs, complexes with a pure equatorial crystal-field are rarely reported. The best-known complex was made by Tang *et al.* in 2014 (Figure 1.19).¹³ This $\text{Er}[\text{N}(\text{SiMe}_3)_2]_3$ complex has three $\text{N}(\text{SiMe}_3)_2$ ligands coordinated on the equatorial plane in local C_{3v} -symmetry. This complex gives a U_{eff} of 85 cm^{-1} (122 K), while the Dy^{3+} version does not show any slow magnetic relaxation. In this case, it can be explained that the prolate Er^{3+} ion is favoured by the equatorial crystal-field, while the ground state of oblate Dy^{3+} ion is not well stabilized.



temperature of 12 K (Figure 1.21).⁹⁸ This symmetry of the dysprosium can be switched to octahedral after removing a molecule of MeOH, i.e., $[\text{Zn}_2\text{DyL}_2(\text{MeOH})]\text{NO}_3\cdot\text{H}_2\text{O}$ ($U_{\text{eff}} = 44 \text{ cm}^{-1}$, $H_{\text{dc}} = 1.2 \text{ kOe}$). Based on *ab initio* calculations, the D_{5h} is a better symmetry than O_h , which may explain the dramatic barrier change between these two structures.

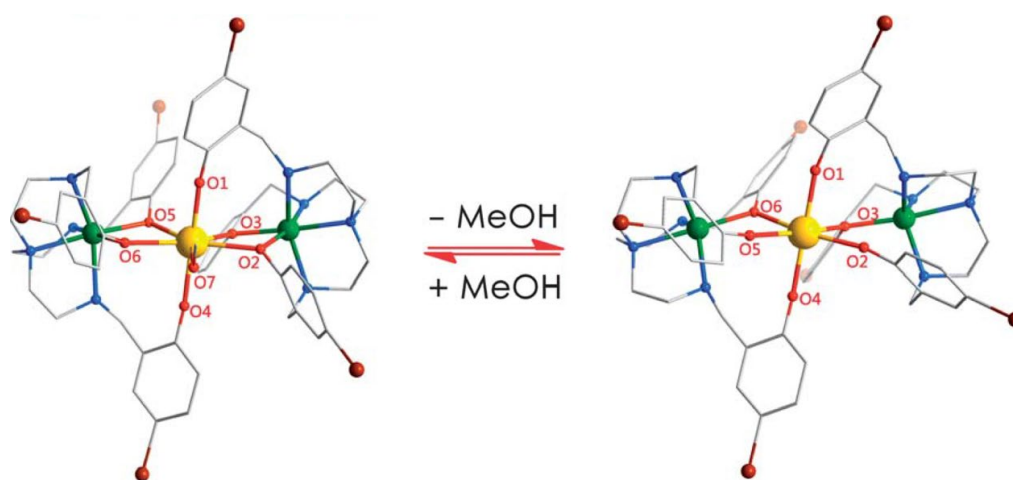


Figure 1.21 Structures of $[\text{Zn}_2\text{DyL}_2(\text{MeOH})]\text{NO}_3\cdot 3\text{MeOH}\cdot\text{H}_2\text{O}$ (left) and $[\text{Zn}_2\text{DyL}_2(\text{MeOH})]\text{NO}_3\cdot\text{H}_2\text{O}$ (right), Reproduced from Ref. 98, with permission from Royal Society of Chemistry.⁹⁸

Subsequently, Tong *et al.* reported another D_{5h} -symmetric complex, $[\text{Dy}(\text{bbpen})\text{Br}]$ (Figure 1.22 left, $\text{H}_2\text{bbpen} = \text{N,N}'\text{-bis}(2\text{-hydroxybenzyl})\text{-N,N}'\text{-bis}(2\text{-methylpyridyl})\text{-ethylenediamine}$), which increased the effective energy barrier to 712 cm^{-1} (1025 K) with a blocking temperature of 14 K. A similar molecule $[\text{Dy}(\text{bbpen})\text{Cl}]$ gave an effective barrier of 492 cm^{-1} (708 K). The difference is possibly caused by a stronger axial crystal-field and weaker Dy-Br bond in the bromide SMM.⁹⁹ Coincidentally, Zheng *et al.* increased the barrier record effectively to 1260 cm^{-1} (1815 K) in the same year.¹⁰⁰ As well, the trigonal bipyramidal $[\text{Dy}(\text{O}^t\text{Bu})_2(\text{py})_5][\text{BPh}_4]$ complex (Figure 1.22 right) has a D_{5h} geometry symmetry, coordinated by five pyridine ligands in the equatorial plane with a near-linear O–Dy–O angle (178.9°). The weaker Dy–N bonds apparently reduce the transverse crystal-field effect to result in a stronger axial anisotropy.

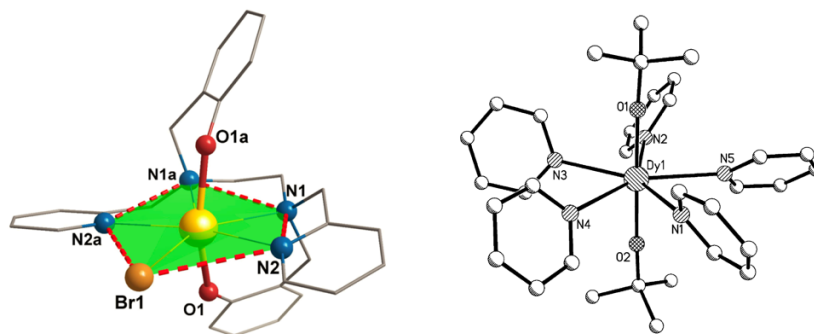


Figure 1.22 *Left*: Structures of $[\text{Dy}(\text{bbpen})\text{Br}]$. Reprinted from Ref. 99, with permission from American Chemical Society.⁹⁹ *Right*: Structure of $[\text{Dy}(\text{O}^t\text{Bu})_2(\text{py})_5]^-$ anion. Reprinted from Ref. 100, with permission from John Wiley & Sons.¹⁰⁰

A revolutionary breakthrough happened in the following years. The first ‘equatorial ligand-free’ lanthanide metallocene single-ion SMM was described by Layfield *et al.* and Mills *et al.* respectively in 2017.^{11, 12} This bis(cyclopentadienyl)-sandwich complex $[\text{Dy}(\text{Cp}^{\text{ttt}})_2][\text{B}(\text{C}_6\text{F}_5)_4]$ (Figure 1.23, $\text{Cp}^{\text{ttt}} = 1,2,4\text{-tri(tert-butyl)-cyclopentadienide}$) shows extraordinary magnetic properties, including a record blocking temperature of 60 K and an effective energy barrier of 1277 cm^{-1} (1837 K). This amazing behaviour is due to its unique molecular geometry, in which the equatorial crystal-field has been removed. Therefore, even with a slight bent in the $\text{Cp}_c\text{-Dy-Cp}_c$ angle (158.8°), there is a strong axial anisotropy.¹⁰¹

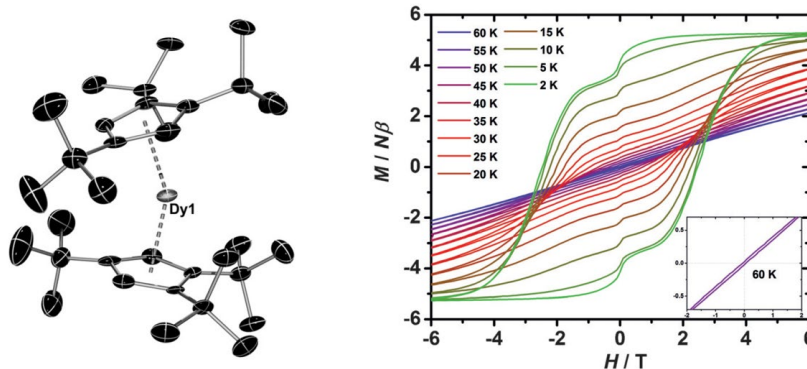


Figure 1.23 Structure of $[\text{Dy}(\text{Cp}^{\text{ttt}})_2]^+$ cation and the hysteresis loops in various temperature. Reprinted from Ref. 11, with permission from John Wiley & Sons.¹¹

This record did not stand for long, as the following year the Layfield group set a new milestone for SMMs. In 2018, the blocking temperature to a higher level of 80 K, i.e., *above the liquid-nitrogen temperature* (77 K) was reported. This time, the combination of two distinct ligands, Cp^{iPr5} (penta-isopropyl-cyclopentadienyl) and Cp* (C₅Me₅), was crucial in achieving this landmark, exemplified in complex [(Cp^{iPr5})Dy(Cp*)][B(C₆F₅)₄] (Figure 1.24).⁵ The crystal-field creates shorter Dy–Cp_c (Cp_c = Cp centroid) distance as well as a less-bent angle of Cp_c–Dy–Cp_c (162.5°), compared to the [Dy(Cp^{ttt})₂][B(C₆F₅)₄]. Correspondingly, a record of effective energy barrier of 1541 cm⁻¹ (2219 K) was measured. So far, the record U_{eff} and T_B determined for this complex still stands.

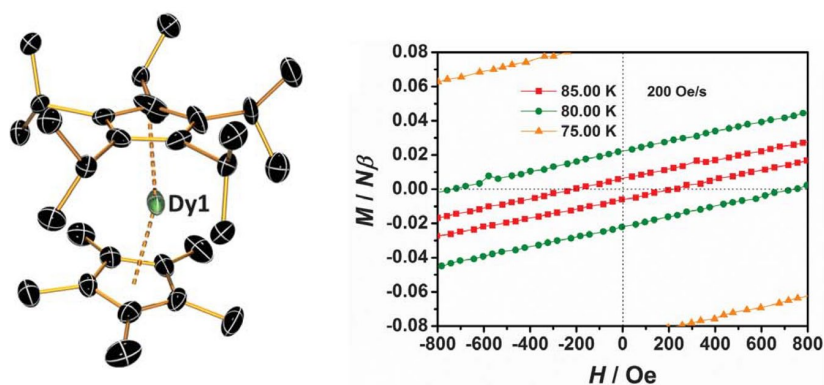


Figure 1.24 Structure of [(Cp^{iPr5})Dy(Cp*)]⁺ cation and hysteresis loops above 75 K. Reprinted from Ref. 5, with permission from AAAS.⁵

1.3.3.4 SMMs Based on Less Common Lanthanides

Except the mentioned lanthanide Tb³⁺, Er³⁺ and Dy³⁺ above, other lanthanide SMMs also get reported, using Pr,¹⁰² Ce,¹⁰³ Nd,¹⁰⁴ Tm¹⁰⁵ and Yb.¹⁰⁶ However, their relaxation behaviour was usually proved to be weak or negligible, so less attention is paid to these lanthanides at present.

1.3.4 Actinide SMMs

Actinide ions have strong spin-orbit coupling and stronger crystal-field effects than those found in lanthanide complexes. This is because 5f electrons are not shielded to

the same extent of 4f electrons. However, actinide SMMs are not widely developed and most studies only focus on U-based SMMs, although a few examples are known with Np^{4+} and Pu^{3+} .^{107, 108} The first uranium SMM, $[(\text{cyclam})\text{M}(\mu\text{-Cl})\text{U}(\text{Me}_2\text{Pz})_4]_2$ ($\text{M} = \text{Ni}, \text{Cu}, \text{Zn}$; cyclam = 1,4,8,11-tetraazacyclotetradecane, $[\text{Me}_2\text{Pz}]^- = 3,5\text{-dimethylpyrazolate}$), was published in 2007 with extremely weak SMM behaviour.¹⁰⁹ Since then, a few samples of diuranium bridged-SMMs were discovered, i.e., $\text{U}^{3+}\text{-U}^{5+}$ and $\text{U}^{4+}\text{-U}^{4+}$ complexes, all of which have very small effective energy barriers.¹¹⁰⁻¹¹² Meanwhile, a series of monometallic U^{3+} SMMs were reported,¹¹³⁻¹¹⁷ with the record of effective energy barrier for this sub-class of SMMs being 33 cm^{-1} (48 K, $H_{dc} = 1.5$ kOe) in a magnetically diluted sample of $[\text{U}(\text{Bp}^{\text{Me}})_3]$ complex ($[\text{Bp}^{\text{Me}}]^- = \text{dihydro-bis(methylpyrazolyl)-borate}$).¹¹⁸

Uranium sandwich single-ion SMMs are quite rare, with the first example being $[\text{U}^{\text{III}}(\text{COT}'')_2]$ complex ($\text{COT}'' = 1,4\text{-bis(trimethylsilyl)-cyclooctatetraenyl dianion}$) with the effective energy barrier of 27 K ($H_{dc} = 1$ kOe).¹¹⁹ In 2019, Layfield *et al.* published two uranium metallocenes, $[(\text{Cp}^{i\text{Pr}5})_2\text{U}^{\text{III}}]^+$ cation and $[(\text{Cp}^{i\text{Pr}5})_2\text{U}^{\text{II}}]$ (Figure 1.25),^{120, 121} which were not able to obtain energy barrier due to a dominant Raman relaxation in the former and efficient QTM in the latter. These two samples illustrate that the metallocene structure does not afford the ideal crystal-field for actinide based SMMs, even though $[(\text{Cp}^{i\text{Pr}5})_2\text{U}]$ has a perfect linear angle ($\text{Cp}_c\text{-U-Cp}_c = 180^\circ$).

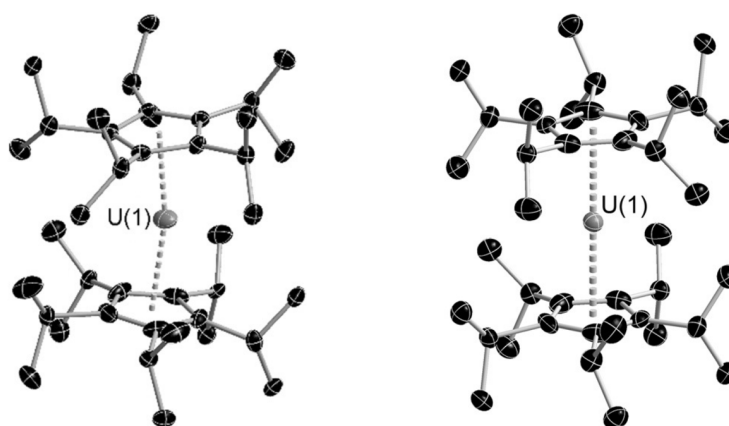


Figure 1.25 Structures of $[(\text{Cp}^{i\text{Pr}5})_2\text{U}]^+$ cation (left) and $[(\text{Cp}^{i\text{Pr}5})_2\text{U}]$ (right). Reprinted from Ref. 120 and 121, with permission from John Wiley & Sons.^{120, 121}

1.4 Synthetic Strategies for High-Temperature Dysprosium SMMs

The impressive evolution of lanthanide SMMs in the last decade should be attributed to the development of synthetic strategies based on the combination of a large number of experimental studies of SMMs and guidance from new theoretical models.¹²² With this approach, the effective energy barrier rose from 229 cm⁻¹ to 1541 cm⁻¹, and the blocking temperature was improved from 1.7 K to 80 K (Figure 1.26). Nowadays, dysprosium plays the most important role in achieving high-performance SMMs, therefore Dy-based SMMs are used to summarize the main synthetic strategies in high-quality SMMs.

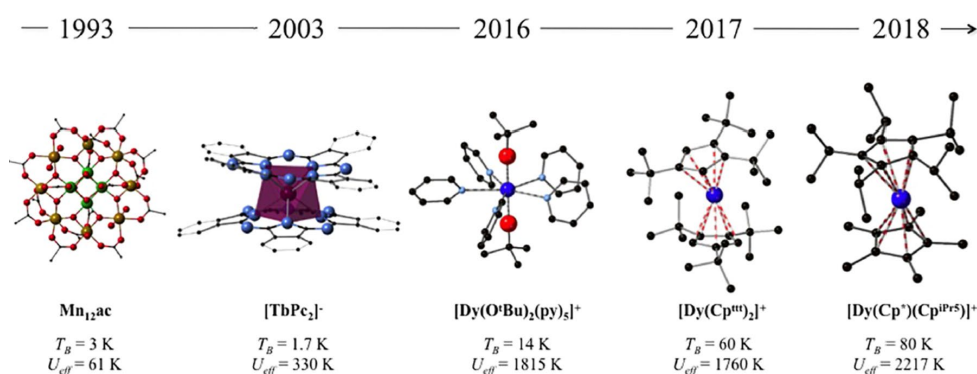


Figure 1.26 Milestones of SMMs in different periods. Reproduced from Ref. 122, with permission from American Chemical Society.¹²²

1.4.1 High-Symmetry Dysprosium Single-ion SMMs

As mentioned above, symmetry-based strategies have been used to enhance the properties of lanthanide single-ion SMMs. For the oblate-shape Dy³⁺ ion, the axial crystal-field is favoured.⁹ However, additional coordination in the equatorial plane is difficult to avoid with traditional synthesis methods. Therefore, highly axial symmetry is required and the strategy must also reduce the equatorial contribution as far as possible, which can be achieved with trigonal bipyramidal dysprosium SMMs. Four high-performance SMMs (Figure 1.27) can be used to illustrate the progress of the symmetry-based strategy.^{98-100, 123} These complexes have similar bipyramidal crystal-

field environments, except for $[\text{Dy}(\text{O}^t\text{Bu})_2(\text{L})_4]^+$ ($\text{L} = 4\text{-phenylpyridine}$), which is D_{4h} -symmetric, whereas the others have local pseudo- D_{5h} symmetry. All of these SMMs have a well-defined magnetic ground state of $M_J = \pm 15/2$ with perfect axiality ($g_x = g_y = 0, g_z = 20$), but with different effective energy barriers in the range 305 cm^{-1} – 1440 cm^{-1} (Table 1.2).

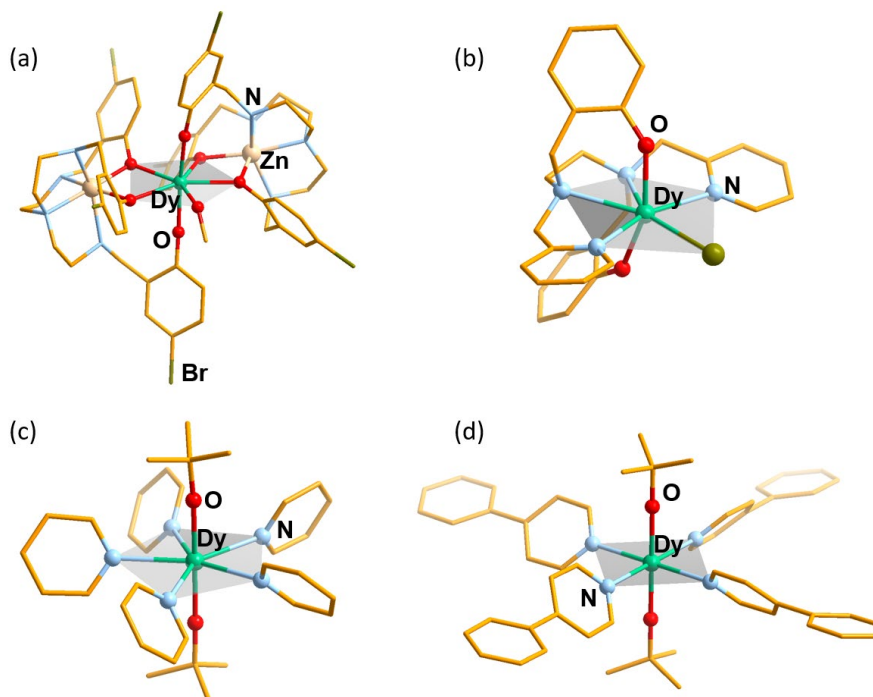


Figure 1.27 Structures of (a) $[\text{Zn}_2\text{DyL}_2(\text{MeOH})]$, (b) $[\text{Dy}(\text{bbpen})\text{Br}]$, (c) $[\text{Dy}(\text{O}^t\text{Bu})_2(\text{py})_5]^-$, (d) $[\text{Dy}(\text{O}^t\text{Bu})_2(\text{L})_4]^+$. Dy, green; Zn, cream; N, blue; Br, olive green; O, red; C, orange. The light-grey area represents the approximate equatorial crystal-field planar. The structures are reproduced based on the cif files from the Ref.98, 99, 100, and 123.^{98-100, 123}

Although ligand coordination in the xy -plane may not be completely eliminated, a weak crystal field can be targeted. For example, $[\text{Zn}_2\text{DyL}_2(\text{MeOH})]$ has the smallest barrier among the four complexes. However, this complex has a larger $\text{O}-\text{Dy}-\text{O}$ angle (168.6°) but a barrier of 305 cm^{-1} , which compares to an analogous angle of 155.8° in $[\text{Dy}(\text{bbpen})\text{Br}]$ with a much larger barrier of 712 cm^{-1} . The equatorial oxygen atoms produce a stronger equatorial crystal field in $[\text{Zn}_2\text{DyL}_2(\text{MeOH})]$ than the nitrogen donors do in the other three compounds. Thus, the transverse anisotropy increases

and the axially is diminished, which leads to a smaller effective energy barrier. For another case, if the equatorial bromide ligand in $[\text{Dy}(\text{bbpen})\text{Br}]$ is replaced by chloride, the effective energy barrier drops to 492 cm^{-1} , due to a stronger Dy–Cl interaction (2.681 \AA).⁹⁹ On the other hand, lower coordination numbers can also reduce the transverse anisotropy. For example, $[\text{Dy}(\text{O}^t\text{Bu})_2(\text{L})_4]^+$ has a perfectly linear O–Dy–O angle compared to an angle of 178.9° in $[\text{Dy}(\text{O}^t\text{Bu})_2(\text{py})_5]^-$, but shorter Dy–N bonds (2.468 \AA). Even though, $[\text{Dy}(\text{O}^t\text{Bu})_2(\text{L})_4]^+$ has fewer equatorial ligands than $[\text{Dy}(\text{O}^t\text{Bu})_2(\text{py})_5]^-$, which causes an improvement in effective energy barrier (1440 cm^{-1}).

Table 1.2 Selected structural parameters and magnetic properties.

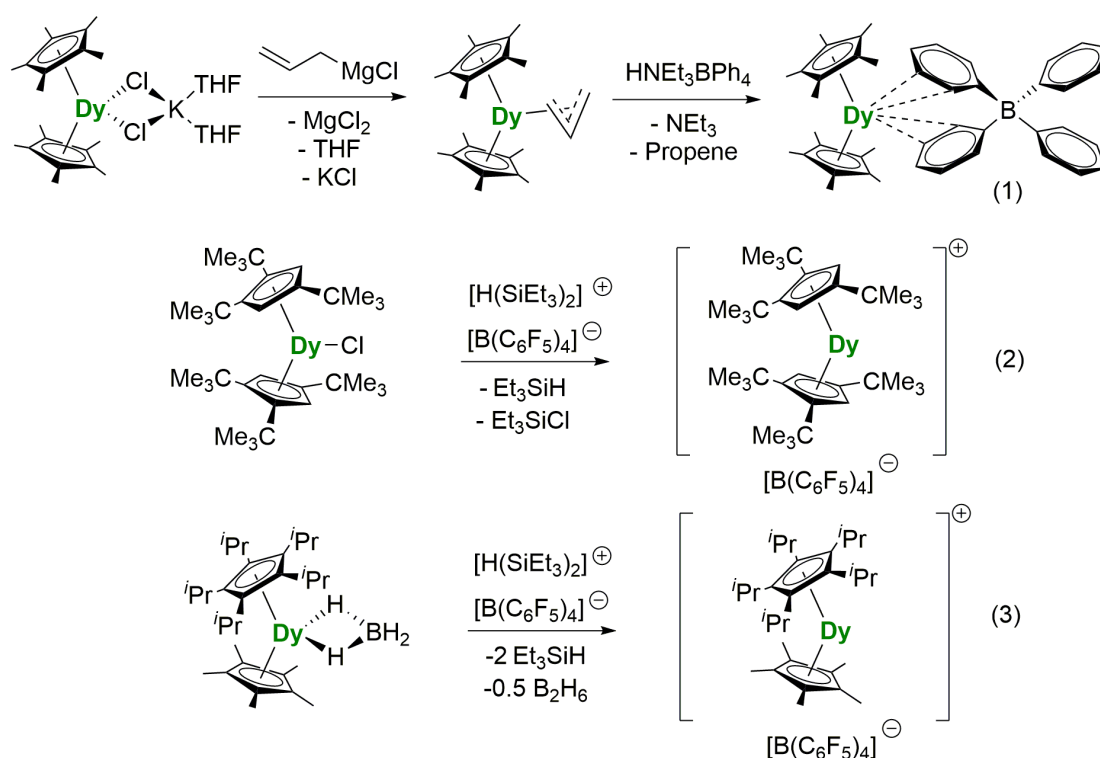
Complex	^f $[\text{Zn}_2\text{DyL}_2(\text{MeOH})]$	$[\text{Dy}(\text{bbpen})\text{Br}]$	$[\text{Dy}(\text{O}^t\text{Bu})_2(\text{py})_5]^-$	^g $[\text{Dy}(\text{O}^t\text{Bu})_2(\text{L})_4]^+$
Pseudo local symmetry	D_{5h}	D_{5h}	D_{5h}	D_{4h}
O–Dy–O/ $^\circ$ ^a	168.6	155.8	178.9	180.0
O–Dy/ \AA ^b	2.195(7) 2.221(6)	2.163(3)	2.110(2) 2.114(2)	2.066(8)
O–, Br–, N–Dy/ \AA ^c	Dy–O: 2.366(6)- 2.427(6)	Dy–N: 2.578(4) 2.594(4)	Dy–N: 2.534(3)-2.580(3)	Dy–N: 2.468(6)
		Dy–Br: 2.8515(6)		
$U_{\text{eff}}/\text{cm}^{-1}$ ^d	305	712	1260	1440
T_B/K ^e	12	14	14	5
^a Angle from the axial direction. ^b O–Dy distance from the axial direction. ^c O–, Br–, N–Dy distance from the equatorial planar. ^d Determined in zero DC field. ^e Defined as the maximum hysteresis temperature. ^f $\text{L} = 2,2',2''\text{-}(((\text{nitrilo-tris(ethane-2,1-diyl)})\text{-tris(azanediyl)})\text{-tris(methylene)})\text{-tris(4-bromo-phenol)})$. ^g $\text{L} = 4\text{-phenylpyridine}$.				

1.4.2 High-Performance Dysprosium Metallocene SMMs

Since the discovery of ferrocene^{124, 125} and the first lanthanide metallocenes^{124, 125} in the 1950s, the bis-cyclopentadienyl (Cp) sandwich structure has made a big impact.¹²⁶ The introduction of metallocenes has also contributed to the evolution of SMMs. Compared to the [COT]²⁻ and [Pc]²⁻ ligands, [Cp]⁻ can produce stronger axial crystal-fields, which matches the oblate-ion model developed for Dy³⁺.

(1) Synthesis of Dysprosium Metallocene SMMs

Traditional three-coordinated [Dy(Cp')₃] (Cp' = C₅H₄SiMe₃) structure or four-coordinated complexes of the type [DyCp₂(NH₃)₂]⁺ cannot eliminate the transverse crystal-field.^{127, 128} In order to remove the equatorial ligands, the synthetic protocol shown in Scheme 1.1 was developed.



Scheme 1.1 Three synthesis paths of dysprosium metallocene cations.^{127, 128}

Although not for the purposes of synthesizing an SMM, the first attempt to remove the equatorial chloride ligand in Ln metallocene structure was reported by Evans *et al.*^{129, 130} In the first step, [(Cp*)₂LnCl₂K(THF)₂] (Ln = Sm, Tm, Nd, Gd, Y) were reacted

with allylmagnesium chloride to obtain the precursors of $[(\text{Cp}^*)_2\text{Ln}(\text{C}_3\text{H}_5)]$. Then, a deprotonation reaction with $[\text{Et}_3\text{NH}][\text{BPh}_4]$ yielded $[(\text{Cp}^*)_2\text{Ln}][\text{BPh}_4]$. Using this approach, $[(\text{Cp}^*)_2\text{Dy}][\text{BPh}_4]$ complex was made by Long *et al.* in 2014 (Scheme 1.1-1).⁷⁷ However, for this compound, the equatorial crystal-field has not been thoroughly eliminated since two phenyl rings of the $[\text{BPh}_4]^-$ anion coordinate to the Dy ion, with the Dy–C distances of 2.830(4) and 2.836(1) Å, which leads to a $\text{Cp}_c\text{–Dy–Cp}_c$ angle of 134°. Thus, with the distorted Cp crystal-field and the transverse effect from the $[\text{BPh}_4]^-$, an effective energy barrier of 314 cm^{-1} is obtained under a zero DC field.¹³¹

As the $[(\text{Cp}^{\text{ttt}})_2\text{DyCl}]$ reacts with the extremely electrophilic $[(\text{Et}_3\text{Si})_2\text{H}]^+$ cation to cleave the Dy–Cl bond, it produced the $[\text{Dy}(\text{Cp}^{\text{ttt}})_2][\text{B}(\text{C}_6\text{F}_5)_4]$ (Scheme 1.1-2). Indeed, the formation of the $[\text{Dy}(\text{Cp}^{\text{ttt}})_2]^+$ cation proved that the Cp^{ttt} ligand is bulky enough to obstruct the potential coordination from the $[\text{B}(\text{C}_6\text{F}_5)_4]^-$ with a Dy–F distance of 5.8145(4) Å. Similar reactivity of $[(\text{Et}_3\text{Si})_2\text{H}][\text{B}(\text{C}_6\text{F}_5)_4]$ towards other Dy–X bonds has been developed (X = I, BH_4).¹³²

Bulkier Cp substituents tend to require longer reaction times and higher temperatures to be transferred to lanthanides than smaller Cp ligand. Then, when the huge substituent ligand Cp^{iPr5} was introduced for synthesis of $[(\text{Cp}^*)\text{Dy}(\text{Cp}^{\text{iPr5}})][\text{B}(\text{C}_6\text{F}_5)_4]$ (Scheme 1.1-3), the starting material $\text{DyCl}_3(\text{THF})_{3.5}$ was replaced by $\text{Dy}(\text{BH}_4)_3(\text{THF})_3$. Doing so allowed the initial synthesis of $[\text{Dy}(\text{Cp}^{\text{iPr5}})(\text{BH}_4)_2(\text{THF})]$, followed by the reaction with KCp^* to give $[(\text{Cp}^*)\text{Dy}(\text{Cp}^{\text{iPr5}})(\text{BH}_4)]$. The subsequent reaction of this metallocene with the silylium reagent produced the SMM $[(\text{Cp}^*)\text{Dy}(\text{Cp}^{\text{iPr5}})][\text{B}(\text{C}_6\text{F}_5)_4]$.

(2) Ligand, Angle and Distance.

In the metallocenium cations, the equatorial crystal-field has been greatly minimized. Compared with the bipyramid single-ion SMMs, the metallocene SMMs display a substantial increase in blocking temperature. Therefore, it seems that the equatorial crystal-field can significantly restrain T_B for oblate lanthanide ions. The bis-Cp sandwich structure is a much simpler environment dysprosium coordination environment, such that the SMM properties focus on three factors: the Cp substituents, the $(\text{Cp}_c\text{–Dy–Cp}_c)$ angle; and the $(\text{Cp}_c\text{–Dy})$ distances. Here, three typical

sandwich cations (Figure 1.28) are chosen to illustrate the main points, with selected parameters listed in Table 1.3.^{5, 11, 132}

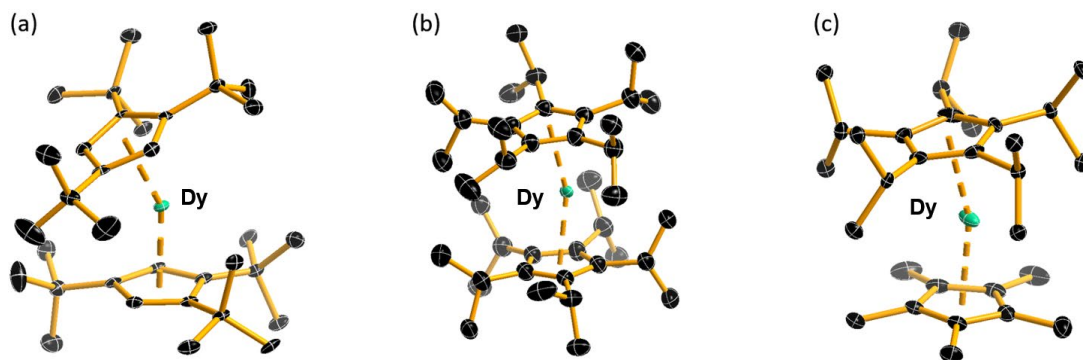


Figure 1.28 Thermal ellipsoid representation (30 % possibility) of molecular structures of (a) [Dy(Cp^{tnt})₂]⁺, (b) [Dy(Cp^{ipr5})₂]⁺, (c) [(Cp*)Dy(Cp^{ipr5})]⁺. Dy, green; C, black. The structures are reproduced based on the cif files from the Ref. 5, 11 and 132.^{5, 11, 132}

Based on Table 1.3, these SMMs are somewhat bent and not strictly linear, however all of them have excellent magnetic properties. However, even a slight changing in the angle will impact on T_B and U_{eff} . The initial strategy is to use the substituted Cp-ligands to control the Cp_c–Dy–Cp_c angle. It was believed that bulky Cp ligands can increase the steric hindrance, which should protect the Dy³⁺ ion from potential coordination of the [B(C₆F₅)₄][−] anion and from other solvent. Steric effects can also enhance the repulsion between two Cp-rings so that the Cp_c–Dy–Cp_c angle tends to 180°. Hence, a series of substituted bis-Cp sandwich complexes have been made with a range of bulky Cp ligands. The strategy seemingly works. For example, [Dy(Cp^{ipr5})₂]⁺ has much bigger Cp^{ipr5} ligands than [Dy(Cp^{tnt})₂]⁺, which leads to a larger U_{eff} (1334 cm^{−1}) and a slight lift in T_B (66 K). However, the added repulsion between two Cp-ligands inevitably increases the Cp_c–Dy distances, which weakens the crystal-field. In [(Cp*)Dy(Cp^{ipr5})]⁺, the bulky Cp^{ipr5} ligand provides the steric hindrance and the less-bulky Cp* helps reduce the repulsion between the two ligands, which leads to shorter distances of both Cp^{ipr5}–Dy (2.296 Å) and Cp*–Dy (2.284 Å) when compared to the related SMMs. The result is a record effective energy barrier of 1540 cm^{−1} and a blocking temperature

of 80 K. According to the *ab initio* calculations, $[\text{Dy}(\text{Cp}^{\text{ttt}})_2]^+$ and $[(\text{Cp}^*)\text{Dy}(\text{Cp}^{\text{ipr5}})]^+$ both have the well stabilized ground state ($M_J = \pm 15/2$) and highest excited 5th KD and 6th KD respectively. The Orbach relaxation of thermally assisted QTM could happen at the fifth KD for $[(\text{Cp}^*)\text{Dy}(\text{Cp}^{\text{ipr5}})]^+$, while at fourth KD for $[\text{Dy}(\text{Cp}^{\text{ttt}})_2]^+$. As a conclusion, the strategy of using two different substituted Cp-ligands can promote a much more linear $\text{Cp}_c\text{-Dy-Cp}_c$ angle and short Cp–Dy distances, which helps reach a good balance between the need for a crystal field which is both strong and highly axial.

able 1.3 Selected structural parameters and magnetic properties.

Complex	$[\text{Dy}(\text{Cp}^{\text{ttt}})_2]^+$	$[\text{Dy}(\text{Cp}^{\text{ipr5}})_2]^+$	$[\text{Cp}^*\text{DyCp}^{\text{ipr5}}]^+$
Local symmetry	C_∞	C_∞	C_∞
$\text{Cp}_c\text{-Dy-Cp}_c/^\circ$	152.8	157.8–167.9	162.5
$\text{Cp}_c\text{-Dy}/\text{\AA}$	2.309(1) 2.324(1)	2.321(10)–2.358(10)	2.296(1) (Cp^{ipr5}) 2.284(1) (Cp^*)
$U_{\text{eff}}/\text{cm}^{-1\text{a}}$	1277	1334	1540
T_B/K^{b}	60	66	80
^a Determined in zero applied DC field.			
^b Defined as the maximum hysteresis temperature.			

1.4.3 Radical-Bridged Organolanthanide SMMs

Long *et al.* reported a radical-bridged structure, $[(\text{Cp}^*_2\text{Ln})_2(\mu\text{-bpym}^*)]^+$ (Ln = Gd, Tb, Dy), which contains the radical anion of 2,2'-bipyrimidine (bpym) ligand (Figure 1.29 *left*).⁷⁷ The Tb^{3+} and Dy^{3+} version have effective energy barriers of 87.8 cm^{-1} and 44 cm^{-1} , respectively. For the dysprosium version, the opened hysteresis loops were observed at the temperature lower than 7 K under zero field. In contrast to exchange-coupled polynuclear lanthanide SMMs based on classical coordination chemistry methods,^{70, 133-141} the Gd^{3+} , Tb^{3+} and Dy^{3+} radical-bridged complexes all exhibit a strong antiferromagnetic coupling, with an exchange coupling constant of $J = -10\text{ cm}^{-1}$, determined for the gadolinium version ($-2J$ formalism). A very similar phenomenon is observed in another trinuclear radical-bridged structure $\text{Cp}^*_6\text{Ln}_3(\mu_3\text{-HAN})$ (Ln = Gd, Tb, Dy; HAN = hexaazatrinaphthylene).¹⁴² Another example was published by Layfield *et*

al. in 2017, which is a double-reduced radical system (Figure 1.29 *right*).¹⁴³ The indigo-bridged complexes $[\{(Cp^*)_2Ln\}_2(\mu-ind)]^{n-}$ ($Ln = Gd, Dy, n = 0, 1, 2$) have distinct coupling behaviour for the first and second reduction. The $[\{(Cp^*)_2Ln\}_2(\mu-ind)]^-$ shows very strong antiferromagnetic exchange, with $J = -11 \text{ cm}^{-1}$ for the gadolinium version. However, the hysteresis loops are closed under zero field even at a low temperature of 1.8 K.

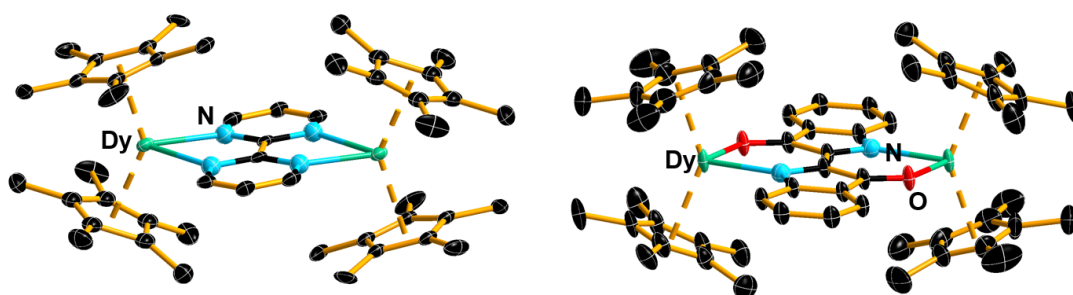


Figure 1.29 Thermal ellipsoid representation (30 % possibility) of molecular structures of $[(Cp^*)_2Dy]_2(\mu-bpym^*)^+$ (*left*) and $[\{(Cp^*)_2Dy\}_2(\mu-ind)]^-$ (*right*). Dy, green; C, black; O, red; N, blue. The structures are reproduced based on the cif files from the Ref. 77 and 143.^{77, 143}

1.5 Summary

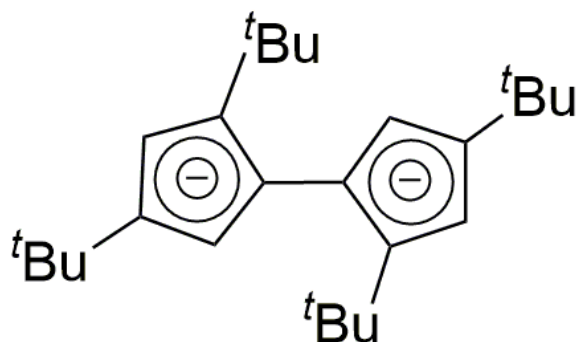
After three decades of continued development, the SMMs enter an exciting period with great progress achieved not only in quantity but also in quality. Based on a large amount of early research, principles and mechanisms have been revealed as well as synthetic approach and theoretical models. Recently, the huge success in lanthanide single-ion SMMs inspire us to pursue even better performing SMMs. Using the proverbial lessons taught by metallocene sandwich SMMs, and specifically the importance of symmetry in developing high performing SMMs, I am employing two novel aromatic Cp ligands for this Ph.D. project, in order to achieve the goal of better SMMs. My efforts are discussed in the following chapters.

Chapter 2

Dimetallic Dysprosocenium Single-Molecule Magnets Based on Fulvalene Ligands

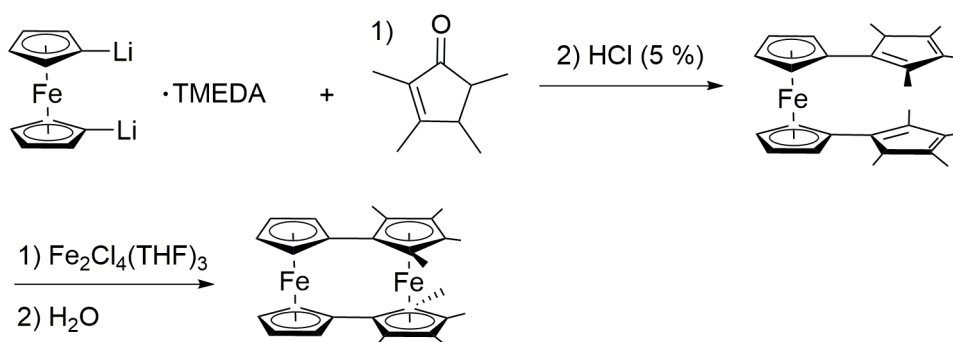
2.1 Introduction to Fulvalenyl Complexes

The main aim of the work in this chapter is to synthesize a dysprosium 'double metallocene' and to study the magnetic properties, including SMM behaviour and how it is influenced by intramolecular magnetic exchange interactions. As described in the introduction, the bridged-sandwich or double metallocene structure is rare in lanthanide chemistry. Therefore, to obtain the desired compounds, the fulvalenyl ligand $[1,1',3,3'-(C_5^tBu_2H_2)_2]^{2-}$ (Fv^{tttt} , Scheme 2.1), which is essentially a dicyclopentadienyl dianion, is used to obtain a series of magnetic complexes involving rare-earth elements for the first time.



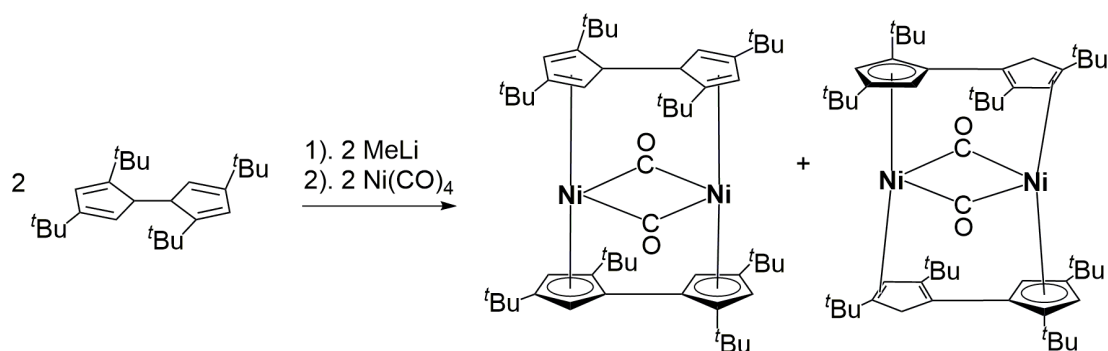
Scheme 2.1 Structure of fulvalenyl ligand $[1,1',3,3'-(C_5^tBu_2H_2)_2]^{2-}$ (Fv^{tttt}).

Very few complexes of Fv^{tttt} are known. An early strategy used in transition metal chemistry to build a fulvalenyl-ligated double metallocene structure involves a multi-step reaction starting with a single ferrocene (Scheme 2.2).¹⁴⁴ The dilithioferrocene is reacted with the 2,3,4,5-tetramethyl-2-cyclopenten-1-one followed by acidic work-up to give a ferrocene with 1,1'-dicyclopentadienyl substituents, which is then sandwiched with the $Fe_2Cl_4(THF)_3$ to give a bis-fulvalenyl-substituted ferrocene.



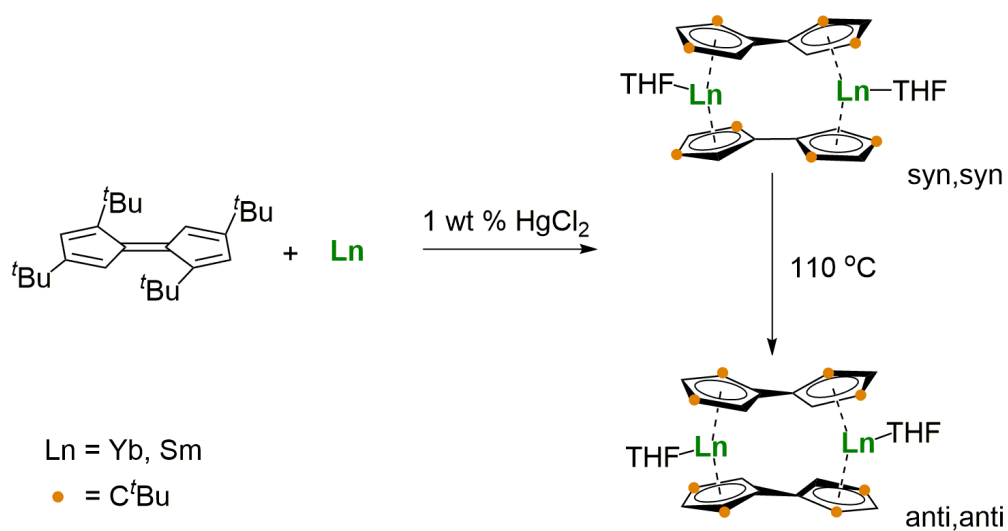
Scheme 2.2 Synthesis approach of 1,1'-ferrocene-diylbis(η^5 -2,3,4,5-tetramethylcyclopentadienyl) iron.¹⁴⁴

Another example uses doubly deprotonated Fv^{tttt} as the dilithium salt in a reaction reaction with $Ni(CO)_4$, which finally gives two bridged metallocene-like structures (Scheme 2.3).¹⁴⁵ However, the Ni-Cp coordinating modes vary as η^2 and η^5 .



Scheme 2.3 Synthesis of (η^5 : η^5 - Fv^{tttt}) (η^2 : η^2 - Fv^{tttt}) $Ni_2(CO)_2$ and (η^2 : η^5 - Fv^{tttt}) $_2Ni_2(CO)_2$.¹⁴⁵

The only bis(fulvalenyl) structures containing lanthanides was reported by Neif *et al.*¹⁴⁶ Mixing elemental samarium or ytterbium and tetra-*tert*-butylpentafulvalene with HgCl₂ (1 %) in THF produces a *syn-syn* configuration of (Fv^{tttt})₂Ln₂(THF)₂; after heating to 110°C, an *anti-anti* structure is then formed (Scheme 2.4).

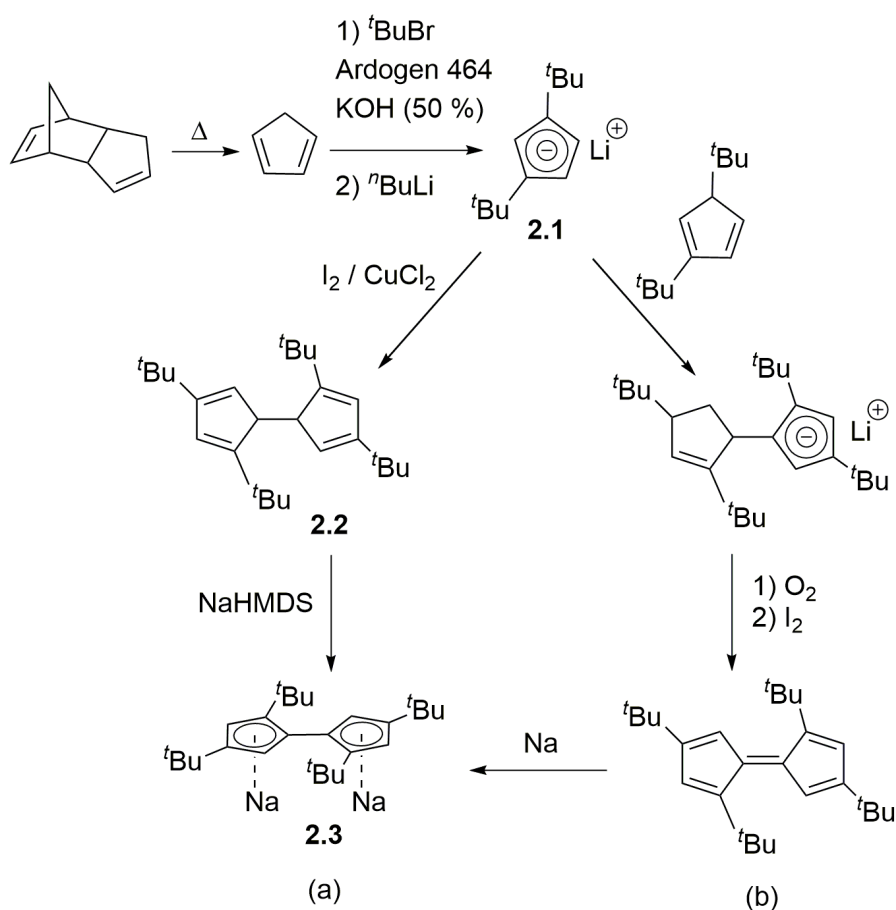


Scheme 2.4 Synthesis of the divalent lanthanide complexes (Fv^{tttt})₂Ln₂(THF)₂ (Ln = Sm, Yb).¹⁴⁶

2.2 Synthesis of Fulvalenyl Ligand and Bridged Complexes

2.2.1 Synthesis of the Fv^{tttt} Ligand

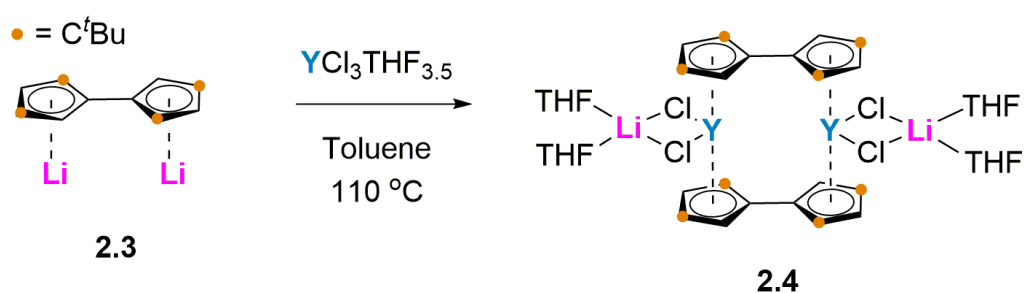
Two approaches have been developed to obtain the Fv^{tttt} ligand and its alkali metal salts (Scheme 2.4).^{147, 148} Route **a** is reported to have better yields and fewer steps than route **b**. Compound **2.2** actually forms as a mixture isomer, which does not affect the subsequent steps. Different alkali metals, Li, Na, K, have been tried to form the corresponding M_2Fv^{tttt} compounds. After optimizing the reaction conditions, the sodium salt Na_2Fv^{tttt} (**2.3**) proved most useful for the next steps, with the isolated yield of 43 %.



Scheme 2.5 Synthesis of Na_2Fv^{tttt} .^{147, 148}

2.2.2 Synthesis of $[Fv^{tttt}YCl_2Li(THF)_2]_2$

Inspired by the previous work from Nief *et al.*,¹⁴⁵ the yttrium double-sandwich complex $[(\eta^5-Fv^{tttt})Y(\mu-Cl)_2Li(THF)_2]_2$ (**2.4**) was produced by reacting $[YCl_3(THF)_{3.5}]$ and Na_2Fv^{tttt} (Scheme 2.5 and Figure 2.1). The double metallocene structure was a promising start; however, the unexpected co-complexation by $\{Li(THF)_2(\mu-Cl)\}$ seemingly obstructs further reaction with $[(Et_3Si)_2H][B(C_6F_5)_4]$, aiming to remove the chloride ligands and obtain the desired double metallocenium cation $[Y_2(Fv^{ttt})_2]^{2+}$. Furthermore, with an extremely low yield, only trace amounts (isolated yield < 1 %) of complex **2.4** could be obtained as single crystals. to reveal the cell parameters. Consistent with this, the reaction of $[DyCl_3(THF)_{3.5}]$ with Na_2Fv^{tttt} did not produce any isolable material.



Scheme 2.6 Synthesis of $[(\eta^5-Fv^{tttt})Y(\mu-Cl)_2Li(THF)_2]_2$ and molecular structure.

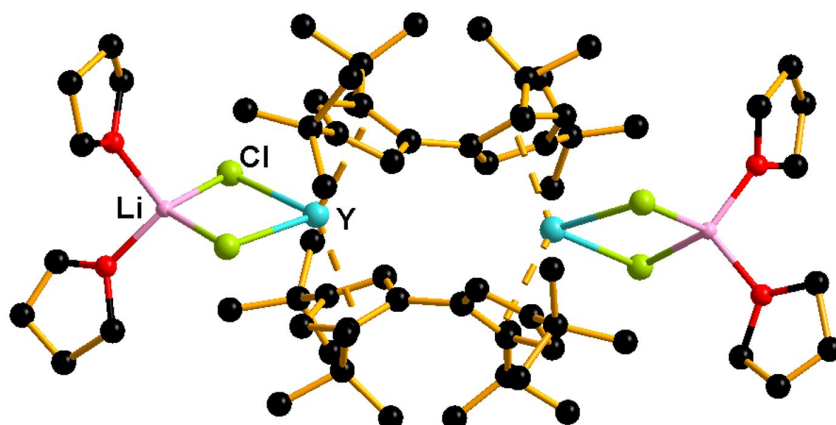
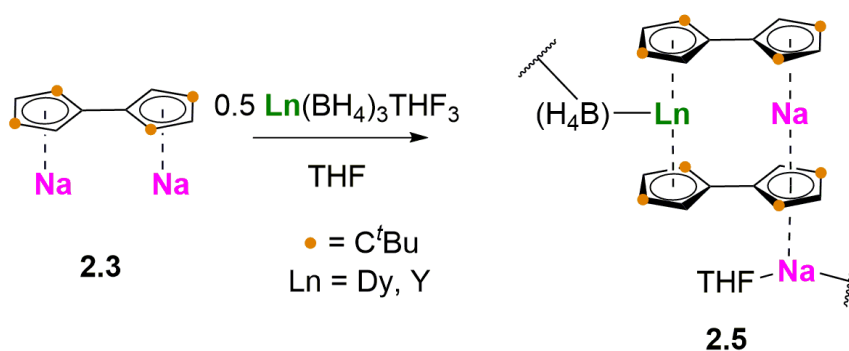


Figure 2.1 Structure of complex **2.4**, Y, blue; C, black; Cl, green; Li, pink; O, red.

2.2.3 Synthesis of Heterobimetallic Fulvalene-Bridged Double Metallocene

In light of the undesired outcomes when using rare-earth chlorides in the reactions with $\text{Na}_2\text{Fv}^{\text{tttt}}$, we switched to the borohydride complexes $[\text{Ln}(\text{BH}_4)_3(\text{THF})_3]$ ($\text{Ln} = \text{Dy}, \text{Y}$). The 1:1 reaction of $\text{Na}_2\text{Fv}^{\text{tttt}}$ and $[\text{Ln}(\text{BH}_4)_3(\text{THF})_3]$ does not, however, give any result. In contrast, the coordination polymers $[\text{LnNa}(\eta^5\text{-Fv}^{\text{tttt}})_2\text{Na}(\text{THF})(\mu\text{-BH}_4)]$ (**2.5**) (Scheme 2.7) can be produced by adding a second equivalent of $\text{Na}_2\text{Fv}^{\text{tttt}}$, with a poor isolated yield of 4 %. The double-sandwich structure consists of yttrium or dysprosium sandwiched with sodium in the double metallocene, with an additional μ -bridging interaction via a cyclopentadienyl to the second sodium ion. The coordination polymer assembles by virtue of the bridging Cp unit and a borohydride ligand bound to the rare-earth metal (Figure 2.2).



Scheme 2.7 Synthesis of complexes 2.5 ($\text{Ln} = \text{Y}, \text{Dy}$).

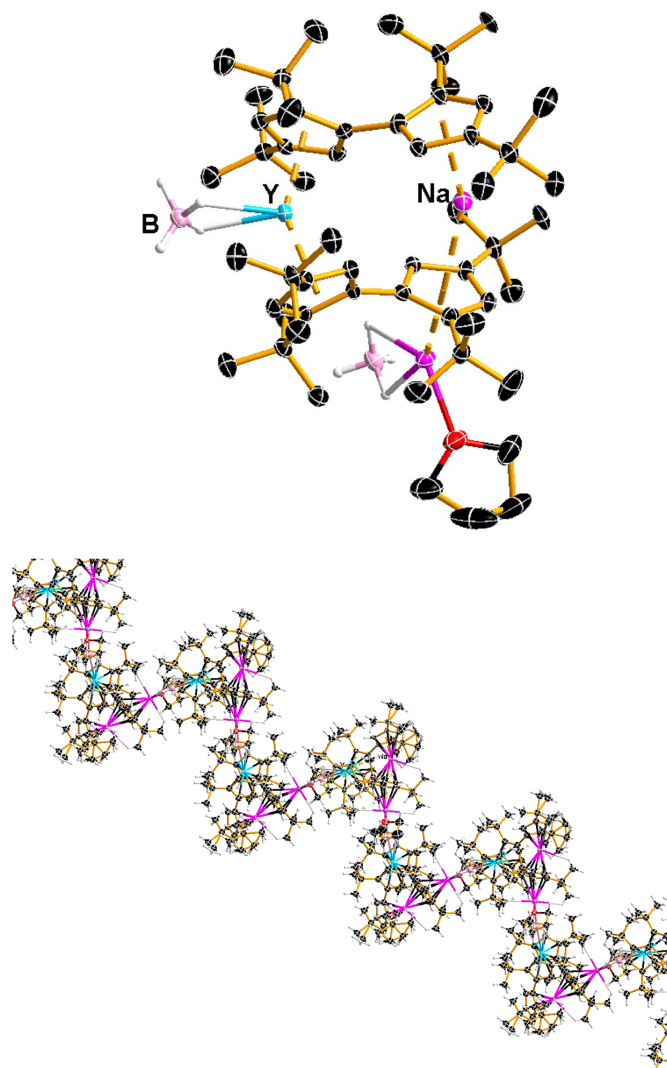


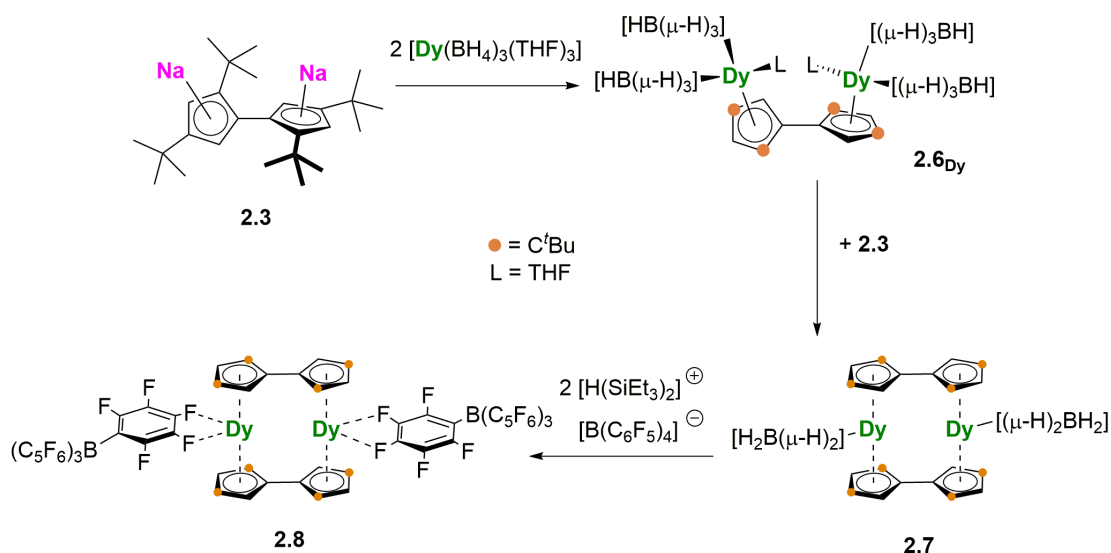
Figure 2.2 Thermal ellipsoid representation (30 % possibility) of molecular structure of complex **2.5-Y** and the spiral-chain structure after unit growing. Y, blue; C, black; B, pink; Na, purple; H, white.

Compounds **2.4** and **2.5** both illustrate the difficulty of synthesizing desired dilanthanide double metallocene through a one-step reaction. Therefore, the synthesis procedures should be modified in order to obtain the target complexes.

2.2.4 Synthesis of $[DyFv^{tttt}]_2[B(C_6F_5)_4]_2$

According to the previous results, a stepwise synthesis procedure is applied based on $[Dy(BH_4)_3THF_3]$, with the aim of first isolating a ‘double half sandwich’ complex and then moving on to target a double metallocene. The expected double half-sandwich

complex $[\text{Fv}^{\text{tttt}}\{\text{Dy}(\text{BH}_4)(\text{THF})\}_2]$ (**2.6_{Dy}**) was obtained (isolated yield = 29 %) via the reaction of $\text{Na}_2\text{Fv}^{\text{tttt}}$ with two equivalents of $[\text{Dy}(\text{BH}_4)_3](\text{THF}_3)$ (Scheme 2.8). Then, one more equivalent $\text{Na}_2\text{Fv}^{\text{tttt}}$ was added to make the double metallocene complex $[(\text{BH}_4)\text{DyFv}^{\text{tttt}}]_2$ (**2.7**), which has a borohydrides coordinated on each of the dysprosium ions. In order to remove the BH_4 ligands, a further reaction of **2.7** with two equivalents of $[(\text{Et}_3\text{Si})_2\text{H}][\text{B}(\text{C}_6\text{F}_5)_4]$ yielded the double metallocene dication $[\text{DyFv}^{\text{tttt}}]_2[\text{B}(\text{C}_6\text{F}_5)_4]_2$ (**2.8**, isolated yield: 89 %), whose structure is revealed by a crystal data in poor quality. However, the coordination of the anion via $\text{F}\cdots\text{Dy}$ interactions was observed, probably due to the significant twisting around the C–C bond that connects the Cp rings.



Scheme 2.8 Synthesis of complexes **2.6–2.8**.

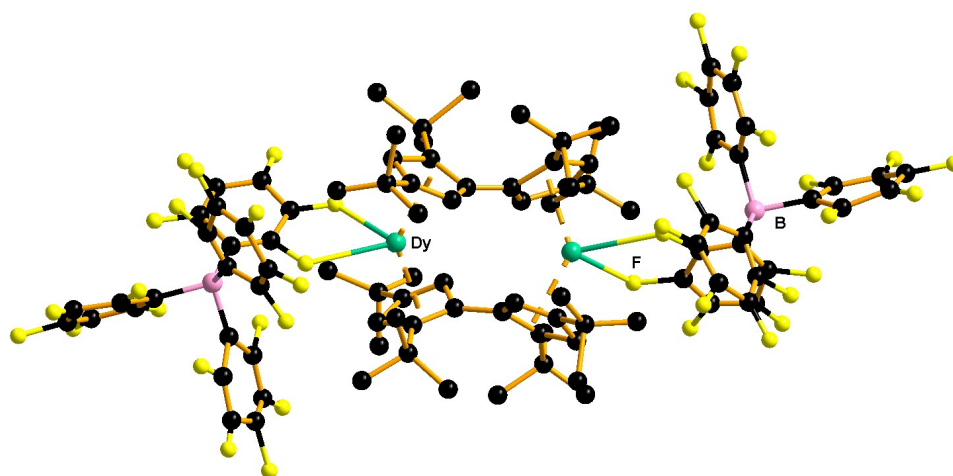
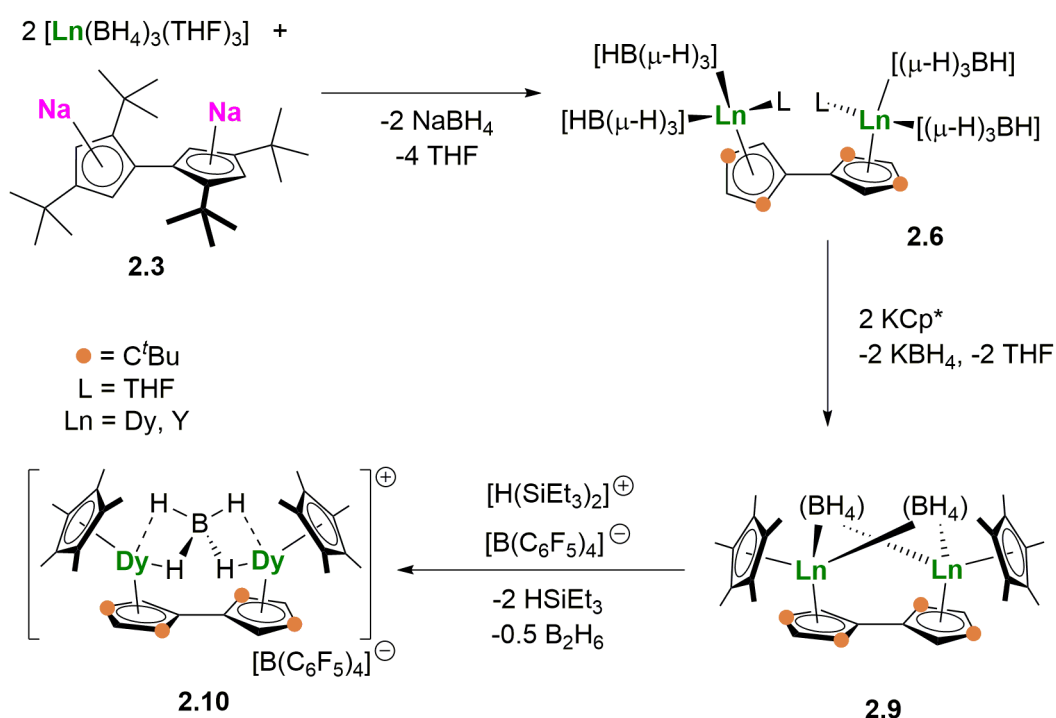


Figure 2.3 The molecule structure of complex **2.8**. Dy, green; C, black; B, pink; H, white; F, yellow.

2.2.5 Synthesis of $\{[Ln(Cp^*)(BH_4)]_2(Fv^{tttt})\}$

In light of the difficulties of obtaining a *bis*(fulvalenyl) double metallocene, a modified approach was adopted in which a different type of double metallocene was targeted, which involves a single bridging fulvalenyl ligand coordinated to two separate $\{CpM\}$ units. Therefore, two equivalents of KCp^* were reacted with **2.6** to yield $\{[Ln(\eta^5-Cp^*)(\mu-BH_4)]_2(\eta^5:\eta^5-Fv^{tttt})\}$ (**2.9**), in which two BH_4 bridged between the lanthanide cores ($Ln = Dy, Y$). Thus, a key target compound has been synthesized, with the isolated yield of 36 % and 40 % for Dy and Y versions, respectively. To obtain a metallocene cation, compound **2.9_{Dy}** was reacted with one equivalent of $[(Et_3Si)_2H][B(C_6F_5)_4]$ to give the desired separated ion-pair $\{[Dy(\eta^5-Cp^*)]_2(\mu-BH_4)(\eta^5:\eta^5-Fv^{tttt})\}[B(C_6F_5)_4]$ (**[2.10]** $[B(C_6F_5)_4]$, isolated yield = 29 %), with a single BH_4 bridged between the dysprosium ions (Scheme 2.9). Notably, adding one more equivalent of $[(Et_3Si)_2H][B(C_6F_5)_4]$ does not remove the other borohydride bridge.



Scheme 2.9 Synthesis of complexes **2.9** and **2.10**.

2.3 X-Ray Diffraction Studies

The molecular structures of complexes **2.6**, **2.7**, **2.9** and **2.10** were measured by X-ray diffraction using good quality single-crystals. For complexes **2.4**, **2.5** and **2.8**, the data were not of publication quality due to poor crystallinity.

2.3.1 Crystal Structure of $[Fv^{t\text{ttt}}Ln_2(BH_4)_2THF]$

The molecular structures of compounds **2.6_{Dy}** and **2.6_Y** are shown in Figure 2.4 and selected bond lengths and angles parameters are shown in Table 2.1. For complex **2.6_{Dy}**, the coordination environment of each dysprosium consists of a Cp-ring of a $Fv^{t\text{ttt}}$ ligand in an η^5 -manner, two κ^3 -borohydride ligands, and a molecule of THF. The Dy1–C distances are in the range of 2.607(4)–2.698(4) Å, and in the range 2.619(4)–2.696(4) Å for Dy2–C. The Dy–C_p (centroid) distance is 2.361(1) Å for Dy1 and 2.362(1) Å for Dy2. The Dy...B distances are 2.490(6) and 2.506(6) Å for Dy1, and 2.496(6) and 2.498(6) Å for Dy2. Coordination of THF gives a Dy–O bond length of 2.338(3) Å for Dy1 and 2.342(3) Å for Dy2. The two planes of Cp-rings give a twist angle of 70.302 (5)°, which results in an intramolecular Dy...Dy distance of 5.443(1) Å. The FTIR spectrum shows a medium-strength absorption at $\tilde{\nu} = 2127\text{--}2467\text{ cm}^{-1}$ for the terminal and bridging B–H groups (Figure 7.1 in the Experimental Section). The **2.6_Y** has a similar structure to **2.6_{Dy}** with only slight difference in parameters, therefore, the detailed values will not be described. The ^1H and ^{13}C NMR spectra are also consistent with the solid-state structure of **2.6_Y** (Figure 7.2–7.5).

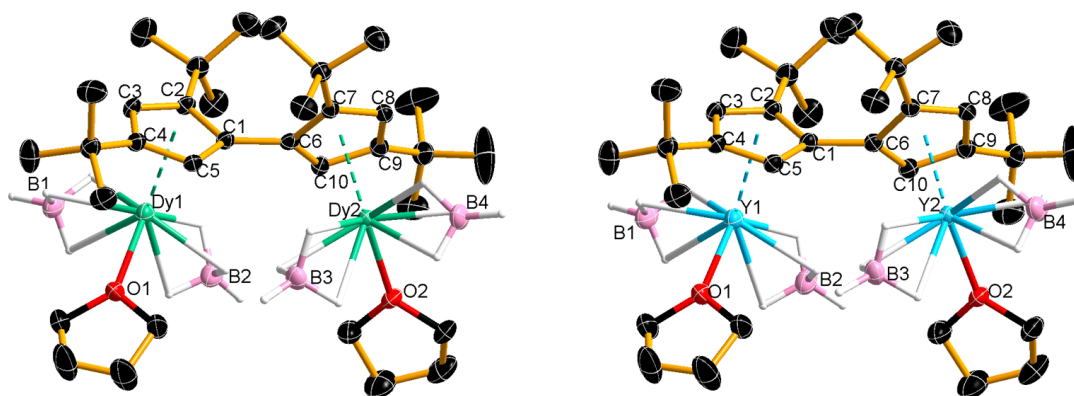


Figure 2.4 Thermal ellipsoid representation (30 % possibility) of molecular structures of **2.6_{Dy}** and **2.6_Y**.

Table 2.1 Selected bond lengths (Å) for **2.6_Y** and **2.6_{Dy}**.

	2.6_Y	2.6_{Dy}
M–C(Fv ^{tttt})	Y1–C1: 2.695(2) Y1–C2: 2.663(3) Y1–C3: 2.611(3) Y1–C4: 2.633(3) Y1–C5: 2.632(3) Y2–C6: 2.691(2) Y2–C7: 2.664(2) Y2–C8: 2.616(2) Y2–C9: 2.633(3) Y2–C10: 2.632(2)	Dy1–C1: 2.698(4) Dy1–C2: 2.668(4) Dy1–C3: 2.607(4) Dy1–C4: 2.640(4) Dy1–C5: 2.641(4) Dy2–C6: 2.696(4) Dy2–C7: 2.668(4) Dy2–C8: 2.619(4) Dy2–C9: 2.648(4) Dy2–C10: 2.635(4)
M–Cp _c (Fv ^{tttt} centroid)	Y1–Cp _c : 2.356(1) Y2–Cp _c : 2.355(1)	Dy1–Cp _c : 2.361(1) Dy2–Cp _c : 2.362(1)
M ₁ –M ₂	Y1–Y2: 5.445(1)	Dy1–Dy2: 5.443(1)
M–O	Y1–O1: 2.321(2) Y2–O2: 2.313(2)	Dy1–O1: 2.338(3) Dy2–O2: 2.342(3)
M–B	Y1–B1: 2.505(4) Y1–B2: 2.488(4) Y2–B3: 2.493(3) Y2–B4: 2.497(4)	Dy1–B1: 2.506(6) Dy1–B2: 2.490(6) Dy2–B3: 2.498(6) Dy2–B4: 2.496(6)

2.3.2 Crystal Structure of $[(BH_4)DyFv^{tttt}]_2$

The dimetalloocene complex **2.7** consists of two dysprosium centres, in which each Dy is η^5 -sandwiched by two Cp units of the two fulvalenyl ligands and a κ^2 -bridging borohydride ligand (Figure 2.5). The Dy1 and Dy2 have a similar Dy–C distance range, i.e. 2.602(5)–2.681(4) and 2.584(5)–2.682(4) Å respectively. The Dy–Cp_c distances are 2.360(1) and 2.363(1) Å for Dy1, and 2.354(1) and 2.360(1) Å for Dy2. Compared to **2.6_{Dy}**, compound **2.7** has a shorter Dy...Dy distance of 5.044(1) Å, with Cp_c–Dy–Cp_c angles of 136.406(12)° for Dy1 and 137.767(12)° for Dy2. The larger steric effect from two bulky fulvalenyl ligands results in longer Dy...B distance of 2.645(6) and 2.648(6) Å. The IR spectrum of **2.7** shows a borohydride absorption band at $\tilde{\nu} = 2373$ – 2466 cm⁻¹ (Figure 7.6 in the Experimental Section).

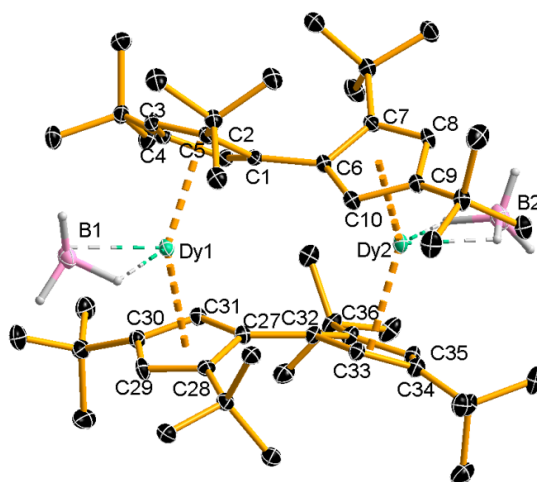


Figure 2.5 Thermal ellipsoid representation (30 % possibility) of molecular structure of **2.7**.

Table 2.2 Selected bond lengths (Å) and angles (°) for **2.7**.

Dy–C(Fv ^{tttt})	Dy1–C1: 2.662(4) Dy1–C2: 2.602(5) Dy1–C3: 2.654(5) Dy1–C4: 2.658(4) Dy1–C5: 2.658(4) Dy1–C27: 2.659(4) Dy1–C28: 2.681(4) Dy1–C29: 2.653(5) Dy1–C30: 2.668(4) Dy1–C31: 2.608(4) Dy2–C6: 2.625(4) Dy2–C7: 2.679(5) Dy2–C8: 2.649(5) Dy2–C9: 2.669(4) Dy2–C10: 2.609(4) Dy2–C32: 2.682(4) Dy2–C33: 2.584(5) Dy2–C34: 2.660(5) Dy2–C35: 2.660(5) Dy2–C36: 2.660(5)
Dy–Cp _c (Fv ^{tttt} centroid)	Dy1–Cp _c 1: 2.363(1) Dy1–Cp _c 2: 2.360(1) Dy2–Cp _c 1: 2.354(1) Dy2–Cp _c 2: 2.360(1)
Dy ₁ ···Dy ₂	Dy1–Dy2: 5.044(1)
Dy···B	Dy1–B1: 2.645(6) Dy2–B2: 2.648(6)
Cp _c –Dy–Cp _c (°)	Dy1: 136.406(12) Dy2: 137.767(12)

2.3.3 Crystal Structure of $[\{\text{Ln}(\eta^5\text{-Cp}^*)(\mu\text{-BH}_4)\}_2(\eta^5\text{-Fv}^{\text{tttt}})]$

In complexes **2.9_{Dy}** and **2.9_Y**, each metal centre is sandwiched by one $\eta^5\text{-Cp}^*$ ligand and one five-membered ring from the $\eta^5\text{-Fv}^{\text{tttt}}$ ligand; in addition, two borohydride ligands bridge between the metals (Figure 2.6). For compound **2.9_{Dy}**, the Dy1–C bond lengths are in the range of 2.630(2)–2.704(4) Å to the fulvalenyl ligand and 2.643(3)–2.667(2) Å to the Cp* ligand. A similar range of 2.633(3)–2.698(4) Å and 2.647(3)–2.660(3) Å was found for Dy2. The Dy–Cp* distances are 2.362(1) Å and 2.360(1) Å, making them slightly shorter than those to the Dy–Fv^{tttt} centroids, i.e. Dy1–Cp_c = 2.378(1) Å and Dy2–Cp_c = 2.375(1) Å. Due to the bridging BH₄ ligands, the Dy...Dy distance is significantly reduced to 4.148(1) Å relative to compound **2.6_{Dy}**, with Cp*–Dy–Cp^{Fv} bending angles of 137.913(1)° and 139.143(1)° for Dy1 and Dy2, respectively. The Dy...B distance increases to 2.782(6)–3.323(1) Å. The two cyclopentadienyl units of the fulvalenyl ligand have a twisted angle of 30.82(11)° (defined as the angle formed between the mean planes of the two C₅ rings of Fv^{tttt}), which is much smaller than that in **2.6_{Dy}**. The IR spectrum of **2.9_{Dy}** shows a borohydride absorption band at $\tilde{\nu} = 2124\text{--}2473\text{ cm}^{-1}$ (Figure 7.8 in the Experimental Section). For compound **2.9_Y**, the related parameters are listed in Table 2.3, also with the diagnostic ¹H, ¹³C and ¹¹B NMR spectra (Figure 7.10–7.12, Experimental Section).

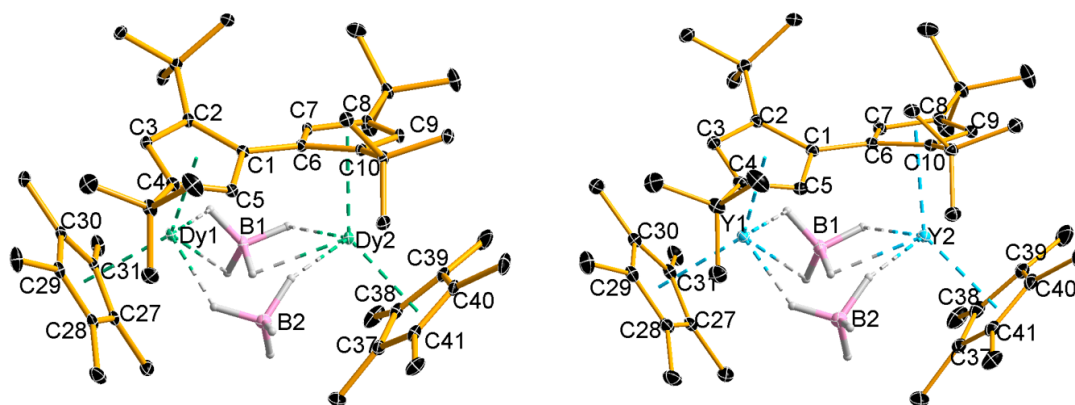


Figure 2.6 Thermal ellipsoid representation (30 % possibility) of molecular structures of **2.9_{Dy}** and **2.9_Y**.

Table 2.3 Selected bond lengths (Å) and angles (°) for **2.9**.

	2.9_Y	2.9_{Dy}
M–C(Fv ^{tttt})	Y1–C1: 2.646(2) Y1–C2: 2.676(2) Y1–C3: 2.663(2) Y1–C4: 2.693(2) Y1–C5: 2.627(2) Y2–C6: 2.650(2) Y2–C7: 2.625(2) Y2–C8: 2.694(2) Y2–C9: 2.660(2) Y2–C10: 2.675(2)	Dy1–C1: 2.653(2) Dy1–C2: 2.687(3) Dy1–C3: 2.670(3) Dy1–C4: 2.704(3) Dy1–C5: 2.630(2) Dy2–C6: 2.649(3) Dy2–C7: 2.633(3) Dy2–C8: 2.698(3) Dy2–C9: 2.671(3) Dy2–C10: 2.677(3)
M–C(Cp*)	Y1–C27: 2.639(2) Y1–C28: 2.639(2) Y1–C29: 2.650(2) Y1–C30: 2.634(2) Y1–C31: 2.664(2) Y2–C37: 2.659(2) Y2–C38: 2.655(2) Y2–C39: 2.643(2) Y2–C40: 2.620(2) Y2–C41: 2.638(2)	Dy1–C27: 2.643(3) Dy1–C28: 2.645(3) Dy1–C29: 2.659(2) Dy1–C30: 2.646(2) Dy1–C31: 2.667(2) Dy2–C37: 2.663(3) Dy2–C38: 2.660(3) Dy2–C39: 2.650(3) Dy2–C40: 2.630(3) Dy2–C41: 2.647(3)
M–Cp _c (Fv ^{tttt} centroid)	Y1- Cp _c : 2.370(1) Y2- Cp _c : 2.371(1)	Dy1- Cp _c : 2.378(1) Dy2- Cp _c : 2.375(1)
M–Cp _c (Cp* centroid)	Y1- Cp _c : 2.353(1) Y2- Cp _c : 2.355(1)	Dy1- Cp _c : 2.362(1) Dy2- Cp _c : 2.360(1)
M ₁ ···M ₂	Y1–Y2: 4.162(1)	Dy1–Dy2: 4.148(1)
M···B	Y1–B1: 2.902(2) Y1–B2: 3.066(3) Y2–B1: 2.785(2) Y2–B2: 3.311(1)	Dy1–B1: 2.909(3) Dy1–B2: 3.037(4) Dy2–B1: 2.782(6) Dy2–B2: 3.323(1)
Cp(Fv ^{tttt})–M–Cp(Cp*)	Y1:138.028(1) Y2:138.967(1)	Dy1: 137.913(1) Dy2: 139.143(1)

2.3.4 Crystal Structure of $\{[Dy(\eta^5-Cp^*)]_2(\mu-BH_4)(\eta^5:\eta^5-Fv^{tttt})\}[B(C_6F_5)_4]$

For complex **[2.10]** $[B(C_6F_5)_4]$, the coordination environment of the dysprosium centres is similar to that observed in **2.9**, but with only one bridging borohydride ligand (Figure 2.7). The Dy1–C bond lengths are in the range 2.594(7)–2.650(8) Å to the Cp* ligand and 2.578(7)–2.742(8) Å to the Fv^{tttt} ligand, which is similar to the range for Dy2 (Table 2.4). Due to loss of one BH₄ ligand, the Dy-centroid distances are shorter for both the Cp* and Fv^{tttt} ligands, with lengths of 2.355(1) and 2.322(1) Å for Dy1, respectively, and 2.348(1) and 2.310(1) Å for Dy2. A longer Dy⋯Dy distance of 4.701(1) Å was found. Meanwhile, the Cp*–Dy–Cp^{Fv} angles are less bent at 145.727(1)° and 146.246(1)° for Dy1 and Dy2, respectively, with a Cp–Cp twist angle of 78.2° in the Fv^{tttt} ligand. The sole borohydride ligand is bridging in a κ^2 manner for both of the dysprosium ions, with a shorter Dy⋯B distance of 2.715(10) Å Dy1 and 2.696(5) Å for Dy2. The IR spectrum reveals a weak peak at $\tilde{\nu} = 2230\text{ cm}^{-1}$ for the borohydride group (Figure 7.13).

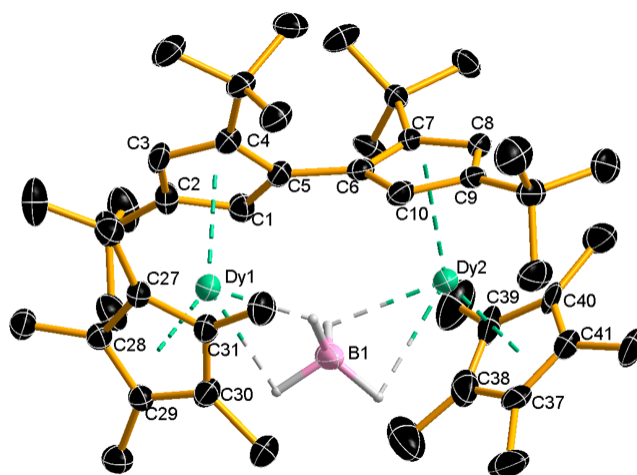


Figure 2.7 Thermal ellipsoid representation (30 % possibility) of molecular structure of **[2.10]**[−] cation.

Table 2.4 Selected bond lengths (Å) and angles (°) for [2.10]⁺ cation.*

	2.10 (disordered part 1)	2.10 (disordered part 2)
Dy–C(Fv ^{tttt})	Dy1–C1: 2.578(7) Dy1–C2: 2.592(8) Dy1–C3: 2.644(8) Dy1–C4: 2.742(8) Dy1–C5: 2.675(7) Dy2–C6: 2.687(7) Dy2–C7: 2.699(10) Dy2–C8: 2.613(7) Dy2–C9: 2.589(7) Dy2–C10: 2.591(8)	
Dy–C(Cp*)	Dy1–C27: 2.634(8) Dy1–C28: 2.594(7) Dy1–C29: 2.599(7) Dy1–C30: 2.622(8) Dy1–C31: 2.650(8) Dy2–C37: 2.600(16) Dy2–C38: 2.620(20) Dy2–C39: 2.594(18) Dy2–C40: 2.599(15) Dy2–C41: 2.610(15)	Dy2–C37A: 2.620(20) Dy2–C38A: 2.620(20) Dy2–C39A: 2.655(18) Dy2–C40A: 2.699(6) Dy2–C41A: 2.652 (18)
Dy–Cp _c (Fv ^{tttt} centroid)	Dy1–Cp _c : 2.355(1) Dy2–Cp _c : 2.348(1)	
Dy–Cp _c (Cp* centroid)	Dy1–Cp _c : 2.322(1) Dy2–Cp _c : 2.310(1)	Dy2–Cp _c : 2.356(1)
Dy ₁ ···Dy ₂	Dy1–Dy2: 4.701(1)	
Dy···B	Dy1–B1: 2.715(10) Dy2–B1: 2.696(5)	
Cp(Fv ^{tttt})–Dy–Cp(Cp*)	Dy1: 145.727(1) Dy2: 146.246(1)	Dy2: 145.656(1)

* One of the Cp*(C37–C41) disordered over two sites.

2.4 Magnetic Property Characterization

The magnetic properties of compounds **2.6_{Dy}**, **2.7**, **2.9_{Dy}** and **[2.10][B(C₆F₅)₄]** were studied, including DC and AC magnetic susceptibility and isothermal magnetization measurements. Magnetic hysteresis measurements were also performed. These measurements were conducted in collaboration with Prof. J. Tang at the Changchun Institute of Applied Chemistry, China.

2.4.1 DC Magnetic Measurements

The temperature dependence of the molar magnetic susceptibility plots as $\chi_M T$ versus T was measured for the four complexes under a 1 kOe DC field (Figure 2.8). The values of $\chi_M T$ at 300 K were determined as 27.3, 27.2, 27.2 and 27.5 $\text{cm}^3 \text{K mol}^{-1}$ for **2.6_{Dy}**, **2.7**, **2.9_{Dy}** and **[2.10][B(C₆F₅)₄]** respectively, which are close to the theoretical value of 28.2 $\text{cm}^3 \text{K mol}^{-1}$ for two non-interacting Dy³⁺ ions with ⁶H_{15/2} ground terms.¹⁴⁹

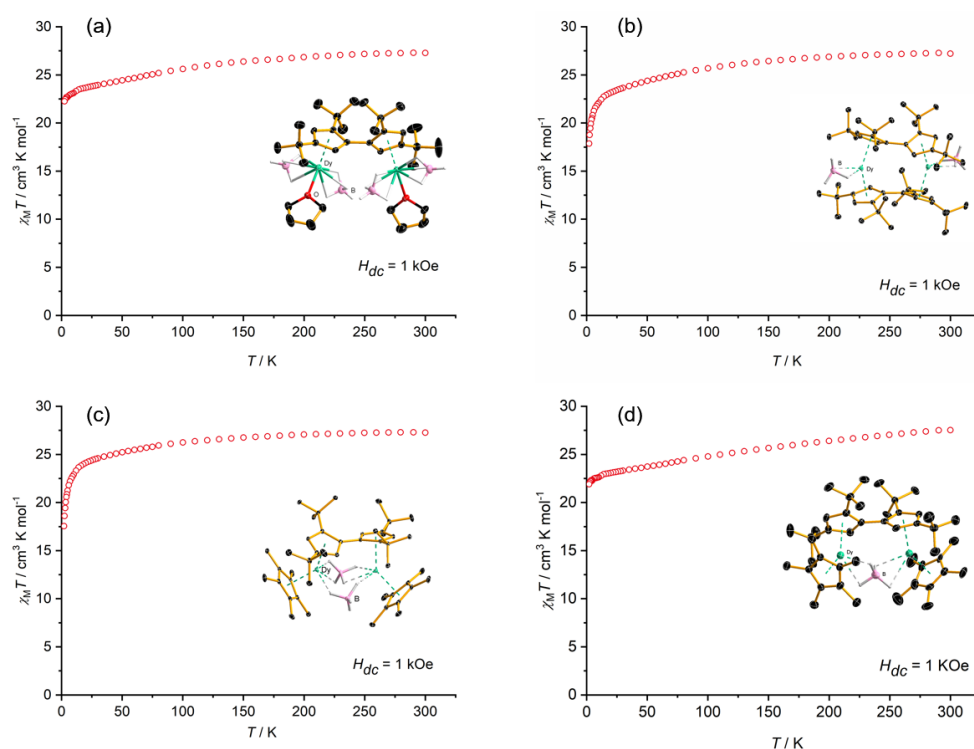


Figure 2.8 Plots of $\chi_M T$ versus temperature for (a) **2.6_{Dy}**, (b) **2.7**, (c) **2.9_{Dy}** and (d) **[2.10][B(C₆F₅)₄]** in an applied magnetic field of 1 kOe.

All the $\chi_{\text{M}}T$ values of the four compounds begin to slowly decrease with decreasing temperature. For **2.6_{Dy}** and **[2.10][B(C₆F₅)₄]**, the decreases in $\chi_{\text{M}}T$ at low temperature are similar, dropping slightly to 22.2 cm³ K mol⁻¹ for both compounds at 2.0 K. Compounds **2.7** and **2.9_{Dy}** show a sharper decrease in $\chi_{\text{M}}T$ below 20 K, which reaches 17.9 cm³ K mol⁻¹ for **2.7** and 17.5 cm³ K mol⁻¹ for **2.9_{Dy}** at 2.0 K. The decrease in $\chi_{\text{M}}T$ can be ascribed to the thermal depopulation of the excited crystal field levels of Dy³⁺ and/or the weak antiferromagnetic exchange. As the temperature gets lower, the antiferromagnetic exchange coupling makes more contributions, which is evident in particular in compounds **2.7** and **2.9_{Dy}**.

On the other hand, the isothermal field-dependence of the magnetization i.e., M versus H , were measured at 1.90 K, 3.0 K and 5.0 K (Figure 2.9). The maximum M values are 9.89, 10.11, 9.80 and 9.60 N β from **2.6_{Dy}** to **[2.10][B(C₆F₅)₄]** respectively at 1.9 K and 7 T, without quite reaching saturation. These values are considerably lower than the theoretical value of 20 N β for a dysprosium dimer,¹⁵⁰ a feature typically attributed to the strong magnetic anisotropy.

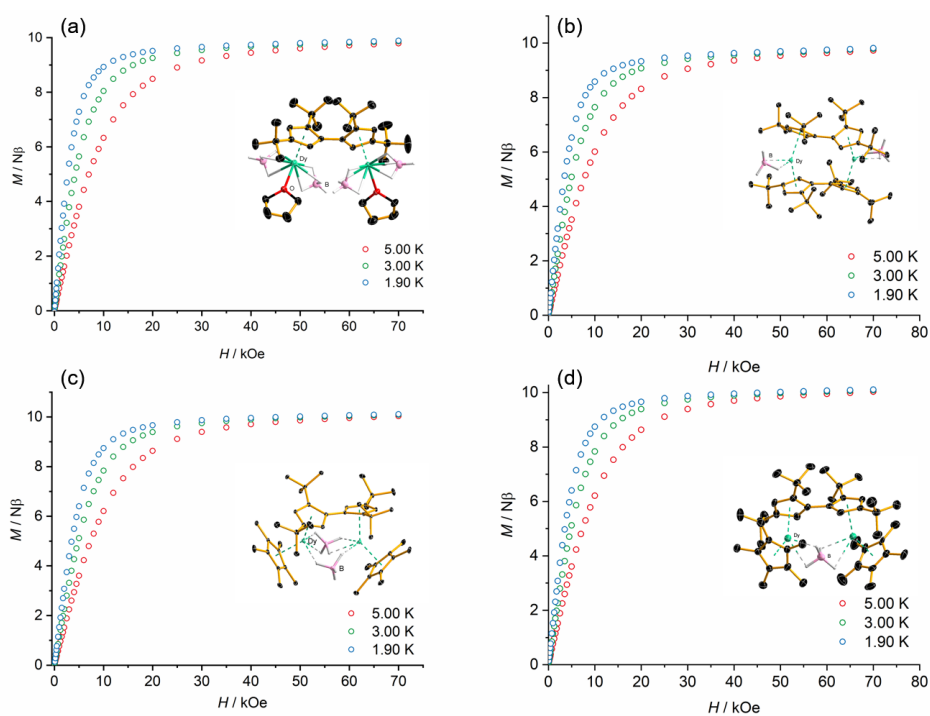


Figure 2.9 Plots of field dependent magnetization for (a) **2.6_{Dy}**, (b) **2.7**, (c) **2.9_{Dy}** and (d) **[2.10][B(C₆F₅)₄]** at 2 K, 3 K and 5 K.

2.4.2 AC Magnetic Measurement

The frequency (ν) dependence of the in-phase (χ') and the out-of-phase (χ'') magnetic susceptibility was measured using a small 3 Oe AC field and zero DC field. The results are shown in Figures 2.10–2.14 for **2.6_{Dy}**, **2.7**, **2.9_{Dy}** and **[2.10][B(C₆F₅)₄]**, respectively. Their Cole-Cole plots are also given in Figures 2.11b–2.14b. The corresponding relaxation fitting parameters with Debye model (Equation 4 on page 21) are listed in Table 2.5–2.8.

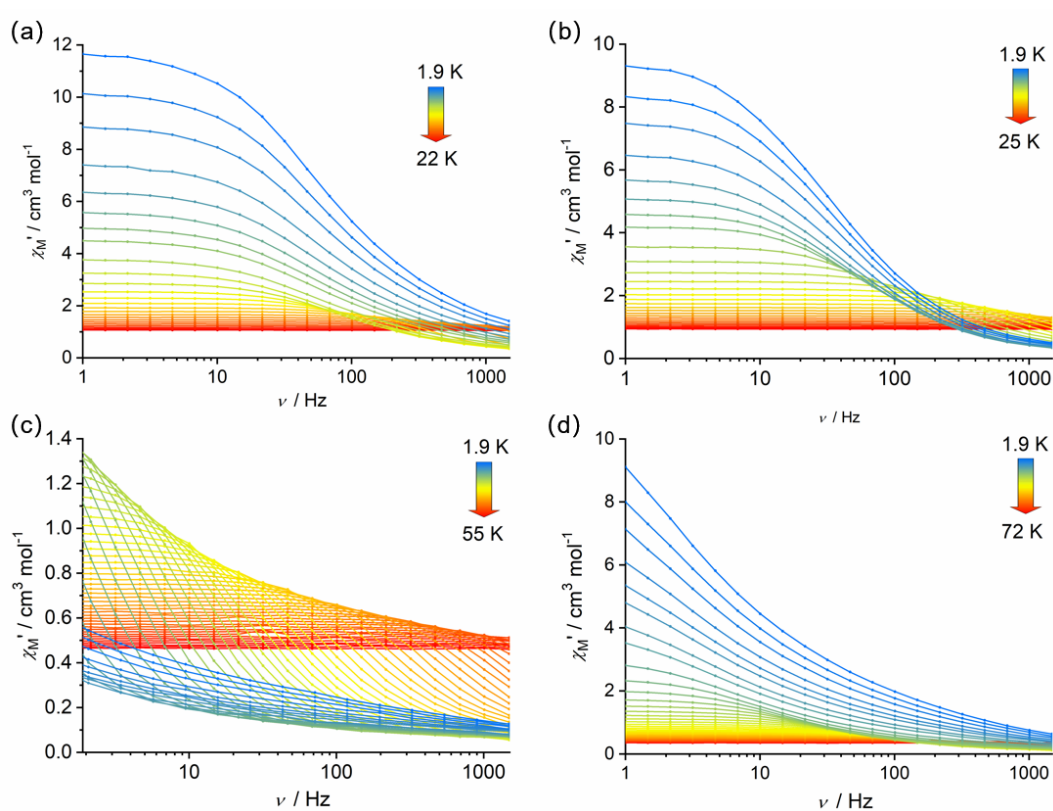


Figure 2.10. Frequency dependence of the in-phase susceptibility (χ') for (a) **2.6_{Dy}**, (b) **2.7**, (c) **2.9_{Dy}** and (d) **[2.10][B(C₆F₅)₄]** at AC field frequencies of 1–1488 Hz in zero DC field.

For compound **2.6_{Dy}**, with a measurement temperature range of 1.9–22 K, maxima in $\chi''(\nu)$ were observed up to 14 K (Figure 2.10a). Fits of the data were achieved using the equation $\tau^{-1} = \tau_0^{-1}e^{-U_{\text{eff}}/k_{\text{B}}T} + CT^n + \tau_{\text{QTM}}^{-1}$, with the parameters: $U_{\text{eff}} = 154(15)$

cm^{-1} with pre-exponential factor of $\tau_0 = 3.93(6) \times 10^{-11} \text{ s}$, $C = 8.16(3) \times 10^{-4} \text{ s}^{-1} \text{ K}^{-n}$, $n = 5.87(1)$ and a QTM time of $\tau_{\text{QTM}} = 2.31(1) \times 10^{-3} \text{ s}$ (Figure 2.11a). According to the dependence of $\ln(\tau/s)$ on T^{-1} , the magnetic relaxation processes are dominated by the quantum tunnelling below 6 K because the relaxation time is temperature-independent. Above 6 K (the dependence of $\ln(\tau/s)$ on T^{-1} is linear, indicating a thermally activated (Orbach) relaxation mechanism (Figure 2.11c). The fitting with the Debye model yields α parameters in a range of 0.12–0.30, which also suggests a small distribution of the relaxation times (Table 2.5).

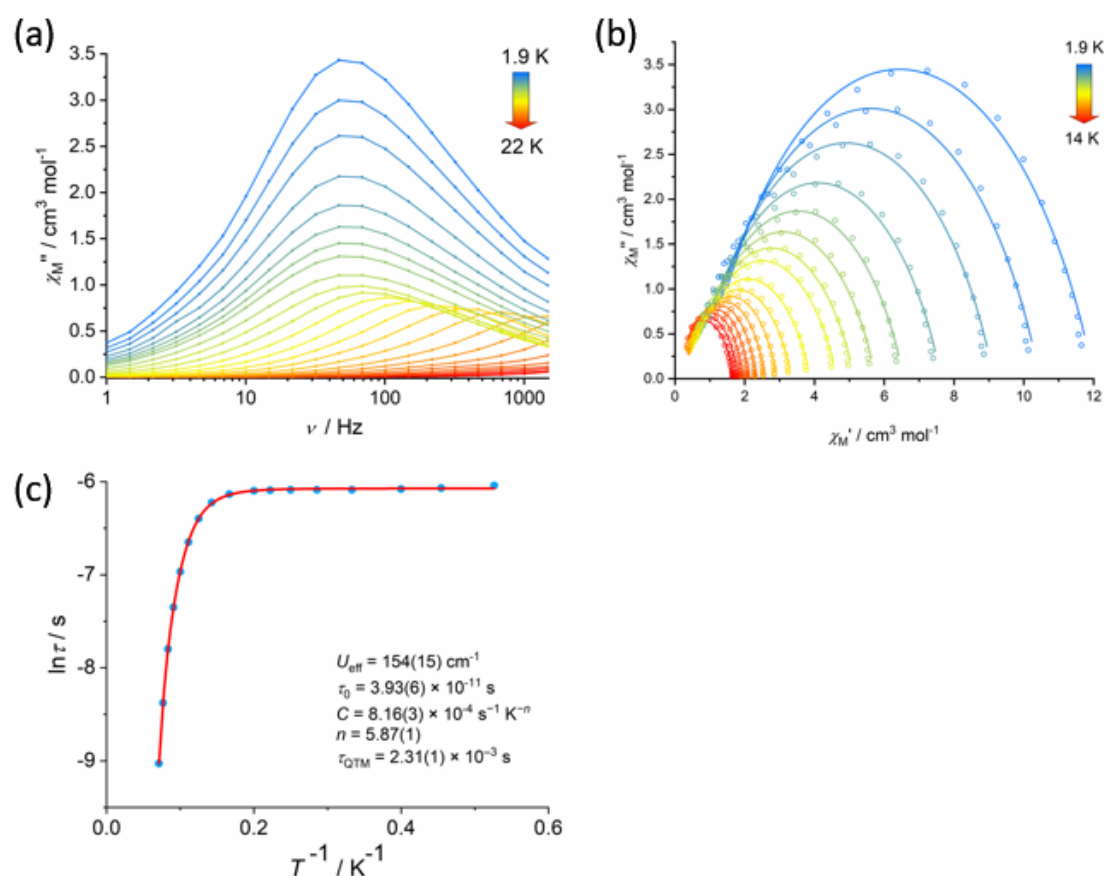


Figure 2.11. Frequency dependence of the in-phase and out-of-phase (b) susceptibility (χ'') for **2.6Dy** in zero DC field at AC frequencies of 1–1488 Hz; Solid lines are a guide to the eye. (c) Cole-Cole plots for **2.6Dy** in zero DC field; Solid lines are fits of data with Equation 4 on page 21 (adjusted $R^2 = 0.99900$ – 0.99999). (d) The Plots of natural log of the relaxation time (τ) versus inverse temperature for **2.6Dy**. The blue points are from

the AC susceptibility measurements. The solid red line is the best fit using Equation 3 on page 16 (adjusted $R^2 = 0.99987$).

Table 2.5. Relaxation fitting parameters for **2.6_{Dy}** corresponding to Figures 2.10a and 2.11a (adjusted $R^2 = 0.99900$ – 0.99999).

T / K	$\chi_T / \text{cm}^3 \text{mol}^{-1}$	$\chi_S / \text{cm}^3 \text{mol}^{-1}$	α	τ / s
14.06	1.65224	0 [§]	0.15263	1.20E-04
13.03	1.77967	0.05386	0.13526	2.30E-04
12	1.92129	0.14236	0.11958	4.10E-04
11	2.09779	0.19103	0.13083	6.43E-04
10	2.31333	0.22883	0.15463	9.43E-04
9	2.57102	0.25952	0.18765	0.00129
8	2.91312	0.28278	0.22664	0.00167
7	3.34096	0.29652	0.26529	0.00198
6	3.88481	0.31078	0.29171	0.00217
5	4.64557	0.35246	0.30024	0.00225
4.5	5.14155	0.38302	0.30116	0.00226
4	5.76087	0.43	0.29925	0.00227
3.5	6.56279	0.48492	0.2982	0.00227
3	7.63392	0.56247	0.29588	0.00227
2.5	9.14251	0.67345	0.29315	0.00229
2.2	10.457	0.76801	0.29196	0.00231
1.9	12.00758	0.86028	0.29476	0.00238

[§] These parameter values were restricted to being non-negative.

Complex **2.7** was measured using a similar temperature range of 1.9–25 K, in which the maxima are observed (Figure 2.12a). Using the same fitting procedure as for **2.6_{Dy}**, for compound **2.7**, a lower effective energy barrier of $U_{\text{eff}} = 108(10) \text{ cm}^{-1}$ was obtained, with $\tau_0 = 3.17(3) \times 10^{-9} \text{ s}$. The strong curvature in the data indicate that Raman processes are significant in this system, which were fitted with $C = 4.46(6) \times 10^{-1} \text{ s}^{-1} \text{ K}^{-n}$ and $n = 3.93(6)$. The QTM time is $\tau_{\text{QTM}} = 4.44(1) \times 10^{-3} \text{ s}$, and this process plays the dominant role below 4 K (Fig 2.12c). The α parameters show a small distribution of relaxation times in range of 0.11–0.27 (Table 2.6).

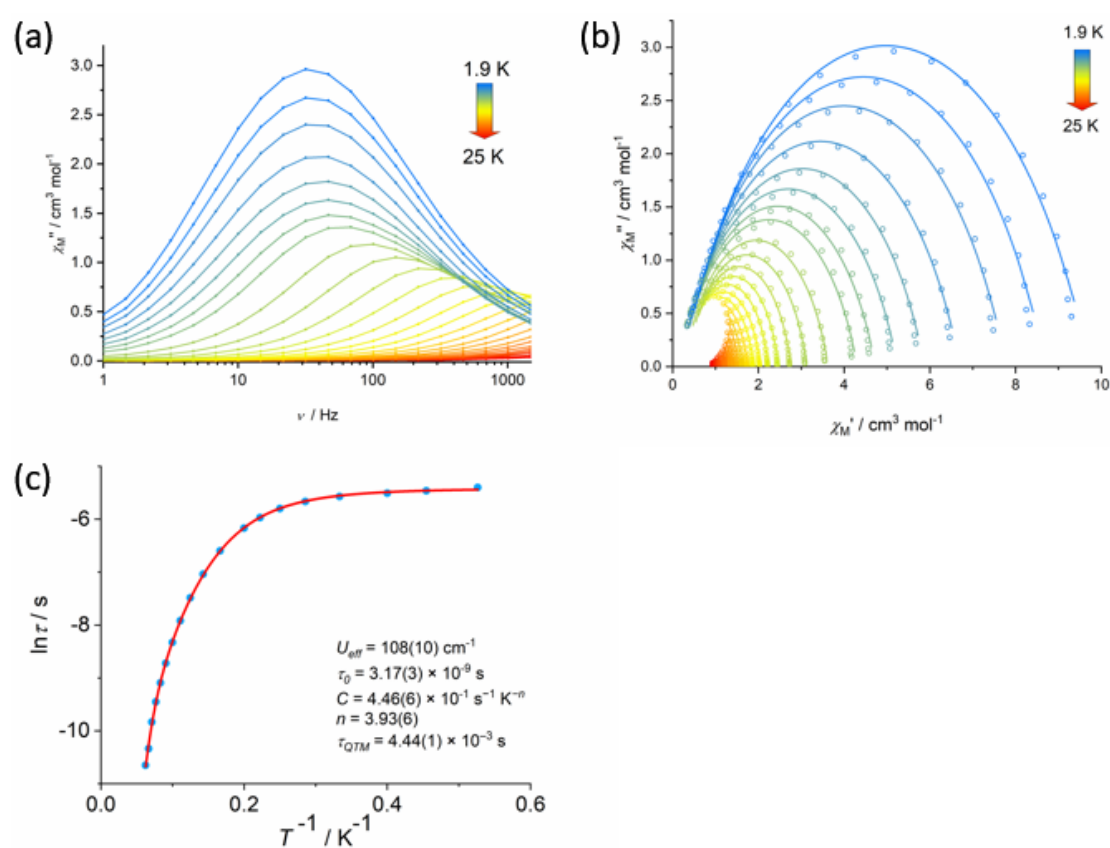


Figure 2.12 (a) Frequency dependence of the out-of-phase susceptibility (χ'') for **2.7** in zero DC field at AC frequencies of 1–1488 Hz; Solid lines are a guide to the eye. (b) Cole-Cole plots for **2.7** in zero DC field; Solid lines are fits of data with equation 4 on page 21 (adjusted $R^2 = 0.99846$ – 0.99999). (c) The Plots of natural log of the relaxation time (τ) versus inverse temperature for **2.7**. The blue points are from the AC susceptibility measurements; The solid red line is the best fit using Equation 3 on page 16 (adjusted $R^2 = 0.99975$).

Table 2.6 Relaxation fitting parameters for **2.7** corresponding to Figures 2.10b and 2.12a (adjusted $R^2 = 0.99846\text{--}0.99999$).

T / K	$\chi_{\text{T}} / \text{cm}^3 \text{mol}^{-1}$	$\chi_{\text{S}} / \text{cm}^3 \text{mol}^{-1}$	α	τ / s
16	1.43097	0 [§]	0.11862	2.36766E-5
15	1.52209	0.00865	0.11908	3.23854E-5
14.05	1.61838	0.22986	0.10549	5.35244E-5
13.02	1.73552	0.2905	0.10466	7.84564E-5
12	1.87257	0.33061	0.10725	1.1253E-4
11.02	2.02657	0.36067	0.10911	1.62942E-4
10	2.21863	0.37534	0.11465	2.4211E-4
9	2.45435	0.37765	0.12909	3.63562E-4
8	2.74685	0.37434	0.14763	5.60601E-4
7	3.12382	0.3463	0.17613	8.7614E-4
6	3.62432	0.27987	0.21398	0.00136
5	4.30387	0.19618	0.24661	0.0021
4.5	4.72913	0.17063	0.256	0.00255
4	5.24422	0.1681	0.25946	0.00304
3.5	5.87373	0.17095	0.26412	0.00346
3	6.70103	0.18686	0.26623	0.0038
2.5	7.77876	0.20525	0.26874	0.00406
2.2	8.68182	0.21597	0.27232	0.00424
1.9	9.70562	0.22727	0.27846	0.00452

[§] These parameter values were restricted to being non-negative.

Compound **2.9_{Dy}** was measured in the temperature range of 1.9–55 K, and the maxima were observed between 6–40 K. Thus, the QTM process even at low temperatures is not significant in this SMM (Figure 2.13a). Without the QTM part, the equation of $\tau^{-1} = \tau_0^{-1}e^{-U_{\text{eff}}/k_{\text{B}}T} + CT^n$ results in an effective energy barrier of $U_{\text{eff}} = 252(4) \text{ cm}^{-1}$ with $\tau_0 = 1.94(3) \times 10^{-8} \text{ s}$ and the Raman parameters of $C = 4.56(2) \times 10^{-4} \text{ s}^{-1} \text{ K}^{-n}$ and $n = 4.12(1)$ (Figure 2.13c). The Debye model fitting gives a narrow distribution of relaxation time for the α parameters of $0.03 < \alpha < 0.17$ from 6–40 K (Table 2.7).

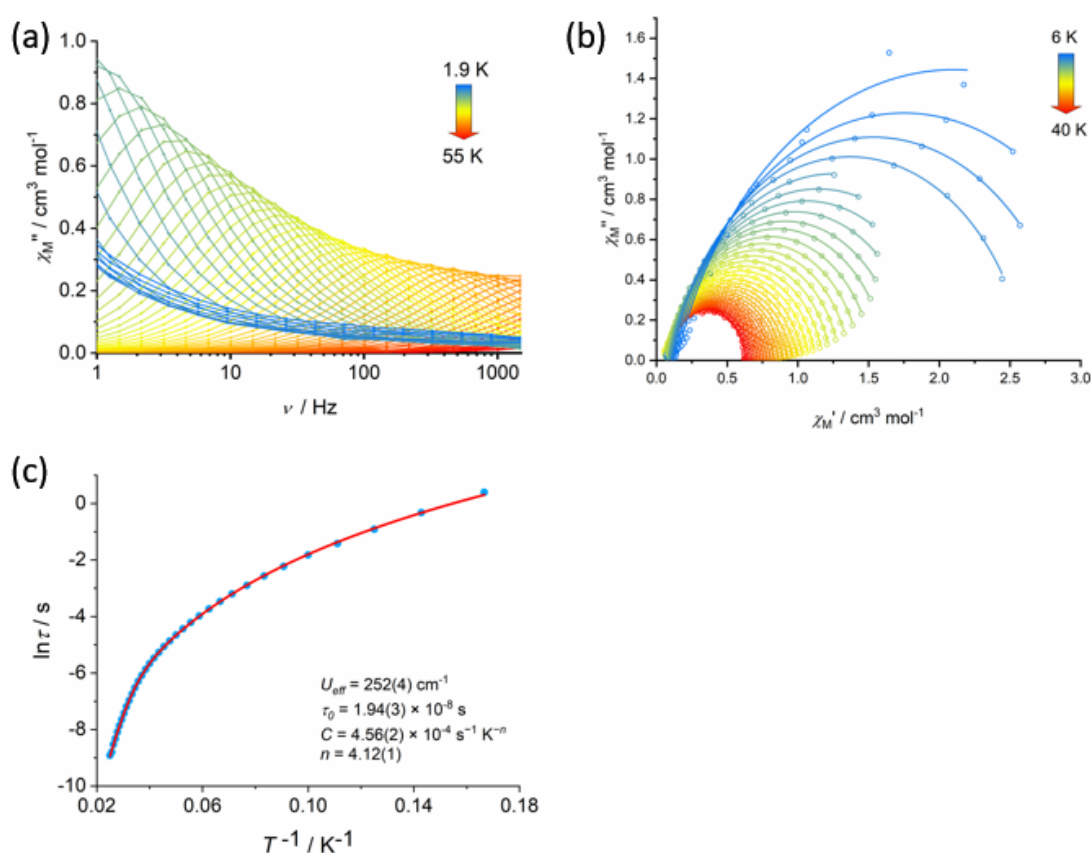


Figure 2.13 (a) Frequency dependence of the out-of-phase susceptibility (χ'') for **2.9_{Dy}** in zero DC field at AC frequencies of 1–1488 Hz; Solid lines are a guide to the eye. (b) Cole-Cole plots for **2.9_{Dy}** in zero DC field; Solid lines are fits of data with equation 4 on page 21 (adjusted $R^2 = 0.99321$ – 0.99996). (c) The Plots of natural log of the relaxation time (τ) versus inverse temperature for **2.9_{Dy}**. The blue points are from the AC susceptibility measurements; The solid red line is the best fit using Equation 3 on page 16 (adjusted $R^2 = 0.99991$).

Table 2.7 Relaxation fitting parameters for **2.9_{Dy}** corresponding to Figures 2.10c and 2.13a (adjusted $R^2 = 0.99321\text{--}0.99996$).

T / K	$\chi_T / \text{cm}^3 \text{mol}^{-1}$	$\chi_S / \text{cm}^3 \text{mol}^{-1}$	α	τ / s
40	0.62631	0.11981	0.03639	1.34283E-4
39	0.64266	0.08219	0.06929	1.51005E-4
38	0.65831	0.09873	0.05898	1.97059E-4
37	0.67575	0.09391	0.0698	2.42631E-4
36	0.69388	0.09755	0.0701	3.06877E-4
35	0.71298	0.09445	0.07609	3.83478E-4
34	0.73338	0.09147	0.08271	4.78412E-4
33	0.7554	0.08733	0.09098	5.9663E-4
32	0.77858	0.08599	0.09871	7.51126E-4
31	0.80468	0.08398	0.10429	9.39476E-4
30	0.82926	0.07956	0.10946	0.00118
29	0.85913	0.079	0.11053	0.00148
28	0.88923	0.07754	0.11354	0.00184
27	0.92247	0.0742	0.11604	0.00228
26	0.95737	0.07072	0.11743	0.00281
25	0.99482	0.06845	0.11754	0.00345
24	1.0358	0.06575	0.1181	0.00422
23	1.0786	0.06623	0.1129	0.00515
22	1.12603	0.06626	0.11096	0.00634
21	1.1787	0.06444	0.11107	0.00774
20	1.23448	0.06694	0.10731	0.00954
19	1.29855	0.06826	0.10692	0.01186
18	1.36856	0.06973	0.10741	0.0148
17	1.44545	0.07178	0.10672	0.01871
16	1.53454	0.07419	0.10914	0.02402
15	1.63439	0.07604	0.11132	0.03126
14.05	1.7414	0.08038	0.11614	0.0408
13.02	1.86995	0.08475	0.12007	0.05515
12	2.02548	0.08829	0.12724	0.07692
11.02	2.19284	0.09336	0.13202	0.10824
10	2.41217	0.09985	0.13934	0.16131
9	2.62604	0.10686	0.1387	0.24186
8	2.94926	0.11607	0.1543	0.40079
7	3.3717	0.12681	0.17469	0.72298
6	4.07094	0.14183	0.03639	1.47795

Finally, compound **[2.10][B(C₆F₅)₄]** was measured in the temperature range 1.9–72 K, with the maxima obtained at 1.9–60 K (Figure 2.14a). A fitting of the AC data gave $U_{\text{eff}} = 384(18) \text{ cm}^{-1}$ with $\tau_0 = 1.37(6) \times 10^{-8} \text{ s}$, and Raman parameters $C = 6.55(4) \times 10^{-1} \text{ s}^{-1} \text{ K}^{-n}$, $n = 2.03(2)$, and a QTM time of $\tau_{\text{QTM}} = 2.31(1) \times 10^{-3} \text{ s}$ (Figure 2.14c). The fitting of data with Debye model gives the α parameters of 0.02–0.55, indicating a broad distribution of relaxation time (Table 2.8).

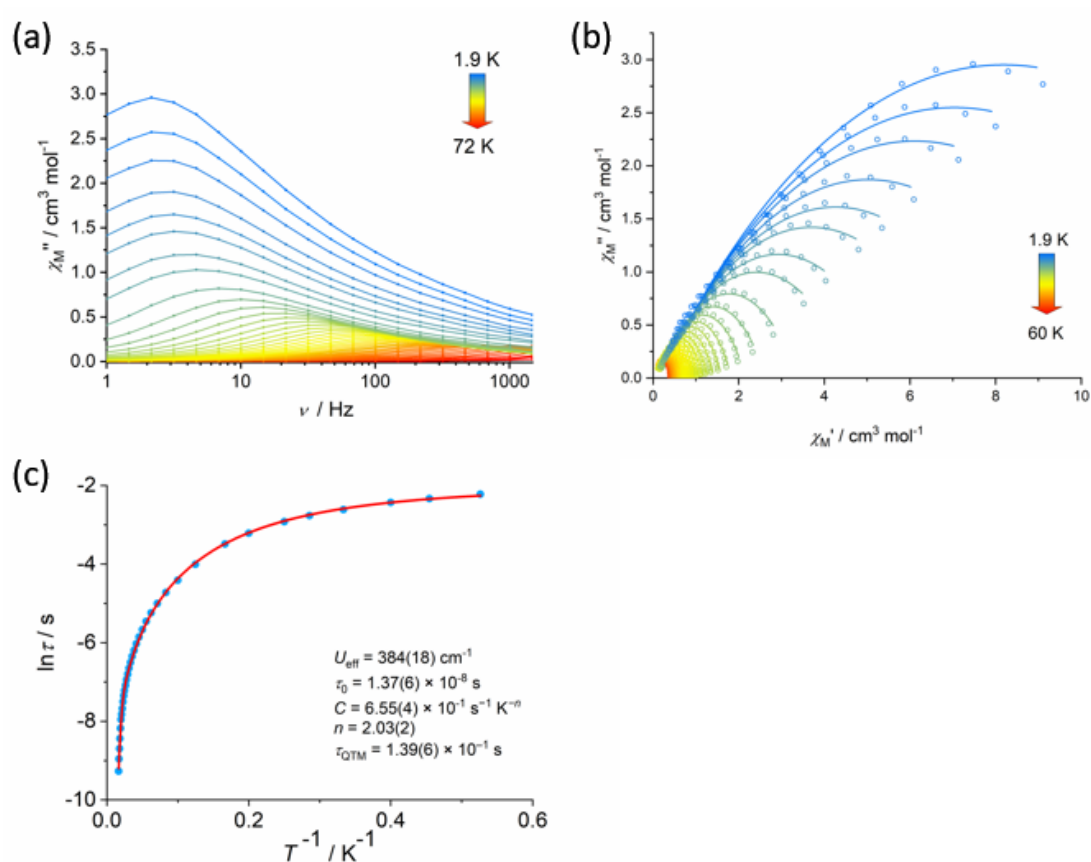


Figure 2.14 (a) Frequency dependence of the out-of-phase susceptibility (χ'') for **[2.10][B(C₆F₅)₄]** in zero DC field at AC frequencies of 1–1488 Hz; Solid lines are a guide to the eye. (b) Cole-Cole plots for **[2.10][B(C₆F₅)₄]** in zero DC field; Solid lines are fits of data with Equation 4 on page 21 (adjusted $R^2 = 0.99766$ – 0.99993) (c) The Plots of natural log of the relaxation time (τ) versus inverse temperature for **[2.10][B(C₆F₅)₄]**. The blue points are from the AC susceptibility measurements; The solid red line is the best fit using Equation 3 on page 16 (adjusted $R^2 = 0.99963$).

Table 2.8 Relaxation fitting parameters for [2.10][B(C₆F₅)₄] corresponding to Figures 2.10d and 2.14a (adjusted $R^2 = 0.99766\text{--}0.99993$).

T / K	$\chi_T / \text{cm}^3 \text{mol}^{-1}$	$\chi_S / \text{cm}^3 \text{mol}^{-1}$	α	τ / s
60	0.41817	0.0615	0.02535	9.43398E-5
58	0.43313	0.07291	0.05029	1.28887E-4
56	0.44755	0.06384	0.0666	1.67114E-4
54	0.46511	0.06115	0.08383	2.15456E-4
52	0.48126	0.06971	0.08024	2.79484E-4
50	0.50038	0.07553	0.09832	3.49799E-4
48	0.52032	0.0708	0.11221	3.9843E-4
46	0.5435	0.06923	0.12607	4.63012E-4
44	0.56682	0.07852	0.12038	5.50927E-4
42	0.59284	0.08215	0.12602	6.40314E-4
40	0.62221	0.0834	0.1258	7.30166E-4
38	0.65381	0.08515	0.13076	8.34743E-4
36	0.68994	0.08802	0.1328	9.63924E-4
34	0.73071	0.09288	0.1425	0.00111
32	0.77451	0.09708	0.14123	0.0013
30	0.82737	0.09916	0.14839	0.0015
28	0.88666	0.10871	0.1529	0.00175
26	0.95573	0.1112	0.16284	0.00204
24	1.03721	0.11724	0.17212	0.00241
22	1.1337	0.12377	0.18556	0.00287
20	1.24977	0.13349	0.19959	0.00346
18	1.39346	0.1463	0.21637	0.00426
16	1.57556	0.15706	0.23938	0.00531
14.05	1.80742	0.16857	0.26784	0.00671
12	2.13018	0.1897	0.30082	0.00889
10	2.59703	0.19585	0.34904	0.01214
8	3.33853	0.19888	0.4037	0.01824
6	4.63934	0.18721	0.4639	0.03054
5	5.66126	0.18923	0.48719	0.04024
4	7.21053	0.18399	0.51062	0.05397
3.5	8.34882	0.17699	0.52169	0.06283
3	9.87787	0.17392	0.53163	0.07345
2.5	12.06304	0.16088	0.54286	0.08787
2.2	13.91804	0.15956	0.54814	0.09708
1.9	16.20812	0.16343	0.55109	0.10851

Comparing all the parameters obtained from the AC susceptibility measurements, it can be seen that, from **2.6_{Dy}** to **[2.10][B(C₆F₅)₄]**, the effective energy barrier increases from 154 cm⁻¹ to 384 cm⁻¹. Qualitatively, this can be explained in terms of the crystal field experienced by dysprosium in these compounds becoming stronger and more axial and/or less equatorial, i.e., a stronger influence of the Cp ligands and/or diminishing influence of the borohydride and THF ligands.

For complex **2.6_{Dy}**, the oblate Dy³⁺ ions are coordinated by equatorial THF and BH₄ ligands, which has a negative impact on the axial anisotropy arising from the Cp ligand. Complex **2.7** gives a smaller effective energy barrier even though the molecule adopts a double sandwich structure. The phenomenon is possibly caused by a combination of equatorial crystal-field from the borohydride ligand, but with strong bending of Cp–Dy–Cp angles (136 and 137°) the axiality is clearly diminished. For compound **2.9_{Dy}**, the double-metallocene with combined effects of the Cp* and Fv^{tttt} ligands has a less-influential equatorial crystal field than in complex **2.6_{Dy}**. Compared to complex **2.7**, although the Dy³⁺ centres are bridged by two borohydride ligands and the Cp–Dy–Cp angles of 138–139° are similar, the Cp* ligands give a shorter Dy–Cp_c distance, which increase the strength of the axial crystal field. For complex **[2.10][B(C₆F₅)₄]**, after removing one bridging BH₄ ligands, the equatorial crystal-field effect is reduced, and also produces the benefit of less bending in the Cp–Dy–Cp angles (146°), which is likely to produce the larger effective energy barrier. The improvement in the SMM properties is also revealed by the larger temperature range observed for maxima in the plots of $\chi''(\nu)$. The exchange interactions between the Dy³⁺ possibly also suppresses the QTM process. Following the progressively reducing order of Dy...Dy distance **2.6_{Dy} > 2.7 > 2.10 > 2.9_{Dy}**, the corresponding relaxation time of QTM gets slower.

The SMM property improvement is also reflected in the hysteresis loops $M(H)$ in the magnetic field range of 5 T with an average scan rate of 23 Oe s⁻¹ (Figure 2.15). For compounds **2.6_{Dy}** and **2.7**, the hysteresis measurement does not show open loops. For compounds **2.9_{Dy}** and **2.10**, narrow-opening in the hysteresis loops can be observed around ± 2.5 kOe and ± 1.0 kOe at 1.90 K, respectively. Even though, the poor

performance of all the hysteresis results indicates the negative influence from the equatorial borohydride ligands, which effectively restrain the blocking temperature.

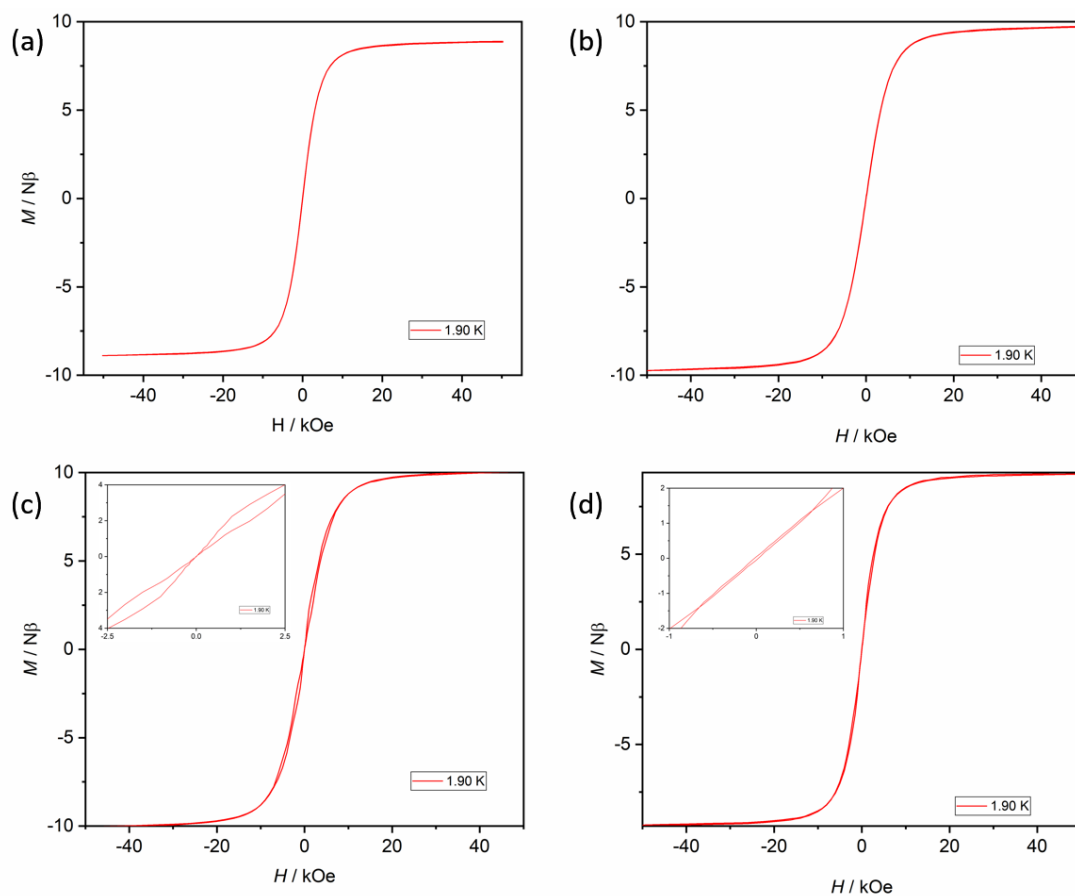


Figure 2.15 Magnetic hysteresis loops for (a) **2.6_{Dy}**, (b) **2.7**, (c) **2.9_{Dy}** and (d) **2.10**.

2.4.3 Magnetic Property Measurements on Diluted Samples

In order to further study the effects of exchange coupling, a magnetically dilute sample was synthesized by doping of 10 mol % of **2.6_{Dy}** into **2.6_v** to yield the Dy@**2.6_v** complex. Compared to **2.6_{Dy}**, the diluted sample Dy@**2.6_v** produces similar $\chi''(\nu)$ data in the temperature range 1.9–20 K, and the maxima were observed at 4–17 K (Figure 2.16). However, the fitting process gave two different relaxation paths, which share the same Orbach process parameters of $U_{\text{eff}} = 178(38) \text{ cm}^{-1}$ with $\tau_0 = 1.0(3) \times 10^{-11} \text{ s}$. The Raman process parameters are $C = 1.28(0.4) \times 10^{-5} \text{ s}^{-1} \text{ K}^{-n}$, $n = 7.4(0.1)$ without quantum tunnelling for process P1 (Figure 2.16c P1) and $C = 6.6(1) \times 10^{-5} \text{ s}^{-1} \text{ K}^{-n}$, $n = 6.8(0.6)$ with the $\tau_{\text{QTM}} = 5.6(0.4) \times 10^{-4} \text{ s}$ for process P2 (Figure 2.16c P2). The fitting α

parameters for P1 and P2 have the range of 0.01–0.43 (α_1) and 0–0.49 (α_2), both of which indicate a wide distribution of relaxation time (Table 2.9).

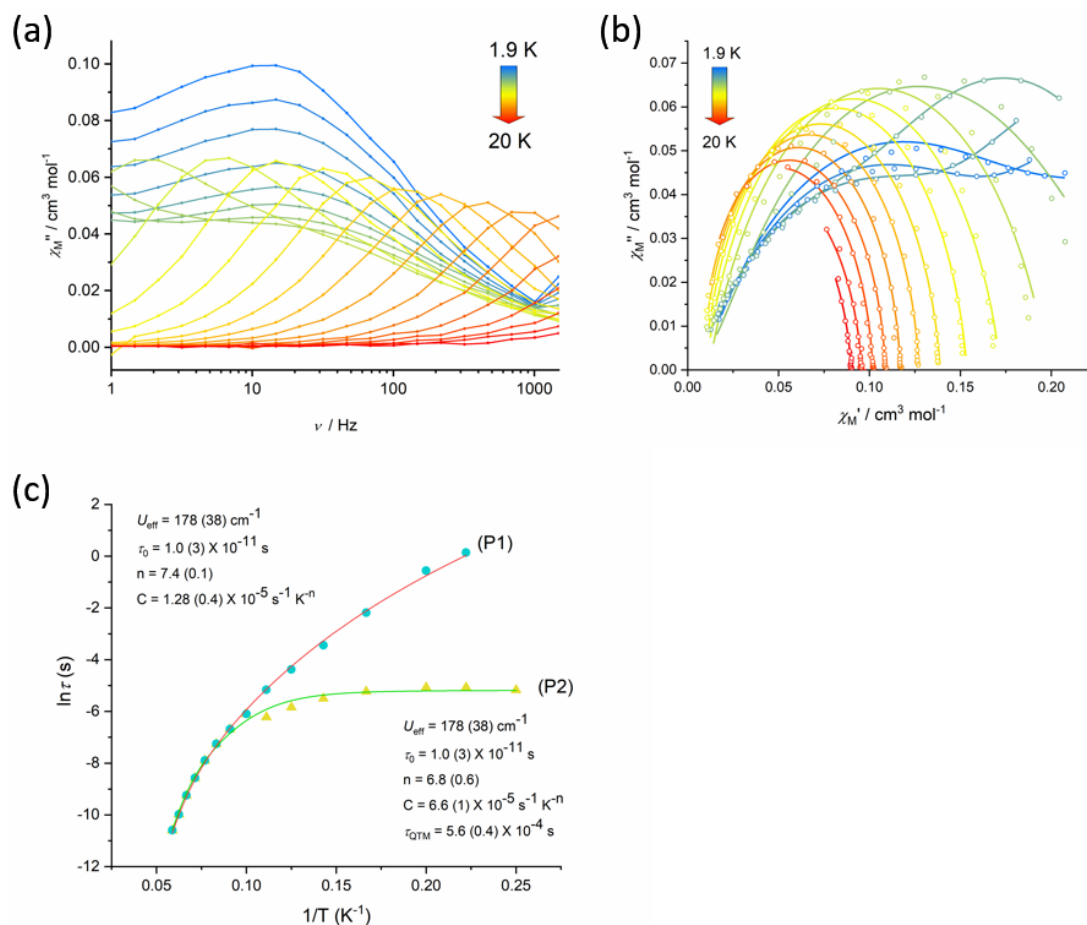


Figure 2.16 (a) Frequency dependence of the out-of-phase susceptibility (χ'') for Dy@2.6Dy in zero DC field at AC frequencies of 1–1488 Hz; Solid lines are a guide to the eye. (b) Cole-Cole plots for Dy@2.6Dy in zero DC field; Solid lines are fits of data with Equation 4 on page 21 (adjusted $R^2 = 0.99891$ – 0.99992) (c) The Plots of natural log of the relaxation time (τ) versus inverse temperature for Dy@2.6Dy; The solid red line is the best fit using Equation 3 on page 16 (adjusted $R^2 = 0.99702$).

The Cole-Cole plots also indicate more than one path involved in the diluted Dy@2.6Dy at low temperature (Figure 2.16b). It is not clear that why the path separation happens in the diluted system, however it could be due to the two qualitatively different metal coordination sites being quantitatively different. In addition, narrowly opened hysteresis loops were obtained between 0 and ± 5 kOe but close at centre point. (Figure 2.17).

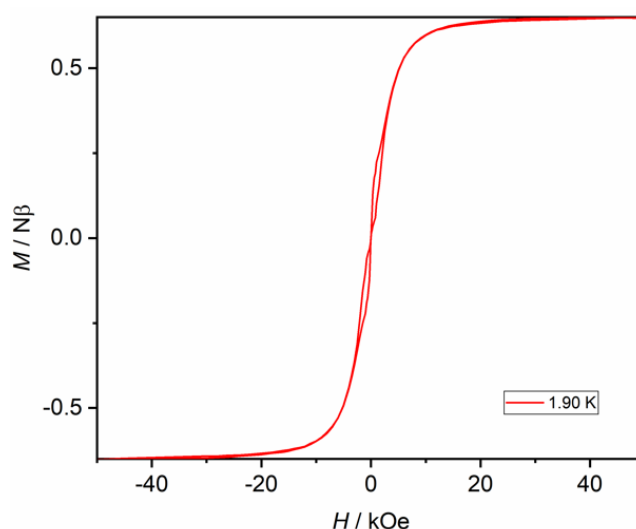


Figure 2.17 Magnetic hysteresis loops for Dy@2.6 γ .

Table 2.9 Relaxation fitting parameters for Dy@2.6 γ (adjusted $R^2 = 0.99891\text{--}0.99992$).

T / K	$\chi_{\tau} / \text{cm}^3 \text{mol}^{-1}$	$\chi_s / \text{cm}^3 \text{mol}^{-1}$	α_1	τ_1 / s	α_2	τ_2 / s
1.9	0.49006	0.02398	0.28772	0.00451	0.38075	0.06366
2.2	0.43323	0.02059	0.28795	0.00416	0.38401	0.07029
2.5	0.38584	0.01821	0.29786	0.00426	0.40596	0.07897
3	0.34198	0.0134	0.32821	0.00447	0.45836	0.11067
3.5	0.31188	0.01148	0.34715	0.00464	0.48432	0.17675
4	0.3401	0.00776	0.40321	0.00567	0.49849	0.98806
4.5	0.34584	0.00672	0.42664	0.00629	0.32671	1.14826
5	0.32224	0.00527	0.43734	0.00628	0.23111	0.57156
6	0.26119	0.00457	0.43082	0.00535	0.14928	0.11274
7	0.21604	0.00542	0.38654	0.00409	0.06704	0.03193
8	0.18653	0.00549	0.32983	0.00291	0.01669	0.01253
9	0.16487	0.00541	0.28513	0.00199	0	0.00573
10	0.00913	0.15365	0.12014	0.00224	0.12014	0.00224
11	0.00762	0.13889	0.09908	0.00125	0.09908	0.00125
12	0.00685	0.12725	0.0726	7.05801E-4	0.0726	7.05801E-4
13	0.0052	0.11704	0.06143	3.70547E-4	0.06143	3.70547E-4
14	0.00348	0.10873	0.06011	1.89609E-4	0.06011	1.89609E-4
15	0 [§]	0.10179	0.06309	9.64219E-5	0.06309	9.64219E-5
16	0 [§]	0.09578	0.09198	4.64277E-5	0.09198	4.64277E-5
17	0 [§]	0.09003	0.09199	2.50438E-5	0.09199	2.50438E-5
18	0 [§]	0.08505	0.08522	1.40599E-5	0.08522	1.40599E-5
19	0 [§]	0.0807	0.11986	8.05728E-6	0.11986	8.05728E-6
20	0 [§]	0.07665	0.12024	5.00749E-6	0.12024	5.00749E-6

[§] These parameter values were restricted to non-negative.

Afterwards, through a reaction of two equivalents of KCp^* with the complex Dy@2.6_Y , a diluted compound Dy@2.9_Y (10 mol % Dy) was obtained. A quick scan of thermal dependence of the out-of-phase susceptibility (χ'') at 1000 Hz in zero dc field gave the same maxima at 38 K as for 2.9_{Dy} (Figure 2.18a). A tail was observed in the data for Dy@2.9_Y below 10 K, as it was for 2.9_{Dy} . The sharp increase in χ'' is probably due to QTM.⁷⁰ The hysteresis loop for Dy@2.9_Y are slightly open around ± 10 kOe (Figure 2.18b), indicating that exchange coupling in 2.9_{Dy} is probably responsible for the rapid QTM.

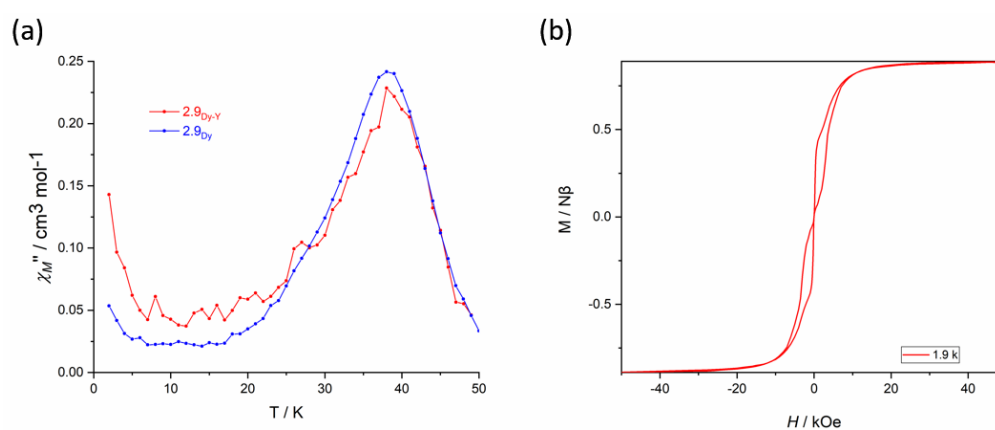


Figure 2.18 (a) Temperature dependence of the out-of-phase (χ'') for doped Dy@2.9_Y (red) and 2.9_{Dy} (blue) at 1000 Hz AC frequency under zero DC field. (b) Magnetic hysteresis loop for Dy@2.9_Y .

2.4.4 Theoretical Calculations

Multireference *ab initio* calculations were carried by Dr Akseli Mansikkamäki at the University of Oulu as part of a collaboration with the Layfield group. The results of calculations on compounds of 2.6_{Dy} , 2.9_{Dy} and 2.10 are presented (Figure 2.19–2.21). The crystal field split levels with the ground multiplet of Dy^{3+} are displayed, with transitions between levels indicated with red arrows. The stronger red arrows indicate larger absolute value of the transition magnetic moment matrix elements between the respective states (Figure 2.19a–2.21a), i.e., a probable transition. The barriers for

the Dy2 ions are omitted since they are similar to those of the Dy1 ions (Figure 2.19b–2.21b).

For compound **2.6_{Dy}**, the first-excited Kramers doublets (KDs) for Dy1 and Dy2 are located at 176 cm^{-1} and 181 cm^{-1} , whose value is approaching to the experimental barrier of $U_{\text{eff}} = 154 \text{ cm}^{-1}$. Meanwhile, the angles between the principal magnetic axes of ground state and first excited-state were determined as 41.3 and 43.0° for Dy1 and Dy2, respectively. Therefore, the first QTM event should happen through the first excited-state KD. (Table 2.10)

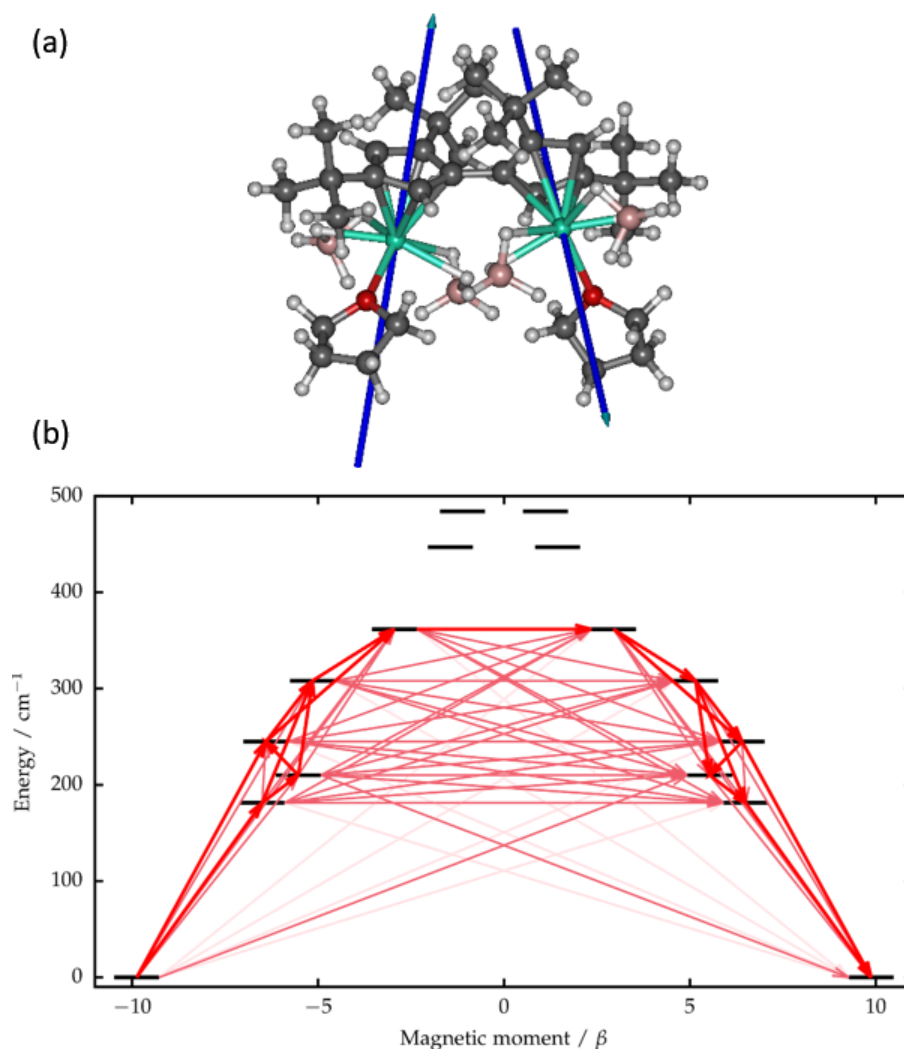


Figure 2.19 (a) The principal magnetic axes of the ground KDs of the Dy^{3+} ions in **2.6_{Dy}**. (b) Calculated effective *ab initio* barriers for the relaxation of magnetization at the Dy1 ions **2.6_{Dy}**

Table 2.10 Properties of the eight lowest KDs of the Dy1 ion in **2.6_{Dy}** corresponding to the crystal-field split states in the ground ${}^6\text{H}_{15/2}$ multiplet.

KD	E / cm^{-1}	g_x	g_y	g_z	$\theta / ^\circ$ ^a
KD1	0	0.00479	0.00848	19.74999	
KD2	176	0.25436	0.82958	17.60282	41.3
KD3	204	0.12011	1.08487	15.65517	44.7
KD4	250	0.87397	1.44122	13.88335	17.2
KD5	312	1.23520	3.38453	11.93809	30.1
KD6	358	4.43288	4.77529	11.34784	110.9
KD7	443	2.37298	3.11198	12.06285	83.3
KD8	475	1.12223	5.86668	14.92877	83.0

^aThe angle between the principal magnetic axis of the given doublet and the that of the ground doublet.

For compound **2.9_{Dy}**, the theoretical barrier could involve up to the third-excited KD, with the magnetic axes for these states being nearly collinear. The third-excited KD has the barrier of 452 cm^{-1} and 457 cm^{-1} for Dy1 and Dy2, which are surprisingly far from the experimental barrier of 252 cm^{-1} . Thus, the relaxation possibly take place *via* the first-excited KD, which has a closer barrier of 214 cm^{-1} and 208 cm^{-1} . (Table 2.11)

Table 2.11 Properties of the eight lowest KDs of the Dy1 ion in **2.9_{Dy}** corresponding to the crystal-field split states in the ground ${}^6\text{H}_{15/2}$ multiplet.

KD	E / cm^{-1}	g_x	g_y	g_z	$\theta / ^\circ$ ^a
KD1	0	0.00274	0.00399	19.73043	
KD2	214	0.03671	0.04357	17.03462	4.5
KD3	364	0.30682	0.35781	14.55476	12.7
KD4	452	2.66307	3.29566	10.58803	11.7
KD5	504	2.13873	4.13363	11.50150	100.5
KD6	523	2.05568	3.44784	14.26742	91.1
KD7	606	0.41509	0.51420	16.45785	88.4
KD8	742	0.00248	0.02175	19.41816	89.4

^aThe angle between the principal magnetic axis of the given doublet and the that of the ground doublet.

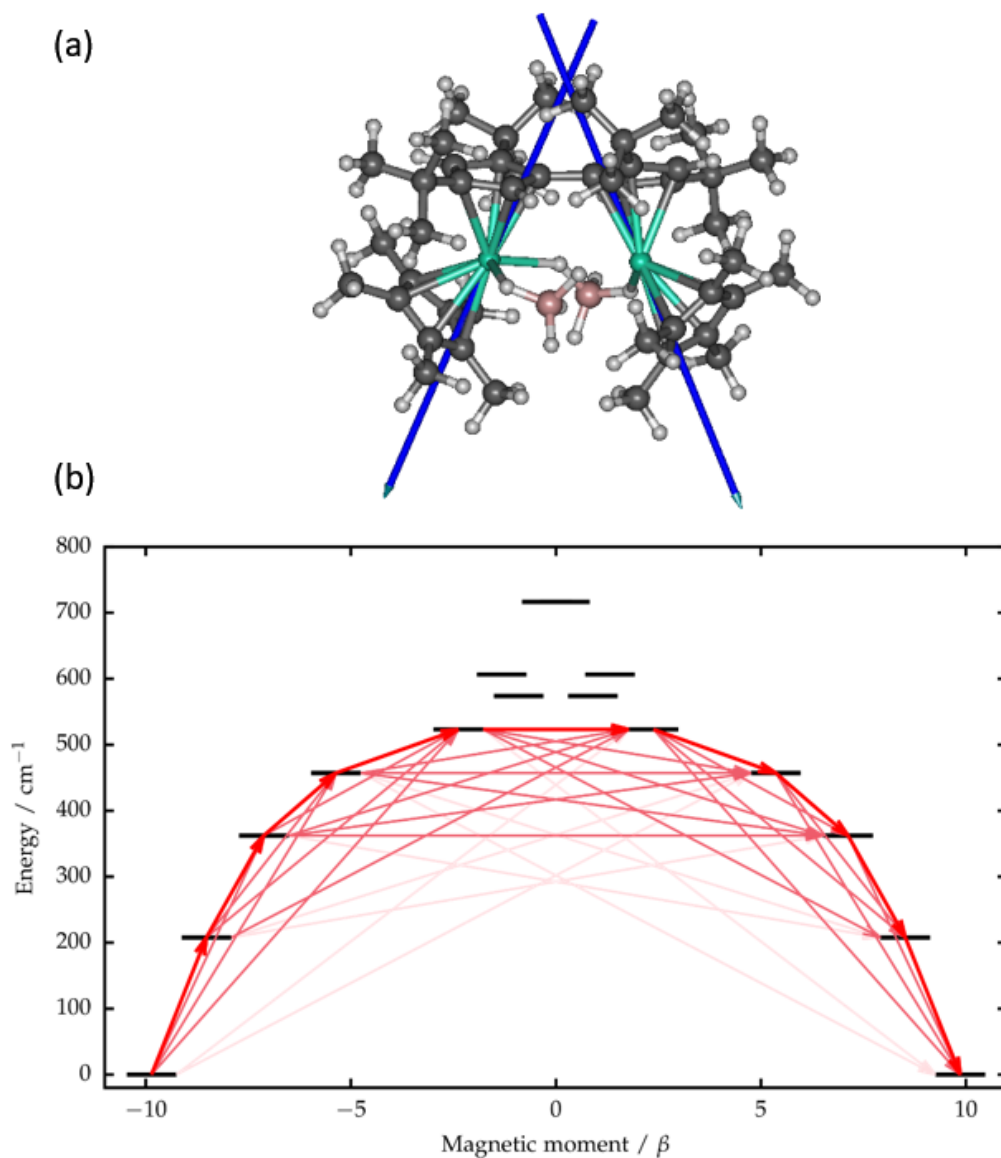


Figure 2.20 (a) The principal magnetic axes of the ground KDs of the Dy³⁺ ions in **2.9_{Dy}**. (b) Calculated effective *ab initio* barriers for the relaxation of magnetization at the Dy1 ion in **2.9_{Dy}**.

In complex **2.10**, the magnetic axes are roughly collinear up to the third-excited KD for Dy1 (667 cm⁻¹) and the second-excited KD for Dy2 (555 cm⁻¹). However, the experimental energy barrier of 384 cm⁻¹ is much closer to the first-excited KDs for Dy1 (336 cm⁻¹) and Dy2 (339 cm⁻¹). (Table 2.12)

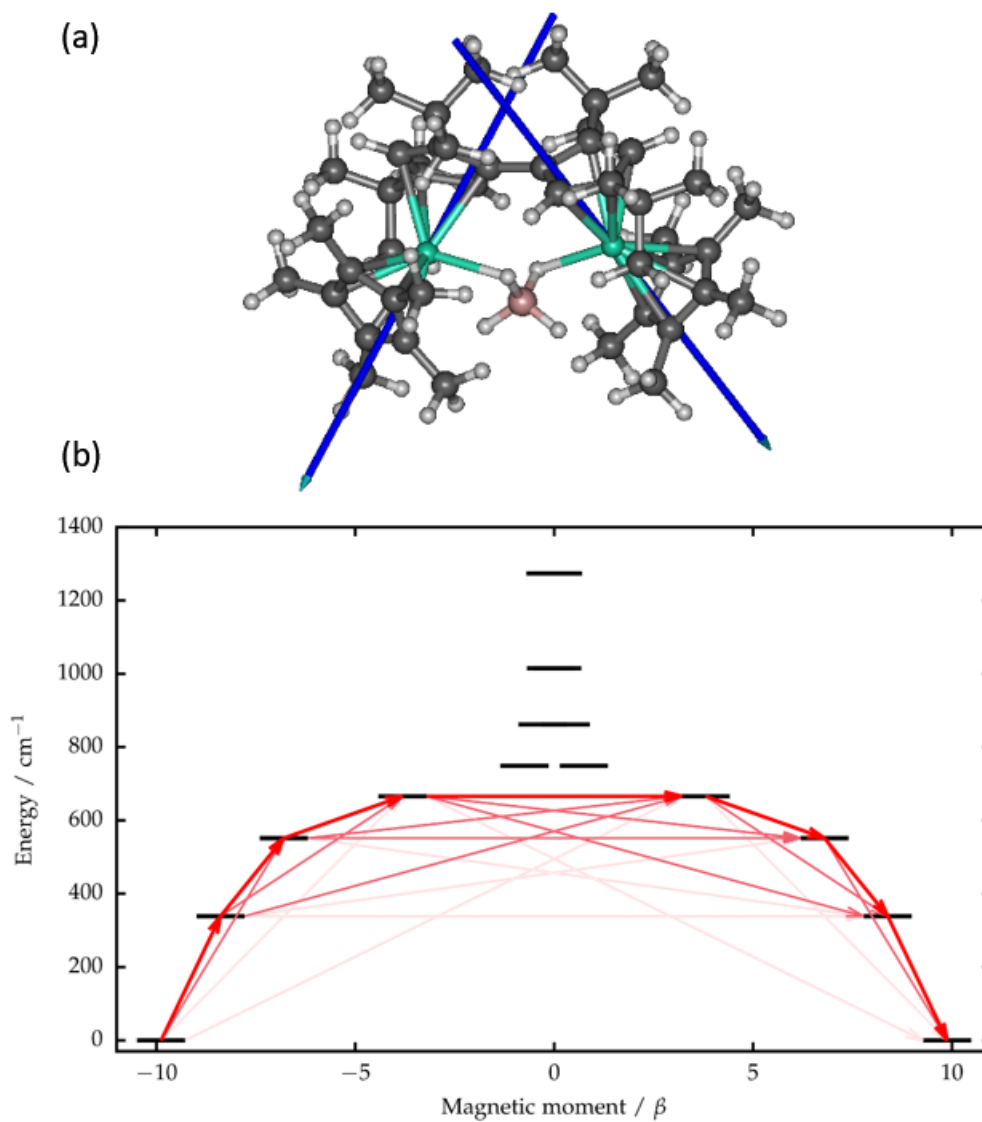


Figure 2.21 (a) The principal magnetic axes of the ground KDs of the Dy³⁺ ions in **2.10**. (b) Calculated effective *ab initio* barriers for the relaxation of magnetization at the Dy1 ion of **2.10**.

Table 2.12. Properties of the eight lowest KDs of the Dy1 ion in **2.10** corresponding to the crystal-field split states in the ground ${}^6\text{H}_{15/2}$ multiplet.

KD	E / cm^{-1}	g_x	g_y	g_z	$\theta / ^\circ$ ^a
KD1	0	0.00088	0.00125	19.79452	
KD2	336	0.03341	0.04471	16.86470	2.4
KD3	546	0.58986	0.81103	13.87933	3.9
KD4	667	3.87667	4.83694	9.23525	4.5
KD5	754	3.37642	4.60129	9.14094	89.4
KD6	860	0.19052	0.51856	13.14480	90.3
KD7	996	0.10953	0.19171	16.44215	90.5
KD8	1223	0.00842	0.01449	19.55260	90.1

^a The angle between the principal magnetic axis of the given doublet and the that of the ground doublet.

Due to the lack of an appreciable temperature-dependence of $\chi_{\text{M}}T$ in **2.6_{Dy}** and **2.10** (Figure 2.7), only **2.9_{Dy}** was studied theoretically to gain insight into the intramolecular interactions, which were studied using the Lines model.¹⁵¹ An Ising-type formula was applied according to Equation 5:

$$\hat{H} = -(J_{\text{ex}} + J_{\text{dipolar}})\tilde{S}_{z,1}\tilde{S}_{z,2} = -J_{\text{tot}}\tilde{S}_{z,1}\tilde{S}_{z,2} \quad (5)$$

In Equation 5, the pseudospin operator of \tilde{S} equals to 1/2 for a double Dy^{3+} ions on the ground state. Based on the calculation, the exchange parameter J_{ex} is -1.185 cm^{-1} and the J_{dipolar} is -2.477 cm^{-1} for compound **2.9_{Dy}**, which gives the total exchange interaction $J_{\text{tot}} = -3.662 \text{ cm}^{-1}$. The total exchange interaction is therefore relatively strong for a lanthanide-based system, with magnitude of J_{tot} being consistent with the changes in the hysteresis profile for this compound.

2.5 Conclusions and Perspectives

In this chapter, a series of double metallocene dysprosium SMMs based on bridging fulvalenyl ligand was presented. These results include the first multimetallic dysprosium metallocene cation SMM. The double sandwich structure is able to provide the strong axial crystal-field from the cyclopentadienyl units. Compounds **2.6_{Dy}**, **2.7**, **2.9_{Dy}** and [**2.10**][B(C₆F₅)₄] were synthesized using a stepwise approach and characterized by X-ray crystallography and IR spectroscopy. AC magnetic susceptibility data revealed improvement in the energy barrier U_{eff} was observed as the equatorial crystal-field effect becomes less influential and the axial cyclopentadienyl ligands from Cp* and Fv^{tttt} become more dominant. The effective energy barriers were determined as: $U_{\text{eff}} = 154(15) \text{ cm}^{-1}$ in **2.6_{Dy}** to $U_{\text{eff}} = 384(18) \text{ cm}^{-1}$ in [**2.10**][B(C₆F₅)₄], which again proves the efficient strategy of using the sandwiched structures. Compared to the single metallocene [(Cp^{iPr5})Dy(Cp*)(BH₄)] ($U_{\text{eff}} = 7 \text{ cm}^{-1}$),⁵ the larger experimental barriers of **2.9_{Dy}** and **2.10** show a large improvement. The particular bridging manner of the Fv^{tttt} ligand may reduce the transverse crystal-field effect. According to the hysteresis data and the theoretical calculations, compound **2.9_{Dy}** shows positive effect of the intramolecular coupling to suppress the QTM process.

For future research, the magnetic properties of the double cation compound **2.8** i.e. [DyFv^{tttt}]₂[B(C₆F₅)₄]₂ should be characterized and theoretically analysed. On the other hand, as the fluorine atoms are coordinated to dysprosium in **2.8**, other bulkier substituted fulvalenyl ligands should be considered.¹⁵² The bridging distance should also be considered, however longer Cp-bridges may cause a larger bending angle and result in the formation of a single-ion metallocene. For example, in an unfinished piece of analysis, I found that a single-ion dysprosium sample is obtained with the bis-Cp ligand of Me₂Si(C₅Me₄)₂ (Figure 2.22).

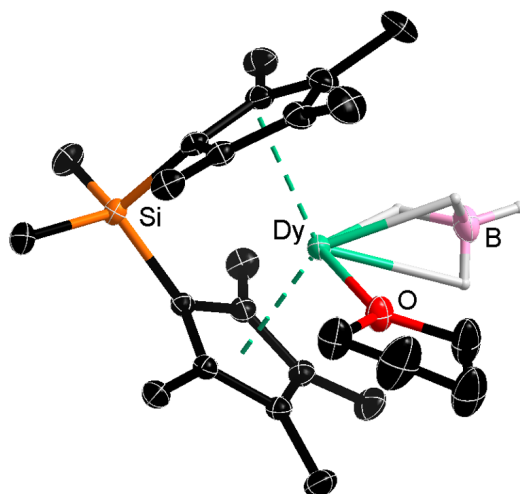


Figure 2.22 Thermal ellipsoid representation (30 % possibility) of molecular structure of [Me₂Si(C₅Me₄)Dy(BH₄)(THF)].

Chapter 3

Fulvalene-Bridged Trimetallic Dysprosocenium SMMs

3.1 Introduction

In addition to the trimetallic dysprosium SMMs discussed in Chapter 1 (e.g. Figure 1.20),⁶⁴ several other triangular dysprosium clusters were also reported by Tang *et al.*,^{81, 82, 153} For example, the complex $[\text{Dy}_3\text{L}(\mu^3\text{-OH})_2(\text{SCN})_4(\text{H}_2\text{O})_2] \cdot 3\text{MeOH} \cdot 2\text{H}_2\text{O}$ has an effective energy barrier of $U_{\text{eff}} = 11 \text{ cm}^{-1}$ in an applied DC field of 500 Oe (Figure 3.1 *left*). Linear trimetallic SMMs are also known,^{79, 80} such as $[\text{Dy}_3(\text{HSA})_5(\text{SA})_2(\text{phen})_3]$, which has an effective energy barrier of $U_{\text{eff}} = 11 \text{ cm}^{-1}$ in an applied DC field of 188 Oe (Figure 3.1 *right*, H_2SA = salicylic acid and phen = 1,10-phenanthroline).

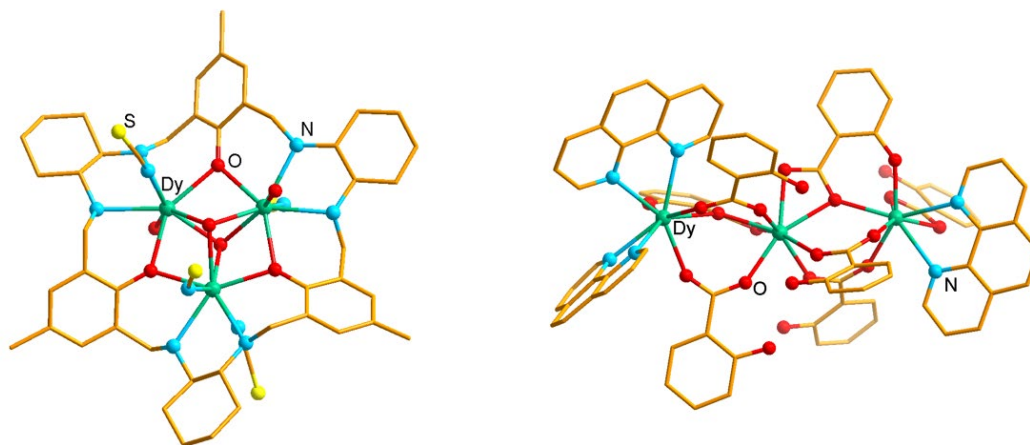
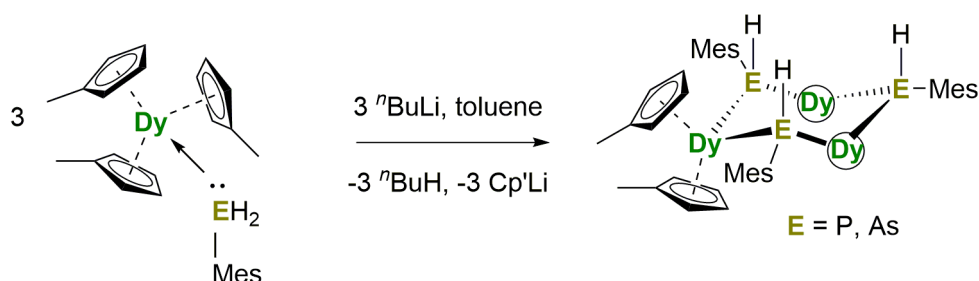


Figure 3.1 Thermal ellipsoid representation (30 % possibility) of molecular structures of $[\text{Dy}_3\text{L}(\mu^3\text{-OH})_2(\text{SCN})_4(\text{H}_2\text{O})_2]$ (*left*) and $[\text{Dy}_3(\text{HSA})_5(\text{SA})_2(\text{phen})_3]$ (*right*). Dy, green; C, orange; O, red; N, blue; S, yellow. The structures are reproduced based on the cif files from the Ref. 80 and 82.^{80, 82}

A series of triangular dysprosium metallocene SMMs was reported by our group.^{141, 154, 155} These compounds include heteroatom-bridged trimers $[(\eta^5\text{-Cp}')_2\text{Dy}]\{\mu\text{-E(H)Mes}\}_3$ (E = P, As, Scheme 3.1).



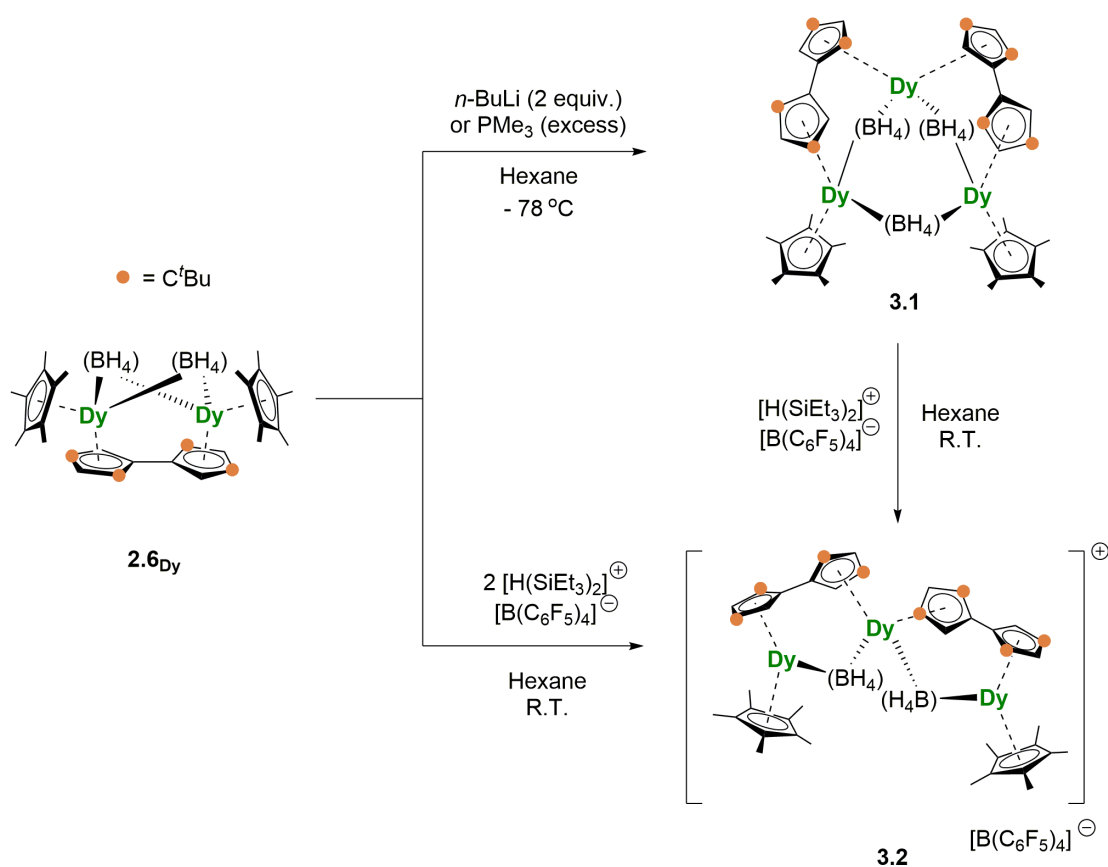
Scheme 3.1 Synthesis of $[(\text{Cp}')_2\text{Dy}\{\text{E(H)Mes}\}]_3$ (E = P, As).^{141, 154, 155}

3.2 Synthesis of Fulvalenyl-Bridged Trimetallic Dysprosocenium Complexes

Inspired by the results described in Chapter 2, the di-dysprosocenium compound **2.6_{Dy}** was selected as the starting material for the synthesis of a trimetallic dysprosocenium SMM. After reacting **2.6_{Dy}** with two equivalents of *n*BuLi in hexane, the borohydride-bridged dysprosium triangle $[(\mu\text{-BH}_4)\{\text{Dy}(\eta^5\text{-Cp}^*)(\mu\text{-BH}_4)\}_2\text{Dy}(\eta^5\text{:}\eta^5\text{-Fv}^{\text{tttt}})_2]$ (**3.1**) was obtained, with the isolated yielded 42 % (Scheme 3.2). In compound **3.1**, two of the dysprosium centres are sandwiched by a Cp* ligand and one half of a fulvalenyl ligand. The other dysprosium is sandwiched by two cyclopentadienyl groups of two different Fv^{tttt} ligands. The triangular structure of **3.1** is formed by reorganizing of a unit of **2.6_{Dy}**, which formally loses a two Cp* ligands, a borohydride ligand and one dysprosium, suggesting the formation of $[(\text{Cp}^*)_2\text{Dy}(\text{BH}_4)]$ as a by-product, possibly as a co-complex of *n*BuLi. Similarly, a reaction of **2.6_{Dy}** with the excess of PMe₃ (e.g., 30 equiv.) can also yield the same product of **3.1** (isolated yield: 32 %).

On the other hand, as described in Chapter 2, a mixture of one equivalent of $[(\text{Et}_3\text{Si})_2\text{H}][\text{B}(\text{C}_6\text{F}_5)_4]$ and **2.6_{Dy}** will yield complex **2.9_{Dy}**, but no reaction was observed with further addition of the $[(\text{Et}_3\text{Si})_2\text{H}][\text{B}(\text{C}_6\text{F}_5)_4]$. However, reacting **2.6_{Dy}** with two

equivalents of $[(Et_3Si)_2H][B(C_6F_5)_4]$ in hexane at room temperature produced the trinuclear complex $[Dy(\eta^5-Cp^*)(\mu-BH_4)(\eta^5:\eta^5-Fv^{tttt})Dy(\eta^5:\eta^5-Fv^{tttt})(\mu-BH_4)Dy(\eta^5-Cp^*)][B(C_6F_5)_4]$ (**3.2**)[$B(C_6F_5)_4$, Scheme 3.2), with an isolated yield of 28 %. Complex **3.2**[$B(C_6F_5)_4$] also can also be synthesized by adding one equivalent of $[(Et_3Si)_2H][B(C_6F_5)_4]$ to complex **3.1** in hexane at room temperature (isolated yield = 42 %).



Scheme 3.2 Synthesis of compound **3.1** and **3.2**[$B(C_6F_5)_4$].

3.3 X-Ray Diffraction Study

3.3.1 Crystal Structure of Compound **3.1**

The crystal structure of **3.1** is illustrated in Figure 3.2 and selected geometric parameters are listed in Table 3.1. For Dy1 and Dy3, each ion is η^5 -coordinated by a cyclopentadienyl unit of an Fv^{tttt} ligand and a Cp* ligand, while the Dy2 is η^5 -sandwiched by two cyclopentadienyl units from different Fv^{tttt} ligands. Thus, Dy1 and Dy3 occupy similar environments with Dy–C distances of 2.638(4)–2.709(4) Å and 2.615(4)–2.775(4) Å to Fv^{tttt}, respectively, and 2.641(5)–2.688(5) Å and 2.663(4)–2.686(4) Å to the Cp* ligands, respectively. The distances Dy1–Cp_c (centroid) are 2.391(3) to Fv^{tttt} and 2.382(3) to Cp*, which is similar to the range for Dy3. For Dy2, the Dy–C distances to the Fv^{tttt} ligands are 2.618(4)–2.747(4) Å and 2.620(4)–2.733(4) Å. The Cp_c–Dy–Cp_c angles are 135.708(12)°, 139.205(11)° and 132.835(7)° from Dy1 to Dy3 respectively.

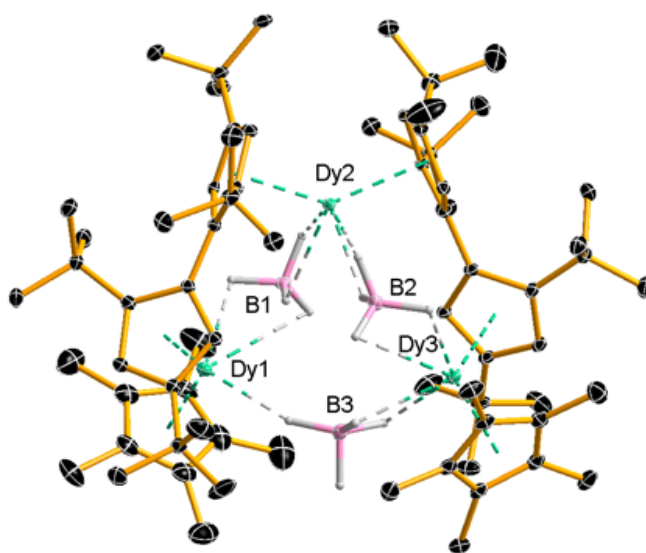


Figure 3.2 Thermal ellipsoid representation (30 % possibility) of molecular structure of **3.1**.

Table 3.1 Selected bond lengths (Å) and angles (°) for **3.1**.

Dy–C (Fv ^{tttt})	Dy1–C1: 2.709(4) Dy1–C2: 2.718(4) Dy1–C3: 2.654(4) Dy1–C4: 2.674(4) Dy1–C5: 2.638(4) Dy2–C6: 2.668(4) Dy2–C7: 2.618(4) Dy2–C8: 2.689(4) Dy2–C9: 2.686(4) Dy2–C10: 2.747(4)	Dy2–C37: 2.663(4) Dy2–C38: 2.733(4) Dy2–C39: 2.682(4) Dy2–C40: 2.694(4) Dy2–C41: 2.620(4) Dy3–C42: 2.725(4) Dy3–C43: 2.615(4) Dy3–C44: 2.663(4) Dy3–C45: 2.688(4) Dy3–C46: 2.775(4)
Dy–C (Cp*)	Dy1–C27: 2.688(5) Dy1–C28: 2.669(4) Dy1–C29: 2.650(5) Dy1–C30: 2.641(5) Dy1–C31: 2.666(5) Dy3–C63: 2.686(4) Dy3–C64: 2.665(4) Dy3–C65: 2.663(4) Dy3–C66: 2.683(4) Dy3–C67: 2.679(4)	
Dy–centroid (Fv ^{tttt})	Dy1-centroid: 2.391(3) Dy2-centroid1: 2.394(1)	Dy2-centroid2: 2.391(1) Dy3-centroid: 2.407(2)
Dy–centroid (Cp*)	Dy1-centroid: 2.382(3) Dy3-centroid: 2.389(2)	
Dy...Dy	Dy1...Dy2: 4.741(4) Dy1...Dy3: 5.685(3)	Dy2...Dy3: 4.715(3)
Dy...B	Dy1...B1: 2.741(4) Dy1...B3: 3.362(5) Dy2...B1: 2.943(4)	Dy2...B2: 2.895(4) Dy3...B2: 2.783(5) Dy3...B3: 2.887(5)
Cp _c –Dy–Cp _c	Dy1: 135.708(12) Dy2: 139.205(11)	Dy3: 132.835(7)

The Dy1...Dy2 and Dy2...Dy3 distances are 4.741(4) Å and 4.715(3) Å, respectively, making them shorter than the distance of Dy1...Dy3 of 5.685(3) Å. The Dy1...B distance of 3.362(5) Å is much longer than the other Dy...B distances of 2.741(4)–2.943(4) Å. The two fulvalenyl ligands have twist angles of 51.62(16)° and 51.69(18)°. The IR stretches for the borohydride ligands were observed around $\tilde{\nu} = 2213\text{--}2438\text{ cm}^{-1}$ (Figure 7.14, Experimental Section).

3.3.2 Crystal Structure of the Cation **3.2**

The range of Dy–C distances to the Fv^{tttt} bound to Dy2 are 2.626(5)–2.757(5) Å, while significantly shorter ranges of 2.587(5)–2.719(5) Å and 2.589(5)–2.668(5) Å were found for Dy1 and Dy3, respectively. The range of Dy–C distances to the Cp* is 2.590(5)–2.620(5) Å for Dy1 and 2.601(5)–2.630(5) Å for Dy3. The Dy–Fv^{tttt} (centroid) distance is reduced to 2.340(3) Å for Dy1 and 2.336(3) Å for Dy3; but for Dy2, the change in the distance is only 0.002–0.023(3) Å. The Dy–Cp* (centroid) distance is also shorter, being 2.311(3) Å for Dy1 and 2.314(3) Å for Dy3. The Dy1⋯Dy2 distance is 4.880(4) Å, similar to the Dy2⋯Dy3 of 4.867(5) Å, which are slightly longer than the analogous values in compound **3.2**. The Dy1⋯Dy3 distance has a large increase to a value of 7.908(1) Å. The Dy⋯B distance of 2.980(7) Å for Dy2⋯B1 and 2.951(7) Å for Dy2⋯B2 are greater than Dy1⋯B1 (2.688(7) Å) and Dy3⋯B2 (2.691(6) Å). Due to the remove of BH₄, the Cp_c–Dy–Cp_c angles markedly increase to 147.752(14)°, 147.578(14)° and 149.159(16)° for Dy1, Dy2 and Dy3, respectively. The IR stretch for the borohydride ligands occurs at $\tilde{\nu} = 2185\text{--}2470\text{ cm}^{-1}$ (Figure 7.15, Experimental Section).

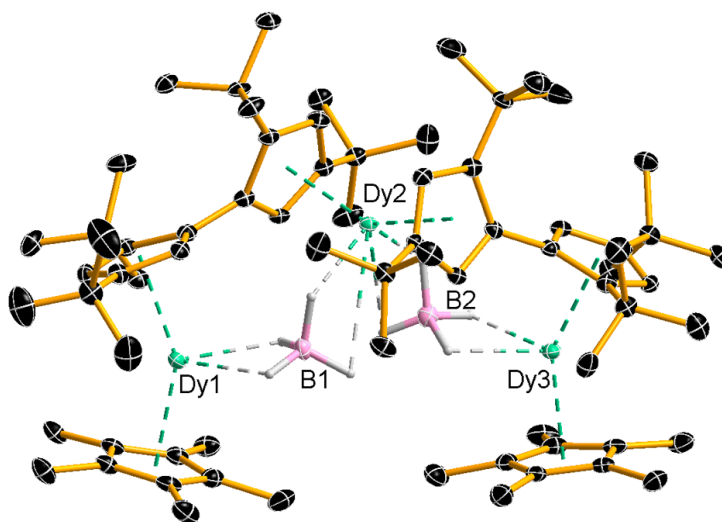


Figure 3.3 Thermal ellipsoid representation (30 % possibility) of molecular structure of **3.2** cation.

Table 3.2 Selected bond lengths (Å) and angles (°) for **3.2** cation.

Dy–C (Fv ^{tttt})	Dy1–C1: 2.672(5) Dy1–C2: 2.719(5) Dy1–C3: 2.629(5) Dy1–C4: 2.587(5) Dy1–C5: 2.562(5) Dy2–C6: 2.723(5) Dy2–C7: 2.626(5) Dy2–C8: 2.686(5) Dy2–C9: 2.659(5) Dy2–C10: 2.726(5)	Dy2–C37: 2.730(5) Dy2–C38: 2.757(5) Dy2–C39: 2.680(5) Dy2–C40: 2.691(5) Dy2–C41: 2.645(5) Dy3–C42: 2.639(5) Dy3–C43: 2.598(5) Dy3–C44: 2.630(5) Dy3–C45: 2.613(5) Dy3–C46: 2.668(5)
Dy–C (Cp*)	Dy1–C27: 2.606(5) Dy1–C28: 2.620(5) Dy1–C29: 2.605(5) Dy1–C30: 2.590(5) Dy1–C31: 2.606(5) Dy3–C63: 2.603(5) Dy3–C64: 2.601(5) Dy3–C65: 2.606(5) Dy3–C66: 2.609(6) Dy3–C67: 2.630(5)	
Dy–centroid (Fv ^{tttt})	Dy1-centroid: 2.340(3) Dy2-centroid1: 2.396(1)	Dy2-centroid2: 2.414(3) Dy3-centroid: 2.336(3)
Dy–centroid (Cp*)	Dy1-centroid: 2.311(3) Dy3-centroid: 2.314(3)	
Dy...Dy	Dy1...Dy2: 4.880(4) Dy2...Dy3: 4.867(5) Dy1...Dy3: 7.908(1)	
Dy...B	Dy1...B1: 2.688(7) Dy2...B1: 2.980(7)	Dy2...B2: 2.951(7) Dy3...B2: 2.691(6)
Cp _c –Dy–Cp _c	Dy1: 147.752(14) Dy2: 147.578(14)	Dy3: 149.159(16)

3.4 Magnetic Property Measurements

3.4.1 DC Magnetic Measurements

The plot of the $\chi_M T$ versus temperature was measured for **3.1** and **[3.2]** $[\text{B}(\text{C}_6\text{F}_5)_4]$ in a DC field of 1 kOe (Figure 3.4). The values of $\chi_M T$ at 300 K are 40.5 and 39.6 $\text{cm}^3 \text{K mol}^{-1}$ for **3.1** and **[3.2]** $[\text{B}(\text{C}_6\text{F}_5)_4]$, respectively, both of which are close to the theoretical value ($42.5 \text{ cm}^3 \text{K mol}^{-1}$) for three uncoupled Dy^{3+} ions with $^6\text{H}_{15/2}$ ground multiplets.¹⁴⁹ With decreasing temperature, the $\chi_M T$ values gradually reduce to become 32.9 and 31.9 $\text{cm}^3 \text{K mol}^{-1}$ at 2.0 K, but without a sharp drop at low temperature, hence their behaviours very similar to observed for complexes **2.6_{Dy}** and **[2.10]** $[\text{B}(\text{C}_6\text{F}_5)_4]$. These data indicate that any exchange coupling present in these two complexes is likely to be very weak, which is normal for lanthanides.⁶⁴

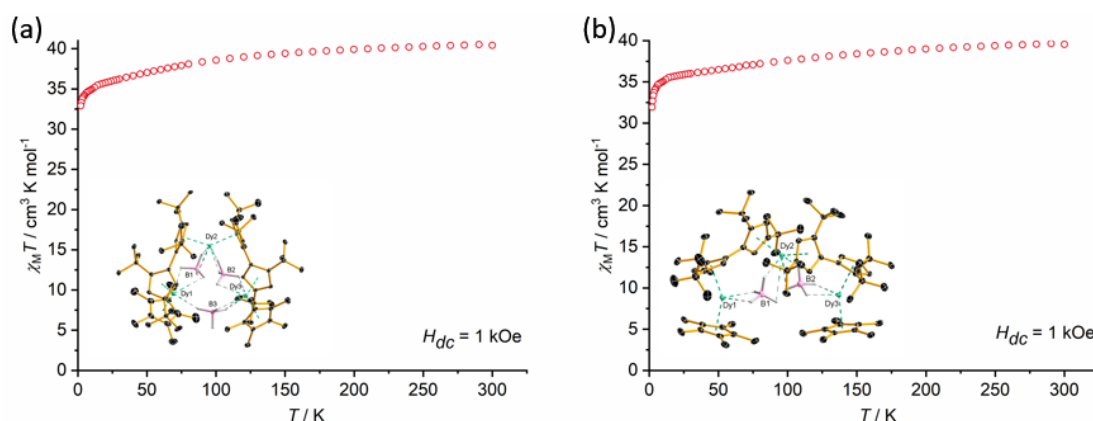


Figure 3.4 Plots of $\chi_M T$ versus temperature for (a) **3.1** and (b) **[3.2]** $[\text{B}(\text{C}_6\text{F}_5)_4]$ in an applied DC magnetic field of 1 kOe.

The field dependence of the magnetization plots (M versus H) for both complexes were measured at 2.0, 3.0 and 5.0 K and are shown in Figure 3.5. The maximum M values are 14.6 and 14.5 $N\beta$ for **3.1** and **[3.2]** $[B(C_6F_5)_4]$ at 1.9 K and 7 T. Again, these values are typical of a trimetallic dysprosium complex, falling well below the maximum theoretical value of $M = 15 N\beta$ because of strong magnetic anisotropy.

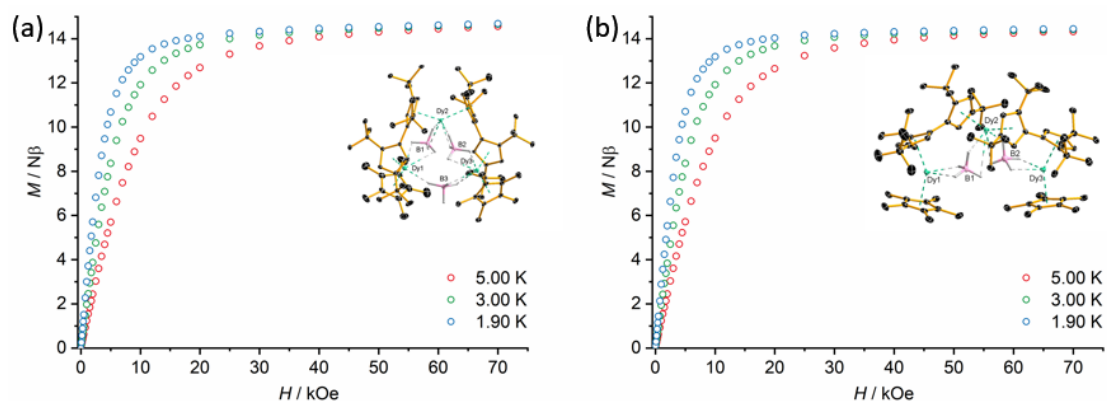


Figure 3.5 Plots of field dependent magnetization for (a) **3.1** and (b) **[3.2]** $[B(C_6F_5)_4]$ at 2 K, 3 K and 5 K.

3.4.2 AC Magnetic Measurements

The frequency dependence of the in-phase (χ') and out-of-phase (χ'') AC magnetic susceptibility was measured in zero DC field and an AC field of 3 Oe, using AC frequencies of $\nu = 1$ –1488 Hz for **3.1** and **[3.2]** $[B(C_6F_5)_4]$ (Figure 3.6–3.8).

For compound **3.1**, χ' and χ'' were measured in the temperature range 2.0–50 K, with maxima in χ'' being observed from 10–46 K (Figure 3.6b). At temperatures below 10 K, maxima were not observed. Furthermore, the position of the maxima in the $\chi''(\nu)$ shifts with each change in temperature, indicating that the magnetic relaxation does not enter a pure QTM regime under these measurement conditions. Hence, a fit of the relaxation time data was achieved without a QTM term using the equation of $\tau^{-1} = \tau_0^{-1}e^{-U_{\text{eff}}/k_B T} + CT^n$, which resulted in an effective energy barrier of $U_{\text{eff}} =$

138(4) cm^{-1} with $\tau_0 = 5.44(7) \times 10^{-7}$ s and the Raman parameters $C = 8.03(4) \times 10^{-4} \text{ s}^{-1} \text{ K}^{-n}$ and $n = 4.05(2)$. (Figure 3.6d). The α parameters yield a small distribution of relaxation times in range of 0.04–0.25 (Table 3.3).

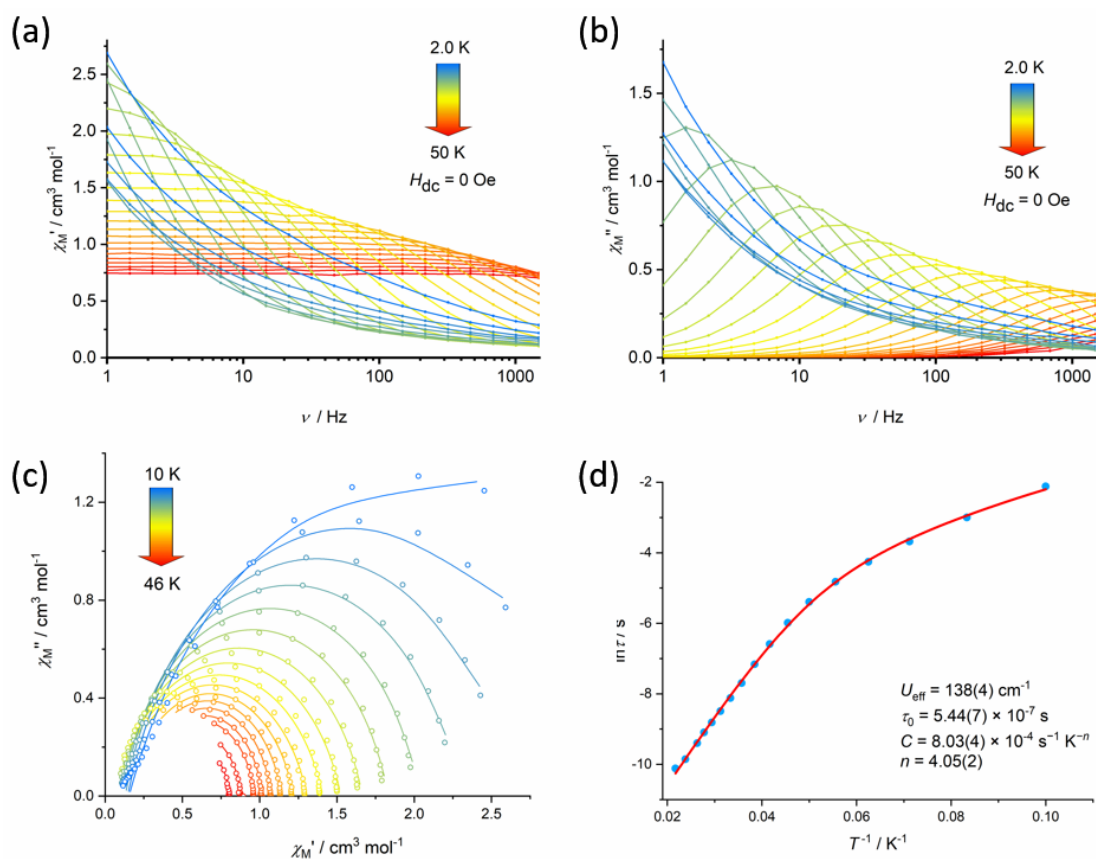


Figure 3.6 Frequency dependence of in-phase (χ') (a) and the out-of-phase (χ'') (b) susceptibility for **3.1** in zero DC field at AC frequencies of 1–1488 Hz; Solid lines are a guide to the eye. (c) Cole-Cole plots for **3.1** in zero DC field; Solid lines are fits of data with Equation 4 on page 21 (adjusted $R^2 = 0.99548$ – 0.99998). (d) The Plots of natural log of the relaxation time (τ) versus inverse temperature for **3.1**. The blue points are from the AC susceptibility measurements; The solid red line is the best fit using Equation 3 on page 16 without QTM process (adjusted $R^2 = 0.99922$)

Table 3.3 Relaxation fitting parameters for **3.1**. (adjusted $R^2 = 0.99548\text{--}0.99998$)

T / K	$\chi_{\tau} / \text{cm}^3 \text{mol}^{-1}$	$\chi_s / \text{cm}^3 \text{mol}^{-1}$	α	τ / s
46	0.80248	0.38336	0.04023	4.03794E-5
42	0.87604	0.31494	0.06413	5.25607E-5
38	0.96177	0.28151	0.06757	8.29553E-5
36	1.01367	0.27233	0.07804	1.12475E-4
34	1.07314	0.23862	0.09638	1.49175E-4
32	1.13962	0.19038	0.12611	2.04756E-4
30	1.21678	0.14552	0.15614	2.97303E-4
28	1.30477	0.08859	0.18361	4.55152E-4
26	1.40833	0.07191	0.18907	7.75102E-4
24	1.52557	0.06584	0.18541	0.00138
22	1.66416	0.07285	0.17289	0.00251
20	1.83046	0.08714	0.15716	0.00455
18	2.03129	0.10296	0.14492	0.00807
16	2.29451	0.11584	0.14722	0.01414
14	2.63514	0.13043	0.15823	0.02527
12	3.14624	0.14542	0.18754	0.04974
10	4.06799	0.15412	0.25149	0.12033

The mono-cation **3.2** displays $\chi''(\nu)$ curves over a wider temperature range of 2.0–67 K, with the maxima observed in the range of 12–60 K. Below 10 K, the data are similar to compound **3.1** and also without maxima. Fitting the $\ln\tau$ vs. T^{-1} data using the same equation $\tau^{-1} = \tau_0^{-1}e^{-U_{\text{eff}}/k_{\text{B}}T} + CT^n$ gave the effective energy barrier of $U_{\text{eff}} = 411(23) \text{ cm}^{-1}$ and $\tau_0 = 4.16(3) \times 10^{-9} \text{ s}$, whilst the Raman parameters are $C = 2.66(3) \times 10^{-4} \text{ s}^{-1} \text{ K}^{-n}$ and $n = 2.92(1)$ (Figure 3.7d). The α parameters show the range of 0.04–0.26, indicating a small distribution of relaxation times (Table 3.4).

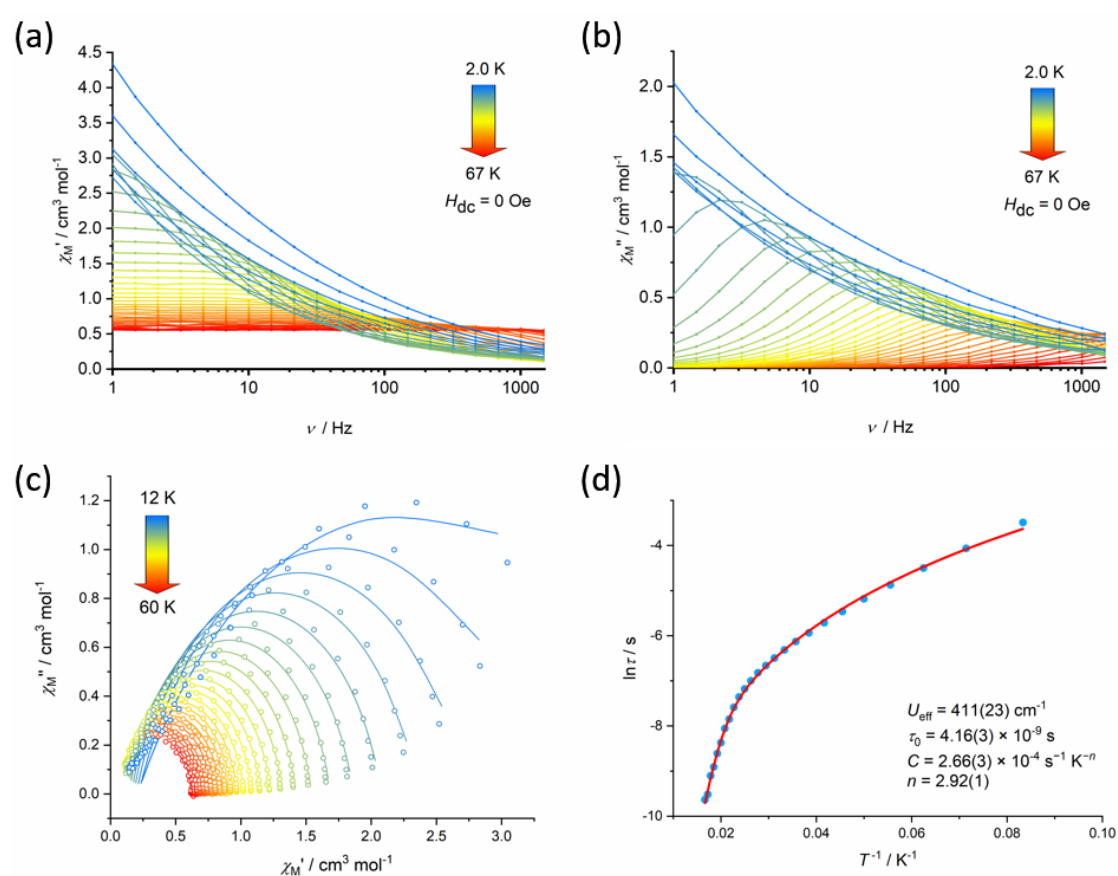


Figure 3.7 Frequency dependence of in-phase (χ') (a) and the out-of-phase (χ'') (b) susceptibility for **3.2** in zero DC field at AC frequencies of 1–1488 Hz; Solid lines are a guide to the eye. (c) Cole-Cole plots for **3.2** in zero DC field; Solid lines are fits of data with Equation 4 on page 21 (adjusted $R^2 = 0.99534$ – 0.99989). (d) The Plots of natural log of the relaxation time (τ) versus inverse temperature for **3.2**. The blue points are from the AC susceptibility measurements; The solid red line is the best fit using Equation 3 on page 16 without QTM process (adjusted $R^2 = 0.99899$)

Table 3.4 Relaxation fitting parameters for **3.2** cation. (adjusted $R^2 = 0.99534\text{--}0.99989$)

T / K	$\chi_{\tau} / \text{cm}^3 \text{mol}^{-1}$	$\chi_s / \text{cm}^3 \text{mol}^{-1}$	α	τ / s
60	0.62435	0.22126	0.04743	6.54302E-5
58	0.64414	0.16072	0.09222	7.36857E-5
56	0.66786	0.17756	0.08292	1.11018E-4
54	0.69181	0.1348	0.09906	1.35223E-4
52	0.71945	0.11415	0.11253	1.8203E-4
50	0.74704	0.0979	0.12433	2.31602E-4
48	0.77848	0.09997	0.10456	3.16942E-4
46	0.81142	0.07592	0.11684	3.90158E-4
44	0.84688	0.08251	0.11476	5.07021E-4
42	0.88513	0.08936	0.10258	6.36583E-4
40	0.92737	0.07981	0.1082	7.59387E-4
38	0.97318	0.07782	0.11201	9.12904E-4
36	1.02584	0.08694	0.10946	0.00109
34	1.0868	0.0878	0.10754	0.00128
32	1.15418	0.0916	0.11277	0.00151
30	1.22928	0.10443	0.11142	0.00181)
28	1.31774	0.10999	0.11256	0.00218
26	1.42075	0.1189	0.11516	0.00264
24	1.54063	0.12857	0.12069	0.00331
22	1.68516	0.14265	0.12866	0.00424)
20	1.86118	0.14511	0.14386	0.00561
18	2.0763	0.16371	0.15513	0.00765)
16	2.35489	0.18021	0.17482	0.01108
14	2.72747	0.19845	0.20777	0.01715
12	3.30624	0.21436	0.2629	0.03039

Compared with the barrier of 138 cm^{-1} determined for compound **3.1**, the **3.2** cation shows a significant improvement in effective energy barrier to 411 cm^{-1} . A plausible explanation for the different U_{eff} values could involve the shorter Dy1–Cp* and Dy3–Cp* centroid distances ($2.311(3)$ – $2.314(3)\text{ \AA}$) and the shorter Cp–Fv^{tttt} distances ($2.336(3)$ – $2.340(3)\text{ \AA}$) than the corresponding distance of $2.382(3)$ – $2.389(2)\text{ \AA}$ and $2.391(3)$ – $2.407(2)\text{ \AA}$ for **3.1**, which effectively strengthen the axial crystal field. Furthermore, the Cp–Dy–Cp angles in **3.2** are $147.578^\circ(14)$, $147.752^\circ(14)$ and $149.159^\circ(16)$ for Dy1, Dy2 and Dy3, respectively, making them more axial than the analogous angles of $132.835(7)^\circ$, $135.708(12)^\circ$ and $139.205(11)^\circ$ for **3.1**. Hence, in **3.2** cation, the crystal field is also more axial as well as stronger. The elimination of one equatorial borohydride ligand from compound **3.1** upon forming **3.2** also results in a decreasing equatorial crystal-field. Thus, all the structural changes result in improved SMM performance for the cation **3.2**.

The Cole-Cole plots in Figures 3.6c and 3.7c show that **3.1** and **3.2** only have one path for each relaxation process. The hysteresis loops $M(H)$ for **3.1** and **3.2** were measured at 1.9 K with an average scan rate of 2.7 Oe s^{-1} . For the both, narrow loops were observed at field values of $\pm 10\text{ kOe}$, but with closure at zero field. Thus, despite the minor role played QTM effects in these SMMs, the rapid drop in magnetization around zero field is likely to be due to the equatorial crystal-field from the equatorial borohydride ligands.

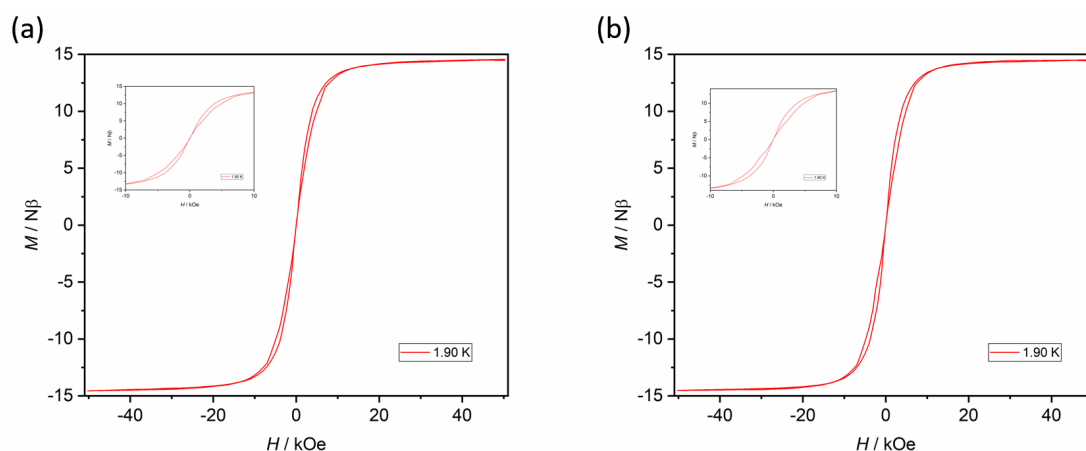


Figure 3.8 Magnetic hysteresis loops for **3.1** (a) and **3.2** (b).

3.4.3 Theoretical Calculations

The *ab initio* calculation results on **3.1** and **3.2** are presented in Figure 3.9–3.10, in which red arrows indicate the transitions between energy levels. The crystal-field split states in the ground multiplet of Dy³⁺ ions are listed in the Tables 7.12–7.17 (Experimental Section).

For compound **3.1**, the theoretical barrier should at least be counted from second, third and second excited KDs for Dy1, Dy2 and Dy3 respectively, which has the barrier height of 330 cm⁻¹ to 427 cm⁻¹. However, the local barrier is much higher than the experimental barrier (138(4) cm⁻¹). The first excited KDs has a closer energy range of 151–190 cm⁻¹ to the experimental data, which indicates the relaxation should take place at this level.

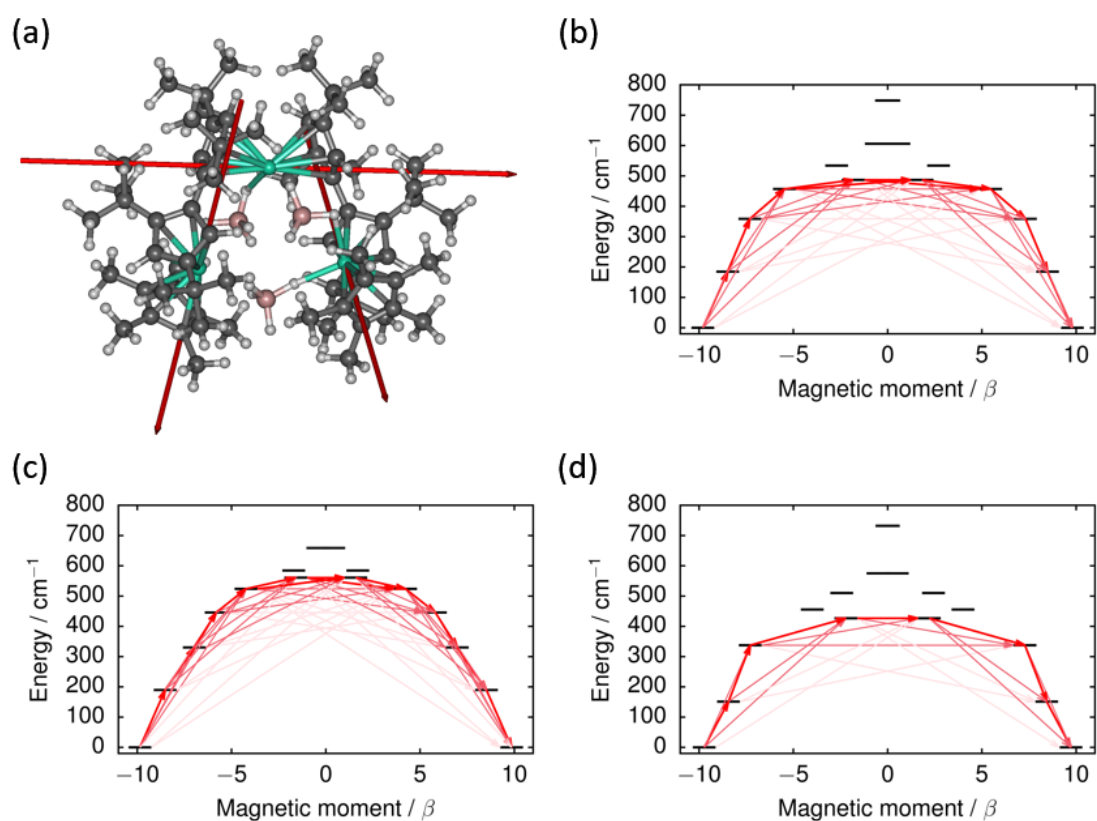


Figure 3.9 (a) The principal magnetic axes of the ground KDs of the Dy³⁺ ions in **3.1**. Calculated effective *ab initio* barriers for the relaxation of magnetization at the Dy1 (b), Dy2 (c) and Dy3 (d) ions of **3.1**.

In compound **3.2**, the calculated local barriers should be crossed earliest at the first, second and first excited KDs for Dy1, Dy2 and Dy3 respectively, which gives an energy range of 324–453 cm^{-1} . This computational result shows good agreement with the experimental value (411(23) cm^{-1}).

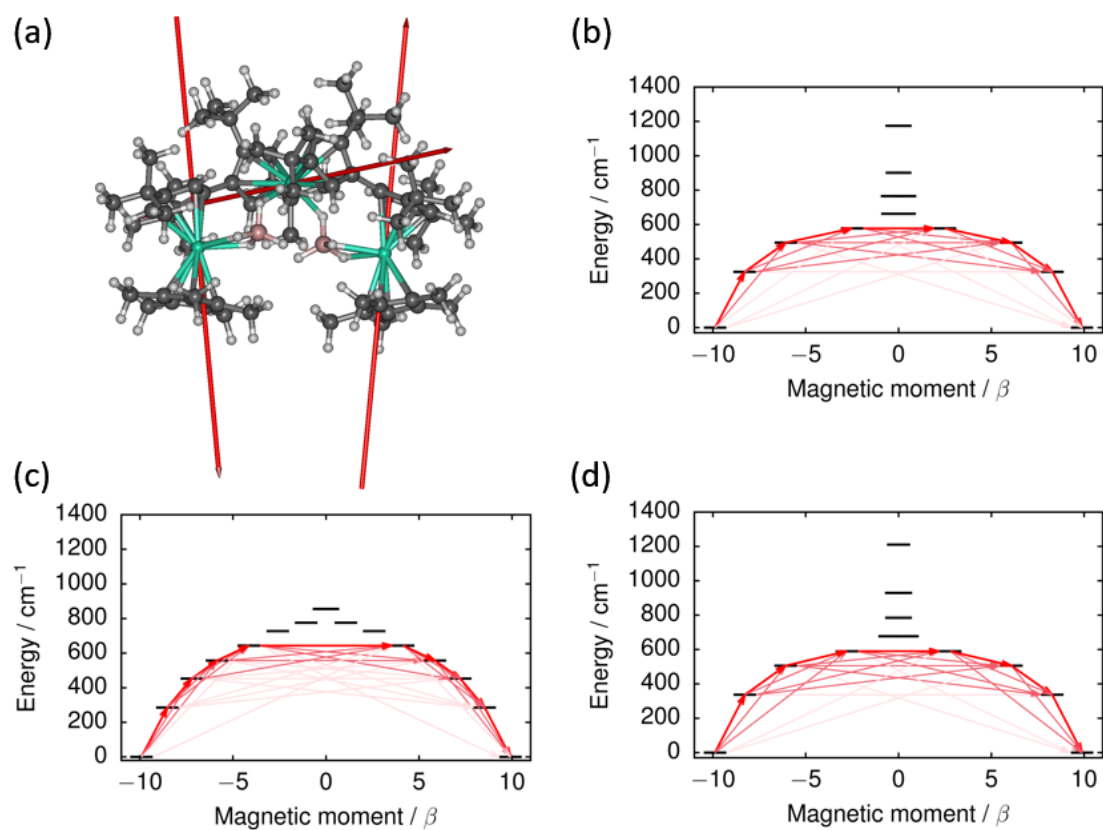


Figure 3.10 (a) The principal magnetic axes of the ground KDs of the Dy³⁺ ions in **3.2**. Calculated effective *ab initio* barriers for the relaxation of magnetization at the Dy1 (b), Dy2 (c) and Dy3 (d) ions of **3.2**.

Due to the weak contribution of other magnetic interaction effects, based on calculation, only the dipolar coupling is considered in the system of **3.1** and **3.2**. An Ising-type formula was applied according to Equation 6:

$$\hat{H} = -J_{12}\tilde{S}_{z,1}\tilde{S}_{z,2} - J_{13}\tilde{S}_{z,1}\tilde{S}_{z,3} - J_{23}\tilde{S}_{z,2}\tilde{S}_{z,3} \quad (6)$$

where the indices 1, 2 and 3 correspond to the same indices of the Dy³⁺ ions used in the crystal structure, and the parameter \tilde{S} equals to 1/2. As a result, compound **3.1** gives nearest-neighbour exchange parameters of $J_{12} = 1.81 \text{ cm}^{-1}$, $J_{23} = -1.71 \text{ cm}^{-1}$ and $J_{13} = 0.07 \text{ cm}^{-1}$. Due to the longer distance (7.908(1) Å) between ions Dy1 and Dy3 leading to less interaction effect, the cation **3.2** only has the nearest-neighbour exchange parameters of $J_{12} = -1.19 \text{ cm}^{-1}$ and $J_{23} = -1.25 \text{ cm}^{-1}$.

3.5 Conclusions

Two novel tri-nuclear dysprosocenium SMMs based on fulvalenyl ligands were reported in this chapter. This work represents the first synthetic method for the synthesis of dysprosium metallocene clusters. The SMM properties of both compounds were measured in a zero DC field, which resulted in an increase in the effective energy barrier from 138(4) in **3.1** to 411(23) cm^{-1} in **3.2** cation. The *ab initio* calculation indicates that both of the tri-dysprosium systems have the intramolecular interaction within the neighbour ions, which is dominated by the dipolar coupling effect.

Chapter 4

A Phosphole-Ligated Dysprosocenium Single-Molecule Magnet

4.1 Introduction

The impressive SMM performance of the metallocenium SMMs $[\text{Dy}(\text{Cp}^{\text{ttt}})]_2^+$ and $[(\text{Cp}^{\text{iPr5}})\text{Dy}(\text{Cp}^*)]^+$ provide inspiration for the exploration of other Cp-like ligands containing heteroatoms in place of carbon.^{5,11}

Despite the ready availability of heteroatom-containing cyclopentadienyl ligands, lanthanide SMMs containing such ligands are rare. Five-membered rings with heteroatoms such as phosphorus, arsenic and antimony could enhance the axial anisotropy as stronger electron-donors.¹⁵⁶ Gao *et al.* reported the sandwich compound $[(\eta^5\text{-Dsp})\text{Er}(\eta^8\text{-COT})]$, in which Dsp is the phosphorus-containing ligand 3,4-dimethyl-2,5-bis-trimethylsilylphospholy (Figure 4.1a).¹⁵⁷ The prolate erbium³⁺ ions interact with the two ligands with Er–COT and Er–Dsp distances of 2.321 Å and 1.687 Å, respectively. This molecule has a modest effective energy barrier of $U_{\text{eff}} = 249 \text{ cm}^{-1}$ in zero DC field, with blocking temperature of 9 K. The properties of the phosphole-ligated Er-SMM are better than those of $[(\text{Cp}^*)\text{Er}(\text{COT})]$, which has the $U_{\text{eff}} = 137 \text{ cm}^{-1}$.⁶⁰ However, the COT / Dsp combination of ligands is not suitable for oblate Dy^{3+} ions since $[(\eta^5\text{-Dsp})\text{Er}(\eta^8\text{-COT})]$ has an effective energy barrier of only 40 cm^{-1} under a induced DC field of 2000 Oe.

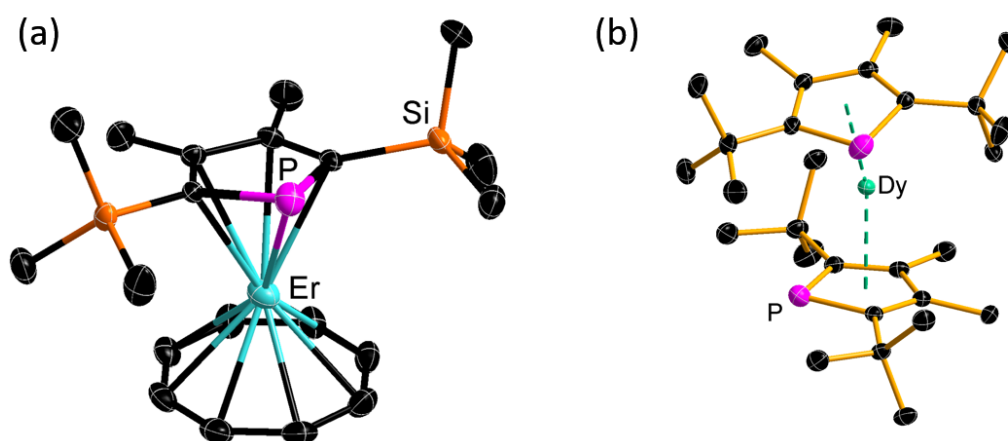


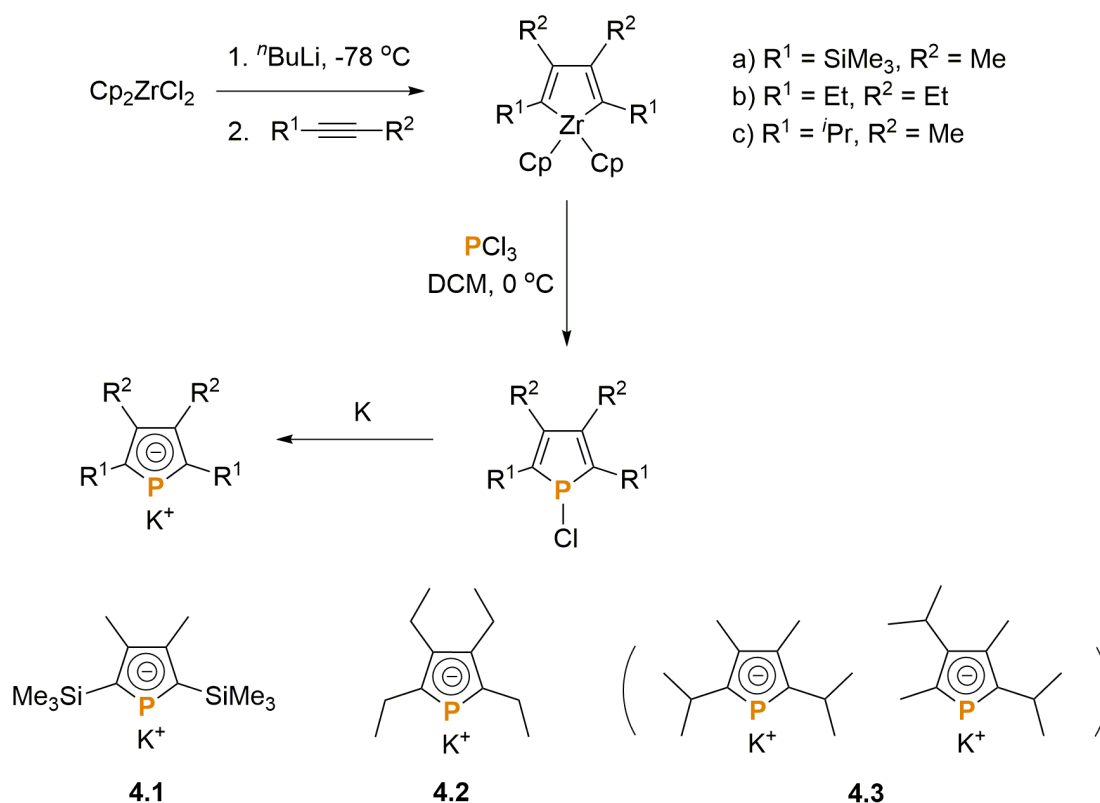
Figure 4.1 Thermal ellipsoid representation (30 % possibility) of molecular structures of $[(\text{Dsp})\text{Er}(\text{COT})]$ (a) and $[\text{Dy}(\text{Dtp})_2]^+$ (b). The structures are reproduced based on the cif files from the Ref. 157 and 158.^{157, 158}

Mills *et al.* reported the bis(monophospholyl) dysprosocenium complex $[\text{Dy}(\text{Dtp})_2]^+[\text{Al}\{\text{OC}(\text{CF}_3)_3\}_4]^-$, in which Dtp is the phosphole ligand 2,5-*t*Bu₂-3,4-Me₂PC₄ (Figure 4.1b).¹⁵⁸ Compared to the cation $[\text{Dy}(\text{Cp}^{\text{ttt}})_2]^+$, the $[\text{Dy}(\text{Dtp})_2]^+$ is less bent with a Dtp_c-Dy-Dtp_c angle of 157.9°, but a larger Dtp-Dy distance of 2.354 Å (*cf.* Cp_c-Dy-Cp_c = 152.8°, Cp_c-Dy = 2.309 and 2.324 Å in $[(\text{Cp}^{\text{ttt}})_2\text{Dy}]^+$). The result of the different structural properties in $[\text{Dy}(\text{Dtp})_2]^+$ is a lower effective energy barrier of 1223 cm⁻¹ with the magnetic hysteresis observed up to only 48 K. Notably, the authors also state that the reaction of $[\text{DyI}(\text{Dtp})_2]$ with $[(\text{Et}_3\text{Si})_2\text{H}][\text{B}(\text{C}_6\text{F}_5)_4]$, which was intended to produce $[\text{Dy}(\text{Dtp})_2][\text{B}(\text{C}_6\text{F}_5)_4]$, yielded an unknown mixture. Hence, the authors replaced the electrophilic silicon reagent with $[\text{NEt}_3\text{H}][\text{Al}\{\text{OC}(\text{CF}_3)_3\}_4]$.

4.2 Synthesis of Phospholyl Ligands and Phosphole-Ligated SMMs

4.2.1 Synthesis of Mono-Phospholyl Ligands and Phospholide Compounds

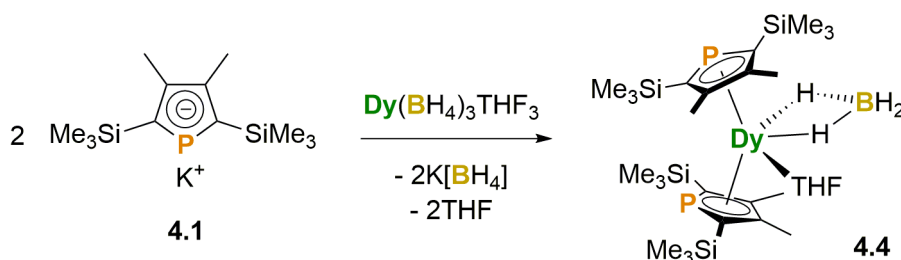
At the outset, three phospholyl ligands were targeted (**4.1–4.3**). The synthesis procedures for these potassium phospholide salts are similar and begins with the reaction of zirconocene dichloride with *n*-butyllithium and two equivalents of alkyne, according to a literature procedure.¹⁵⁹ Using 1-(trimethylsilyl)propyne, 3-hexyne or 4-methyl-2-pentyne yields the zirconacyclopentadienes depicted in Scheme 4.1. Then the corresponding phospholes are obtained following addition of one equivalent of PCl_3 . Finally, excess potassium metal is added to give the potassium phospholides, which are abbreviated as **4.1** (KDsp, Dsp = 2,5-bis(trimethylsilyl)-3,4-dimethylphospholide), **4.2** ($\text{KCp}^{\text{Et}4\text{P}}$, $\text{Cp}^{\text{Et}4\text{P}}$ = tetraethylphospholide) and **4.3** ($\text{KCp}^{\text{iPr}2\text{Me}2}$, $\text{Cp}^{\text{iPr}2\text{Me}2}$ = diisopropyldimethylphospholide). For compound **4.3**, the reaction generates two isomers that cannot be separated. Thus, only compound **4.1** and **4.2** were used in the following syntheses.



Scheme 4.1 Synthesis of **4.1**, **4.2** and **4.3**.

4.2.2 Synthesis of a Bis(monophospholy) Dysprosium Complex

Two equivalents of KDsp (**4.1**) were reacted with $[\text{Dy}(\text{BH}_4)_3(\text{THF})_3]$ in toluene and the bis(monophospholy)dysprosium compound $[(\text{Dsp})_2\text{Dy}(\text{BH}_4)(\text{THF})]$ (**4.4**) was obtained (Scheme 4.2). The molecular structure of **4.4** was determined by X-ray diffraction and is discussed in Section 4.3.1. Evidently, the methyl and trimethylsilyl groups are not bulky enough to avoid coordination of THF to dysprosium ion. Hence, to obtain a bis(monophospholy) sandwich structure, bulkier substituents are required to increase the steric hindrance.

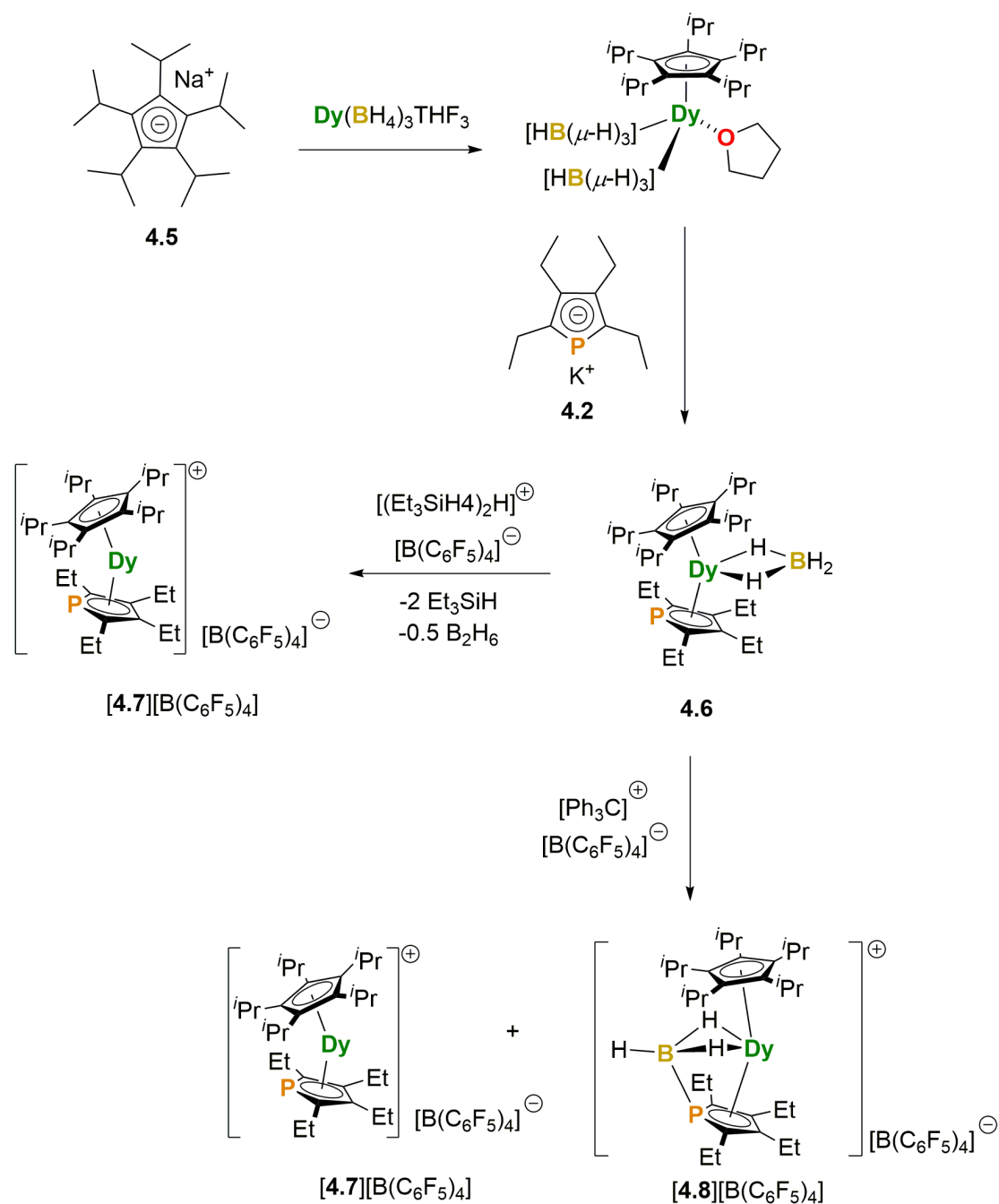


Scheme 4.2 Synthesis of **4.4**.

4.2.3 Synthesis of $[(\text{Cp}^{i\text{Pr}5})\text{Dy}(\text{Cp}^{\text{Et}4\text{P}})][\text{B}(\text{C}_6\text{F}_5)_4]$

In light of the result obtained when using a moderately bulky phospholy ligand, a bulkier phosphorus-containing dysprosium metallocene cation was targeted. The aim was therefore to synthesize $[(\text{Cp}^{i\text{Pr}5})\text{Dy}(\text{Cp}^{\text{Et}4\text{P}})][\text{B}(\text{C}_6\text{F}_5)_4]$, in light of structural similarities between this compound and the record-breaking SMM $[(\text{Cp}^{i\text{Pr}5})\text{Dy}(\text{Cp}^*)][\text{B}(\text{C}_6\text{F}_5)_4]$. The synthesis is detailed in Scheme 4.3. First, $\text{NaCp}^{i\text{Pr}5}$ was reacted with $[\text{Dy}(\text{BH}_4)_3(\text{THF})_3]$ to give the known compound $[(\text{Cp}^{i\text{Pr}5})\text{Dy}(\text{BH}_4)_2\text{THF}]$.⁵ The half-sandwich complex was then reacted with the potassium phospholide (**4.2**) to give the borohydride-ligated metallocene complex $[(\text{Cp}^{i\text{Pr}5})\text{Dy}(\text{Cp}^{\text{Et}4\text{P}})(\text{BH}_4)]$ (**4.6**). The borohydride ligand in **4.6** was then targeted for removal by adding $[(\text{Et}_3\text{Si})_2\text{H}][\text{B}(\text{C}_6\text{F}_5)_4]$, which finally yielded complex $[(\text{Cp}^{i\text{Pr}5})\text{Dy}(\text{Cp}^{\text{Et}4\text{P}})][\text{B}(\text{C}_6\text{F}_5)_4]$ (**4.7**). If the slightly milder electrophilic reagent $[\text{Ph}_3\text{C}][\text{B}(\text{C}_6\text{F}_5)_4]$ is used to remove the BH₄ ligand, in addition to **4.7**, the by-product of **4.8** also forms in trace amounts.

Compared to **4.7**, the **4.8** cation contains a κ^2 -BH₃ ligand, which is held in place by a B–P bond to the phospholyl ligand. These two compounds cannot be separated despite repeated attempts.



Scheme 4.3 Synthesis of **4.6** and **[4.7][B(C₆F₅)₄]**.

4.3 X-Ray Diffraction Studies of Dysprosium-Phospholyl Complexes

4.3.1 Crystal Structure of Compound 4.4

For $[(\eta^5\text{-Dsp})_2\text{Dy}(\text{BH}_4)(\text{THF})]$ (**4.4**, Figure 4.2), each of the Dsp ligands is coordinated in an η^5 -manner, with a Dy–C bond lengths in the range 2.767(3)–2.819(3) Å and 2.783(3)–2.823(3) Å for the two Dsp ligands. The Dy–P bond lengths are 2.890(1) and 2.914(1) Å to P1 and P2, respectively. The Cp_c –Dy distances are 2.488(1) and 2.490(2) Å to the Dsp ligands containing P1 and P2, respectively. The $\kappa^3\text{-BH}_4$ and THF ligands produce a Dy···B distance of 2.530(4) Å and a Dy–O bond length of 2.390(2) Å, which also leads to a bent Cp_c –Dy– Cp_c angle of $135.46(5)^\circ$. (Table 4.1)

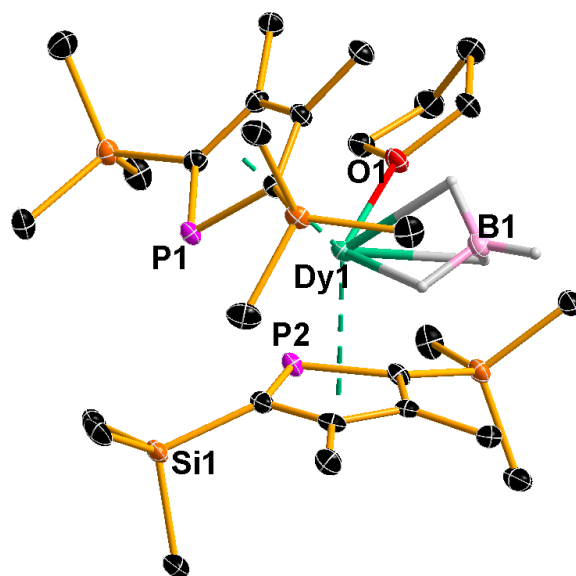


Figure 4.2 Thermal ellipsoid representation (50 % possibility) of molecular structure of **4.4**. Dy, green; C, black; O, red; P, purple; Si, orange; B, pink; H, white.

Table 4.1 Selected bond lengths (Å) and angles (°) for **4.4**.

Dy–C	Dy1–C1: 2.798(3) Dy1–C2: 2.819(3) Dy1–C3: 2.819(4) Dy1–C4: 2.767(3) Dy1–C5: 2.823(3) Dy1–C6: 2.789(3) Dy1–C7: 2.789(3) Dy1–C8: 2.783(3)
Dy–P	Dy1–P1: 2.890(1) Dy1–P2: 2.914(1)
Dy–centroid	Dy1–centroid1: 2.488(1) Dy1–centroid2: 2.490(2)
Dy···B	Dy1···B1: 2.530(4)
Dy–O	Dy1–O1: 2.390(2)
Cp _c –Dy–Cp _c	Dy1: 135.46(5)

4.3.2 Crystal Structure of Compound **4.6**

In compound **4.6**, the Cp^{ipr5} and Cp^{Et4P} ligands are both coordinated in an η⁵-manner. Due to the bulky Cp^{ipr5} ligand, only the borohydride ligand is coordinated from the equatorial plane — no THF or other solvent molecule can coordinate. Compared to **4.4**, the Dy–C bond lengths to the Cp^{ipr5} ligand are much shorter, with the range of 2.628(3)–2.683(3) Å. The range of Dy–C bond lengths to the Cp^{Et4P} ligand are also shorter, being in the range of 2.693(3)–2.746(3) Å. The Dy–P bond length of 2.8526(7) Å is also markedly shorter than the analogous distances in complex **4.4**. Thus, the distances between Dy and the Cp centroids are reduced to 2.355(2) Å and 2.415(2) Å for Cp^{ipr5} and Cp^{Et4P}, respectively. As the distance between the two Cp-planes gets closer, the Dy···B distance to the κ³-BH₄ ligand increases to 2.688(4) Å. The Cp_c–Dy–Cp_c angle increases substantially to 147.69(4)°.

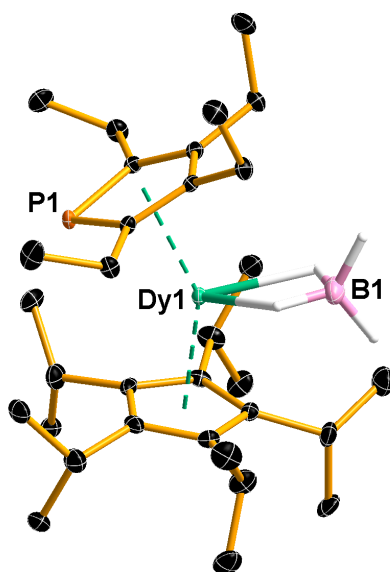


Figure 4.3 Thermal ellipsoid representation (50 % possibility) of molecular structure of **4.6**. Dy, green; C, black; P, orange; B, pink; H, white.

Table 4.2 Selected bond lengths (Å) and angles (°) for **4.6**.

Dy–C (Cp ^{iPr5})	Dy1–C1: 2.653(3) Dy1–C2: 2.628(3) Dy1–C3: 2.638(3) Dy1–C4: 2.651(3) Dy1–C5: 2.683(3)	Dy–C (Cp ^{Et4P})	Dy1–C21: 2.693(3) Dy1–C22: 2.746(3) Dy1–C23: 2.738(3) Dy1–C24: 2.741(3)
Dy–P	Dy1–P1: 2.852 (1)		
Dy–centroid (Cp ^{iPr5})	Dy–Cp _c ^{iPr5} : 2.355(2)	Dy–centroid (Cp ^{Et4P})	Dy–Cp _c ^{Et4P} : 2.415(2)
Dy···B	Dy1···B1: 2.688(4)		
Cp _c –Dy–Cp _c	Dy1: 147.69(4)		

4.3.3 Crystal Structure of $[(\text{Cp}^{i\text{Pr}5})\text{Dy}(\text{Cp}^{\text{Et}4\text{P}})][\text{B}(\text{C}_6\text{F}_5)_4]$

The molecular structure of **[4.7]** $[\text{B}(\text{C}_6\text{F}_5)_4]$ was determined at 100 K and 30 K, with the low-temperature structure being collected in the laboratory of Prof. Dr. K. Meyer at Erlangen-Nürnberg University, Germany. The dysprosium atom is disordered across two sites with approximate occupancies of 3:1 at both data collection temperatures. This disorder is illustrated in Figure 4.4 for both structures, for which the differences in bond lengths and angles are not statistically significant. For the major component of the disordered structure at 100 K, the Dy1–C distances are 2.523(10)–2.699(12) Å for the $\eta^5\text{-Cp}^{i\text{Pr}5}$ ligand, whilst the $\eta^5\text{-Cp}^{\text{Et}4\text{P}}$ ligand displays a shorter Dy1–C distance range of 2.632(11)–2.702(10) Å, compared to **4.6**. However, the Dy1–P distance slightly decreases to 2.881(3) Å. The distances between Dy1 and the Cp centroids are reduced to 2.305(1) and 2.369(1) Å for Dy1–Cp^{*iPr*5} and Dy1–Cp^{*Et*4P} respectively. The Cp_c–Dy–Cp_c bending angle is significantly wider 164.8(2)° (Table 4.3). In order to support the phase-purity of the product, ¹¹B and ¹⁹F NMR spectra are illustrated in Figure 7.22–7.23 (Experimental Section) and its powder X-ray diffraction pattern at 290 K is shown in Figure 4.5.

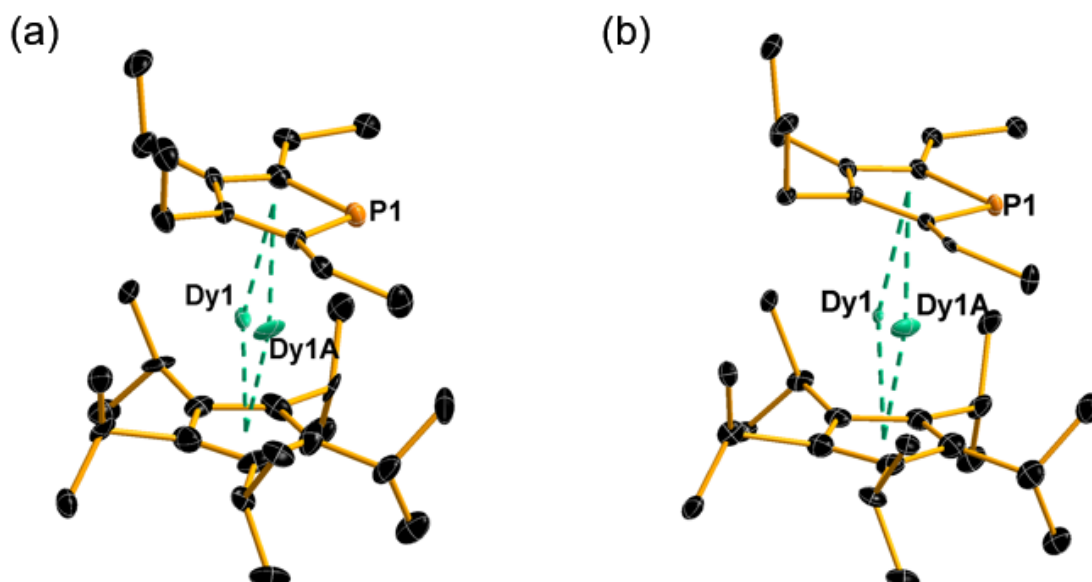


Figure 4.4 Thermal ellipsoid representation (50 % possibility) of molecular structures of **4.7** determined at 100 K (a) and at 30 K (b), illustrating the disorder associated with the dysprosium atom.

At 100 K, the bond lengths and angles to Dy1A are significantly different to those involving Dy1, *i.e.*: Dy–C = 2.370(13)–2.665(11) Å to Cp^{*iPr*5}; Dy–C = 2.614(10)–2.949(12) to Cp^{*Et*4P}; Dy–Cp^{*iPr*5} = 2.209(1); Dy–Cp^{*Et*4P} = 2.458(1); Dy–P = 2.697(6); bending angle at Dy1A = 166.2(2)°. The major structural differences between the two disordered forms of the cation **4.7** at 100 K are also found in the structure at 30 K. The relevant bond lengths and angles are all stated in Table 4.4 along with the percentage occupancies of the two disordered dysprosium positions.

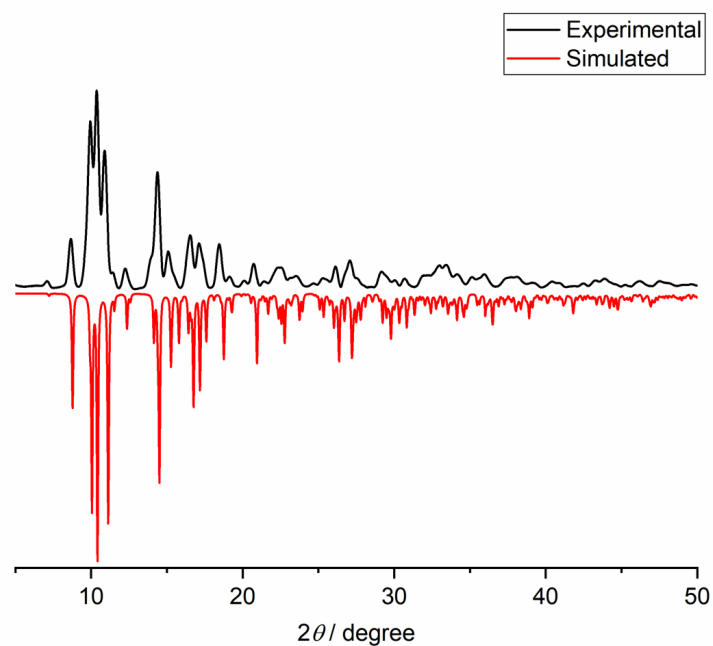
The appreciable differences in the local coordination environment experienced by the dysprosium atoms in **4.7** at 100 K and 30 K could have an impact on the crystal field properties of the complex and, therefore, the SMM behaviour. This aspect is described further in Section 4.4.

Table 4.3 Selected bond lengths (Å) and angles (°) for **4.7** at 100 K.

	Dy1 (74.7 %)	Dy1A (25.3 %)
Dy–C (Cp ^{<i>iPr</i>5})	Dy1–C1: 2.699(12) Dy1–C2: 2.636(12) Dy1–C3: 2.489(11) Dy1–C4: 2.523(10) Dy1–C5: 2.648(11)	Dy1A–C1: 2.370(13) Dy1A–C2: 2.370(13) Dy1A–C3: 2.571(13) Dy1A–C4: 2.665(11) Dy1A–C5: 2.537(12)
Dy–C (Cp ^{<i>Et</i>4P})	Dy1–C21: 2.670(10) Dy1–C22: 2.632(11) Dy1–C23: 2.687(9) Dy1–C24: 2.702(10)	Dy1A–C21: 2.819(11) Dy1A–C22: 2.949(12) Dy1A–C23: 2.875(10) Dy1A–C24: 2.614(10)
Dy–P	Dy1–P1: 2.881(3)	Dy1A–P1: 2.697(6)
Dy–centroid (Cp ^{<i>iPr</i>5})	Dy1–Cp _c ^{<i>iPr</i>5} : 2.305(1)	Dy1A–Cp _c ^{<i>iPr</i>5} : 2.209(1)
Dy–centroid (Cp ^{<i>Et</i>4P})	Dy1–Cp _c ^{<i>Et</i>4P} : 2.369(1)	Dy1A–Cp _c ^{<i>Et</i>4P} : 2.458(1)
Cp _c –Dy–Cp _c	Dy1: 164.8(2)	Dy1A: 166.2(2)

Table 4.4 Selected bond lengths (Å) and angles (°) for **4.7** at 30 K.

	Dy1 (76.4 %)	Dy1A (23.6 %)
Dy–C (Cp ^{ipr5})	Dy1–C1: 2.687(13) Dy1–C2: 2.637(13) Dy1–C3: 2.508(12) Dy1–C4: 2.514(11) Dy1–C5: 2.651(12))	Dy1A–C1: 2.347(14) Dy1A–C2: 2.409(14) Dy1A–C3: 2.584(13) Dy1A–C4: 2.662(13) Dy1A–C5: 2.546(12)
Dy–C (Cp ^{Et4P})	Dy1–C21: 2.671(11) Dy1–C22: 2.641(11) Dy1–C23: 2.689(11) Dy1–C24: 2.709(11)	Dy1A–C21: 2.830(12) Dy1A–C22: 2.971(12) Dy1A–C23: 2.876(12) Dy1A–C24: 2.619(11)
Dy–P	Dy1–P1: 2.881(3)	Dy1A–P1: 2.695(6)
Dy–centroid (Cp ^{ipr5})	Dy1–Cp _c ^{ipr5} : 2.305(1)	Dy1A–Cp _c ^{ipr5} : 2.205(1)
Dy–centroid (Cp ^{Et4P})	Dy1–Cp _c ^{Et4P} : 2.372(1)	Dy1A–Cp _c ^{Et4P} : 2.466(1)
Cp _c –Dy–Cp _c	Dy1: 164.5(2)	Dy1A: 165.7(2)

**Figure 4.5** Powder-XRD spectrum of **4.7** at 290 K.

4.3.4 Crystal Structure of $[(\text{Cp}^{i\text{Pr}5})\text{Dy}(\text{Cp}^{\text{Et}4\text{P}})(\text{BH}_3)][\text{B}(\text{C}_6\text{F}_5)_4]$

The dysprosium centre in the unexpected by-product **4.8** $[\text{B}(\text{C}_6\text{F}_5)_4]$ is also strongly disordered (Figure 4.6). For the major part (87 % occupancy), the Dy–C distances are longer than those in the cation **4.7**, lying in the range 2.559(4)–2.691(4) Å and 2.669(4)–2.874(4) Å for the $\text{Cp}^{i\text{Pr}5}$ ligand and the $\text{Cp}^{\text{Et}4\text{P}}$ ligand, respectively. The Dy–P distance of 2.8406(11) Å is, however, similar to the major disordered component of **4.7**. The distances between the dysprosium ion and the Cp-centroids increase to 2.3253(1) and 2.4581(1) Å. The BH_3 group is bound to the phosphorus atom with a B–P distance of 2.016(6) Å, and bridges to the dysprosium via two $\mu\text{-H}$ atoms with a Dy \cdots B distance of 2.555(5) Å. The bending $\text{Cp}_c\text{-Dy-Cp}_c$ angle is 159.07(1)°. The bond lengths and angles for the minor disordered component are significantly different and are displayed in Table 4.5. The IR spectrum for this mixture products give a weak absorption band at $\tilde{\nu} = 2192\text{--}2511\text{cm}^{-1}$ (Figure 7.24, Experimental Section). However, full characterization of this compound, including CH element analysis was not possible due to a combination of not being able to separate it from the other product of the reaction and also because it forms in very small amounts.

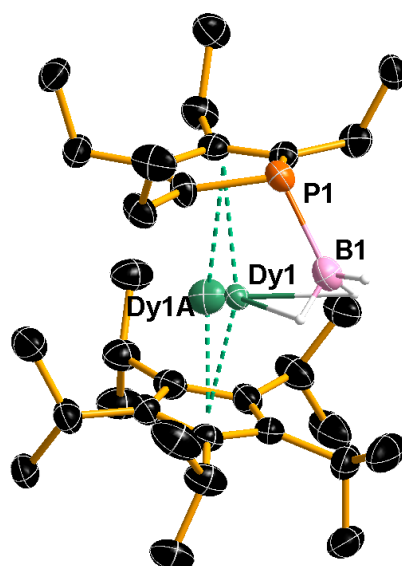


Figure 4.6 Thermal ellipsoid representation (50 % possibility) of molecular structures of **4.8**, illustrating the disorder associated with the dysprosium atom.

Table 4.5 Selected bond lengths (Å) and angles (°) for **4.8**.

	Disordered part 1 (87 %)	Disordered part 2 (13 %)
Dy–C (Cp ^{ipr5})	Dy1–C1: 2.578(4) Dy1–C2: 2.665(4) Dy1–C3: 2.691(4) Dy1–C4: 2.618(5) Dy1–C5: 2.559(4)	Dy1A–C1: 2.718(5) Dy1A–C2: 2.761(5) Dy1A–C3: 2.377(5) Dy1A–C4: 2.034(6) Dy1A–C5: 2.304(5)
Dy–C (Cp ^{Et4P})	Dy1–C21: 2.728(4) Dy1–C22: 2.874(4) Dy1–C23: 2.850(4) Dy1–C24: 2.669(4)	Dy1A–C21: 2.976(5) Dy1A–C22: 2.761(5) Dy1A–C23: 2.739(5) Dy1A–C24: 2.929(5)
Dy–P	Dy1–P1: 2.8406(11)	Dy1A–P1: 3.4045(1)
Dy–centroid (Cp ^{ipr5})	Dy1–Cp _c : 2.3253(1)	Dy1A–Cp _c : 2.1328(1)
Dy–centroid (Cp ^{Et4P})	Dy1–Cp _c : 2.4581(1)	Dy1A–Cp _c : 2.6584(1)
P–B	P1–B1: 2.016(6)	P1–B1: 2.016(6)
Dy···B	Dy1–B1: 2.555(5)	Dy1A–B1: 3.3781(1)
Cp _c –Dy–Cp _c	Dy1: 159.0710(1)	Dy1A: 157.952(1)

4.4 Magnetic Property Measurements

4.4.1 DC Magnetic Susceptibility

For compound **4.6**, the temperature-dependence of the magnetic susceptibility was determined using a 1 kOe DC field (Figure 4.7a). The $\chi_M T$ value of $14.03 \text{ cm}^3 \text{ K mol}^{-1}$ at 300 K matches well with the theoretical value for a single Dy^{3+} ion with a ${}^6\text{H}_{15/2}$ ground multiplet ($14.07 \text{ cm}^3 \text{ K mol}^{-1}$).¹⁴⁹ The $\chi_M T$ value gradually decreases to $11.82 \text{ cm}^3 \text{ K mol}^{-1}$ at 2 K. The field-dependence of the magnetization reaches a magnetization value of $5.34 \text{ N}\beta$ at 2 K and 7 T (Figure 4.7b).

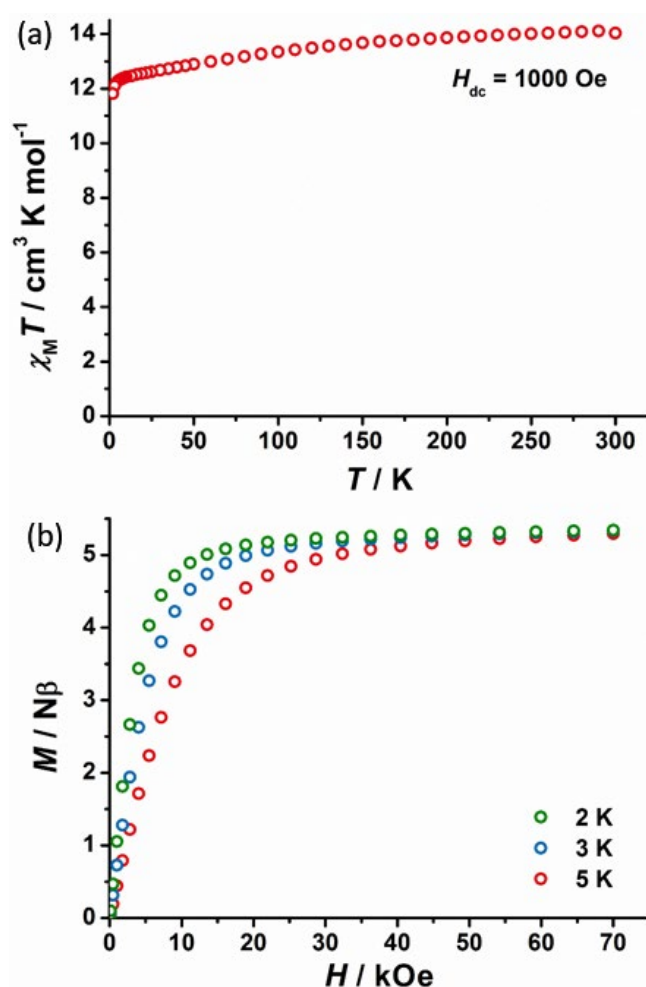


Figure 4.7 Plots of $\chi_M T$ versus temperature in an applied magnetic field of 1 kOe (a) and field dependent magnetization (b) for **4.6**.

For [4.7][B(C₆F₅)₄], $\chi_M T$ is 14.25 cm³ K mol⁻¹ at 300 K, close to the theoretical value of 14.07 cm³ K mol⁻¹. With decreasing temperature, the $\chi_M T$ is gradually reduced until a sharp drop occurs below 30 K. At the lower temperature, the $\chi_M T$ decreases to 3.25 cm³ K mol⁻¹ at 1.8 K, which indicates strong magnetic blocking (Figure 4.8).

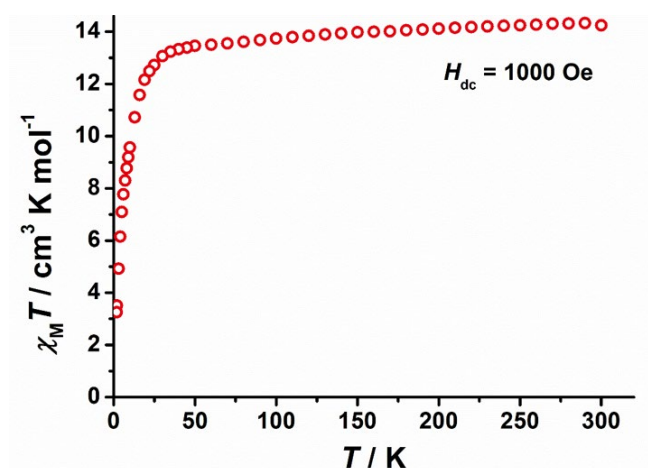


Figure 4.8. Plots of $\chi_M T$ versus temperature in an applied magnetic field of 1 kOe for [4.7][B(C₆F₅)₄].

In order to better understand the temperature-dependence of the magnetic relaxation, plots of magnetization decay versus time were also measured for [4.7][B(C₆F₅)₄] at the temperature range of 2–75 K. For instance, the data of 2 K and 75 K is shown in Figure 4.9 (the other data are provided in the Experimental Section). The magnetization decays close to zero over a period of 15 s at 75 K, whereas the relaxation time increase to more than 500 min at 2 K, which again displays the effective magnetic blocking at low temperature.

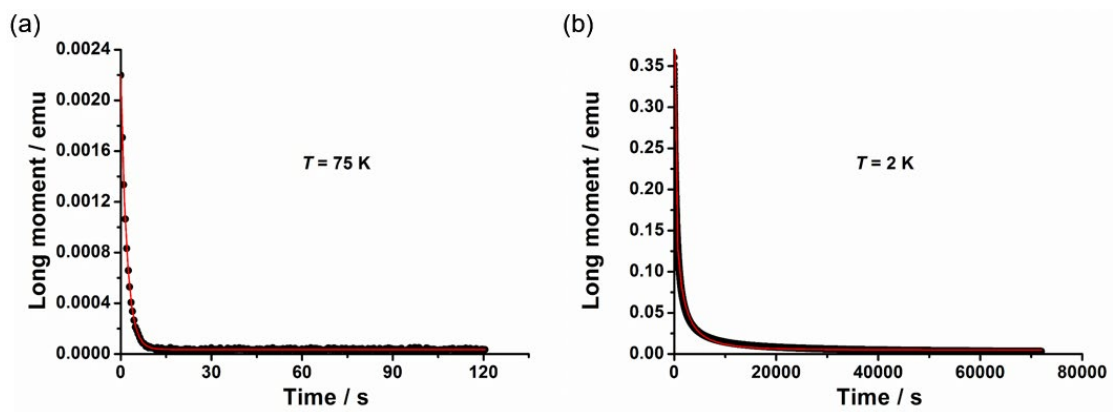


Figure 4.9. Plots of magnetization decay vs. time used to derive relaxation times for [4.7][B(C₆F₅)₄] at 75 K (a) and 2 K (b).

4.4.2 AC Magnetic Measurements

The temperature-dependence of the in-phase (χ') and the out-of-phase (χ'') AC susceptibility were measured in zero DC field at various AC frequencies in the range $\nu = 1$ –1488 Hz from 4 to 60 K for complex **4.6** (Figure 4.10a-b). No maxima in $\chi''(T)$ were observed due to fast magnetic relaxation via QTM even at low temperature. Thus, an additional DC field of 1500 Oe was applied in the temperature range 4–31 K to suppress the QTM, with the maxima observed from 4 to 18 K (Figure 4.10c-d).

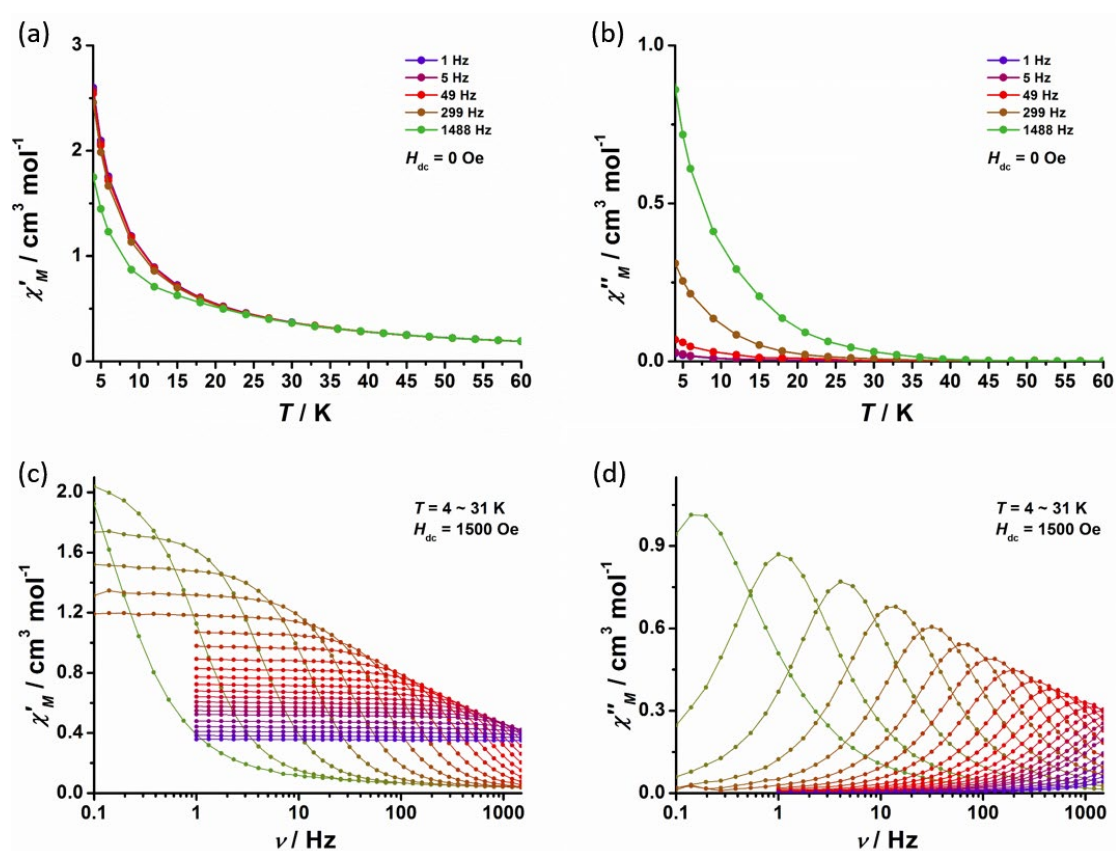


Figure 4.10 Temperature dependence of the in-phase (χ'_M) (a) and out of phase susceptibility (χ''_M) (b) for **4.6** in zero DC field at AC frequencies in the range 1–1488 Hz from 4 to 60 K. Frequency dependence of in-phase (χ'_M) (c) and out-of-phase (χ''_M) (d) susceptibility in a DC field of 1500 Oe at AC frequencies of 1–1488 Hz from 4 to 31 K. Solid lines are a guide to the eye.

Using the Arrhenius equation $\tau^{-1} = \tau_0^{-1} e^{-U_{\text{eff}}/k_B T}$, an effective energy barrier for the relaxation in an applied DC field was determined to be 43 cm^{-1} with $\tau_0 = 2.7 \times 10^{-6}$ s. According to the linear plot of $\ln \tau$ vs. T^{-1} (Figure 4.11a), the Raman process and quantum tunnelling are not prominent, as expected for an in-field measurement. The Cole-Cole plots (Figure 4.11b) were fitted with α parameters in the range of 0.04–0.21 (Table 4.6), which indicates a narrow range of relaxation times and probably one dominant process.

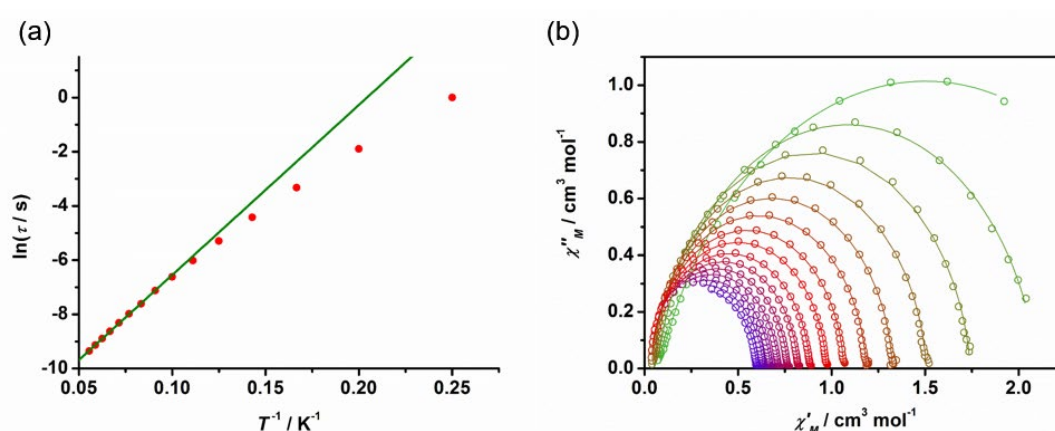


Figure 4.11 (a) Plot of natural log of the relaxation time vs. inverse temperature for **4.6** (adjusted $R^2 = 0.99954$). (b) Cole-Cole plots for the AC susceptibility in a DC field of 1500 Oe for **4.6** from 4–18 K (adjusted $R^2 = 0.99933$ – 0.99994).

Table 4.6 Relaxation fitting parameters for **4.6**. (adjusted $R^2 = 0.99933$ – 0.99994)

T / K	$\chi_T / \text{cm}^3 \text{mol}^{-1}$	$\chi_S / \text{cm}^3 \text{mol}^{-1}$	α	τ / s
18	0.59964	0	0.04395	8.62214E-5
17	0.63332	0	0.04335	1.07507E-4
16	0.67183	0	0.04715	1.36768E-4
15	0.71527	0	0.04615	1.7948E-4
14	0.76412	0.00946	0.04268	2.44724E-4
13	0.81979	0.0164	0.03989	3.41936E-4
12	0.88363	0.02191	0.03679	4.95744E-4
11	0.9709	0.02824	0.03464	8.07515E-4
10	1.06496	0.03046	0.03579	0.00134
9	1.18447	0.03387	0.03999	0.00245
8	1.32505	0.03816	0.04225	0.00501
7	1.50573	0.0439	0.05084	0.01202
6	1.74195	0.05034	0.0665	0.0361
5	2.10152	0.06817	0.10591	0.15077
4	2.92534	0.07609	0.21202	1.00386

For compound [4.7][B(C₆F₅)₄], in-phase and out-of-phase AC susceptibility were measured in a temperature range of 4–130 K, with the zero DC field and a small 5 Oe AC field at various frequencies in the range $\nu = 0.1$ –1488 Hz. Two groups of maxima peaks were observed (Figure 4.12a–b). For the $\chi''(T)$ data, the first group of maxima occur in the temperature range 25–72 K and the second group of maxima occur in the range 73–119 K.

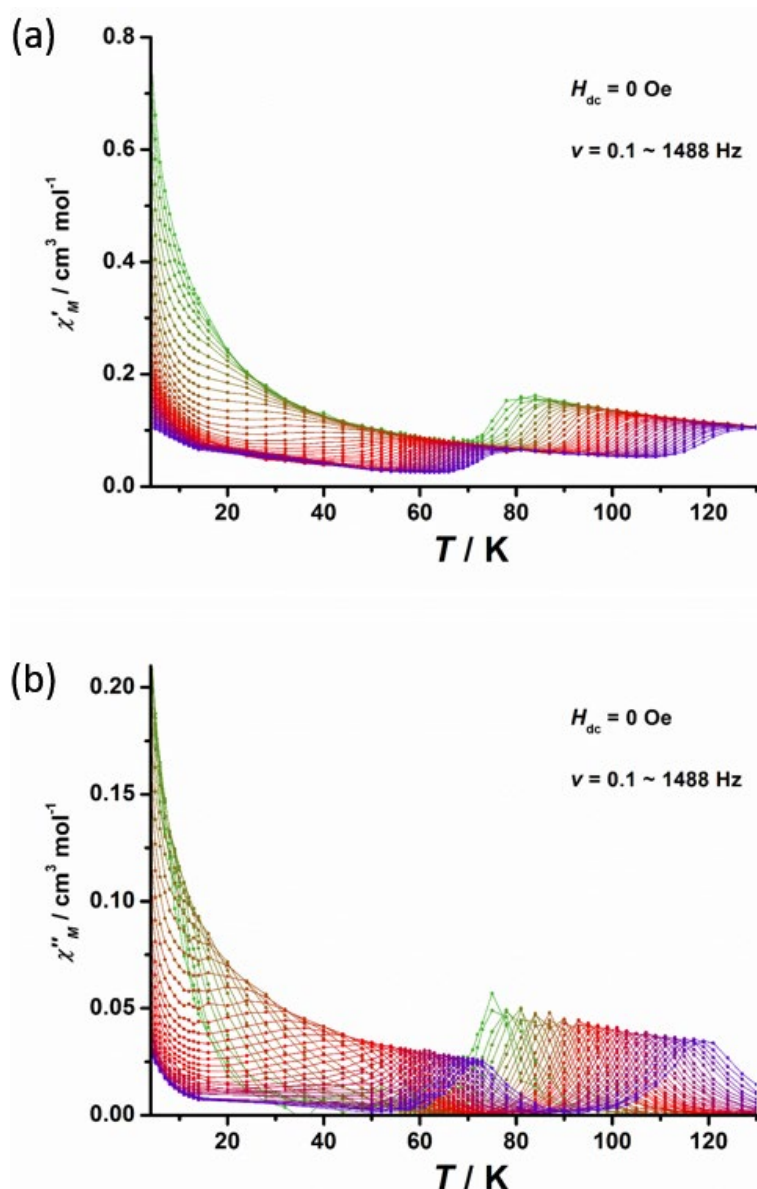


Figure 4.12 Temperature dependence of in-phase (χ'_M) (a) and out-of-phase susceptibility (χ''_M) (b) in a zero DC field at AC frequencies of 0.1–1488 Hz for [4.7][B(C₆F₅)₄].

The appearance of two sets of well-defined maxima at relatively high temperatures is unprecedented and reveals that the single-ion compound should have more than one high-barrier thermal relaxation pathway. The Cole-Cole fitting plots (Figure 7.31–7.39, Experimental Section) yield α parameters of 0–0.53, which show a broad range of relaxation times and indicate that more than one path probably exists in relaxation processes (Table 7.18–7.19, Experimental Section). The plot of $\ln \tau$ versus T^{-1} (Figure 4.13) consists of two distinct curves, one for each group of maxima in the out-of-phase susceptibility. Fits of the data were achieved using Equation 4 (on page 21) and $\tau^{-1} = \tau_0^{-1} e^{-U_{\text{eff}}/k_{\text{B}}T} + CT^n + \tau_{\text{QTM}}^{-1}$.

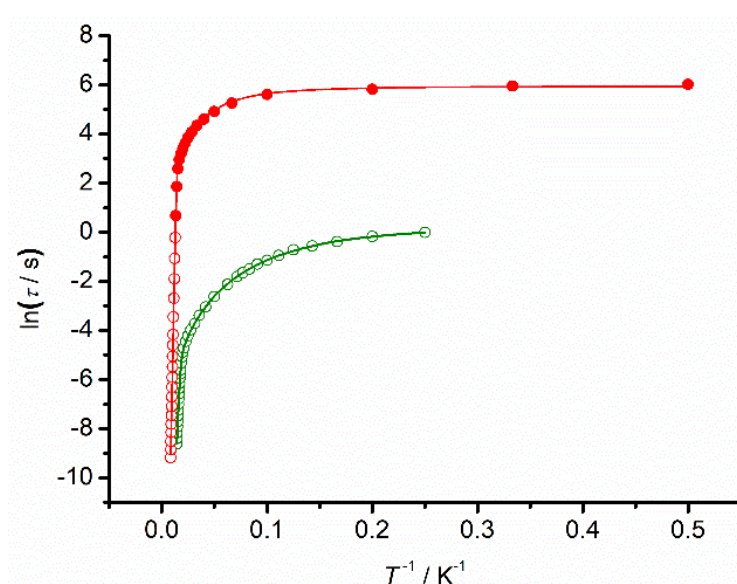


Figure 4.13 Plots of $\ln \tau$ versus T^{-1} for [4.7] $[\text{B}(\text{C}_6\text{F}_5)_4]$. The red data points correspond to the high-temperature processes, the green points correspond to the low-temperature process.

In Figure 4.13, the red fitting line, which refers to the high-temperature process, gives a barrier of $1410(10) \text{ cm}^{-1}$ and $\tau_0 = 4.77 \times 10^{-12} \text{ s}$, with the Raman parameters of $C = 5.36 \times 10^{-6} \text{ s}^{-1} \text{ K}^{-n}$ and $n = 2.23$ and quantum tunnelling time of $\tau_{\text{QTM}} = 381.7 \text{ s}$. The green curve results in $U_{\text{eff}} = 747(7) \text{ cm}^{-1}$, $\tau_0 = 4.23 \times 10^{-11} \text{ s}$, $C = 8.73 \times 10^{-3} \text{ s}^{-1} \text{ K}^{-n}$, $n = 2.43$ and $\tau_{\text{QTM}} = 1.33 \text{ s}$.

The magnetic hysteresis was also measured first using a relatively fast scan rate of 200 Oe s⁻¹ in the temperature range 2–55 K (Figure 4.14a). Subsequently, a lower scan rate of 25 Oe s⁻¹ was applied at temperatures in the range 60–75 K (Figure 4.14b). The loops remained open up to 70 K, which defines the blocking temperature for this SMM. At 2 K and 200 Oe s⁻¹, the M value almost saturates in a field of +70 kOe. A slight decrease in the magnetization occurs on reducing the field to 10 kOe, and around zero field there is sharp drop in the magnetization to 2 N β . Then, as the magnetic field increases to the opposite direction, two distinct steps occur around 8 kOe and 20 kOe, resulting in a sharp decrease in M . To reduce the magnetization to zero, a coercive field (H_c) of 25 kOe is required.

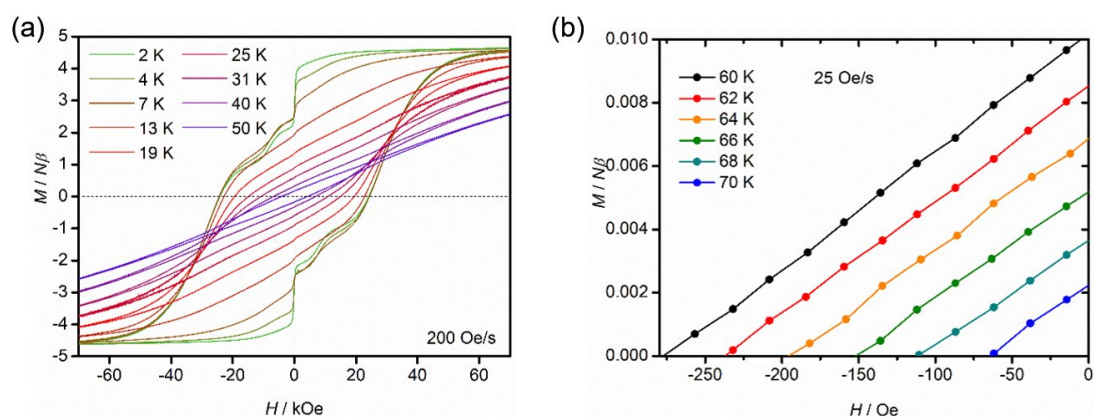


Figure 4.14 Magnetic hysteresis properties of [4.7][B(C₆F₅)₄]: (a) hysteresis loops at various temperatures in the range 2–50 K using a sweep rate of 200 Oe s⁻¹; (b) Section of the hysteresis loops at low fields and temperatures in the range 60–70 K using a sweep rate of 25 Oe s⁻¹.

The two steps in the hysteresis loops at 2 K and 200 Oe s⁻¹ also occur on the opposite side of the loop after reversal of the field direction once again. As the temperature of the hysteresis measurement was increased, the loops gradually begin to close, the coercive field reduces and the two steps in the magnetization become less discernible. When considered in light of the AC susceptibility data, the steps in the hysteresis data for [4.7][B(C₆F₅)₄] are consistent with magnetization reversal involving two different relaxing species. Since no structural phase changes could be detected using X-ray

crystallography, we believe that the phenomena observed in this SMM are most likely to be accounted for the two disordered forms of the cation $[(\text{Cp}^{i\text{Pr5}})\text{Dy}(\text{Cp}^{\text{Et4P}})]^+$ (**4.7**) displaying independent SMM behaviour, with one dysprosium environment experiencing a stronger axial crystal-field than the other.

4.4.3 Theoretical Calculations on $[(\text{Cp}^{i\text{Pr5}})\text{Dy}(\text{Cp}^{\text{Et4P}})]^+$

Based on the experimental data, the complex **4.7** $[\text{B}(\text{C}_6\text{F}_5)_4]$ shows excellent and unusual SMM performance with two large energy barriers and one of the highest known blocking temperatures. The two distinct thermal relaxation processes have not previously been observed in a metallocenium SMM. Hence, multireference *ab initio* calculations were applied to further explain the magnetic behaviour. At the time of writing, only the calculations on the major disordered component (at 100 K) had been completed. According to the angles defined as that formed by the intersection of the magnetic axis in the excited KDs relative to the magnetic axis in the ground KD (θ) (Table 4.7), all eight KDs are highly axial, which reflects the molecular structure. The axiality is also reflected in the g-tensors for the system; however, non-negligible transverse components are encountered in KD5. A barrier-like illustration of the magnetic relaxation is depicted in Figure 4.15. Notably, the transition magnetic moments for barrier-crossing processes (effectively the probability of a transition) are small even in the higher KDs. The experimental energy barrier of $1410(10) \text{ cm}^{-1}$ lies in between the values of 1316 cm^{-1} for KD5 and 1523 cm^{-1} for KD6. This result indicates that the most probable barrier-crossing transition occurs via KD6, although a transition involving KD5 cannot be ruled out. Consequently, the larger experimental barrier can be assigned cautiously to the major disordered component of **4.7** as determined by crystallography.

Table 4.7 Properties of the eight lowest KDs of the Dy³⁺ ion in the major component of the disordered structure of **4.7**, corresponding to the crystal-field split states in the ground ⁶H_{15/2} multiplet.

	E / cm^{-1}	g_x	g_y	g_z	$\theta / ^\circ$ ^a
KD1	0	0.0000	0.0001	19.8868	
KD2	617	0.0023	0.0023	16.9323	2.3°
KD3	926	0.0054	0.0095	14.3764	3.8°
KD4	1122	0.0509	0.0637	11.7576	1.6°
KD5	1316	0.1829	0.2905	9.0740	5.5°
KD6	1523	0.2029	0.6767	6.3613	5.8°
KD7	1698	0.7051	1.5582	3.7751	6.8°
KD8	1794	11.6572	9.3462	1.2506	0.5°

^a Angle between the principal magnetic axis of the doublet and that of the ground doublet.

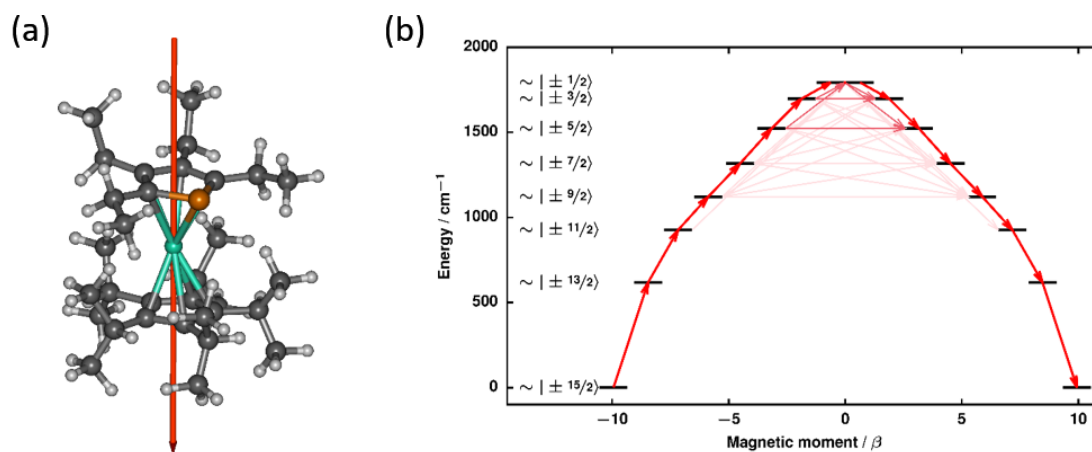


Figure 4.15 (a) The principal magnetic axes of the ground KD of the Dy³⁺ ion in the major disordered component of **4.7**. (b) Calculated effective *ab initio* barrier for the relaxation of magnetization for the Dy³⁺ ion.

4.5 Discussion and Conclusions

A dysprosocenium SMM based on a combination of phospholyl and cyclopentadienyl ligands was synthesized and its molecular structure determined at 100 K and 30 K, with no phase transition occurring. Regardless of temperature, the dysprosium site in the structure is disordered over two positions with relative occupancies of approximately 3:1. This SMM was found to display two thermal relaxation processes, with high energy barriers of 747 cm^{-1} and 1410 cm^{-1} . Based on magnetic hysteresis measurements, a blocking temperature of 70 K was determined, which is the third highest blocking temperature to be reported. Compared to our previous work of $[(\text{Cp}^*)\text{Dy}(\text{Cp}^{i\text{Pr}5})][\text{B}(\text{C}_6\text{F}_5)_4]$, the phosphole-ligated SMM has a more linear Cp–Dy–Cp angle of 169.5° and essentially the same Dy–Cp^{*iPr*5} distance of 2.295 \AA . However, a longer Dy–Cp^{*Et*4P} distance of 2.368 \AA compared to the Dy–Cp* distance of 2.284 \AA for $[\text{Cp}^*\text{DyCp}^{i\text{Pr}5}]^+$ may be responsible for the slightly poorer SMMs. The two distinct thermal relaxation processes are consistent with the presence of two disordered forms of the $[(\text{Cp}^{i\text{Pr}5})\text{Dy}(\text{Cp}^{\text{Et}4\text{P}})]^+$ cation. A theoretical study of the major disordered component indicated that this structure gives rise to the thermal relaxation process with the higher barrier. It is hoped that additional computation results will be available soon to support the experimental observation of the second thermal relaxation with the lower barrier.

Chapter 5

Fulvalene-Bridged Dimetallic Uranocenium Cations

5.1 Introduction

Compared to lanthanides and transition metals, SMMs based on actinides are rare. Organometallic uranium molecular magnets are particularly uncommon, and dimetallic versions even more so.¹⁶⁰ A notable example of a metallocene-like inverse sandwich complex containing uranium was published by Mazzanti *et al.* in 2013.¹¹¹ The compound $[K_2\{U(OSi(O^tBu)_3)_3\}_2(\mu-\eta^6:\eta^6-C_7H_8)]$ consists of two uranium(IV) ions bridged by a doubly reduced toluene ligand and coordinated by siloxide ligands on the terminal sites (Figure 5.1a). In the paper, SMM properties were not described, but the temperature-dependence of the magnetic susceptibility was measured in a DC field of 500 Oe.

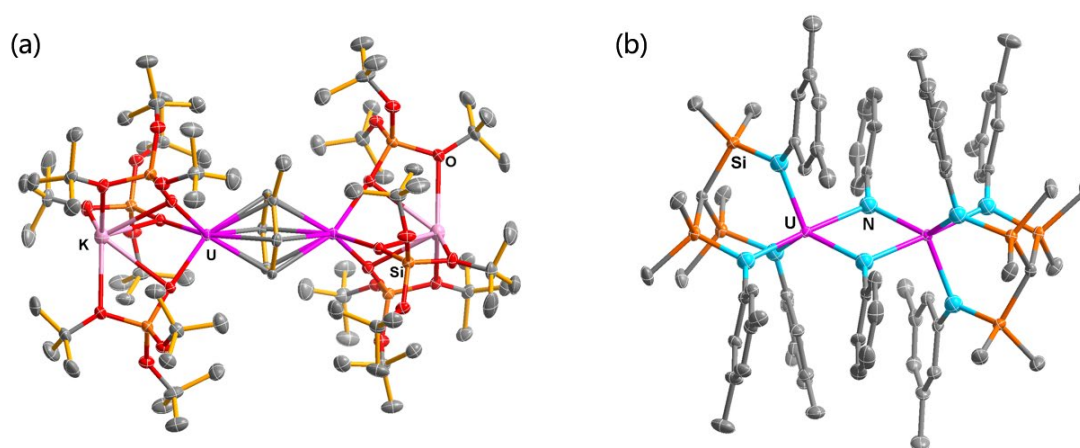


Figure 5.1 Thermal ellipsoid representation (30 % possibility) of molecular structures of $[K_2\{U(OSi(O^tBu)_3)_3\}_2(C_7H_8)]$ (a) and $[U(Ts^{Xy})(\mu-NPh)_2]$ (b). U, purple; C, grey; O, red; N, blue; Si, orange. The structures are reproduced based on the cif files from the Ref. 110 and 111.^{110, 111}

Other examples of structurally similar di-uranium organometallic compounds tend to feature bridging via U–N or U–O interactions in a κ^1 -manner.^{110, 112, 161-163} For example, Liddle *et al.* reported a $U^{3+}-U^{4+}$ dimetallic complex $[U(Ts^{Xy})(\mu-NPh)_2]$ ($Ts^{Xy} = HC(SiMe_2NAr)_3$), in which the uranium atoms are bridged by two imido-aryl ligands

(Figure 5.1b). However, the magnetic properties of these compounds do not include detailed SMM behaviour.¹¹⁰

On the other hand, two uranium metallocenes $[(\text{Cp}^{i\text{Pr5}})_2\text{U}^{\text{III}}]^+$ and $[(\text{Cp}^{i\text{Pr5}})_2\text{U}^{\text{II}}]$ were reported by our group in 2019 and 2020 (Figure 5.2).^{120, 121} Despite the near-linear geometry of the uranium(III) metallocene cation $[(\text{Cp}^{i\text{Pr5}})_2\text{U}^{\text{III}}]^+$ ($\text{Cp-U(III)-Cp} = 167.82(8)^\circ$) or the perfectly linear geometry of the divalent uranocene $[(\text{Cp}^{i\text{Pr5}})_2\text{U}^{\text{II}}]$ ($\text{Cp-U(II)-Cp} = 180^\circ$), neither compound displays significant slow relaxation of the magnetization in zero DC field. Indeed, the relaxation in $[(\text{Cp}^{i\text{Pr5}})_2\text{U}^{\text{III}}]^+$ is described essentially only by a Raman process. These observations are consistent with previous report on uranium SMMs and are thought to be a consequence of the relatively large covalent contribution to the metal-ligand bonding, which partially quenches the orbital contribution to the magnetic moment.

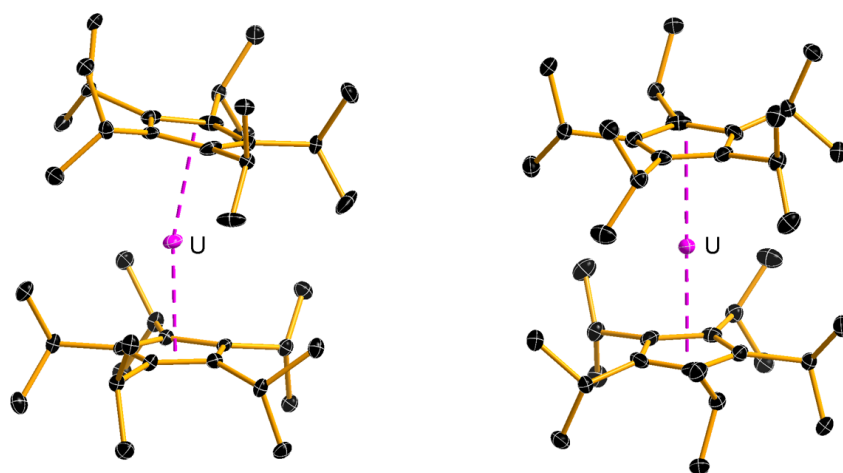
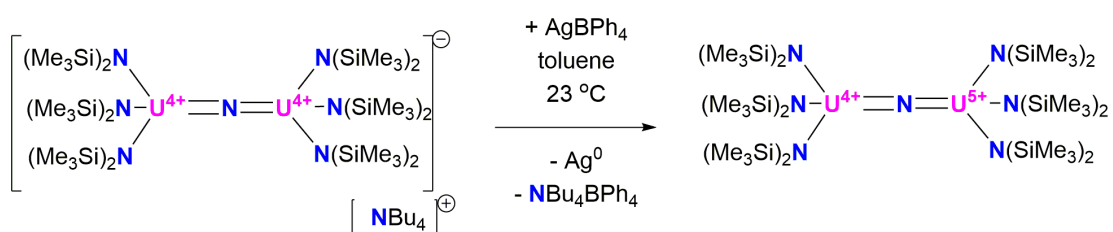


Figure 5.2 Thermal ellipsoid representation (30 % possibility) of molecular structures of $[(\text{Cp}^{i\text{Pr5}})_2\text{U}^{\text{III}}]^+$ (a) and $[(\text{Cp}^{i\text{Pr5}})_2\text{U}^{\text{II}}]$ (b). U, purple; C, black. The structures are reproduced based on the cif files from the Ref. 120 and 121.^{120, 121}

Beyond the confines of molecular magnetism, mixed-valence polynuclear uranium compounds are rare. Mazzanti *et al.* reported a series of multinuclear compounds containing U^{3+} , U^{4+} or U^{5+} in one system.^{112, 164} For instance, the reagent $\text{Ag}(\text{BPh}_4)$ was

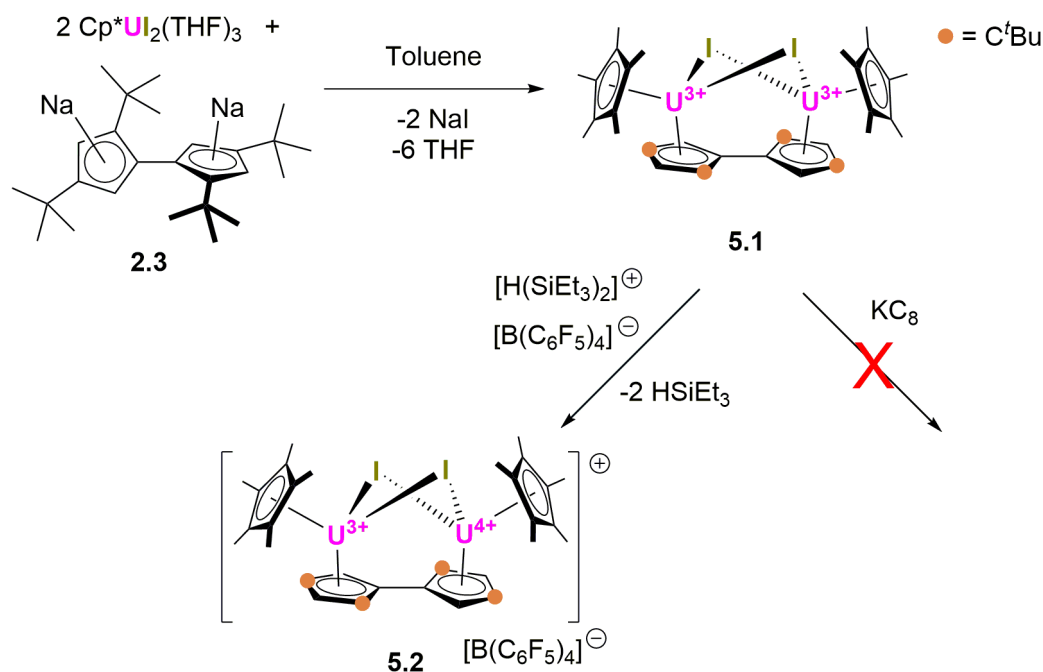
used to oxidize the $[\{(TMS_2N)_3U^{IV}\}_2(\mu-N)]^-$ anion to give $[\{(TMS_2N)_3U^{IV/V}\}_2(\mu-N)]$ in which the $U^{4+}-U^{5+}$ unit is bridged by nitride (Scheme 5.1). According to the temperature-dependence of the magnetic susceptibility, the $U^{4+}-U^{4+}$ system has a higher Néel temperature of 90 K than the mixed-valence $U^{4+}-U^{5+}$ compound, with $T_N = 55$ K. The antiferromagnetic coupling through the linear $U=N=U$ bridge therefore reveals that the uranium oxidation state has a strong influence on the exchange interactions.



Scheme 5.1 Synthesis of $[\{(TMS_2N)_3U^{IV/V}\}_2(\mu-N)]$.

5.2 Synthesis of Fulvalenyl Bridged Di-Uranocenium Complexes

Based on the findings in Chapter 2,²⁵ the fulvalenyl ligand (Fv^{tttt}) is considered as an ideal platform to study the diuranium molecular magnets including, potentially, SMM behaviour, if a diuranium(III) version can be synthesized. In fact, a similar double sandwiched U³⁺-U³⁺ compound [$\{U^{III}(\eta^5\text{-Cp}^*)(\mu\text{-I})_2(\eta^5:\eta^5\text{-Fv}^{tttt})\}$] (**5.1**) was successfully synthesized (Scheme 5.2). Compound **5.1** was synthesized by reacting complex **2.3** with the starting material Cp^{*}UI₂(THF)₃, which yielded the double iodide-bridging complex **5.1**. The synthesis method is complementary to that in which Na₂Fv^{tttt} (compound **2.3**) was used to obtain [$\{\text{Ln}(\text{Cp}^*)(\text{BH}_4)\}_2(\text{Fv}^{tttt})$] (compound **2.6**). Attempts at synthesizing the uranium(III) analogue of 2.6, i.e. [$\{U(\text{Cp}^*)(\text{I})\}_2(\text{Fv}^{tttt})$], did not succeed and only produced a mixture of unidentifiable compounds. The ¹H NMR spectrum of **5.1** in Figure 7.25 (Experimental Section) helped to determine the structure and purity, in which three singlet peaks were found around the chemical shift (δ /ppm) of -0.75 (s, 18H), -4.40 (s, 30H) and -30.84 (s, 18H).



Scheme 5.2 Synthesis of **5.1** and [**5.2**][B(C₆F₅)₄].

After compound **5.1** was isolated, one equivalent of $[(\text{Et}_3\text{Si})_2\text{H}][\text{B}(\text{C}_6\text{F}_5)_4]$ was added with the aim of extracting one iodide ligand to give $\{[\text{U}^{\text{III}}(\eta^5\text{-Cp}^*)(\mu\text{-I})](\eta^5:\eta^5\text{-Fv}^{\text{tttt}})][\text{B}(\text{C}_6\text{F}_5)_4]$. Unexpectedly, however, the ion-pair $\{[\text{U}^{\text{III/IV}}(\eta^5\text{-Cp}^*)(\mu\text{-I})]_2(\eta^5:\eta^5\text{-Fv}^{\text{tttt}})][\text{B}(\text{C}_6\text{F}_5)_4]$ was obtained (**[5.2]** $[\text{B}(\text{C}_6\text{F}_5)_4]$), indicating a one-electron oxidation process rather than removal of an iodide bridge. In the cation **5.2**, one of the U^{3+} ions has seemingly been oxidized to U^{4+} , resulting in a mixed-valence $\text{U}^{3+}\text{-U}^{4+}$ system. Further reaction of **5.2** with an excess of the electrophilic reagent $[(\text{Et}_3\text{Si})_2\text{H}][\text{B}(\text{C}_6\text{F}_5)_4]$ has been tried to remove the bridging iodides, but only starting material was recovered from these reactions. Surprisingly, excess KC_8 (2-5 equiv.) was added to **[5.2]** $[\text{B}(\text{C}_6\text{F}_5)_4]$ in an attempt to reduce the tetravalent uranium back to the trivalent form, however, no product was obtained. The ^{19}F and ^{11}B NMR spectra in 1,2-Dichlorobenzene- D_4 are consistent with the solid-state molecular structure of the anion part $[\text{B}(\text{C}_6\text{F}_5)_4]^-$ (Figure 7.29–7.30, Experimental Section). However, the ^1H NMR in Dichlorobenzene- D_4 shows impurity peaks, which cannot give any information about the structure. Meanwhile, the ^1H NMR (Figure 7.27-7.28) in Dichloromethane- D_2 indicates that **[5.2]** $[\text{B}(\text{C}_6\text{F}_5)_4]$ cannot totally purified by crystallization method, but the main six singlet peaks can be observed in the chemical shifts (δ/ppm) of 22.40 ($-\text{CH}_3$, Fv^{tttt}), 16.32 ($-\text{CH}_3$, Cp^*) and -30.80 ($-\text{CH}_3$, Fv^{tttt}) for one of the U ions and 19.19 ($-\text{CH}_3$, Fv^{tttt}), 17.78 ($-\text{CH}_3$, Cp^*) and -28.53 ($-\text{CH}_3$, Fv^{tttt}) for the other site. However, the **[5.2]** $[\text{B}(\text{C}_6\text{F}_5)_4]$ will slowly decompose in dichloromethane as the chemical shifts (δ/ppm) change and the six peaks turn to three singlet peaks overnight (Figure 7.27-7.28 in Experimental Section): 20.80 ($-\text{CH}_3$, Fv^{tttt}), 11.67 ($-\text{CH}_3$, Cp^*) and -30.48 ($-\text{CH}_3$, Fv^{tttt}). Hence, in future work, the NMR solvent should be replaced as well as purification method.

5.3 X-Ray Diffraction Studies of Dinuclear Uranium Compounds

5.3.1 Structure of $[\{U^{III}(\eta^5-Cp^*)(\mu-I)\}_2(\eta^5:\eta^5-Fv^{tttt})]$ (**5.1**)

The crystal structure of **5.1** shows that the two uranium centres are symmetry-related and the minimum unit cell is a half of the $[\{U^{III}(\eta^5-Cp^*)(\mu-I)\}_2(\eta^5:\eta^5-Fv^{tttt})]$ (Figure 5.3a). Thus, two uranium ions take the similar crystal environment (Figure 5.3b). Here, only the structural parameters for U1 centre are listed in Table 5.1.

Table 5.1 Selected bond lengths (Å) and angles (°) for **5.1**.

U–C(Fv ^{tttt})	U1–C11: 2.794(7) U1–C12: 2.777(8) U1–C13: 2.835(8) U1–C14: 2.774(8) U1–C15: 2.783(7)
U–C(Cp*)	U1–C1: 2.769(8) U1–C2: 2.765(8) U1–C3: 2.772(9) U1–C4: 2.759(7) U1–C5: 2.765(7)
U–Cp _c (Fv ^{tttt} centroid)	U1–Cp _c : 2.517(4)
U–Cp _c (Cp* centroid)	U1–Cp _c : 2.489(4)
U ₁ ···U ₂	U1–U2: 4.293(1)
U–I	U1–I1: 3.265(1) U1–I2: 3.153(1)
Cp(Fv ^{tttt})–U–Cp(Cp*)	U1: 137.45(11)

Similar to compound **2.9**, in compound **5.1**, U1 is η^5 -sandwiched by a Cp* ligand and one half of the fulvalenyl ligand, with U–C bond lengths in the range of 2.774(8)–2.794(7) Å and 2.759(7)–2.772(9) Å, respectively. The U1–centroid distances are 2.489(4) Å and 2.517(4) Å to the Cp* and Fv^{tttt} ligands, respectively. The metallocene angle is significantly bent to 137.45(11)° due to the μ -bridging iodide ligands, with U–I1 and U–I2 distances of 3.153(1) and 3.265(1) Å.

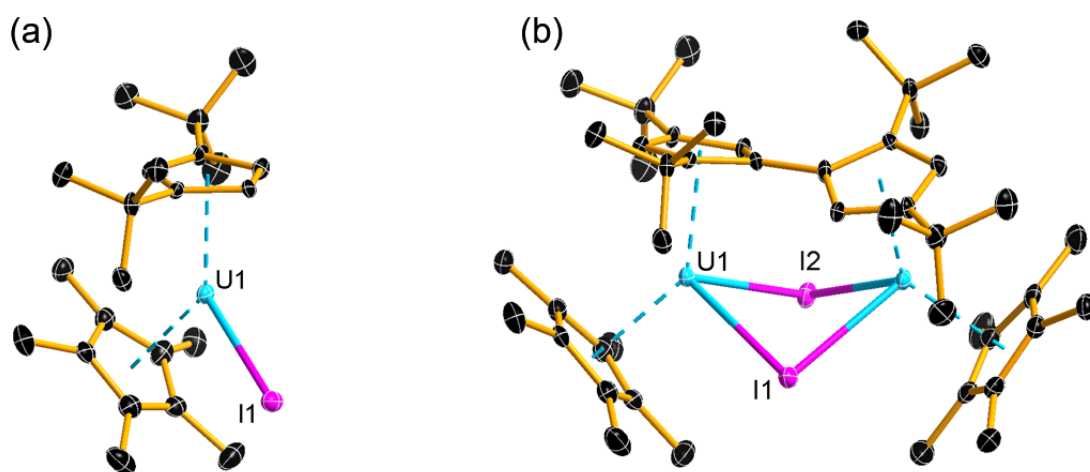


Figure 5.3 Thermal ellipsoid representation (30 % possibility) of molecular structures of the minimum unit cell of **5.1** (a) and the molecular structure of **5.1** after growing (b).

5.3.2 Crystal Structure of $\{[U^{III/IV}(\eta^5-Cp^*)(\mu-I)]_2(\eta^5-\eta^5-Fv^{tttt})\}[B(C_6F_5)_4]$ (**5.2**)

After one of the U^{3+} ions in **5.1** was oxidized to U^{4+} , the geometric parameters around the two uranium ions change for **5.2** (Table 5.2). Overall, however, the qualitative geometries of both uranium atoms are similar to those found in **5.1**.

Table 5.2 Selected bond lengths (Å) and angles (°) for **5.2** based on the data collection with the parameters mentioned in the main text.

U–C(Fv ^{tttt})	U1–C11: 2.688(40)	U2–C24: 2.716(40)
	U1–C12: 2.735(40)	U2–C25: 2.693(40)
	U1–C13: 2.710(40)	U2–C26: 2.705(30)
	U1–C14: 2.815(30)	U2–C27: 2.794(40)
	U1–C15: 2.757(20)	U2–C28: 2.735(40)
U–C(Cp*)	U1–C1: 2.734(30)	U2–C37: 2.741(50)
	U1–C2: 2.737(40)	U2–C38: 2.705(40)
	U1–C3: 2.761(40)	U2–C39: 2.663(40)
	U1–C4: 2.652(40)	U2–C40: 2.762(40)
	U1–C5: 2.705(40)	U2–C41: 2.731(40)
U–Cp _c (Fv ^{tttt} centroid)	U1–Cp _c : 2.441(1)	U2–Cp _c : 2.443(1)
U–Cp _c (Cp* centroid)	U1–Cp _c : 2.445(1)	U2–Cp _c : 2.440(1)
U1…U2	U1–U2: 4.082(1)	
U–I	U1–I1: 3.021(3)	U2–I1: 3.223(3)
	U1–I2: 3.138(3)	U2–I2: 3.106(3)
Cp(Fv ^{tttt})–U–Cp(Cp*)	U1: 134.87(5)	U2: 135.80(4)

The bond length range is 2.652(40)–2.761(40) Å for U1–C(Cp*) and 2.688(40)–2.815(30) Å for U1–C (Fv^{tttt}). For U2, the differences in the corresponding bond lengths are not statistically significant. Compared to **5.1**, the distance between uranium ions and Cp*centroids is shorter for U1 (2.441(1) Å) and U2 (2.443 (1) Å), as is the distance of U–Fv^{tttt} (centroid) of 2.445(1) Å and 2.440 (1) Å for U1 and U2, respectively. As the length of U–I shortens for U1 to 3.021(3) and 3.138(3) Å and to 3.223(3) and 3.106(3)

Å for U2, the distance between the uranium ions decreases to 4.082(1) Å. Furthermore, stronger bending takes place for the metallocene angles of 134.87(5) and 135.80(4)° for U1 and U2. The $[\text{B}(\text{C}_6\text{F}_5)_4]^-$ anion does not coordinate to either uranium centre. Overall, the reduction in the bond lengths in **5.2** as compared to **5.1** are consistent with oxidation of a uranium centre.

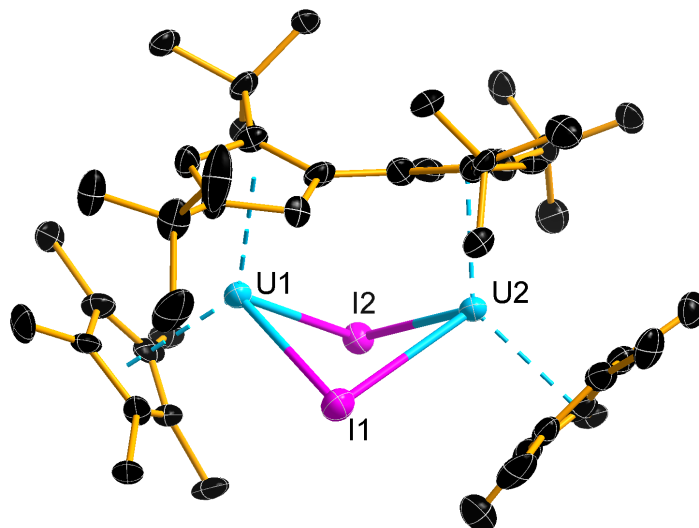


Figure 5.4 Thermal ellipsoid representation (30 % possibility) of molecular structures of the cation **5.2**.

Both single-crystal structures of the di-uranocenium compounds **5.1** and **[5.2][B(C₆F₅)₄]** are well characterized with the full data collection by X-ray diffraction. However, for **5.1**, the CHN element analysis is needed for further determination of the purity; for **[5.2][B(C₆F₅)₄]**, the purification condition should be optimized. In light of this condition, as the time is limited for this Ph.D. project and the unexpected lockdown because of Covid-19 issue, the SQUID measurement cannot be undertaken in this thesis.

5.4 Conclusions and Future Work

In summary, the fulvalenyl ligand Fv^{tttt} was used to synthesize two novel double-uranocene complexes. Compound **5.1** consists of a di-uranium(III) core with the metals bridged by two iodide ligands. An unexpected one-electron oxidation reaction of **5.1** with the electrophile $[(Et_3Si)_2H][B(C_6F_5)_4]$ yielded the corresponding mixed-valence uranium(III)–uranium(IV) complex **5.2** as the salt of $[B(C_6F_5)_4]^-$. The geometric parameters around the uranium centres in **5.2** are shorter than those in **5.1**, consistent with an overall increase in the oxidation state of one metal centre. The NMR spectra of **5.1** and $[5.2][B(C_6F_5)_4]$ are consistent with the solid-state structures, while the $[5.2][B(C_6F_5)_4]$ complex requires a further process for purification.

Time constraints have meant that it was not possible to perform detailed magnetic measurements on either of the uranium compounds described in this chapter. These experiments will form part of the future work.

Chapter 6. General Conclusions

The PhD project aimed to study the magnetic behaviour of bridged polynuclear lanthanide complexes based on the platform of fulvalene and single-ion dysprosium metallocenium complex based on phosphole ligands, in order to discover new strategy to develop high-quality SMMs.

In Chapter 1, the basic knowledge of lanthanide and lanthanide ions are detailed. A brief introduction about the development history of single-molecule magnet demonstrates the revolution of theoretical models and synthetic strategies at different times for SMMs.

In Chapter 2, the fulvalenyl ligand of Fv^{tttt} ($[1,1',3,3'-(C_5^tBu_2H_2)_2]^{2-}$) is adopted to synthesize distinct bridged structure. Seven novel bridged structures i.e., **2.4**, **2.5**, **2.6**, **2.7**, **2.8**, **2.9** and **2.10** are determined with X-Ray diffraction. The further magnetic characterization of compound **2.6_{Dy}**, **2.7**, **2.9_{Dy}** and **2.10** shows the step-wise improvement of their effective energy barriers ($154(15)$ – $384(18)$ cm^{-1}) *via* reducing the effect of the equatorial ligand-field, which creates the stronger axial crystal-field afforded by the cyclopentadienyl units. According to the experimental data and theoretical calculation, the bridged compound **2.9_{Dy}** shows a positive effect to suppress the quantum tunnelling (QTM), which indicates a huge potential for developing high performance SMMs based on the polynuclear lanthanide sandwich structures.

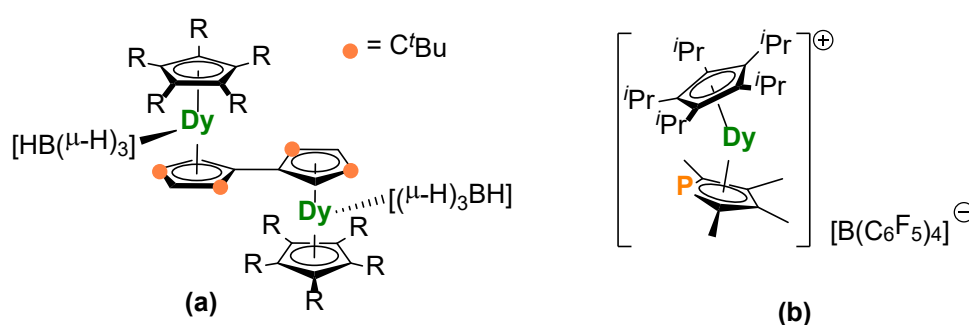
In Chapter 3, two samples of bridged tri-dysprosocenium SMMs based on fulvalenyl and Cp* ligands are reported i.e., **3.1** and **3.2**. The reagents of $nBuLi$, PMe_3 and $[(Et_3Si)_2H][B(C_6F_5)_4]$ are applied to react with the bridging borohydride ligands, which makes the unusual bridged tri-dysprosium clusters. The improvement of energy barrier for **3.2** again proves the significant positive impact from removing the transverse ligand-field. For both samples, the tri-dysprosium system shows an obvious suppression function for the QTM process according to the magnetic measurement, which illustrates the addition of lanthanide centres might enhance the blocking effect for quantum tunnelling.

In Chapter 4, a dysprosocenium-based single-ion magnet [**4.7**] $[B(C_6F_5)_4]$ is successfully synthesized with a combination of Cp* and Cp^{Et4P} ligands, which is well characterized

by XRD and magnetic measurement. The compound **[4.7]** $[\text{B}(\text{C}_6\text{F}_5)_4]$ displays an excellent blocking temperature of 70 K and two separate effective energy barrier of 1410 cm^{-1} and 747 cm^{-1} due to two distinct Orbach processes appearing at high temperature.

In Chapter 5, the fulvalenyl ligand is associated with the uranium(III) ions, which gives a similar di-nuclear compound **5.1** with double bridging iodide atoms between two uranium ions. Different from the single Dy–Cl,¹¹ Dy–I,¹³² Dy– $(\mu\text{-H})_3\text{BH}$,⁵ or U–I,¹⁵³ the double U–I bonds cannot directly severed with the electrophile $[(\text{Et}_3\text{Si})_2\text{H}][\text{B}(\text{C}_6\text{F}_5)_4]$, but with one of the U^{3+} oxidized to U^{4+} , which yields the ion-pair of **[5.2]** $[\text{B}(\text{C}_6\text{F}_5)_4]$. The crystal structures for both compounds above are well collected.

Apart from the continuous work in progress, a series of future research can be proposed based on current result. For example, the dysprosium ions of compound **[2.8]** $[\text{B}(\text{C}_6\text{F}_5)_4]$ takes a coordination from the fluorine atoms, which indicates the less-steric effect of the Fv^{tttt} ligand. Hence, it should be considered to apply much bulky substituent group, increasing the steric hindrance. Furthermore, for compound **2.9**, it will be interesting to replace the Cp^* with other bulky cyclopentadienyl ligands, which possibly yields a single bridging borohydride for each Dy ion (Scheme 6.1a).



Scheme 6.1 Proposed structures for future work.

For compound **[4.7]** $[\text{B}(\text{C}_6\text{F}_5)_4]$, the distance of Dy– Cp^{Et4P} is much longer than that of Dy– Cp^{iPr5} for $[\text{Cp}^*\text{DyCp}^{\text{iPr5}}][\text{B}(\text{C}_6\text{F}_5)_4]$, which gives a negative effect to both of energy

barrier and blocking temperature. Thus, the less-bulky phospholide ligand such as $\text{Cp}^{\text{Me}_4\text{P}}$ (tetramethyl-phospholide) might help reduce the distance (Scheme 6.1b). In addition, the multiply-phospholyl ligands, as a stronger electron-donor, should be employed, such as the mentioned structure $[\text{Dy}(\eta^5\text{-1,2,4-}^t\text{Bu}_3\text{C}_3\text{P}_2)_2]^+$.¹⁵⁶

Chapter 7. Experimental Section

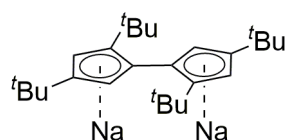
7.1 Chemical Synthesis

7.1.1 General Synthetic Procedures

All reactions were carried out under rigorous anaerobic and anhydrous conditions using argon or nitrogen atmospheres and standard Schlenk or glove-box techniques. Solvents were refluxed over an appropriate drying agent for a minimum of three days (molten potassium for toluene, THF, benzene-D₆, Na/K alloy for hexane) before being distilled, de-gassed and stored in ampoules over activated 4 Å molecular sieves. Glass-coated stirrer bars were used for each reaction. Elemental analyses were carried out at MEDAC Ltd. (Surrey, UK), Mikroanalytisches Labor Pascher Ltd. (Germany) or London Metropolitan University, U.K. IR spectra were collected on a Bruker Alpha FTIR spectrometer fitted with a Platinum ATR module. NMR spectra were acquired on a Varian VNMR S400 spectrometer operating at 400 MHz. [Dy(BH₄)₃(THF)₃]¹⁶⁵ and [(Et₃Si)₂(μ-H)][B(C₆F₅)₄]¹⁶⁶ were prepared according to literature procedures.

7.1.2 Synthesis for Chapter 2

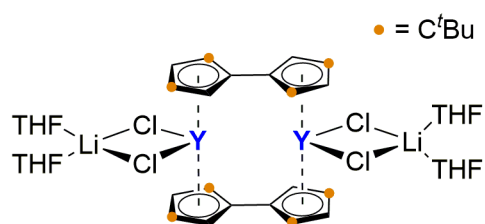
1) 1,1',3,3'-tetra-*tert*-butyl-Pentafulvalene: Na₂Fv^{tttt} (2.3)



Compound **2.3** was synthesized using a modified version of the reported methods by Andersen and Vollhardt *et al.*^{167, 168} : Specifically, potassium hydroxide (1.00 kg, 25.00 mol) was slowly dissolved in 750 mL water in a 3 L round bottom flask containing a PTFE-coated stir bar. After the solution cooled to room temperature, Adogen 464 (5 g, 15.4 mmol) was added, followed by freshly cracked cyclopentadiene (100 mL, 1.2 mol). The mixed solution was then stirred vigorously at 60 °C, followed by dropwise addition of *tert*-butyl bromide (Me₃CBr) (300 mL, 2.7 mol). The reaction was stirred overnight and additional Me₃CBr was added (50 mL, 0.44 mol). After 24 hours, another 50 mL of Me₃CBr was added with heating, and the reaction was then stirred for 5 days

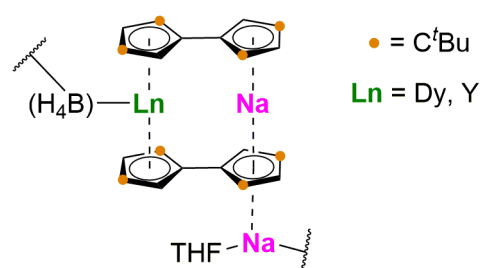
at 60 °C. After cooling to room temperature, the organic phase was separated, followed by further extraction of the aqueous phase with hexane (2 × 50 mL). The combined organic phase was dried with anhydrous NaSO₄. A further distillation of the organic phase at a boiling point range of 60–70 °C finally yielded di-1,3-*tert*-butylcyclopentadiene (Me₃C)₂C₅H₄ as a mixture of isomers in the form of a pale-yellow liquid (60.0 g, 0.34 mol, yield: 28%). GC-MS confirmed that no by-products were formed. Afterwards, the di-*tert*-butylcyclopentadiene isomers (10 g, 56 mmol) was dissolved in 40 mL THF in a 200 mL Schlenk flask and cooled to –78 °C, followed by dropwise addition of ⁿBuLi (23 mL, 2.5 M in hexane, 0.17 mol). The cloudy mixture was allowed to slowly warm to room temperature and stirred overnight. The suspension was cooled to 0 °C in ice water and slowly added to anhydrous CuCl₂ (9.00 g, 67 mmol). The mixture was stirred overnight at room temperature and then the solvent was removed under reduced pressure. After the extraction with hexane (3 × 50 mL), the concentrated product was chromatographed through silica column with petroleum ether as the eluent. The obtained orange oil was checked with GC-MS as the pure Fv^{tttt} (1,1',3,3'-tetra-*tert*-butyl-pentafulvalene), with a yield of 27 % (5.6 g, 15.8 mmol). In the following step, toluene (30 ml) was added to a mixture of Fv^{tttt} (3.54 g, 10.0 mmol) and Na{N(SiMe₃)₂}₂ (3.66 g, 20.0 mmol) pre-cooled to 0 °C. Then the reaction was stirred, warmed to room-temperature and then heated to reflux overnight. The toluene was removed under vacuum and the residue washed with hexane (3 × 30 ml). A light-pink powder of Na₂Fv^{tttt} was obtained after filtration (1.75 g, 4.4 mmol, 43 %), which can be isolated and used without further purification.

2) $[\text{Fv}^{\text{tttt}}\text{YCl}_2\text{Li}(\text{THF})_2]_2$ (**2.4**)



The of $\text{Na}_2\text{Fv}^{\text{tttt}}$ (**2.3**) powder (398 mg, 1 mmol) was mixed with $\text{YCl}_3\text{THF}_{3.5}$ (444 mg, 1 mmol) in a 100 mL ampule flask, followed by addition of 10 mL THF. The mixture was then gently stirred with a glass-coated magnetic bar at room temperature for 24 hours. After removing the solvent under reduced pressure, the residue was extracted with hexane for three times (3×10 mL) and the filtrated solution was concentrated to around 3 mL in a small vial, which was then placed in a freezer at -40 °C. Only trace crystal was observed after several days, which is only enough for single-crystal X-ray diffraction.

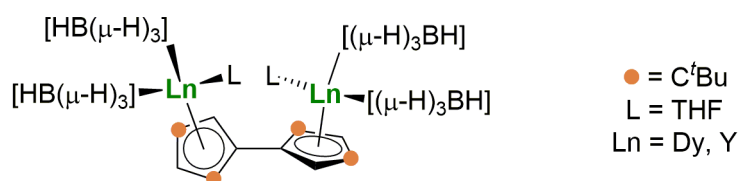
3) $[\text{LnNa}(\text{Fv}^{\text{tttt}})_2\text{Na}(\text{THF})(\text{BH}_4)]$ (Ln = Dy, Y) (**2.5**)



Toluene (10 ml) was added to a mixture of $\text{Na}_2\text{Fv}^{\text{tttt}}$ (**2.3**) (398 mg, 1 mmol) and $[\text{DyCl}_3(\text{THF})_{3.5}]$ (258 mg, 0.5 mmol). The suspension was then gradually heated to reflux at 110 °C and stirred overnight. The solvent was removed and the residue was extracted with toluene three times (3×10 mL). Afterward, removing of toluene under reduced pressure gave an orange powder-like product. The solid was re-dissolved in 5

mL of a solvent mixture (hexane: toluene = 10:1) which gave orange crystals of **2.5_{Dy}** after storing at $-40\text{ }^{\circ}\text{C}$ for 2 days. Isolated yield = 20 mg, 4 %. The yttrium version (**2.5_Y**) was synthesized using an identical procedure, which only yielded trace amounts of crystals.

4) Synthesis of $[\{\text{Ln}(\text{BH}_4)_2(\text{THF})\}_2(\text{Fv}^{\text{tttt}})]$ (Ln = Dy, Y) (**2.6**)



a). For **2.6_{Dy}**: Toluene was added to a mixture of $\text{Na}_2\text{Fv}^{\text{tttt}}$ (**2.3**) (1.00 g, 2.5 mmol) and $[\text{Dy}(\text{BH}_4)_3(\text{THF})_3]$ (2.21 g, 5.3 mmol) at room temperature and the resulting suspension was stirred at $110\text{ }^{\circ}\text{C}$ for 48 hours. The solution colour changed from dark brown to pale orange/yellow. The solvent was removed under vacuum and the product was extracted into hexane ($3 \times 15\text{ ml}$) and filtered. The solvent was removed slowly under vacuum until a crystal-like precipitate formed. Storage at $-40\text{ }^{\circ}\text{C}$ for two days produced pale-yellow crystals of **2.6_{Dy}**. The crystals were washed with cold hexane, re-dissolved in warm hexane and stored at $-40\text{ }^{\circ}\text{C}$, which produced crystals of suitable quality for analysis by single-crystal X-ray diffraction. Isolated yield = 600 mg, 27 %.

Elemental analysis found (calcd.) % for $\text{C}_{34}\text{H}_{72}\text{B}_4\text{O}_2\text{Dy}_2$: C 46.14 (46.34); H 8.03 (8.24).

IR spectrum ($\tilde{\nu}/\text{cm}^{-1}$): 2956s, 2949s, 2899m, 2865w, 2467s, 2244w, 2206w, 2197m, 2127s, 1679w, 1463m, 1393w, 1359m, 1312w, 1238m, 1176s, 1097s, 1056w, 1041w, 1006s, 953m, 925m, 852s, 730w, 702m, 677m, 612w, 572w, 556w, 509w, 434m.

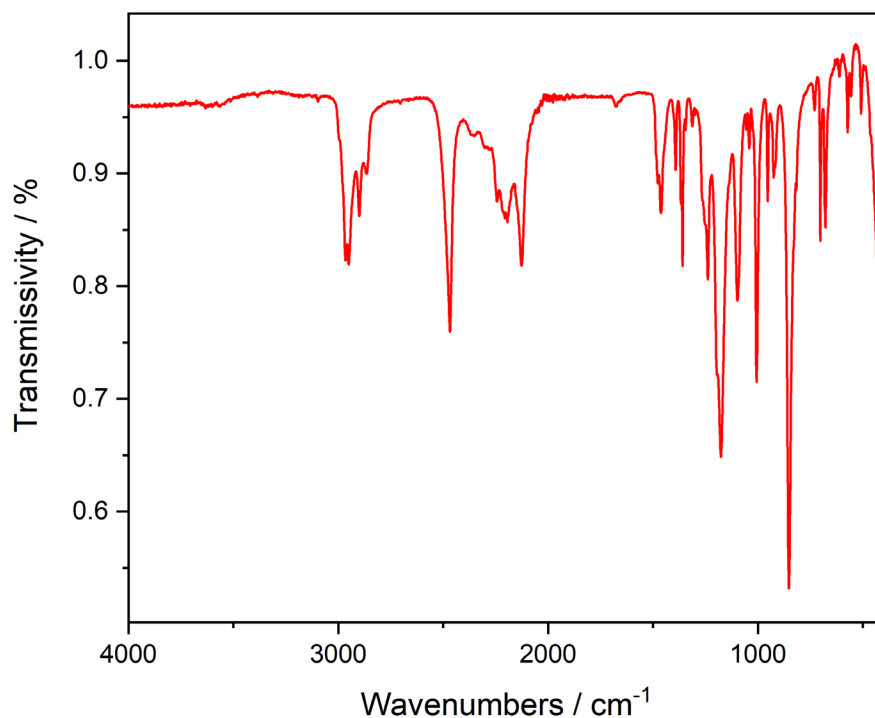


Figure 7.1 Infrared spectrum of compound **2.6_{Dy}**.

b) For **2.6_v**: Compound **2.6_v** was synthesized following the same procedure of compound **2.6_{Dy}**, using $\text{Na}_2\text{Fv}^{\text{tttt}}$ (**2.3**) (1.00 g, 2.5 mmol) and $[\text{Y}(\text{BH}_4)_3(\text{THF})_3]$ (1.83 g, 5.3 mmol). Isolated yield = 531 mg, 29 % of pale-yellow crystals. ^1H NMR (δ/ppm , benzene- D_6): 7.04 (d, $J = 3.1$ Hz, 2H), 6.51 (d, $J = 3.1$ Hz, 2H), 3.83 (s, 8H), 1.39 (s, 18H), 1.28 (s, 18H), 1.11 (s, 8H), 1.73 ~ 0.73 (m, 16H). $^{13}\text{C}\{^1\text{H}\}$ NMR (δ/ppm): 140.91 (d, $J = 1.1$ Hz), 139.42 ((d, $J = 1.1$ Hz), 126.22 (d, $J = 1.1$ Hz), 116.34 (d, $J = 1.1$ Hz), 110.68 (d, $J = 1.1$ Hz), 74.56, 34.18, 33.25, 33.18, 32.04, 24.92. $^{11}\text{B}\{^1\text{H}\}$ NMR (δ/ppm): -22.37.

Elemental analysis found (calcd.) % for $\text{C}_{34}\text{H}_{72}\text{B}_4\text{O}_2\text{Y}_2$: C 54.35 (55.64); H 9.24 (9.89).

IR spectra ($\tilde{\nu}/\text{cm}^{-1}$): 2965s, 2949s, 2899m, 2864w, 2468s, 2251w, 2197m, 2128s, 1674w, 1459m, 1393w, 1359m, 1313w, 1238m, 1177s, 1099s, 1056w, 1041w, 1005s, 954m, 925m, 853s, 728w, 702m, 679m, 613w, 571w, 554w, 507w, 434m.

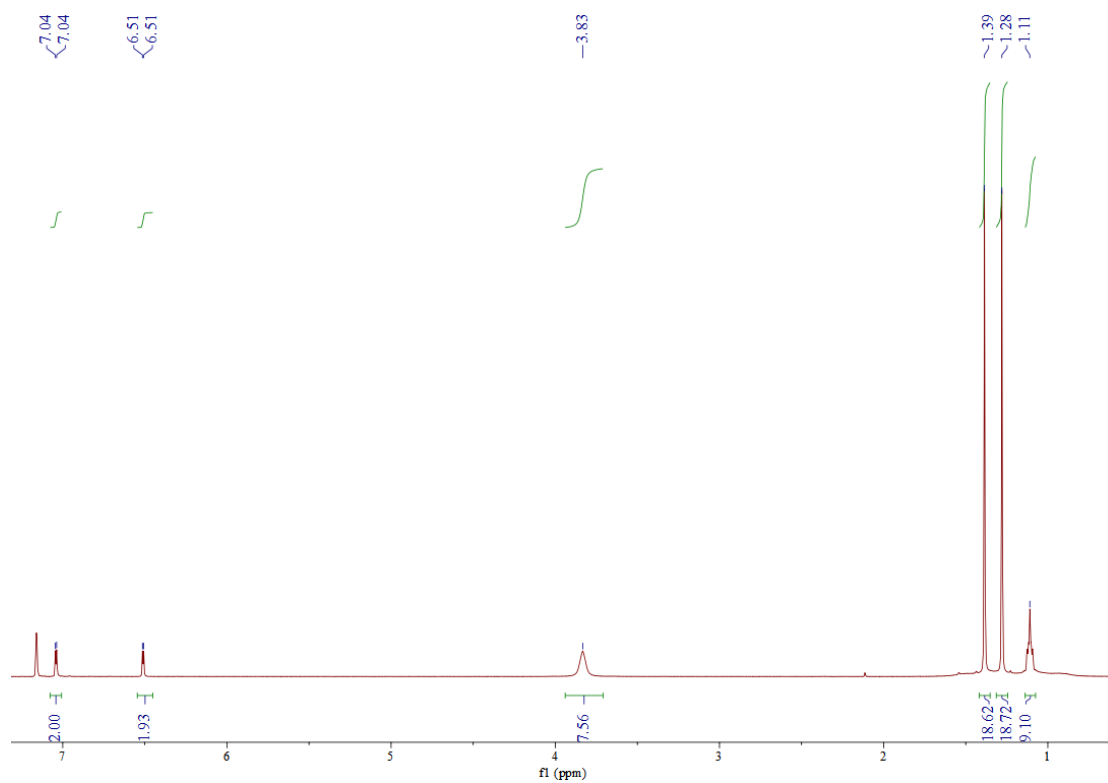


Figure 7.2 ^1H NMR spectrum of **2.6 γ** in D_6 -benzene.

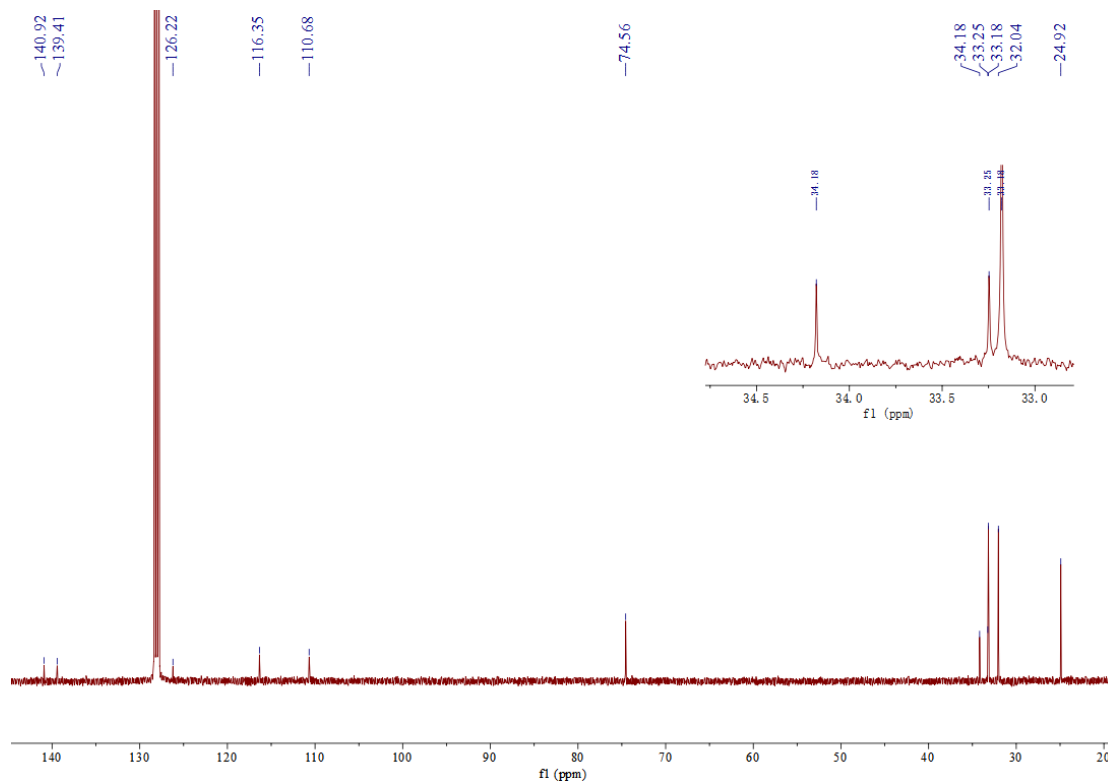


Figure 7.3 ^{13}C NMR spectrum of **2.6 γ** in D_6 -benzene.

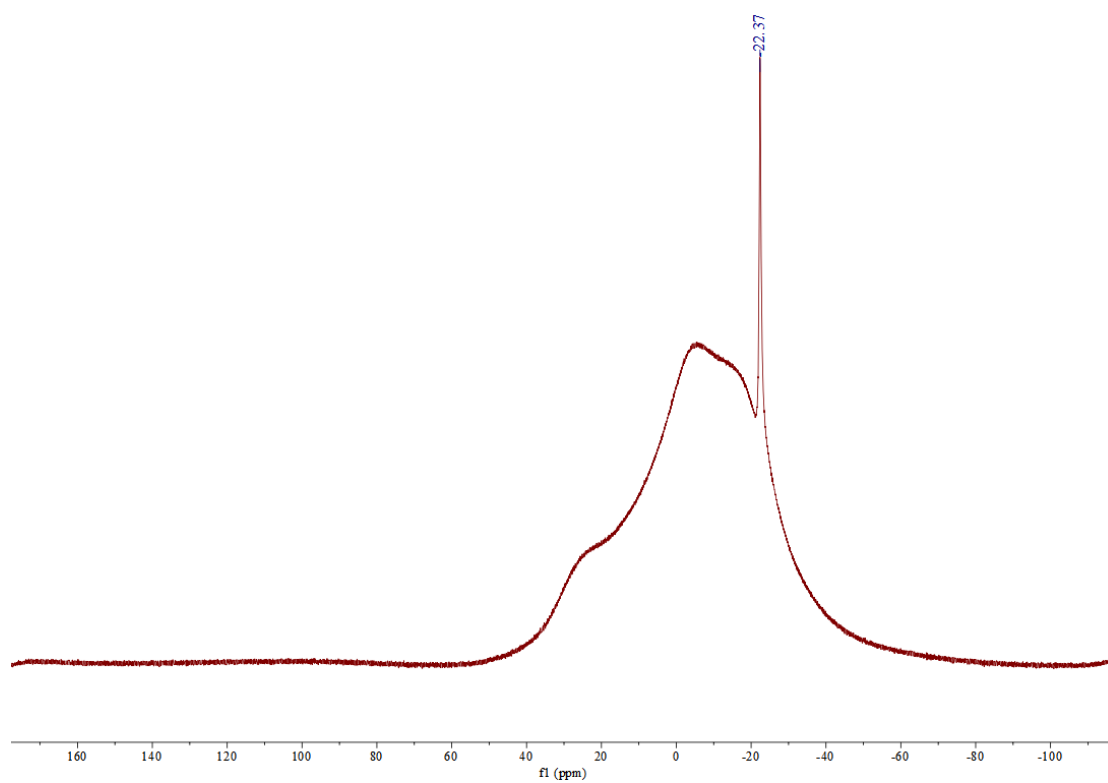


Figure 7.4 ^{11}B NMR spectrum of **2.6v** in D_6 -benzene.

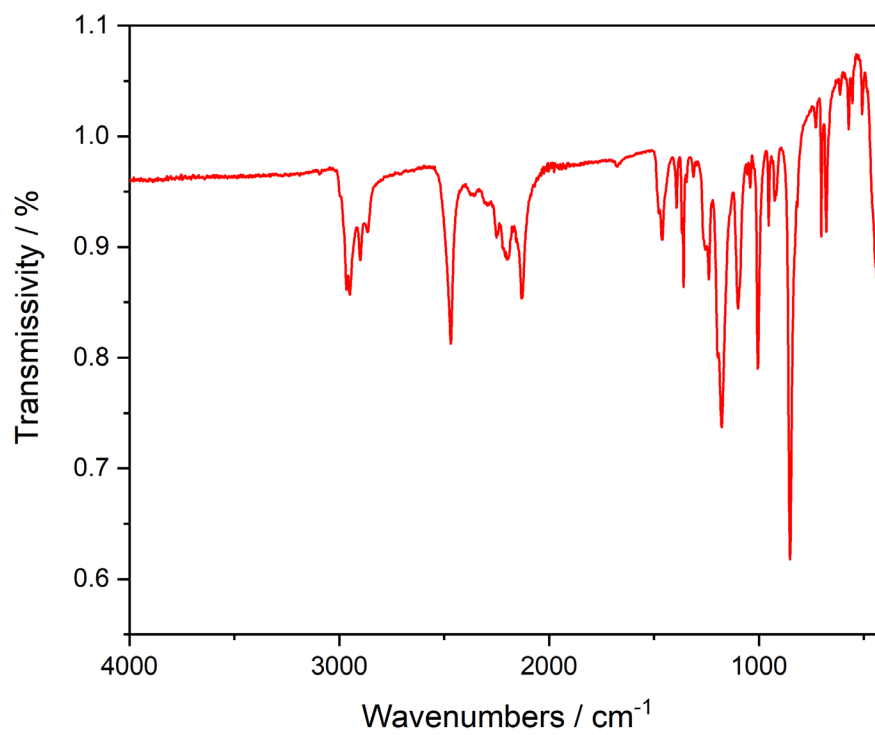
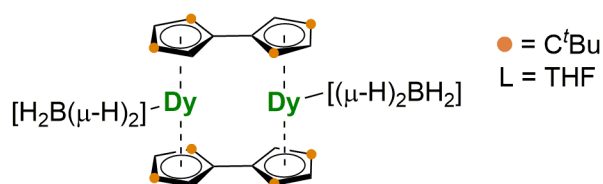


Figure 7.5. Infrared spectrum of compound **2.6v**.

5) Synthesis of $[(\text{BH}_4)\text{DyFv}^{\text{tttt}}]_2$ (**2.7**)



A mixture of $\text{Na}_2\text{Fv}^{\text{tttt}}$ (**2.3**) (1.00 g, 2.5 mmol) and $[(\text{Dy}(\text{BH}_4)_2(\text{THF}))_2(\text{Fv}^{\text{tttt}})]$ (**2.6_{Dy}**) (2.20 g, 2.5 mmol) was refluxed in toluene at 110 °C for 24 hours. Then, the toluene solvent was removed under reduced pressure and the residue was extracted with hexane (3 × 10 mL). after filtration *via* a glass microfiber filter, the yellow solution was slowly concentrated until a crystal-like precipitate formed. Storage at −40 °C overnight produced pale-yellow crystals of **2.7**. The crystals were washed with cold hexane, re-dissolved in warm hexane and stored at −40 °C, which produced crystals of suitable quality for analysis by single-crystal X-ray diffraction. Isolated yield = 100 mg, 3.7 %.

Elemental analysis found (calcd.) % for $\text{C}_{52}\text{H}_{88}\text{B}_2\text{Dy}_2$: C 58.85 (58.93); H 8.50 (8.37).

IR spectra ($\tilde{\nu}/\text{cm}^{-1}$): 2957s, 2903w, 2866m, 2466w, 2412m, 2373w, 2109s, 2128s, 1641w, 1480m, 1462s, 1393m, 1360s, 1311w, 1265w, 1238s, 1196m, 1148w, 1111s, 1084m, 1058w, 1023w, 961s, 927m, 842m, 829s, 791m, 695m, 673s, 612w, 567m, 545s, 511w, 433m.

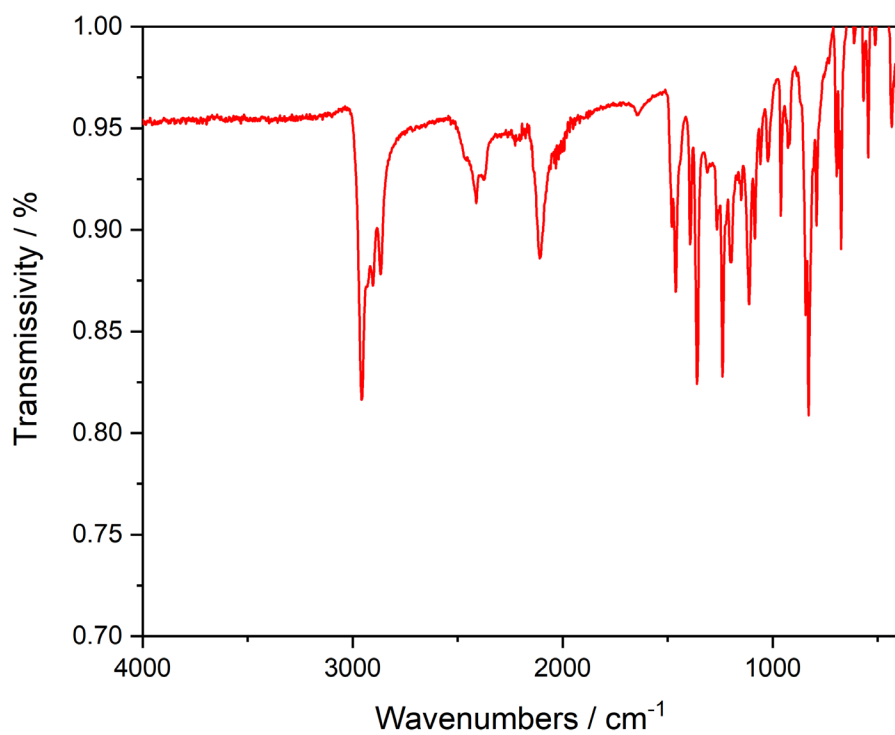
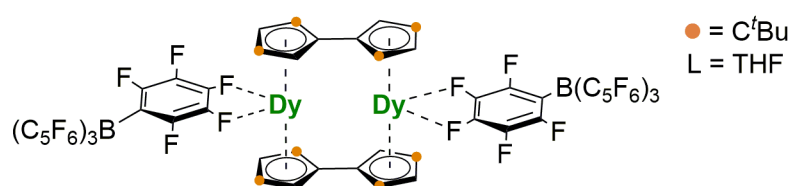


Figure 7.6. Infrared spectrum of compound **2.7**.

6) Synthesis of $[\text{DyFv}^{\text{tttt}}]_2[\text{B}(\text{C}_6\text{F}_5)_4]_2$ (**2.8**)



In a small vial, $[(\text{BH}_4)\text{DyFv}^{\text{tttt}}]_2$ (**2.7**) (50 mg, 0.047 mmol) was dissolved in hexane (10 mL), followed by addition of $[(\text{Et}_3\text{Si})_2(\mu\text{-H})][\text{B}(\text{C}_6\text{F}_5)_4]$ (86 mg, 0.094 mmol). A pale-yellow suspension was gradually formed and stirred for 3 days. After the hexane was removed, the residue was washed with hexane (5×10 ml) and toluene (5×5 ml). The resulting yellow powder was dried under vacuum and then dissolved in the fluorobenzene with a layer of hexane on the top. The bright yellow polycrystalline of **2.8** was obtained after several days. Isolated yield = 98 mg, 89 %.

Elemental analysis found (calcd.) % for $\text{C}_{100}\text{H}_{80}\text{B}_2\text{Dy}_2\text{F}_{40}$: C 50.08 (50.29); H 3.45 (3.38).
IR spectrum ($\tilde{\nu}/\text{cm}^{-1}$): 2935w, 2898m, 2870w, 2260m, 1642m, 1583w, 1511s, 1459s, 1397w, 1365m, 1269m, 1237m, 1194m, 1082s, 1023w, 976s, 839m, 773m, 755s, 741m, 701w, 683s, 660s, 608w, 557m, 557w, 467m.

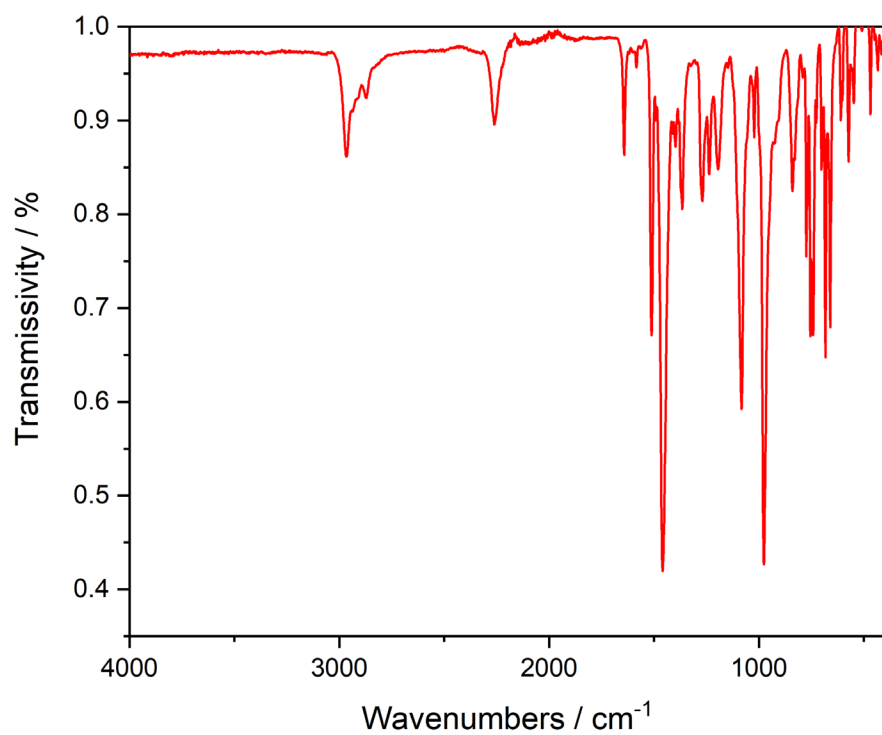
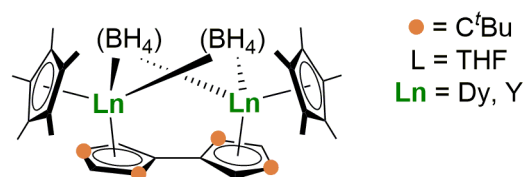


Figure 7.7. Infrared spectrum of compound **2.8**.

7) Synthesis of $[\{\text{Ln}(\text{Cp}^*)(\text{BH}_4)\}_2(\text{Fv}^{\text{tttt}})]$ (Ln = Dy, Y) (2.9)



a) For compound **2.9_{Dy}**: Solid **2.6_{Dy}** (500 mg, 0.6 mmol) was added in portions to a mixture of KCp* (199 mg, 1.1 mmol) and toluene (20 ml) at room temperature. The resulting suspension was refluxed for 48 hours, during which time the solution changed colour from yellow to orange. The toluene was removed under vacuum, and then the product was extracted into hexane (3 × 15 ml) and filtered. The solvent was concentrated slowly under vacuum to the point of incipient crystallization. Storing the resulting solution at $-40\text{ }^\circ\text{C}$ overnight produced colourless crystals of **2.9_{Dy}**, which were re-crystallized to give bright-yellow single crystals of sufficient quality for analysis by X-ray diffraction. Yield = 200 mg, 36 %.

Elemental analysis found (calcd.) % for $\text{C}_{46}\text{H}_{78}\text{B}_2\text{Dy}_2$: C 56.25 (56.51); H 7.69 (8.04).

IR spectrum ($\tilde{\nu}/\text{cm}^{-1}$): 2956s, 2899s, 2861s, 2729w, 2473m, 2407w, 2228s, 2124m, 1608w, 1480w, 1457s, 1389m, 1361s, 1304w, 1265m, 1229s, 1198m, 1149s, 1092s, 1060m, 1022s, 959m, 918m, 850s, 826m, 806s, 697s, 669s, 613w, 594s, 552m, 514w, 432s.

b) For compound **2.9_Y**: The procedure is similar to that described for **2.9_{Dy}**. After a reaction of **2.6_{Dy}** (513 mg, 0.70 mmol) and KCp* (244 mg, 1.40 mmol), **2.9_Y** was obtained with a yield of 236 mg, 40 %. ^1H NMR (δ/ppm , benzene- D_6): 6.81 (d, $J = 2.8$ Hz, 2H), 6.22 (d, $J = 2.8$ Hz, 2H), 2.19 (s, 30H), 1.43 (s, 18H), 1.32 (s, 18H), 0.80 ~ -0.10 (m, 8H). $^{13}\text{C}\{^1\text{H}\}$ NMR (δ/ppm): 134.17 (d, $J = 1.0$ Hz), 134.01 (d, $J = 1.0$ Hz), 123.20 (d, $J = 1.0$ Hz), 122.10 (d, $J = 1.0$ Hz), 120.10 (d, $J = 1.0$ Hz), 108.97 (d, $J = 1.0$ Hz), 33.80, 33.27, 33.06, 32.22, 13.09. $^{11}\text{B}\{^1\text{H}\}$ NMR (δ/ppm): -20.57.

Elemental analysis found (calcd.) % for $\text{C}_{46}\text{H}_{78}\text{B}_2\text{Y}_2$: C 65.94 (66.52); H 9.42 (9.47).

IR spectra (cm^{-1}): 2956s, 2900s, 2863s, 2729w, 2478m, 2407w, 2241s, 2130m, 1612w, 1480w, 1456s, 1391m, 1361s, 1304w, 1265m, 1229s, 1199m, 1149s, 1091s, 1060m, 1022s, 959m, 918m, 850s, 826m, 806s, 697s, 669s, 614w, 596s, 551m, 514w, 434s.

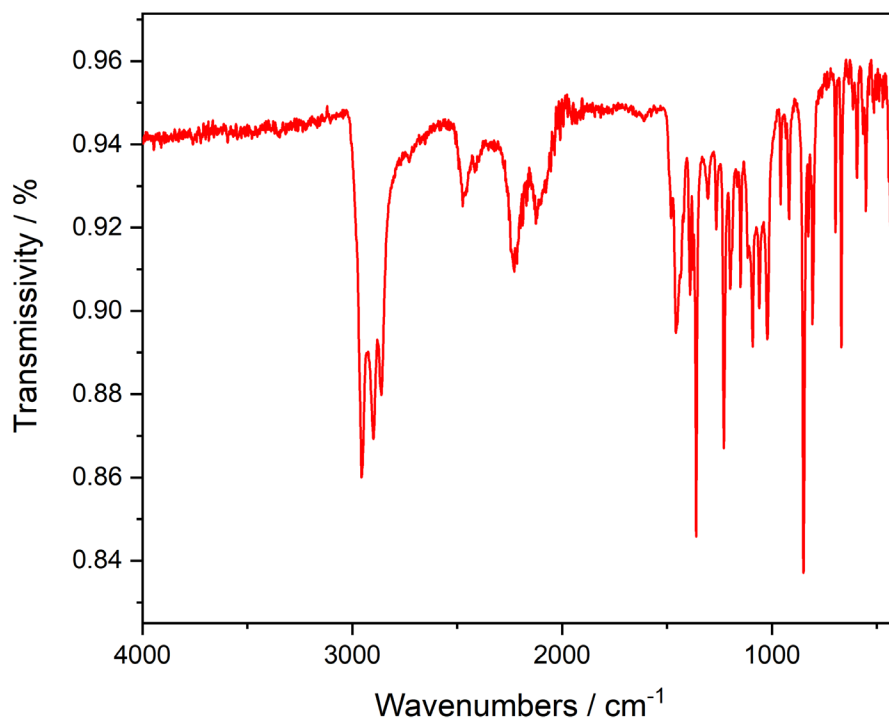


Figure 7.8 Infrared spectrum of compound **2.9_{Dy}**.

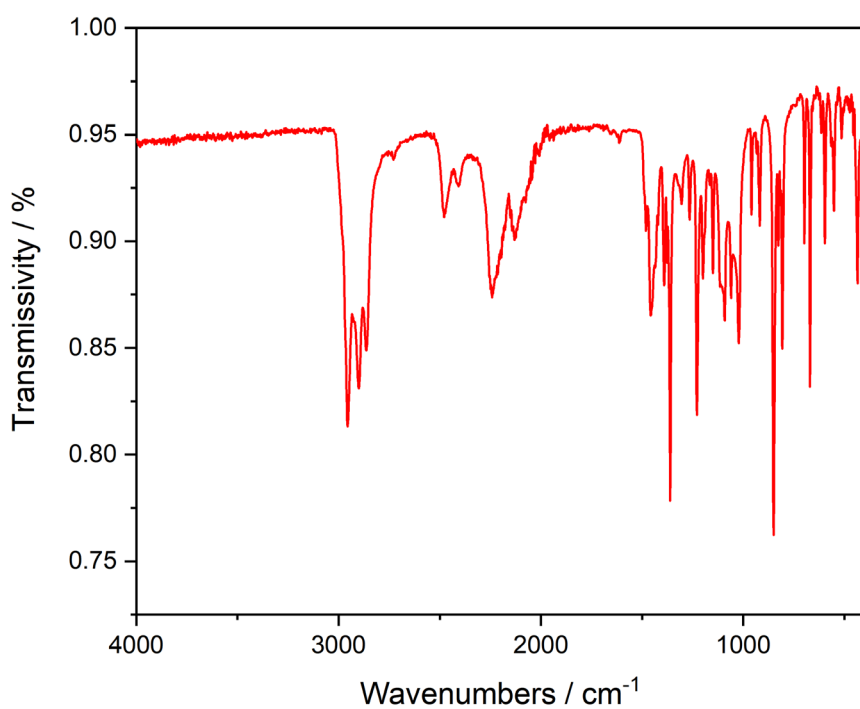


Figure 7.9 Infrared spectrum of compound **2.9v**.

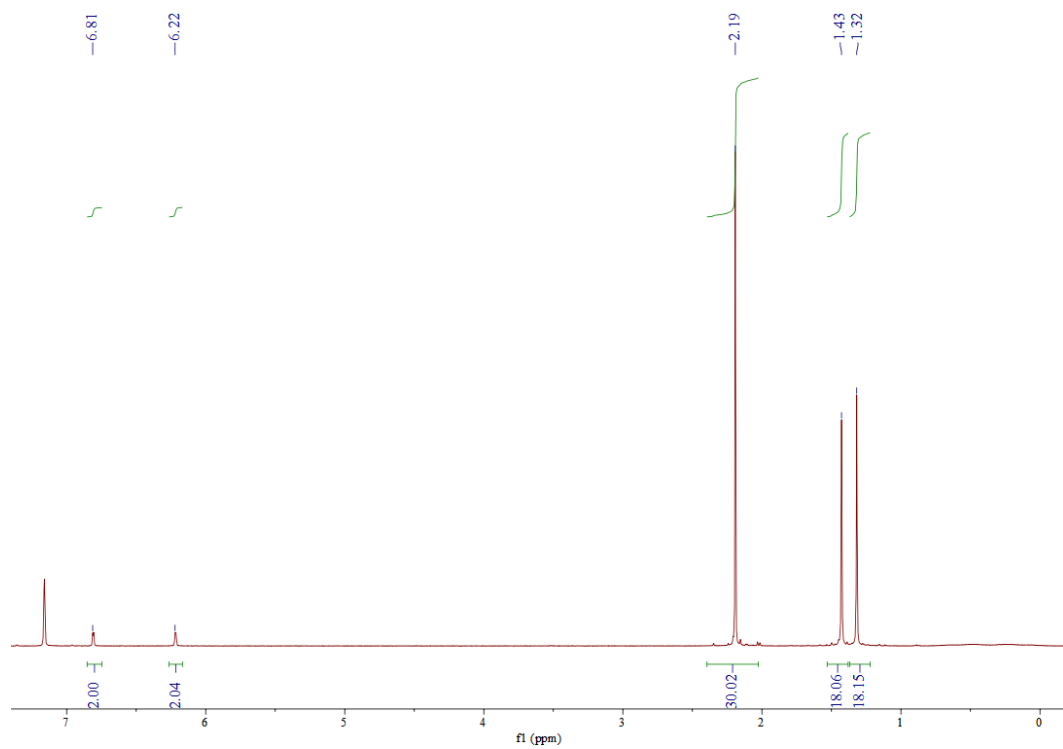


Figure 7.10 ¹H NMR spectrum of **2.9v** in D₆-benzene.

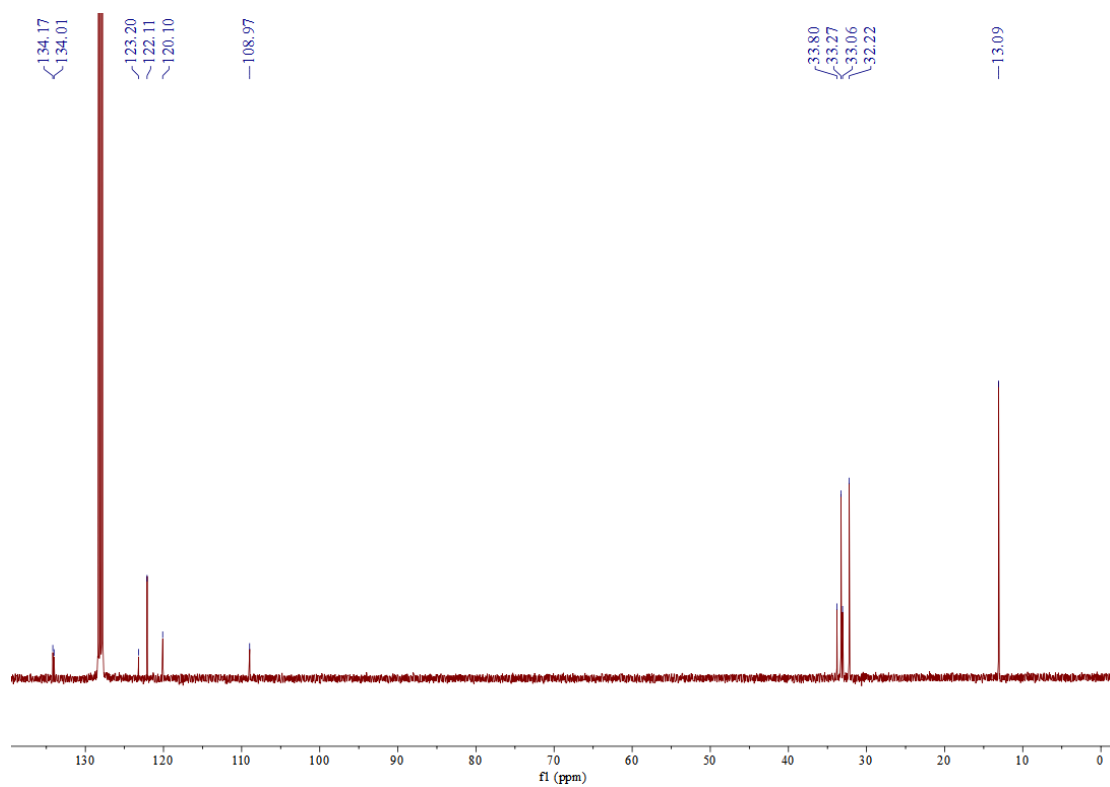


Figure 7.11 ^{13}C NMR spectrum of **2.9 γ** in D_6 -benzene.

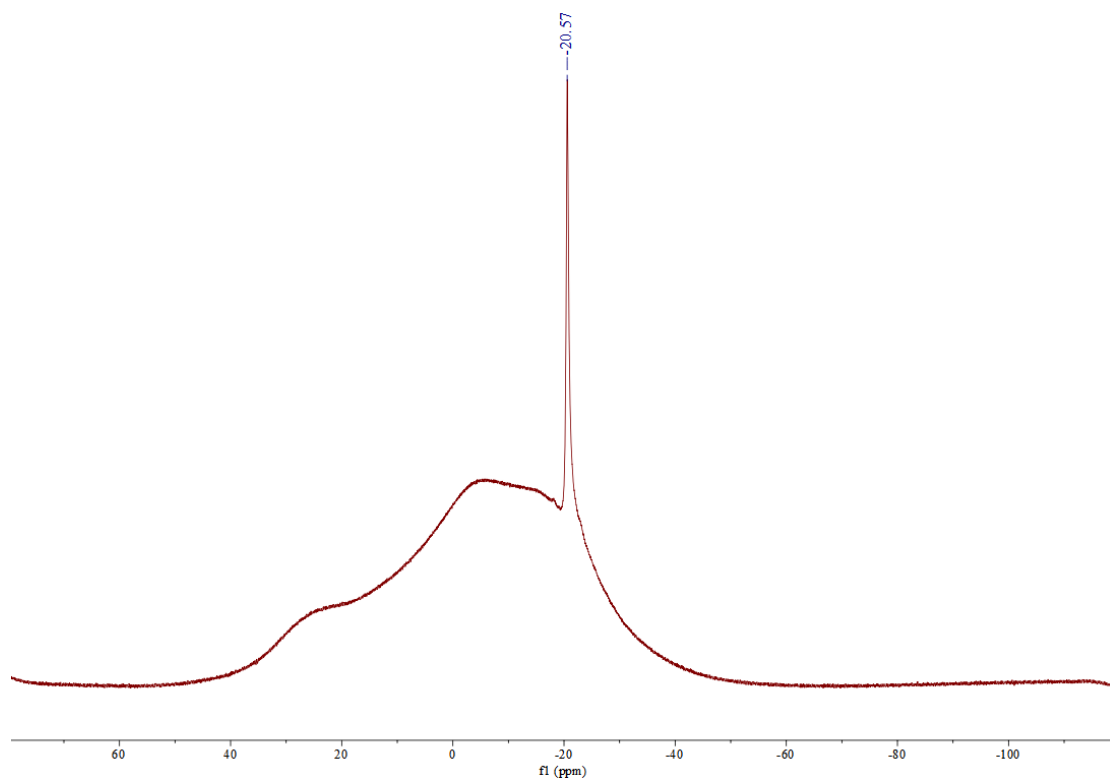
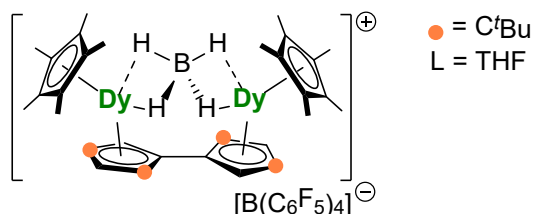


Figure 7.12 ^{11}B NMR spectrum of **2.9 γ** in D_6 -benzene.

8) Synthesis of $[(\text{DyCp}^*)_2(\text{BH}_4) \text{Fv}^{\text{tttt}}][\text{B}(\text{C}_6\text{F}_5)_4] ([2.10] \cdot [\text{B}(\text{C}_6\text{F}_5)_4])$



A solution of **2.9_{Dy}** (205 mg, 0.2 mmol) in hexane (10ml) was added to $[(\text{Et}_3\text{Si})_2(\mu\text{-H})][\text{B}(\text{C}_6\text{F}_5)_4]$ (191 mg, 0.2 mmol) at room temperature, which immediately produced a gel-like material. After stirring for 24 hours, a yellow powder had formed. The hexane was removed, the residue was washed with hexane (5×10 ml) and the resulting yellow powder dried under vacuum. Dissolving the powder in 1,2-dichlorobenzene (5 ml) and layering the solution with hexane at room temperature, produced, after several days, bright yellow crystals. The solvents were then decanted away and the crystals were washed with cold hexane (3×5 ml). The crystallization process was repeated twice in order to obtain single crystals of **2.10** suitable for X-ray diffraction. Yield = 100 mg, 29 %.

Elemental analysis found (calcd.) % for $\text{C}_{70}\text{H}_{74}\text{B}_2\text{F}_{20}\text{Dy}_2$: C 50.09 (51.21); H 4.32 (4.54).

IR spectrum ($\tilde{\nu}/\text{cm}^{-1}$): 2958m, 2929w, 2916w, 2870m, 2230w, 1642m, 1511s, 1462s, 1412w, 1394w, 1382w, 1367w, 1271s, 1236m, 1202w, 1080s, 1028w, 977s, 926w, 906w, 840s, 773s, 756s, 726w, 713w, 682s, 661s, 611m, 572m, 430w.

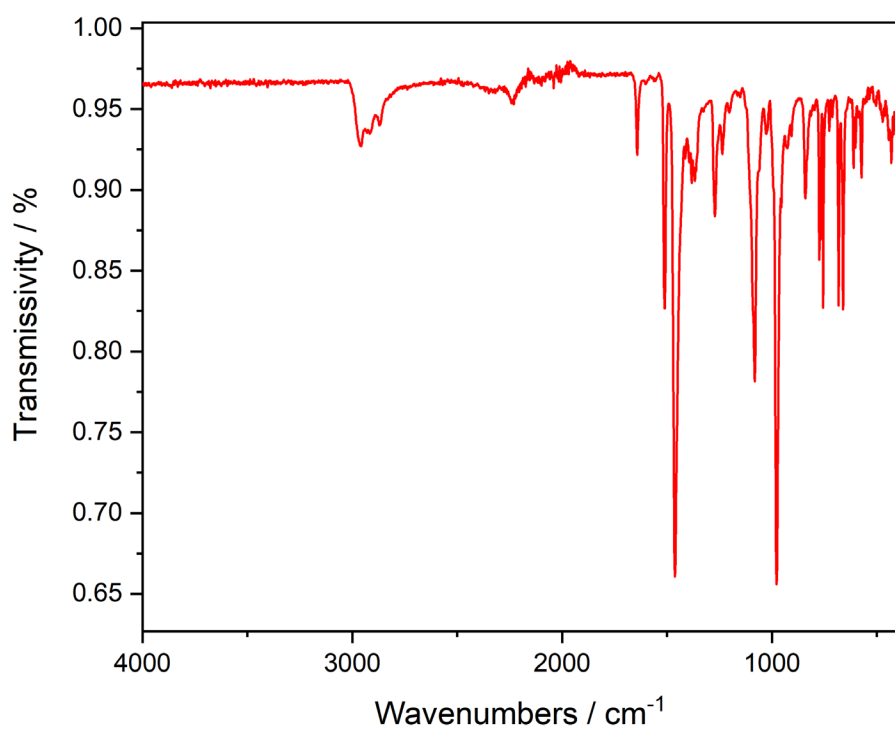
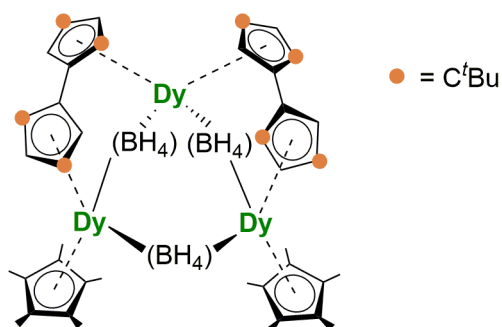


Figure 7.13 Infrared spectrum of compound **2.10**.

7.1.3 Synthesis for Chapter 3

1) Synthesis of $[(\text{BH}_4)\{\text{DyCp}^*(\text{BH}_4)\}_2\text{DyFv}^{\text{tttt}}_2]$ (**3.1**)



$[\{\text{Dy}(\text{Cp}^*)(\mu\text{-BH}_4)\}_2(\text{Fv}^{\text{tttt}})]$ (**2.9_{Dy}**) (300 mg, 0.30 mmol) was dissolved in hexane (20 mL) and cooled to 0 °C for 5 minutes. Then *n*-BuLi solution (243 mL, 2.5 M in hexane, 0.60 mmol) was added dropwise and the resulting suspension was warmed to room temperature, and then stirred overnight, during which time the solution changed colour from yellow to almost colourless. The suspension was filtered and the residue washed with hexane (2 × 10 mL), then filtered and the washings were combined. A light-yellow solution was obtained and the solvent was removed slowly under vacuum until a crystal-like precipitate formed. Storage at −40 °C for two days produced pale-yellow crystals of **3.1**. The crystals were washed with cold hexane, re-dissolved in warm hexane and stored at −40 °C, which produced crystals of suitable quality for analysis by single-crystal X-ray diffraction. Isolated yield = 105 mg, 42 %.

We also find that complex **3.1** can be obtained by using excess of PMe₃ (ca. 1 mL) instead of *n*-BuLi, Isolated yield = 80 mg, 32 %.

Elemental analysis found (calcd.) % for C₇₂H₁₂₂B₃Dy₃·C₆H₁₄ (hexane): C 58.70 (58.78); H 8.55 (8.60).

IR spectrum ($\tilde{\nu}/\text{cm}^{-1}$): 2953s, 2928w, 2901m, 2860m, 2438m, 2263s, 2213m, 1481w, 1459s, 1392m, 1359s, 1304m, 1269w, 1229s, 1199w, 1152w, 1126w, 1111w, 1087s, 1058w, 1023m, 957w, 928w, 858s, 801m, 703m, 672m, 620w, 594w, 571w, 549m, 505w, 430m.

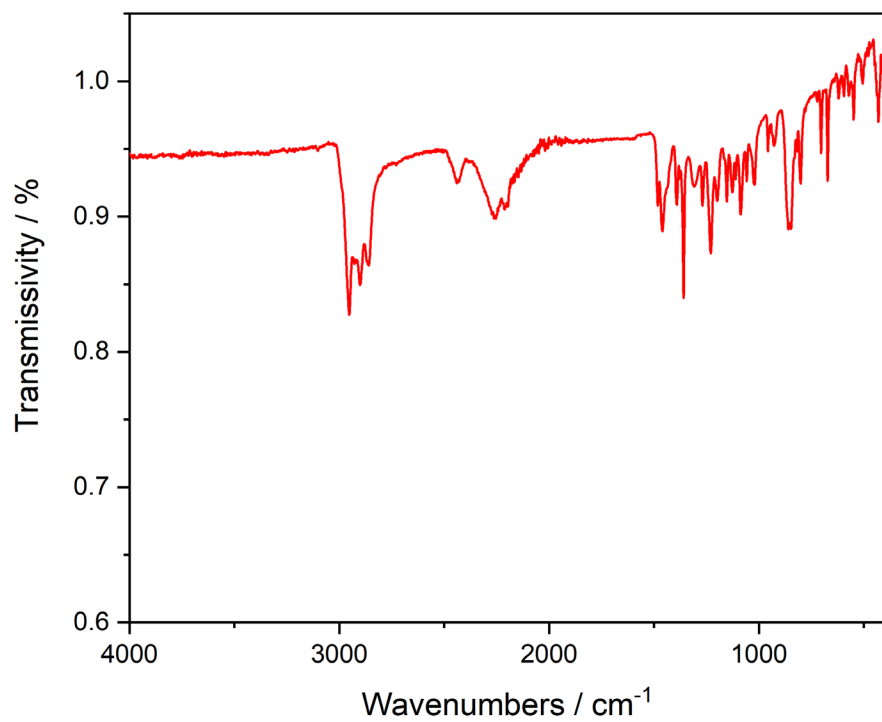
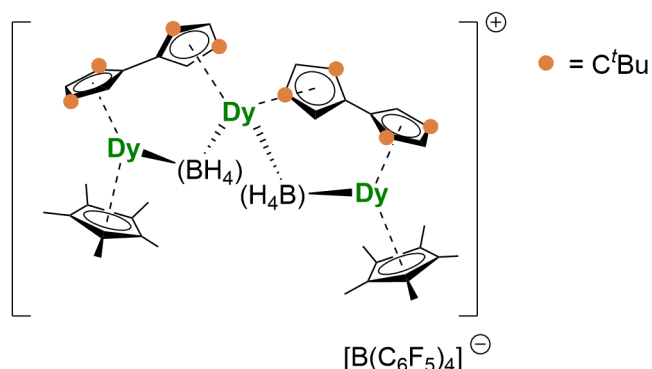


Figure 7.14 Infrared spectrum of compound **3.1**.

2) Synthesis of $[\text{Dy}\{\text{Dy}(\text{Cp}^*)\}_2(\mu\text{-BH}_4)_2(\text{Fv}^{\text{tttt}})_2][\text{B}(\text{C}_6\text{F}_5)_4]$ (**3.2**) $[\text{B}(\text{C}_6\text{F}_5)_4]$)



$[(\text{Et}_3\text{Si})_2(\mu\text{-H})][\text{B}(\text{C}_6\text{F}_5)_4]$ (28 mg, 0.031 mmol) was added to a solution of **3.1** (50 mg, 0.031 mmol) in hexane (10 mL) and the resulting suspension was stirred overnight. A yellow powder formed and then the hexane was removed under vacuum, the residue was washed with hexane (5 \times 10 ml) and the resulting yellow powder dried under vacuum. Dissolving the powder in 1,2-dichlorobenzene (5 ml) and adding a layer of hexane on top produced bright yellow crystals after several days. The solvents were then decanted away and the crystals were washed with hexane (3 \times 5 ml). The crystallization process was repeated twice in order to obtain single crystals of **3.2** suitable for X-ray diffraction. Yield = 20 mg, 28 %.

We also find that complex **3.2** can be obtained by using excess of $[(\text{Et}_3\text{Si})_2(\mu\text{-H})][\text{B}(\text{C}_6\text{F}_5)_4]$ (ca. 184 mg, 0.20 mmol) to react with $\{\text{Dy}(\text{Cp}^*)(\mu\text{-BH}_4)\}_2(\text{Fv}^{\text{tttt}})$ (**2.9_{Dy}**) (99 mg, 0.10 mmol) in hexane. Yield = 46 mg, 42 %.

Elemental analysis found (calcd.) % for $\text{C}_{96}\text{H}_{118}\text{B}_3\text{F}_{20}\text{Dy}_3$: C 52.70 (53.09); H 5.28 (5.48).

IR spectrum ($\tilde{\nu}/\text{cm}^{-1}$): 2961m, 2905w, 2870w, 2470m, 2256m, 2185m, 1643m, 1512s, 1462s, 1393w, 1360m, 1317w, 1269m, 1234m, 1200w, 1083s, 1035m, 979s, 927w, 837s, 774s, 756s, 726w, 707w, 683s, 660s, 610m, 572m, 506w, 476w, 435m.

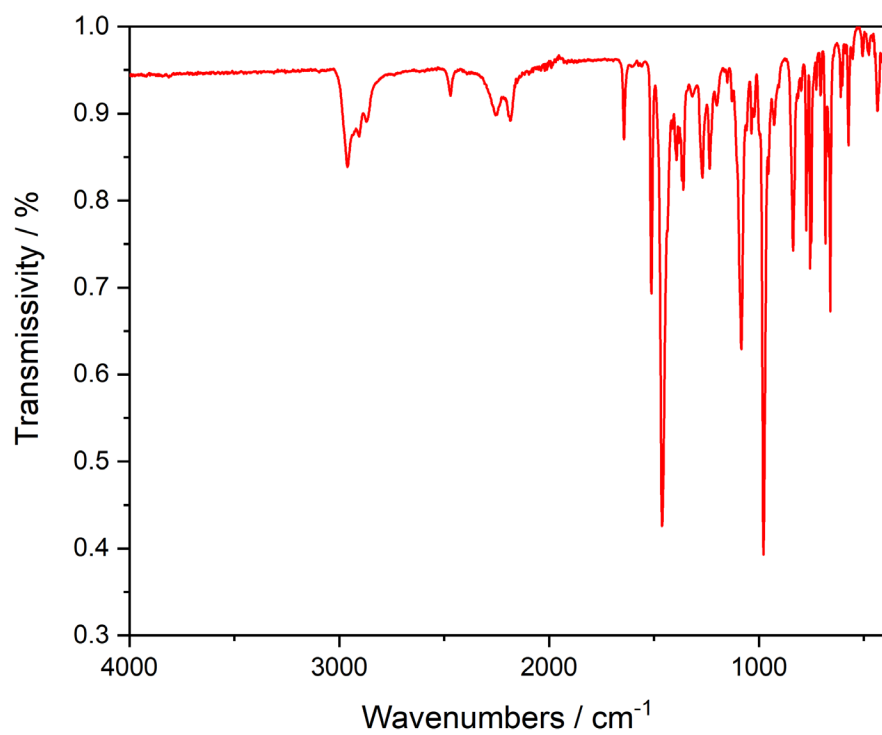
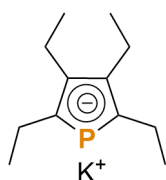


Figure 7.15 Infrared spectrum of compound **3.2**.

7.1.4 Synthesis for Chapter 4

1) Synthesis of potassium tetraethylphospholide: $[\text{K}][\text{Cp}^{\text{Et4P}}]$ (**4.2**)



A solution of tetraethyl-1-chlorophosphole (4.02 g, 17.3 mmol) in THF (100 ml) was added to potassium metal (2.00 g, 51.2 mmol) and a glass coated stirrer bar. The mixture was stirred overnight at room temperature. The resulting orange suspension was filtered through a medium frit and the filtrate was evaporated to dryness under a dynamic vacuum, leaving a pale-yellow powder. The solid was washed with hexane (4 × 10 ml) and dried, yielding $[\text{K}][\text{Cp}^{\text{Et4P}}]$ (**4.2**) as white powder (3.51 g, 86 %). ^1H NMR spectrum (303 K, pyridine- D_5 , δ/ppm) 1.33 (t, 6H, 2 × CH_3 , $^3J = 7.44$ Hz), 1.60 (t, 6H, 2 × CH_3 , $^3J = 7.42$ Hz), 2.80 (q, 4H, 2 × CH_2 , $^3J = 7.44$ Hz), 3.11 (m, 4H, 2 × CH_2 , $^3J = 7.44$ Hz). $^{13}\text{C}\{^1\text{H}\}$ NMR spectrum (303 K, pyridine- D_5 , δ/ppm): 18.32 (s, $\underline{\text{C}}\text{H}_3\text{CH}_2\text{C}_{\text{Ar}}$), 20.52 (d, $\underline{\text{C}}\text{H}_3\text{CH}_2\text{C}_{\text{Ar}}\text{P}$, $^3J = 0.122$ Hz), 22.13 (s, $\underline{\text{C}}\text{H}_2\text{CCP}$), 24.99 (d, $\underline{\text{C}}\text{H}_2\text{CP}$, $^2J = 26.51$ Hz), 131.17 (s, $\underline{\text{C}}-\text{CP}$), 145.52 (d, $\underline{\text{C}}-\text{P}$, $J = 40.25$ Hz). $^{31}\text{P}\{^1\text{H}\}$ NMR spectrum (400 MHz, 303 K, pyridine- D_5 , δ/ppm): 63.6.

IR spectrum ($\tilde{\nu}/\text{cm}^{-1}$): 2948s, 2924s, 2863s, 1456s, 1389m, 1365m, 1313s, 1255w, 1150m, 1093m, 1049m, 1016w, 935w, 895w, 841w, 812w, 769w, 738w, 634w, 616w, 571w, 545w, 507w, 455w, 416s.

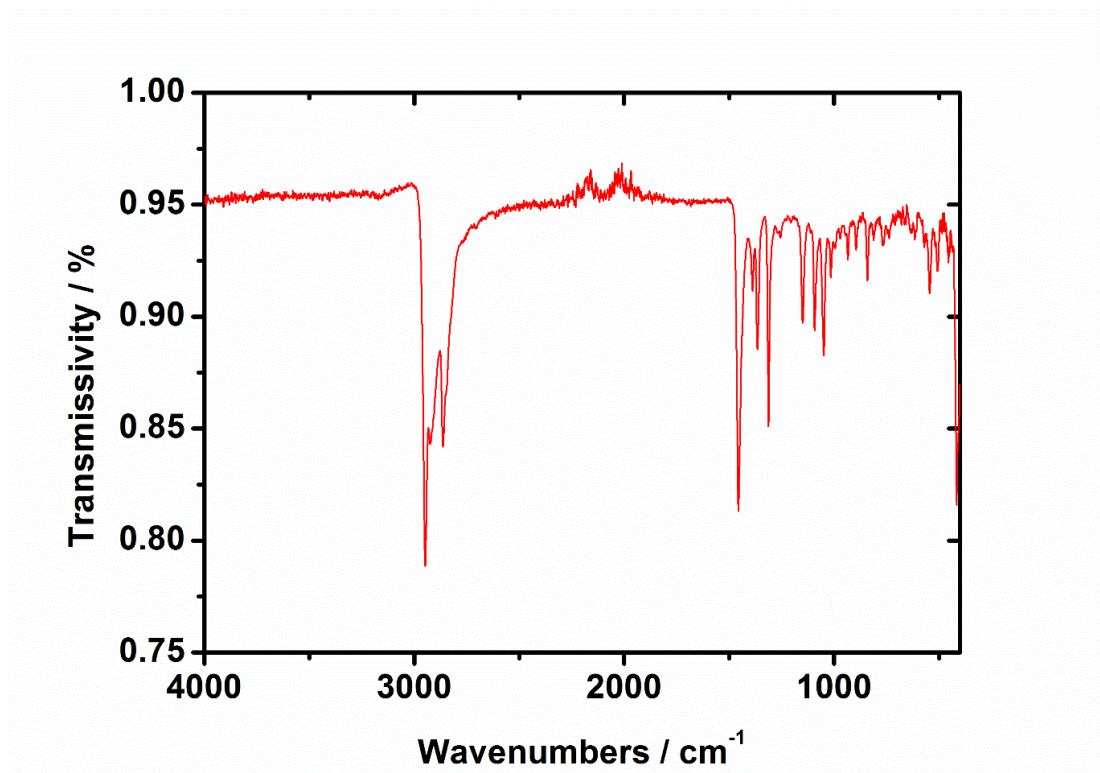


Figure 7.16 Infrared spectrum of compound 4.2.

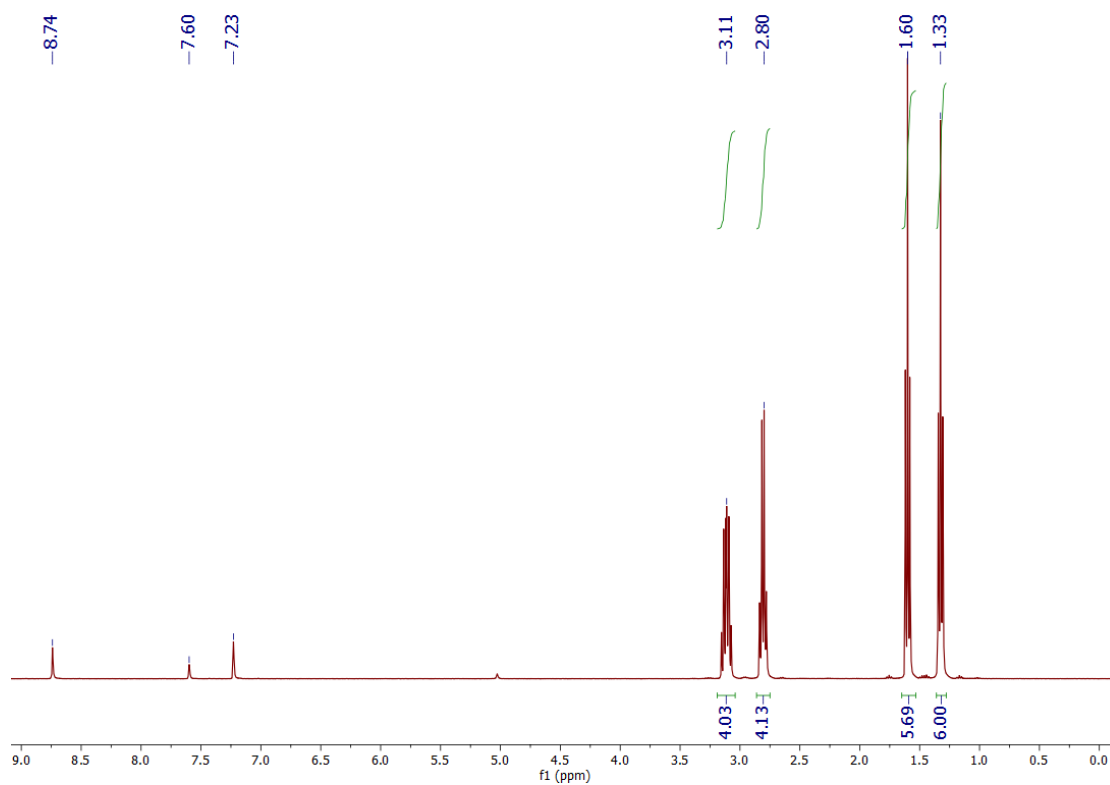


Figure 7.17 ¹H NMR spectrum of 4.2 in pyridine-D₅.

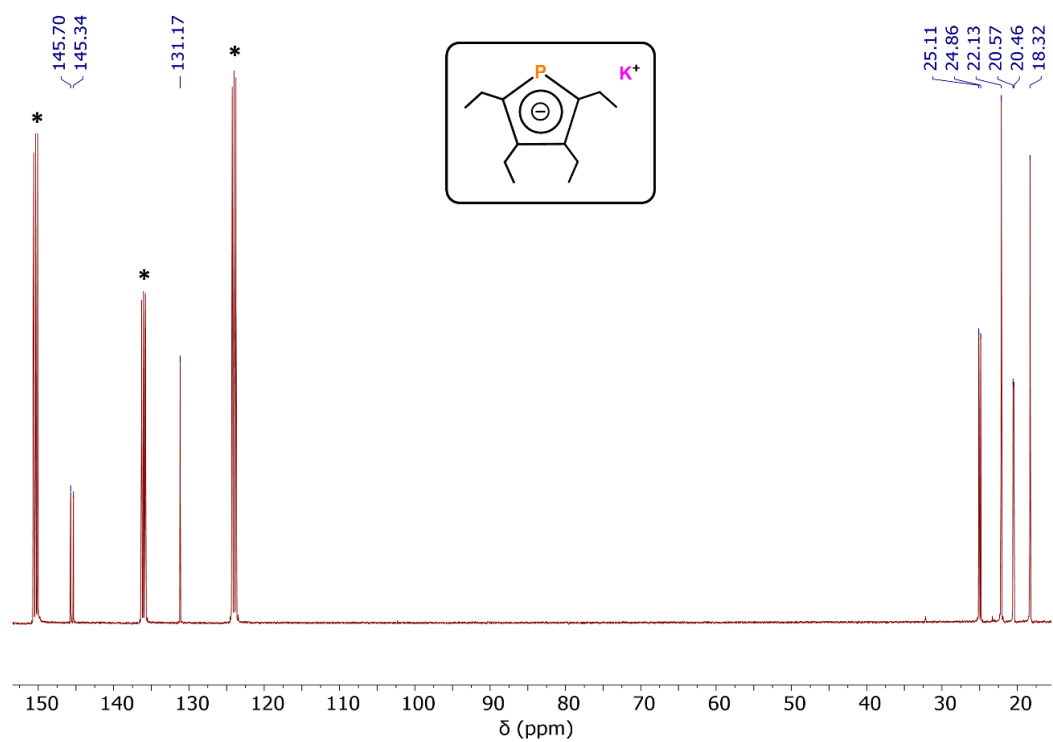


Figure 7.18 ^{13}C NMR spectrum of 4.2 in pyridine- D_5 .

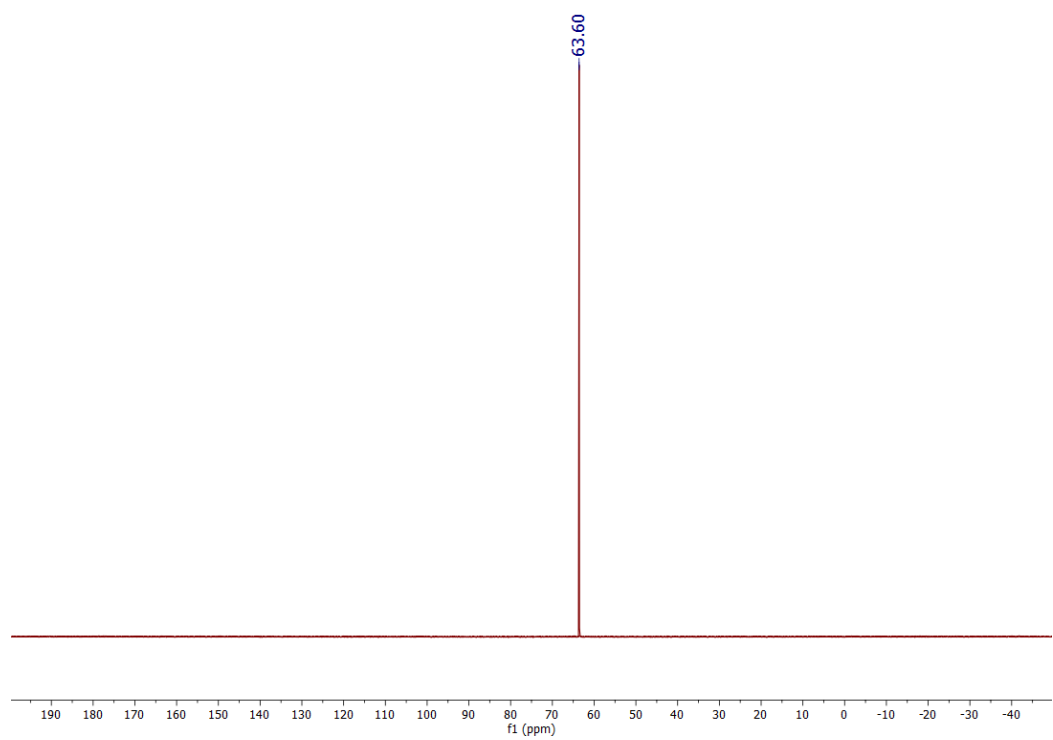
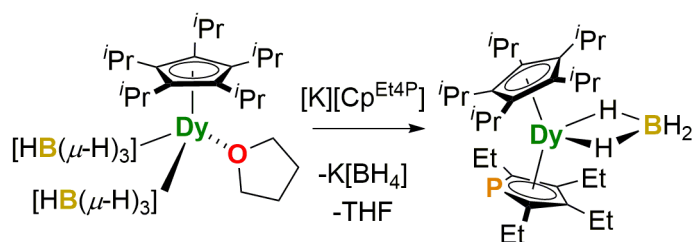


Figure 7.19 ^{31}P NMR spectrum of 4.2 in pyridine- D_5 .

2) Synthesis of $[(\text{Cp}^{i\text{Pr}5})\text{Dy}(\text{Cp}^{\text{Et}4\text{P}})(\text{BH}_4)]$ (**4.6**)



Toluene (15 ml) was added to a solid mixture of $[(\text{Cp}^{i\text{Pr}5})\text{Dy}(\text{BH}_4)_2\text{THF}]$ (532 mg, 1 mmol), $\text{KCP}^{\text{Et}4}$ (234 mg, 1 mmol) and a glass coated stirrer bar, and the resulting suspension was stirred with heating at 110 °C for two days. The toluene was removed under vacuum, and the product was extracted into hexane (5 × 10 mL) and filtered. Removal of the solvent gave a yellow powder, which was recrystallized from hexane at -40 °C to yield yellow crystals of $[(\text{Cp}^{i\text{Pr}5})\text{Dy}(\text{Cp}^{\text{Et}4\text{P}})(\text{BH}_4)]$ (**4.6**). Yield = 350 mg, 54 %.

Elemental analysis found (calc.) for $\text{C}_{32}\text{H}_{59}\text{BDyP}$ (%): C 59.12 (59.30); H 9.43(9.18).

IR spectrum ($\tilde{\nu}/\text{cm}^{-1}$): 2968s, 2926s, 2870s, 2455m, 2398m, 2121m, 2038w, 1451s, 1366s, 1313m, 1291w, 1214w, 1194w, 1159m, 1122s, 1088s, 1056m, 1027w, 973w, 953w, 900w, 843w, 815w, 767w, 751w, 714w, 609w, 565w, 548m, 508s, 482m, 439s.

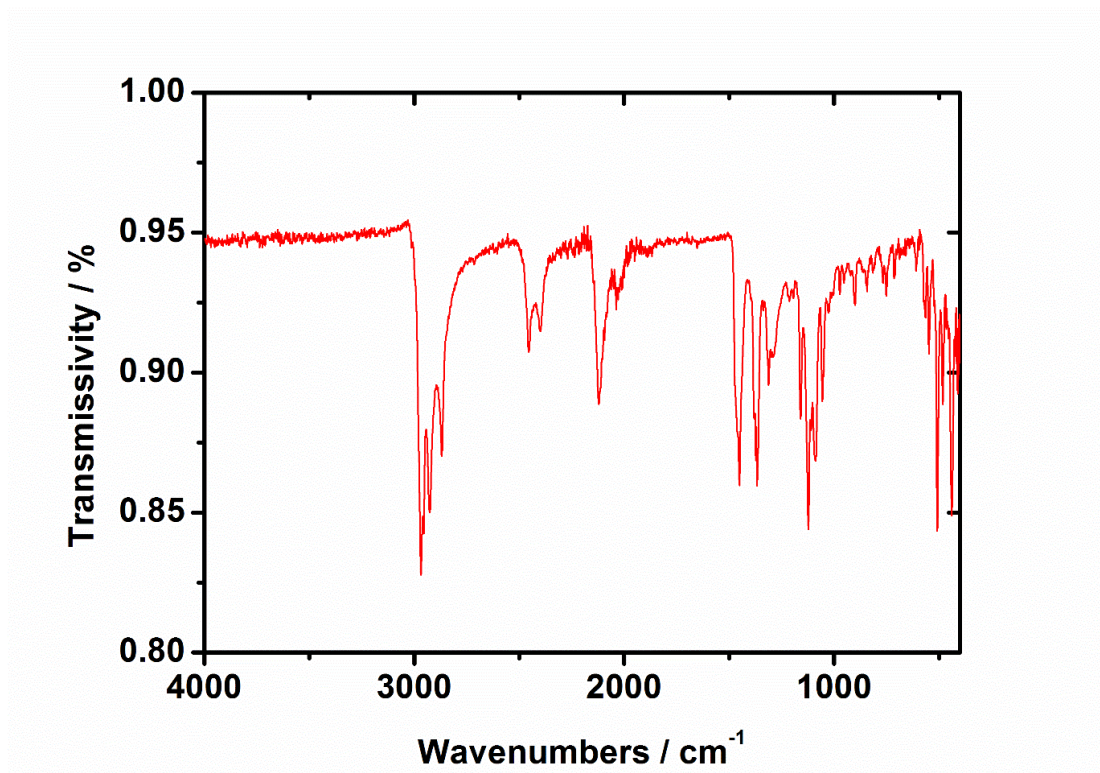
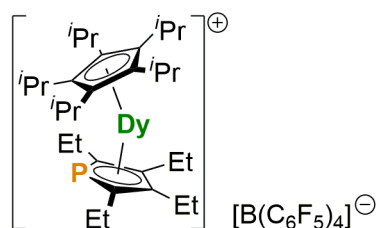


Figure 7.20 Infrared spectrum of compound 4.6.

3) Synthesis of $[(\text{Cp}^{\text{iPr5}})\text{Dy}(\text{Cp}^{\text{Et4P}})][\text{B}(\text{C}_6\text{F}_5)_4]$ (**4.7**) $[\text{B}(\text{C}_6\text{F}_5)_4]$



Cold (-40°C) hexane (10 ml) was added into a cold (-40°C) ampoule containing $[\text{Et}_3\text{Si}(\text{H})\text{SiEt}_3][\text{B}(\text{C}_6\text{F}_5)_4]$ (-40°C) (109 mg, 0.12 mmol) and a glass coated stirrer bar. A cold solution of $[(\text{Cp}^{\text{iPr5}})\text{Dy}(\text{Cp}^{\text{Et4P}})(\text{BH}_4)]$ (**4.6**) in hexane (-40°C , 80 mg, 0.12 mmol in 10 ml) was then slowly added. The resulting suspension was sonicated for 50 minutes and stirred for two days to give a yellow suspension. After letting the solid settle, as much of the solution was decanted away and hexane (10ml) was added. This was

repeated eight times before drying the solid *in vacuo* to give a yellow powder. Toluene (5 ml) was then added and the suspension was heated to 90 °C for 20 minutes to give a yellow solution, which was slowly cooled to room temperature, producing [4.7][B(C₆F₅)₄] as yellow crystals over two days (42 mg, 25 %).

Elemental analysis found (calc.) for C₅₆H₅₅BDyF₂₀P (%): C 51.05 (51.25); H 4.29 (4.22).

IR spectrum ($\tilde{\nu}/\text{cm}^{-1}$): 2983w, 2941w, 2878w, 2785w, 1641m, 1510s, 1460s, 1372m, 1312w, 1274m, 1160w, 1082s, 1054w, 979s, 907w, 775s, 756s, 726w, 683s, 660s, 609w, 572m, 512m, 478w, 431w.

¹¹B NMR (δ/ppm , Dichloromethane-d₂): -36.07, ¹⁹F NMR (δ/ppm): 184.09, 176.97, 150.99.

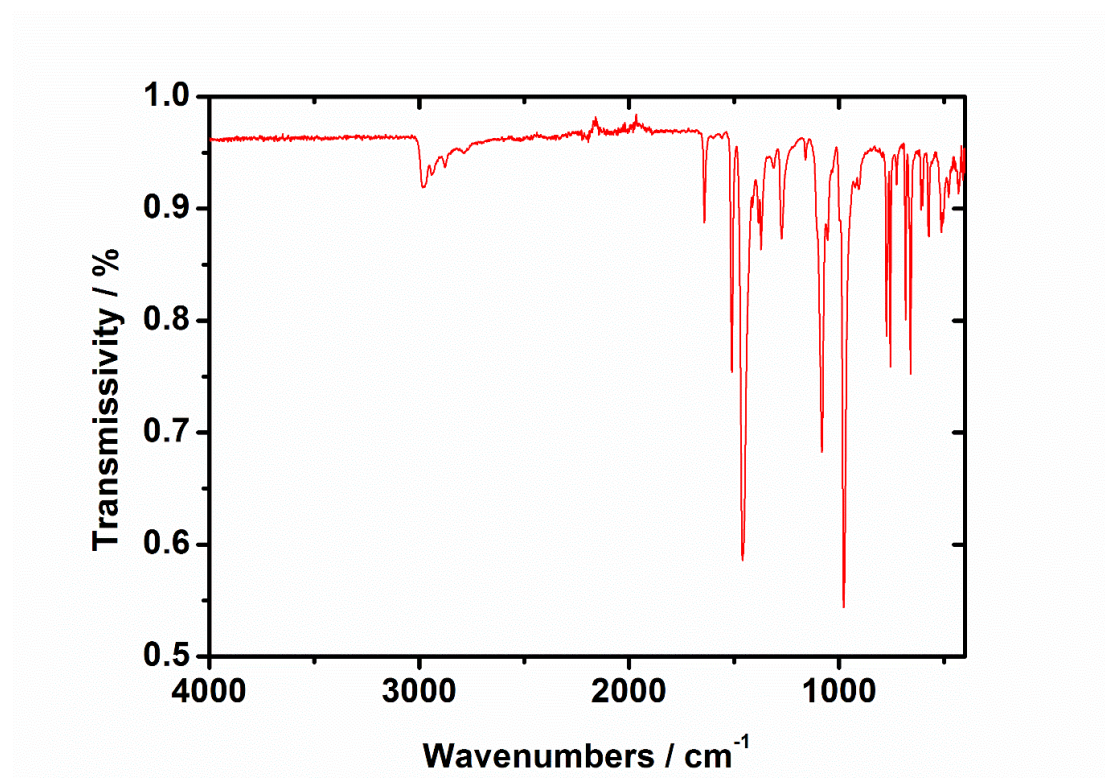


Figure 7.21 Infrared spectrum of compound 4.7.

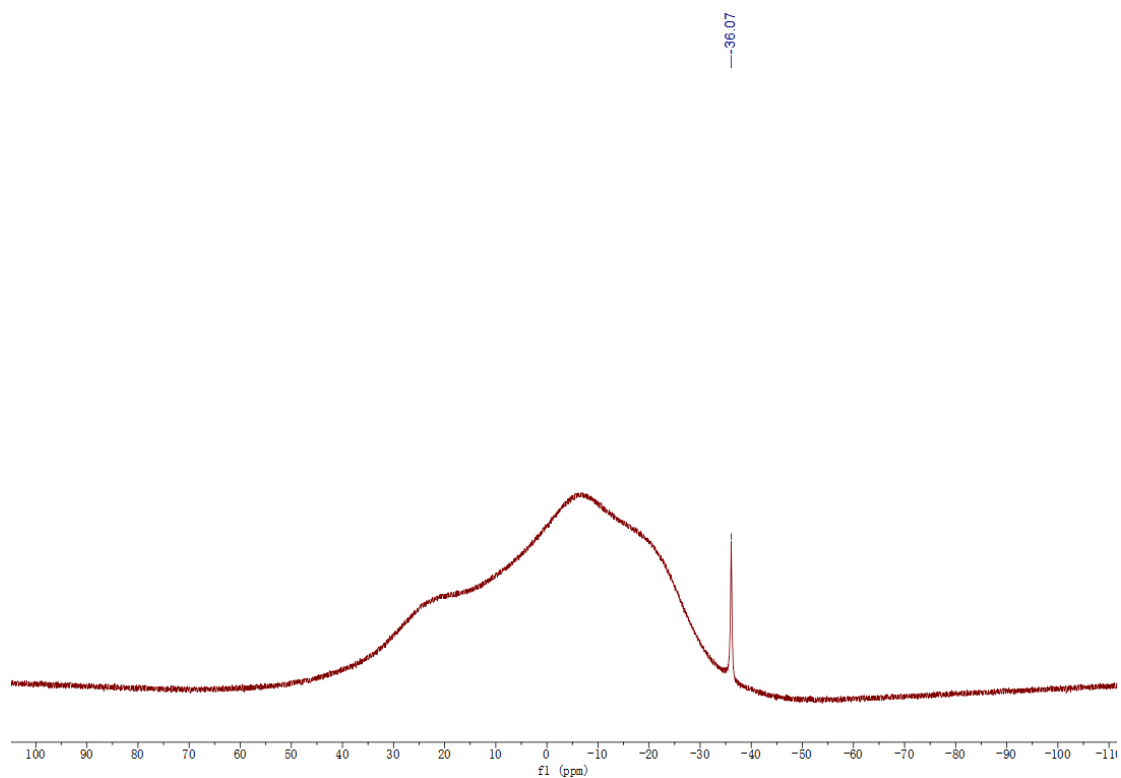


Figure 7.22 ^{11}B NMR spectrum of **4.7** in Dichloromethane- D_2 .

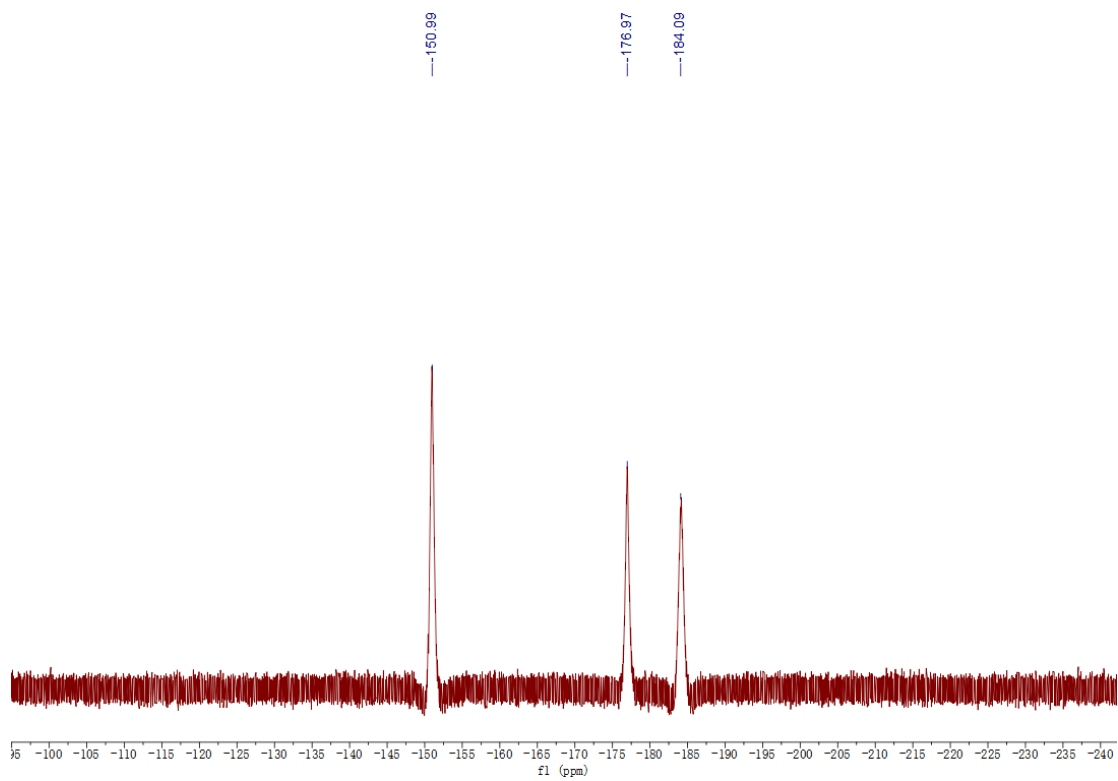
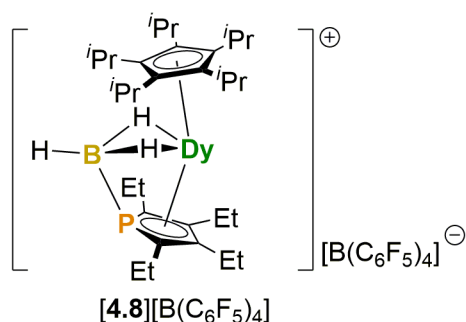


Figure 7.23 ^{11}B NMR spectrum of **4.7** in Dichloromethane- D_2 .

4) Synthesis of a mixture of **[4.7][B(C₆F₅)₄]** and **[4.8][B(C₆F₅)₄]**



A solution of **4.6** (100 mg, 0.15 mmol) in hexane (10mL) was added to $[\text{Ph}_3\text{C}][\text{B}(\text{C}_6\text{F}_5)_4]$ (142 mg, 0.2 mmol) at room temperature with a glass coated stirrer bar, which slowly turned to yellow powder after stirring for 24 hours. The hexane was removed, the residue was washed with hexane (5×10 mL) and the resulting yellow powder dried under vacuum. Dissolving the powder in toluene (5 mL), after 2 days, bright yellow crystals formed. The solvents were then decanted away and the crystals were washed with cold toluene (3×5 mL) and hexane (3×5 mL), which finally a mixture of **4.7** (major) and **4.8** as single crystals.

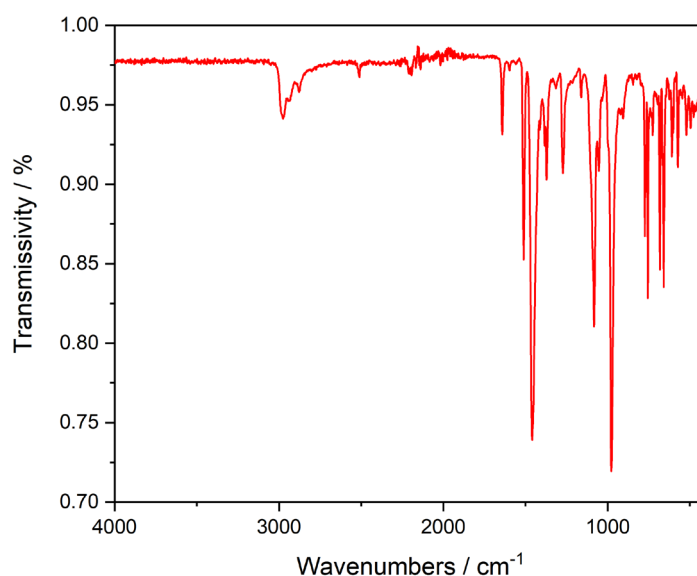
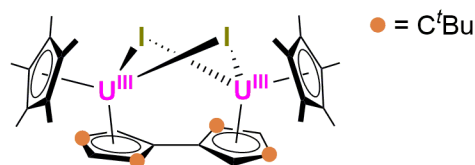


Figure 7.24 Infrared spectrum of a mixture of **4.7** and **4.8**.

7.1.5 Synthesis for Chapter 5

1) Synthesis of $[\text{U}^{\text{III}}(\eta^5\text{-Cp}^*)(\mu\text{-I})_2(\eta^5\text{-}\eta^5\text{-Fv}^{\text{tttt}})]$ (**5.1**)



A mixture of UI_3 (1 g, 1.6 mmol) and KCp^* (279 mg, 1.6 mmol) was added into a 100 mL ampule and THF (20 ml) was added. The reaction was stirred at room temperature overnight with the color changed from dark blue to green. The THF was removed by vacuum and the residue extracted with hexane (3×20 ml). After filtration, the hexane was removed under vacuum, mixed with **2.6_{Dy}** (258 mg, 0.8 mmol) in toluene (20 ml). The mixture was refluxed overnight, then the solvent was removed under vacuum, the residue was extracted with hexane (3×20 ml) and concentrated to 5 mL. Storage at -40 °C produced dark brown crystals of **5.1** after two days. Isolated yield = 150 mg, 14 %.

^1H NMR (δ/ppm , benzene- D_6): -0.75 (s, 18H), -4.40 (s, 30H), -30.84 (s, 18H).

IR spectrum ($\tilde{\nu}/\text{cm}^{-1}$): 2959m, 2898m, 2859w, 2256w, 1641m, 1457s, 1375m, 1365m, 1306w, 1237s, 1196m, 1082s, 1021w, 977s, 837w, 773w, 755m, 726w, 683m, 660m, 611w, 571w, 547w.

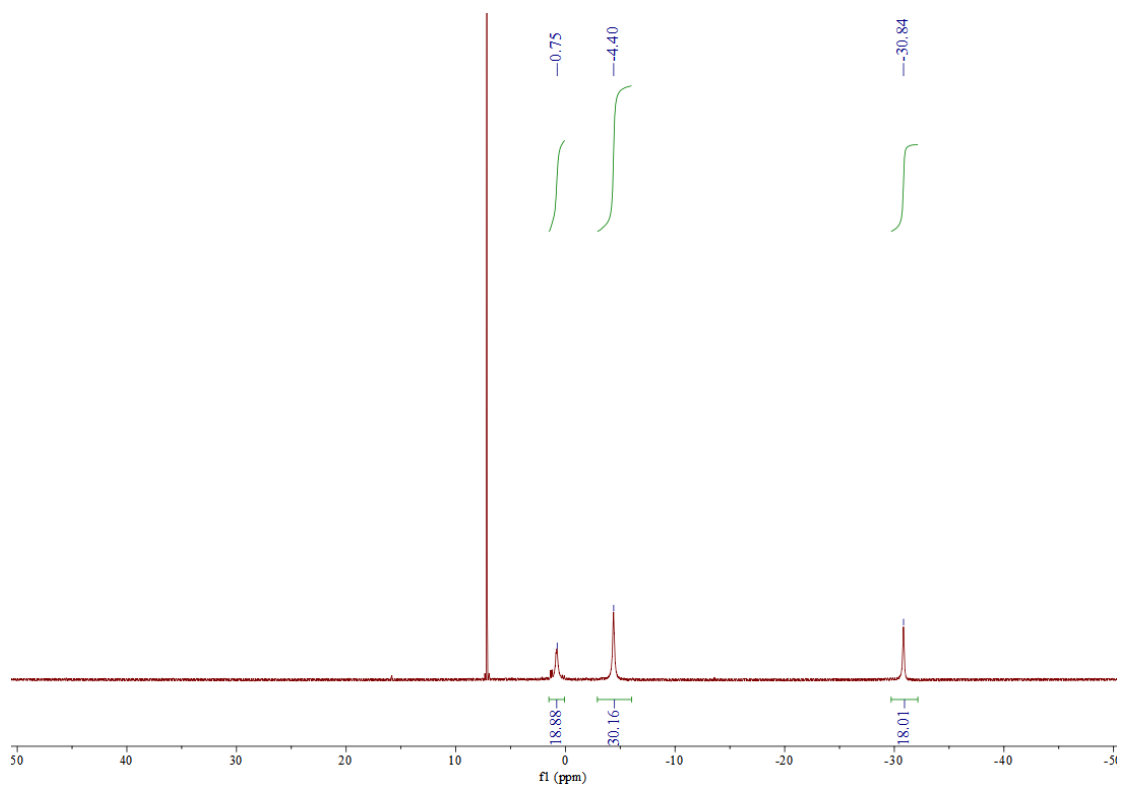


Figure 7.25 ¹H NMR spectrum of 5.1 in D₆-benzene.

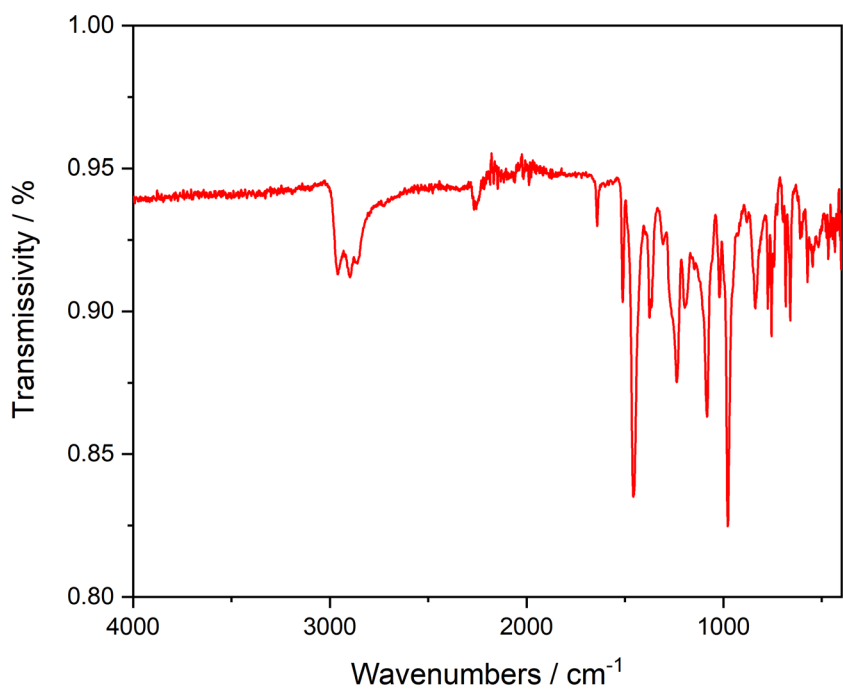
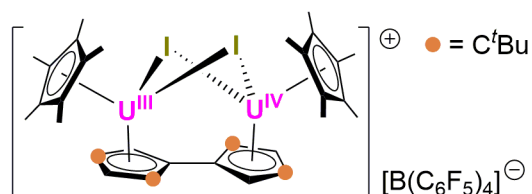


Figure 7.26 Infrared spectrum of compound 5.1.

2) Synthesis of $[\text{U}^{\text{III/IV}}(\eta^5\text{-Cp}^*)(\mu\text{-I})_2(\eta^5:\eta^5\text{-Fv}^{\text{tttt}})] [\text{B}(\text{C}_6\text{F}_5)_4] ([\mathbf{5.2}][\text{B}(\text{C}_6\text{F}_5)_4])$



A solution of **5.1** (50 mg, 0.04 mmol) in hexane (10mL) was added to $[(\text{Et}_3\text{Si})_2(\mu\text{-H})][\text{B}(\text{C}_6\text{F}_5)_4]$ (36 mg, 0.04 mmol) at room temperature. The reaction was stirred for 24 hours and a black gel-like mixture had formed. The hexane was decanted, the residue was washed with hexane (5×10 mL) and the resulting residue dried under vacuum. Dissolving the gel product in 1,2-dichlorobenzene (5 mL) and layering the solution with hexane at room temperature, which produced dark purple crystals after 2 days. The solvents were then decanted away and the crystals were washed with cold hexane (3×5 mL) and toluene (3×5 mL). The crystallization process was repeated twice in order to obtain single crystals of **5.2** suitable for X-ray diffraction. Yield = 20 mg, 27 %.

^1H NMR (δ /ppm, DCM- D_2): 22.40 (s, $-\text{CH}_3$, Fv^{tttt}), 19.19 (s, $-\text{CH}_3$, Fv^{tttt}), 17.78 (s, $-\text{CH}_3$, Cp^*), 16.32 ($-\text{CH}_3$, Cp^*), -28.53 (s, $-\text{CH}_3$, Fv^{tttt}), -30.80 ($-\text{CH}_3$, Fv^{tttt}). ^{19}F NMR (δ /ppm, o-DCB): -132.15 (s), -162.87 (t, $J = 20$ Hz), -166.68 (s). ^{11}B NMR (δ /ppm): -16.62 (s).

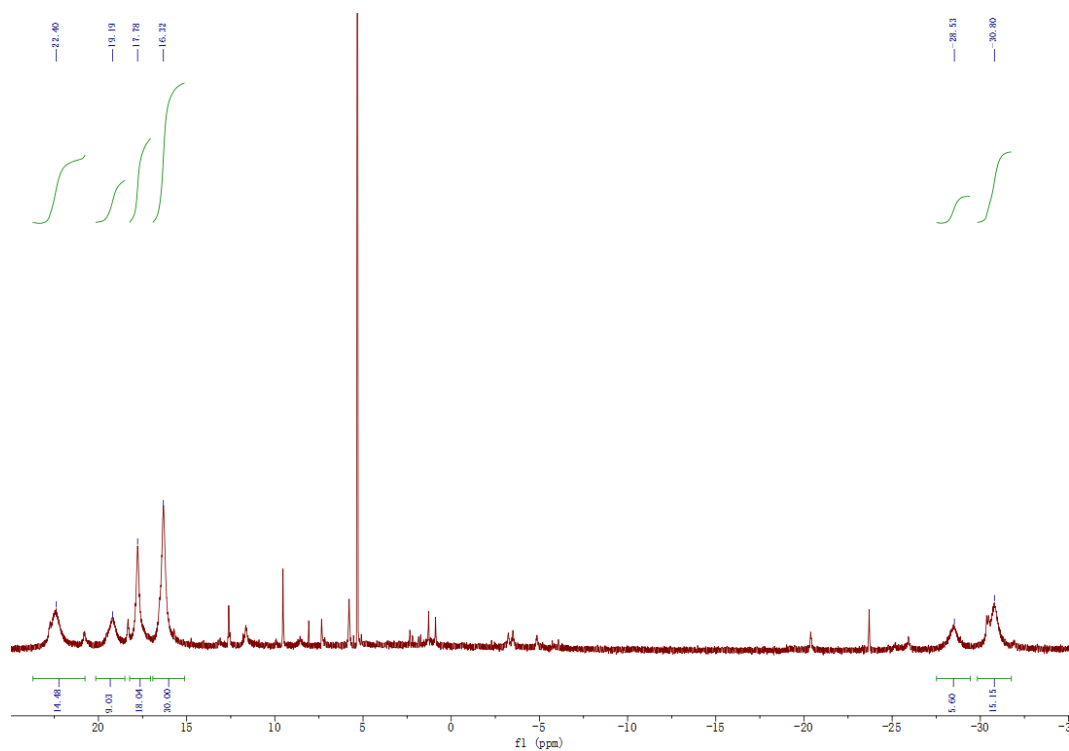


Figure 7.27 ^1H NMR spectrum of **5.2** in dichloromethane- D_2 .

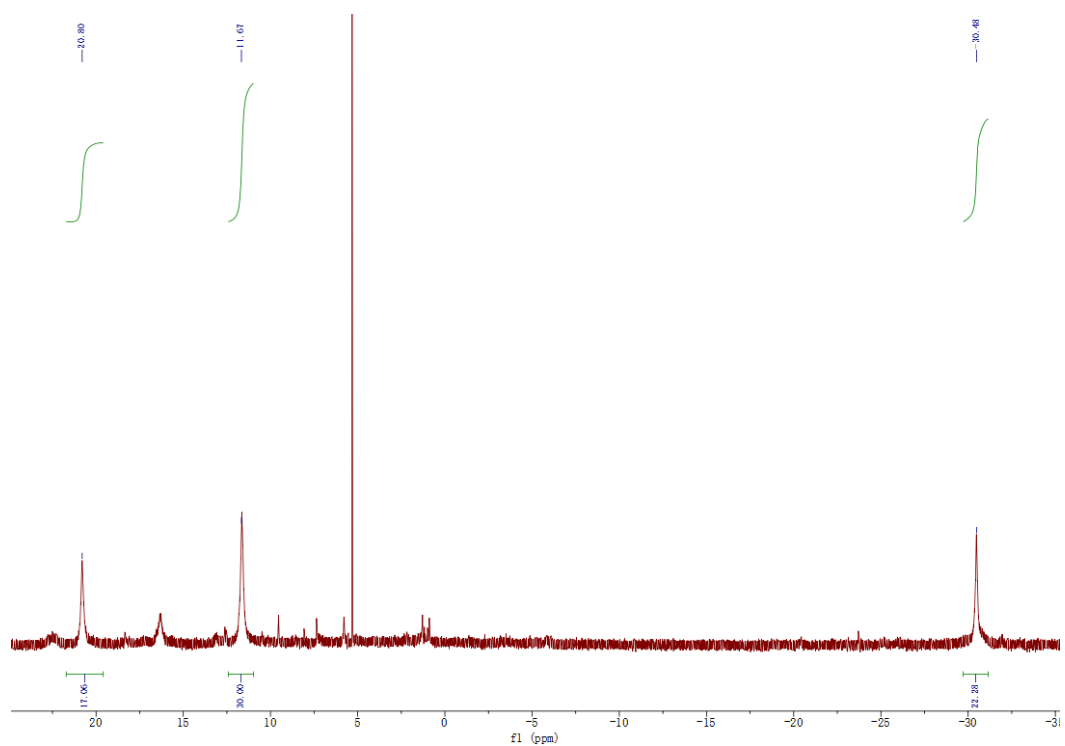


Figure 7.28 ^1H NMR spectrum of **5.2** in dichloromethane- D_2 overnight. The compound **5.2** decomposed as the peaks reduced.

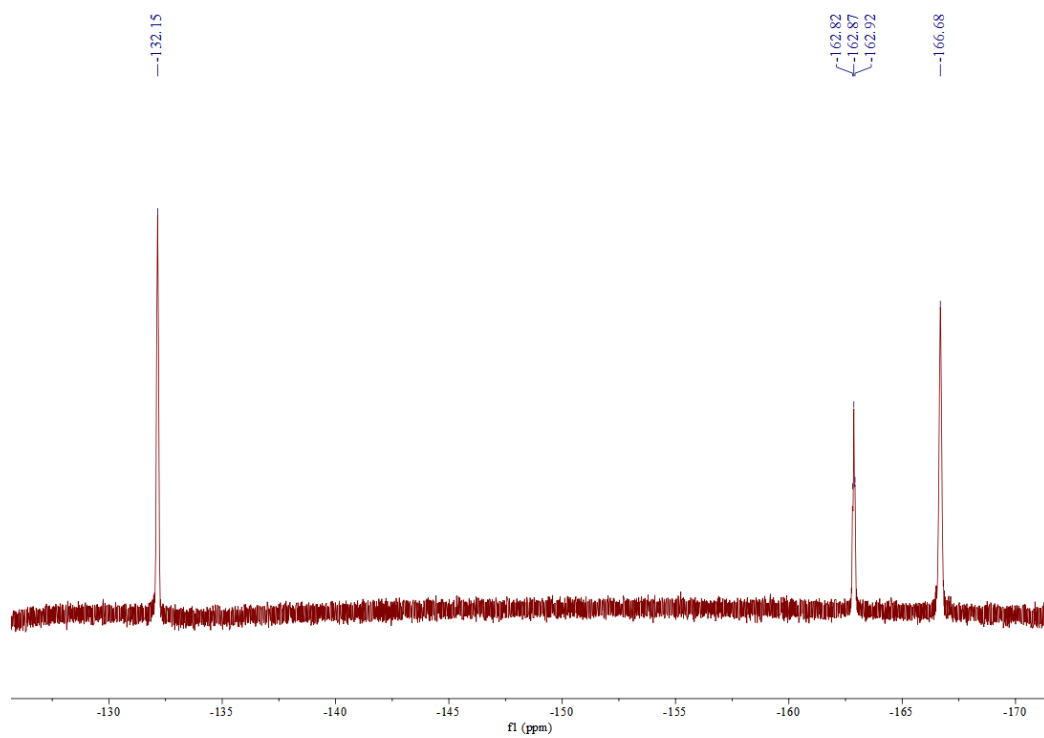


Figure 7.29 ^{19}F NMR spectrum of 5.2 in 1,2-Dichlorobenzene- D_4 .

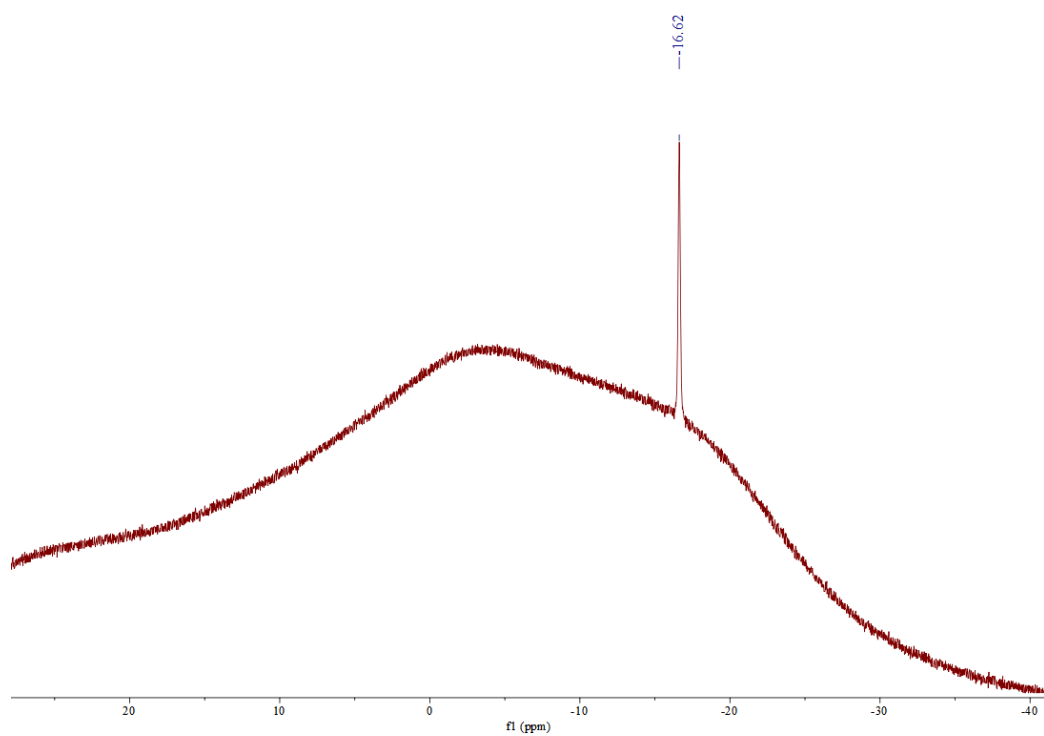


Figure 7.30 ^{11}B NMR spectrum of 5.2 in 1,2-Dichlorobenzene- D_4 .

7.2 X-Ray Crystallography

X-ray diffraction data were collected on an Agilent Gemini Ultra diffractometer and a Rigaku microfocus rotating anode diffractometer, respectively, using Cu $K\alpha$ radiation. Structures were solved in Olex2 with SHELXT using intrinsic phasing and were refined with SHELXL using least squares minimisation.¹⁶⁹⁻¹⁷¹ Anisotropic thermal parameters were used for the non-hydrogen atoms and isotropic parameters for the hydrogen atoms. Hydrogen atoms on carbons were added geometrically and refined using a riding model.

Table 7.1. Crystal data and structure refinement for **2.6**.

Compound reference	2.6_{Dy}	2_Y
empirical formula	C ₃₄ H ₇₂ B ₄ O ₂ Dy ₂	C ₃₄ H ₇₂ B ₄ O ₂ Y ₂
formula weight	881.15	733.97
crystal system	triclinic	triclinic
space group	<i>P</i> −1	<i>P</i> −1
<i>a</i> /Å	10.0067(5)	9.9883(3)
<i>b</i> /Å	14.2962(7)	14.2576(7)
<i>c</i> /Å	16.3689(8)	16.4102(7)
α /°	99.987(4)	100.067(4)
β /°	105.704(4)	105.699(3)
γ /°	107.788(4)	107.719(4)
Volume/Å ³	2061.03(19)	2057.07(16)
<i>Z</i>	2	2
Temperature/K	220	220
ρ_{calc} g/cm ³	1.420	1.185
<i>F</i> (000)	888.0	780.0
Reflections collected	13654	13126
Independent reflections	7793	7772
<i>R</i> _{int}	0.0314	0.0268
Goodness of fit on <i>F</i> ²	1.038	1.016
<i>R</i> ₁ ^{<i>a</i>}	0.0346	0.0335
<i>R</i> _w ^{<i>b</i>}	0.0865	0.0881

$$^a R_1[|I| > 2\sigma(I)] = \sum ||F_o| - |F_c|| / \sum |F_o|; ^b R_w[\text{all data}] = [\sum \{w(F_o^2 - F_c^2)^2\} / \sum \{w(F_o^2)^2\}]^{1/2}$$

Table 7.2. Crystal data and structure refinement for **2.7**.

Compound reference	2.7
empirical formula	C ₅₂ H ₈₈ B ₂ Dy ₂
formula weight	1059.84
crystal system	triclinic
space group	<i>P</i> -1
<i>a</i> /Å	10.2899(5)
<i>b</i> /Å	11.5073(4)
<i>c</i> /Å	23.1393(9)
α /°	88.062(3)
β /°	78.909(4)
γ /°	72.350(4)
Volume/Å ³	2561.28(19)
<i>Z</i>	2
Temperature/K	100
ρ_{calc} g/cm ³	1.374
<i>F</i> (000)	1084.0
Reflections collected	16897
Independent reflections	9685
<i>R</i> _{int}	0.0314
Goodness of fit on <i>F</i> ²	1.008
<i>R</i> ₁ ^{<i>a</i>}	0.0394
<i>R</i> _w ^{<i>b</i>}	0.0992

$$^a R_1[I > 2\sigma(I)] = \sum ||F_o| - |F_c|| / \sum |F_o|; ^b R_w[\text{all data}] = [\sum \{w(F_o^2 - F_c^2)^2\} / \sum \{w(F_o^2)^2\}]^{1/2}$$

Table 7.3. Crystal data and structure refinement for **2.9**

Compound reference	2.9_{Dy}	2.9_Y
empirical formula	C ₄₆ H ₇₈ B ₂ Dy ₂	C ₄₆ H ₇₈ B ₂ Y ₂
formula weight	977.70	830.52
crystal system	monoclinic	monoclinic
space group	<i>P2₁/n</i>	<i>P2₁/n</i>
<i>a</i> /Å	13.3199(1)	13.3158(2)
<i>b</i> /Å	18.1439(1)	18.1359(3)
<i>c</i> /Å	19.6411(2)	19.6598(4)
α /°	90	90
β /°	107.366(1)	107.454(2)
γ /°	10	90
Volume/Å ³	4530.39(7)	4529.13(14)
<i>Z</i>	4	4
Temperature/K	100	100
ρ_{calc} g/cm ³	1.433	1.218
F (000)	1984.0	1768.0
Reflections collected	31291	32319
Independent reflections	8690	8702
<i>R</i> _{int}	0.0402	0.0492
Goodness of fit on <i>F</i> ²	1.024	1.031
<i>R</i> ₁ ^{<i>a</i>}	0.0266	0.0276
<i>R</i> _w ^{<i>b</i>}	0.0655	0.0666

$$^a R_1[I > 2\sigma(I)] = \sum ||F_o| - |F_c|| / \sum |F_o|; ^b R_w[\text{all data}] = [\sum \{w(F_o^2 - F_c^2)^2\} / \sum \{w(F_o^2)^2\}]^{1/2}$$

Table 7.4 Crystal data and structure refinement for [2.10][B(C₆F₅)₄].

Compound reference	2.10
empirical formula	C ₇₀ H ₇₄ B ₂ Dy ₂ F ₂₀
formula weight	1641.91
crystal system	monoclinic
space group	<i>P</i> 2 ₁ / <i>n</i>
<i>a</i> /Å	18.1029(5)
<i>b</i> /Å	20.9327(4)
<i>c</i> /Å	19.4229(5)
α /°	90
β /°	111.812(3)
γ /°	90
Volume/Å ³	6833.2(3)
<i>Z</i>	4
Temperature/K	100
ρ_{calc} g/cm ³	1.596
<i>F</i> (000)	3264.0
Reflections collected	55944
Independent reflections	12172
<i>R</i> _{int}	0.0739
Goodness of fit on <i>F</i> ²	1.055
<i>R</i> ₁ ^{<i>a</i>}	0.0692
<i>R</i> _w ^{<i>b</i>}	0.1762

$$^a R_1[I > 2\sigma(I)] = \sum ||F_o| - |F_c|| / \sum |F_o|; ^b R_w[\text{all data}] = [\sum \{w(F_o^2 - F_c^2)^2\} / \sum \{w(F_o^2)^2\}]^{1/2}$$

Table 7.5. Crystal data and structure refinement for **3.1** and **3.2**.

Compound reference	3.1	3.2
empirical formula	C ₇₈ H ₁₃₆ B ₃ Dy ₃	C ₁₀₂ H ₁₃₂ B ₂ Dy ₃ F ₂₀
formula weight	1593.79	2258.00
crystal system	monoclinic	triclinic
space group	<i>P</i> 2 ₁ / <i>n</i>	<i>P</i> -1
<i>a</i> /Å	14.14480(10)	14.2955(5)
<i>b</i> /Å	21.92880(10)	17.6222(7)
<i>c</i> /Å	26.0721(2)	19.9866(6)
α /°	90	80.945(3)
β /°	98.3090(10)	88.122(3)
γ /°	90	88.861(3)
Volume/Å ³	8002.11(9)	4969.0(3)
<i>Z</i>	4	2
Temperature/K	100	100
ρ_{calc} g/cm ³	1.323	1.509
<i>F</i> (000)	3268.0	2274.0
Reflections collected	55554	34352
Independent reflections	15365	17677
<i>R</i> _{int}	0.0814	0.0429
Goodness of fit on <i>F</i> ²	1.024	1.015
<i>R</i> ₁ ^{<i>a</i>}	0.0407	0.0474
<i>R</i> _w ^{<i>b</i>}	0.1060	0.1225

$$^a R_1[I > 2\sigma(I)] = \sum ||F_o| - |F_c|| / \sum |F_o|; ^b R_w[\text{all data}] = [\sum \{w(F_o^2 - F_c^2)^2\} / \sum \{w(F_o^2)^2\}]^{1/2}$$

Table 7.6 Crystal data and structure refinement for **4.4**.

Compound reference	4.4
empirical formula	C ₂₈ H ₆₀ BDyOP ₂ Si ₄
formula weight	760.37
crystal system	triclinic
space group	<i>P</i> -1
<i>a</i> /Å	10.1543(5)
<i>b</i> /Å	12.5323(6)
<i>c</i> /Å	16.2234(6)
α /°	80.797(4)
β /°	72.156(4)
γ /°	70.035(5)
Volume/Å ³	1843.58(16)
<i>Z</i>	2
Temperature/K	100
ρ_{calc} g/cm ³	1.370
<i>F</i> (000)	786.0
Reflections collected	11840
Independent reflections	6965
<i>R</i> _{int}	0.0497
Goodness of fit on <i>F</i> ²	1.015
<i>R</i> ₁ ^{<i>a</i>}	0.0358
<i>R</i> _w ^{<i>b</i>}	0.0891

$$^a R_1[I > 2\sigma(I)] = \sum ||F_o| - |F_c|| / \sum |F_o|; ^b R_w[\text{all data}] = [\sum \{w(F_o^2 - F_c^2)^2\} / \sum \{w(F_o^2)^2\}]^{1/2}$$

Table 7.7 Crystal data and structure refinement for **4.6**, **[4.7][B(C₆F₅)₄]** and **[4.8][B(C₆F₅)₄]**.

Compound reference	4.6	4.7	4.8
empirical formula	C ₃₂ H ₅₉ BDyP	C ₅₆ H ₅₅ BDyF ₂₀ P	C ₅₆ H ₅₈ B ₂ DyF ₂₀ P
formula weight	648.07	1312.28	1326.11
crystal system	Triclinic	Orthorhombic	monoclinic
space group	<i>P</i> -1	<i>Pna</i> 2 ₁	<i>P</i> 2 ₁ / <i>c</i>
<i>a</i> /Å	9.8357(4)	17.8192(4)	16.7542(2)
<i>b</i> /Å	11.2310(5)	16.9757(5)	14.7179(2)
<i>c</i> /Å	16.6786(6)	17.5726(4)	22.3108(3)
<i>α</i> /°	70.974(4)	90	90
<i>β</i> /°	87.088(3)	90	97.1450(10)
<i>γ</i> /°	67.371(4)	90	90
Volume/Å ³	1601.77(13)	5315.6(2)	5458.82(12)
<i>Z</i>	2	4	4
Temperature/K	100	100	99.8(9)
<i>ρ</i> _{calc} g/cm ³	1.344	1.640	1.614
<i>F</i> (000)	674.0	2628.0	2660.0
Reflections collected	10946	47958	18695
Independent reflections	5711	9379	10342
<i>R</i> _{int}	0.0297	0.0812	0.0300
Goodness of fit on <i>F</i> ²	1.076	1.057	1.039
<i>R</i> ₁ ^{<i>a</i>}	0.0314	0.0834	0.0479
<i>R</i> _w ^{<i>b</i>}	0.0812	0.2101	0.1289

$$^a R_1[|I| > 2\sigma(I)] = \sum ||F_o| - |F_c|| / \sum |F_o|; ^b R_w[\text{all data}] = [\sum \{w(F_o^2 - F_c^2)^2\} / \sum \{w(F_o^2)^2\}]^{1/2}$$

Table 7.8. Crystal data and structure refinement for **5.1** and **[5.2]**[B(C₆F₅)₄].

Compound reference	5.1	5.2
empirical formula	C ₂₃ H ₃₅ IU	C ₇₀ H ₇₀ BF ₂₀ I ₂ U ₂
formula weight	676.44	2031.93
crystal system	orthorhombic	monoclinic
space group	<i>Pccn</i>	<i>P2</i> ₁
<i>a</i> /Å	9.6769(2)	11.9938(3)
<i>b</i> /Å	23.9095(4)	20.3893(3)
<i>c</i> /Å	19.5511(3)	13.8958(3)
α /°	90	90
β /°	90	95.067(2)
γ /°	90	90
Volume/Å ³	4523.53(14)	3384.87(12)
<i>Z</i>	8	2
Temperature/K	100	100
ρ_{calc} g/cm ³	1.987	1.994
<i>F</i> (000)	2544.0	1930.0
Reflections collected	9527	20246
Independent reflections	4047	12656
<i>R</i> _{int}	0.0497	0.0429
Goodness of fit on <i>F</i> ²	1.037	1.192
<i>R</i> ₁ ^a	0.0454	0.1162
<i>R</i> _w ^b	0.1231	0.2852

$$^a R_1[I > 2\sigma(I)] = \sum | |F_o| - |F_c| | / \sum |F_o|; \quad ^b R_w[\text{all data}] = [\sum \{w(F_o^2 - F_c^2)^2\} / \sum \{w(F_o^2)^2\}]^{1/2}$$

7.3 Magnetic property measurements

Magnetic susceptibility measurements were recorded on a Quantum Design MPMS-XL7 SQUID magnetometer for samples in Chapter 2 and 3, and a Quantum Design MPMS3-VSM SQUID magnetometer for samples in Chapter 5, equipped with a 7 T magnet. The samples were restrained in eicosane and sealed in 7 mm NMR tubes. Direct current (DC) magnetic susceptibility measurements were performed on crystalline samples in the temperature range 1.9–300 K using an applied field of 1000 Oe. The AC susceptibility measurements were performed in zero DC field or a mentioned induced DC field. Diamagnetic corrections were made with Pascal's constants for all the constituent atoms.

7.3.1 Additional Magnetic Information for Chapter 2

Table 7.9 Properties of the eight lowest KDs of the Dy²⁺ ion in **2.6_{Dy}** corresponding to the crystal-field split states in the ground ⁶H_{15/2} multiplet.

KD	E / cm^{-1}	g_x	g_y	g_z	$\theta / ^\circ$ ^a
KD1	0	0.00620	0.01058	19.75185	
KD2	181	0.43292	1.36588	17.74407	43.0
KD3	210	0.16902	1.93981	14.94068	42.6
KD4	245	0.63548	1.76575	13.50643	18.6
KD5	308	1.27063	3.41690	12.06350	32.7
KD6	362	4.01888	4.92099	10.98782	109.6
KD7	447	1.67094	2.54136	12.66437	83.6
KD8	484	1.02722	4.73611	15.90613	82.9

^a The angle between the principal magnetic axis of the given doublet and the that of the ground doublet.

Table 7.10 Properties of the eight lowest KDs of the Dy²⁺ ion in **2.9_{Dy}** corresponding to the crystal-field split states in the ground ⁶H_{15/2} multiplet.

KD	E / cm^{-1}	g_x	g_y	g_z	$\theta / ^\circ$ ^a
KD1	0	0.00218	0.00299	19.72401	
KD2	208	0.02531	0.02897	17.08756	4.2
KD3	362	0.31294	0.40615	14.60738	12.7
KD4	457	2.29997	2.49618	10.74650	3.6
KD5	523	4.59049	5.79729	8.26972	100.2
KD6	574	1.08694	3.34816	11.85330	91.2
KD7	606	1.70246	4.35865	14.29206	81.8
KD8	717	0.01208	0.06229	19.31908	88.7

^a The angle between the principal magnetic axis of the given doublet and the that of the ground doublet.

Table 7.11 Properties of the eight lowest KDs of the Dy²⁺ ion in **2.10** corresponding to the crystal-field split states in the ground ⁶H_{15/2} multiplet.

KD	E / cm^{-1}	g_x	g_y	g_z	$\theta / ^\circ$ ^a
KD1	0	0.00149	0.00216	19.76203	
KD2	339	0.05755	0.07880	16.79071	2.7
KD3	551	0.95515	1.34018	13.64853	5.0
KD4	666	7.70619	6.76726	5.06887	92.8
KD5	749	1.38889	3.01956	10.24814	87.0
KD6	862	0.37624	0.48478	13.46090	88.6
KD7	1015	0.15325	0.24826	16.52331	90.1
KD8	1274	0.00829	0.01401	19.55805	90.5

^a The angle between the principal magnetic axis of the given doublet and the that of the ground doublet.

7.3.2 Additional Magnetic Information for Chapter 3

Table 7.12 Properties of the eight lowest KDs of the Dy1 ion in **3.1** corresponding to the crystal-field split states in the ground ${}^6\text{H}_{15/2}$ multiplet.

KD	E / cm^{-1}	g_x	g_y	g_z	$\theta / ^\circ$ ^a
KD1	0	0.00230	0.00346	19.59996	0.0
KD2	185	0.02124	0.02125	16.98948	3.3
KD3	359	0.08296	0.08664	14.66573	4.8
KD4	457	1.91691	2.76384	11.55813	19.3
KD5	487	0.47080	2.80944	14.58713	76.0
KD6	534	4.85026	6.00605	9.37978	73.2
KD7	606	1.06026	1.94509	15.75565	89.0
KD8	748	0.04127	0.11175	19.49623	89.7

^a The angle between the principal magnetic axis of the given doublet and the that of the ground doublet.

Table 7.13 Properties of the eight lowest KDs of the Dy2 ion in **3.1** corresponding to the crystal-field split states in the ground ${}^6\text{H}_{15/2}$ multiplet.

KD	E / cm^{-1}	g_x	g_y	g_z	$\theta / ^\circ$ ^a
KD1	0	0.00033	0.00050	19.71065	0.0
KD2	190	0.00373	0.00434	17.33117	169.5
KD3	330	0.01761	0.01928	15.08573	157.6
KD4	446	0.16215	0.23800	11.64530	176.4
KD5	524	1.76608	2.17045	8.66722	167.2
KD6	561	3.02216	3.56685	13.96279	87.9
KD7	584	1.06925	2.64913	13.51276	103.8
KD8	659	0.23196	0.31895	18.65671	92.5

^a The angle between the principal magnetic axis of the given doublet and the that of the ground doublet.

Table 7.14 Properties of the eight lowest KDs of the Dy³ ion in **3.1** corresponding to the crystal-field split states in the ground ⁶H_{15/2} multiplet.

KD	E / cm^{-1}	g_x	g_y	g_z	$\theta / ^\circ$ ^a
KD1	0	0.00182	0.00354	19.45152	0.0
KD2	151	0.01395	0.01440	16.96267	5.7
KD3	338	0.29931	0.36689	14.61695	4.6
KD4	427	2.71999	3.15657	14.71942	77.3
KD5	456	1.09938	4.67216	9.44583	37.7
KD6	510	4.83652	6.03930	10.34643	86.9
KD7	575	0.52465	0.95643	15.87535	93.0
KD8	732	0.06950	0.13148	19.54688	89.9

^a The angle between the principal magnetic axis of the given doublet and the that of the ground doublet.

Table 7.15 Properties of the eight lowest KDs of the Dy¹ ion in **3.2** corresponding to the crystal-field split states in the ground ⁶H_{15/2} multiplet.

KD	E / cm^{-1}	g_x	g_y	g_z	$\theta / ^\circ$ ^a
KD1	0	0.00336	0.00518	19.76347	0.0
KD2	324	0.15768	0.24916	16.61019	2.6
KD3	495	2.20844	3.75104	12.17989	4.6
KD4	577	6.97279	6.29181	4.92602	13.5
KD5	663	0.19509	0.65238	11.15493	93.0
KD6	765	0.20493	0.22674	13.80091	92.7
KD7	901	0.04413	0.07052	16.64384	90.6
KD8	1175	0.00149	0.00232	19.65495	89.4

^a The angle between the principal magnetic axis of the given doublet and the that of the ground doublet.

Table 7.16 Properties of the eight lowest KDs of the Dy² ion in **3.2** corresponding to the crystal-field split states in the ground ⁶H_{15/2} multiplet.

KD	E / cm^{-1}	g_x	g_y	g_z	$\theta / ^\circ$ ^a
KD1	0	0.00077	0.00082	19.83631	0.0
KD2	285	0.02541	0.02669	17.08366	3.0
KD3	453	0.18604	0.24426	14.51700	6.2
KD4	557	0.49459	0.87408	11.73187	3.1
KD5	643	3.27871	4.83529	8.39311	9.3
KD6	727	7.99094	5.19896	0.57402	95.2
KD7	776	2.11734	4.03301	14.80638	89.8
KD8	855	0.12316	0.31070	18.60654	90.5

^a The angle between the principal magnetic axis of the given doublet and the that of the ground doublet.

Table 7.17 Properties of the eight lowest KDs of the Dy³ ion in **3.2** corresponding to the crystal-field split states in the ground ⁶H_{15/2} multiplet.

KD	E / cm^{-1}	g_x	g_y	g_z	$\theta / ^\circ$ ^a
KD1	0	0.00291	0.00443	19.77139	0.0
KD2	337	0.15944	0.25628	16.56737	1.6
KD3	506	2.19075	3.64597	12.17660	2.3
KD4	590	5.35063	5.82131	6.89882	94.8
KD5	677	0.88917	1.05879	11.12947	90.5
KD6	784	0.11243	0.12730	13.77847	89.2
KD7	929	0.01332	0.02057	16.62206	89.1
KD8	1210	0.00055	0.00093	19.64265	89.9

^a The angle between the principal magnetic axis of the given doublet and the that of the ground doublet.

7.3.3 Additional Magnetic Information for Chapter 4

Table 7.18 Relaxation fitting parameters for [4.7][B(C₆F₅)₄] at the temperature range of 78–119 K.

T / K	$\chi_{\text{T}} / \text{cm}^3 \text{mol}^{-1}$	$\chi_{\text{S}} / \text{cm}^3 \text{mol}^{-1}$	α	τ / s
119	0.11454	0.04239	0.0142	1.03182E-4
117	0.11677	0.04417	0.02389	1.43932E-4
115	0.11843	0.04535	0.01614	2.01127E-4
113	0.12072	0.04796	0.00643	2.90005E-4
111	0.12259	0.04818	0.01097	4.0449E-4
109	0.12479	0.04983	0 [§]	5.79921E-4
107	0.12688	0.05052	0.00263	8.36849E-4
105	0.12937	0.05141	0.00385	0.00122
103	0.1318	0.05231	0.00967	0.00183
101	0.13484	0.05307	0.00565	0.00271
99	0.13709	0.05424	0.00624	0.00418
97	0.14046	0.0552	0.01123	0.00642
95	0.14345	0.05636	0.00598	0.01005
93	0.1448	0.05755	0 [§]	0.01552
90	0.1491	0.0595	0 [§]	0.03163
87	0.15523	0.06118	0.007	0.06791
84	0.15905	0.06309	0.02019	0.15061
81	0.16428	0.06611	0 [§]	0.34238
78	0.17215	0.06755	0.01699	0.80502

[§] These parameter values were restricted to non-negative.

Table 7.19 Relaxation fitting parameters for [4.7] [B(C₆F₅)₄] at the temperature range of 4–70 K.

T / K	$\chi_{\text{T}} / \text{cm}^3 \text{mol}^{-1}$	$\chi_{\text{S}} / \text{cm}^3 \text{mol}^{-1}$	α	τ / s
70	0.07548	0.02146	0.02215	1.8161E-4
69	0.07627	0.02197	0.01665	2.2755E-4
68	0.07697	0.02252	0.01017	2.84347E-4
67	0.0785	0.02258	0.01884	3.62356E-4
66	0.07936	0.02268	0.02073	4.47172E-4
65	0.0805	0.02335	0.01776	5.74249E-4
64	0.08144	0.02341	0.02261	7.10332E-4
63	0.08256	0.02387	0.02105	9.04734E-4
62	0.08438	0.02435	0.01917	0.00113
61	0.08548	0.02429	0.02641	0.00141
60	0.08665	0.02513	0.01929	0.00174
59	0.08834	0.02533	0.02904	0.00212
58	0.08981	0.02589	0.02848	0.00263
57	0.09118	0.02624	0.02953	0.0031
56	0.09295	0.02608	0.04714	0.00369
54	0.09621	0.02699	0.04871	0.00489
52	0.09978	0.02779	0.05102	0.00629
50	0.10256	0.0292	0.03972	0.00753
48	0.10658	0.03013	0.04691	0.00895
44	0.11618	0.03242	0.06849	0.01175
40	0.12722	0.03495	0.06637	0.01478
36	0.13976	0.03866	0.07221	0.01892
32	0.15641	0.04181	0.0893	0.02441
28	0.17986	0.04556	0.12212	0.03379
24	0.20838	0.05204	0.13938	0.04776
20	0.25345	0.05772	0.19998	0.073
16	0.31724	0.06827	0.24742	0.11897
14	0.3704	0.06964	0.31382	0.1635
13	0.40014	0.0732	0.33207	0.19192
12	0.43047	0.07649	0.35323	0.22265
11	0.47763	0.08094	0.37372	0.27257
10	0.52278	0.08505	0.39349	0.31875
9	0.585	0.08967	0.41689	0.38696
8	0.6675	0.09409	0.44595	0.49188
7	0.75236	0.09939	0.46594	0.56904
6	0.87338	0.10416	0.4894	0.68014
5	1.0506	0.10728	0.51602	0.84022
4	1.30082	0.10676	0.53832	0.99147

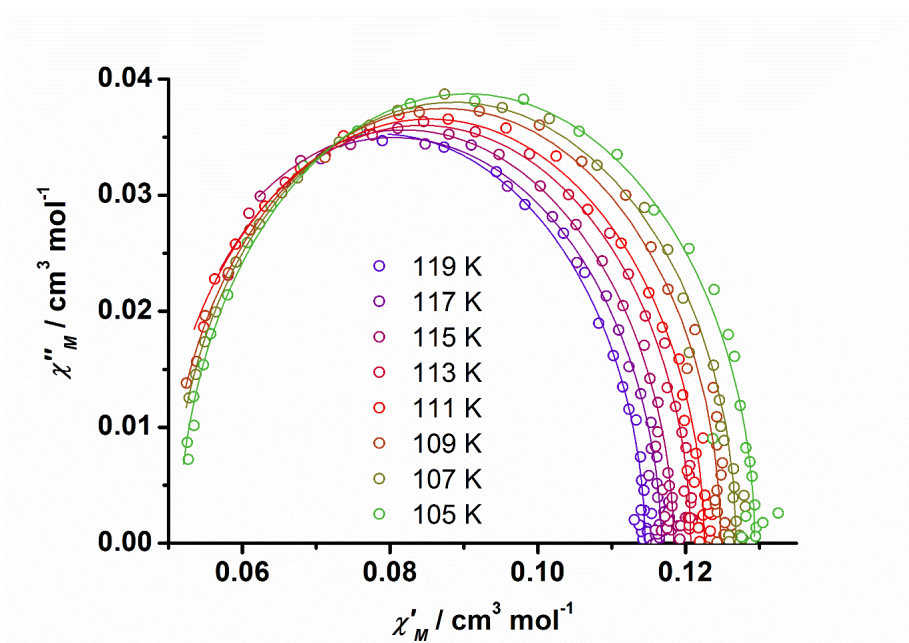


Figure 7.31 Cole-Cole plots for the AC susceptibilities in zero DC field for [4.7][B(C₆F₅)₄] from 105–119 K.

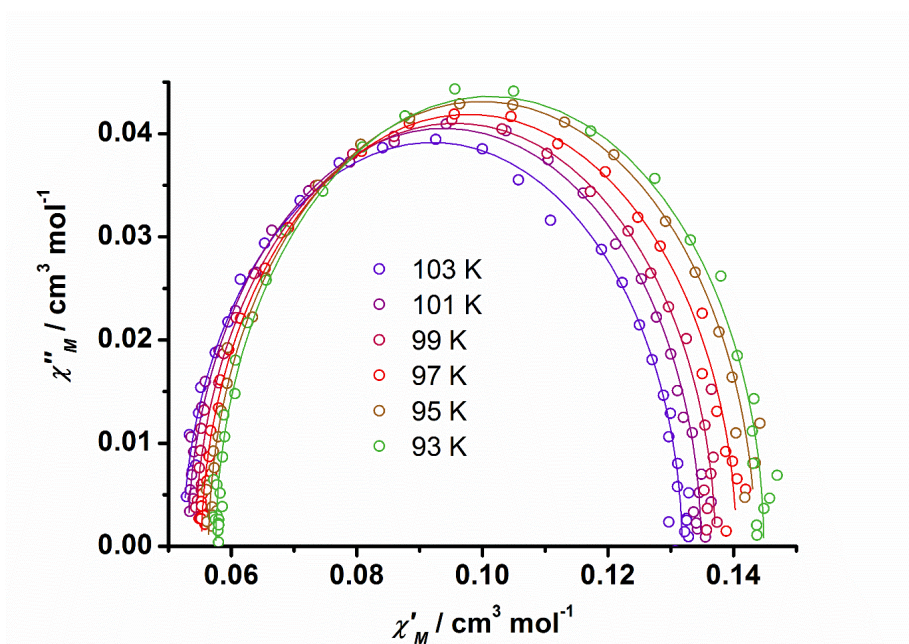


Figure 7.32 Cole-Cole plots for the AC susceptibilities in zero DC field for [4.7][B(C₆F₅)₄] from 93–103 K.

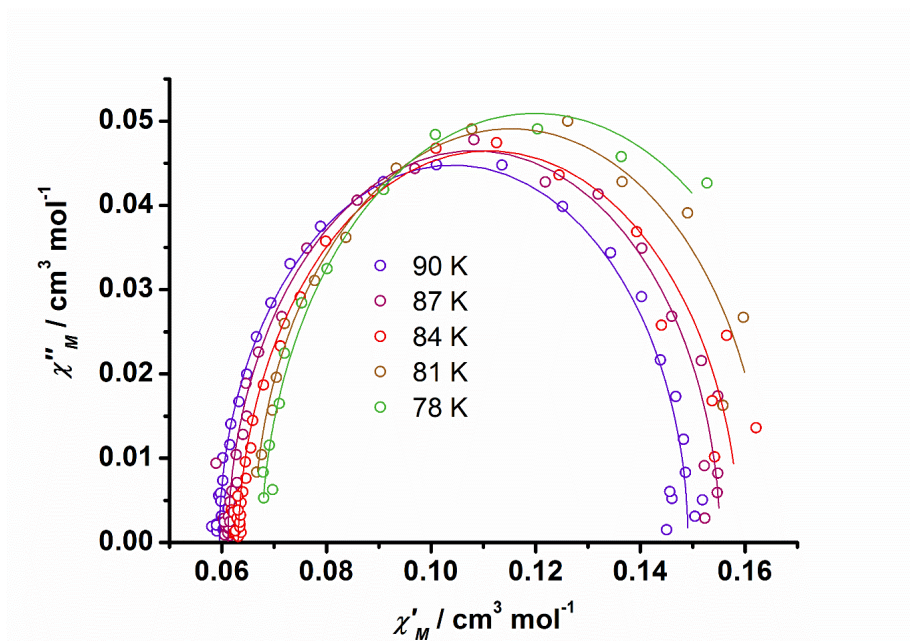


Figure 7.33 Cole-Cole plots for the AC susceptibilities in zero DC field for **[4.7][B(C₆F₅)₄]** from 78–90 K.

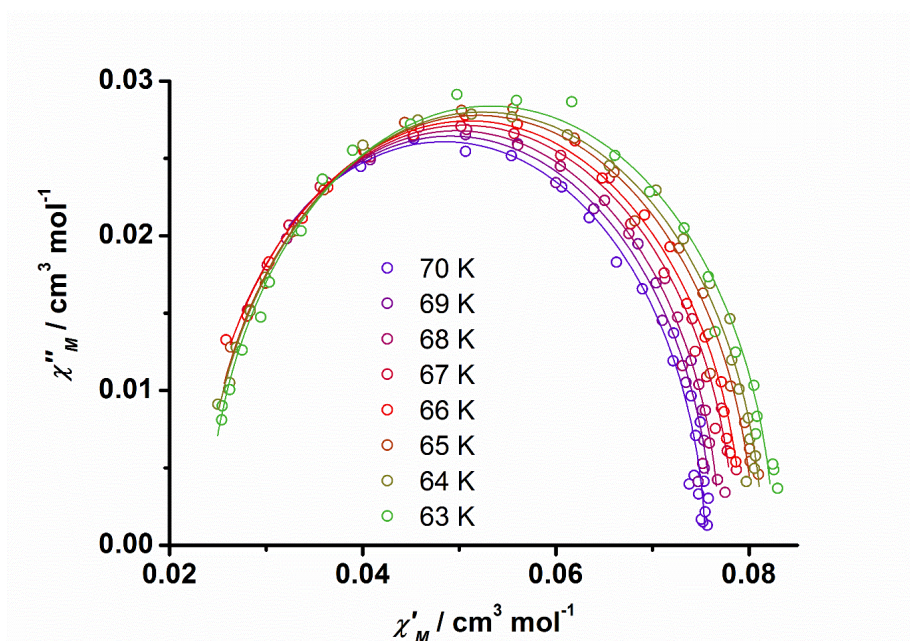


Figure 7.34 Cole-Cole plots for the AC susceptibilities in zero DC field for **[4.7][B(C₆F₅)₄]** from 63–70 K.

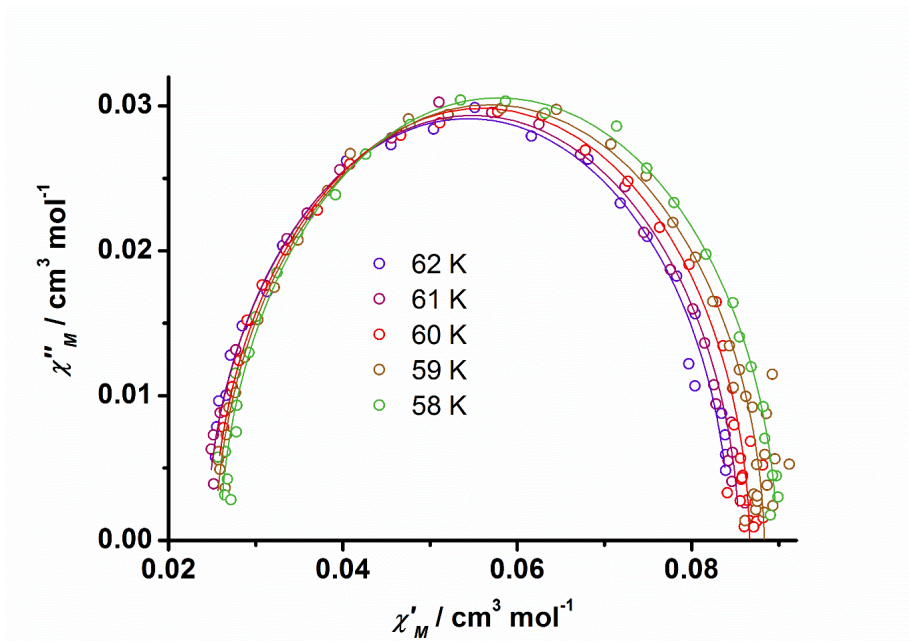


Figure 7.35 Cole-Cole plots for the AC susceptibilities in zero DC field for **[4.7][B(C₆F₅)₄]** from 58–62 K.

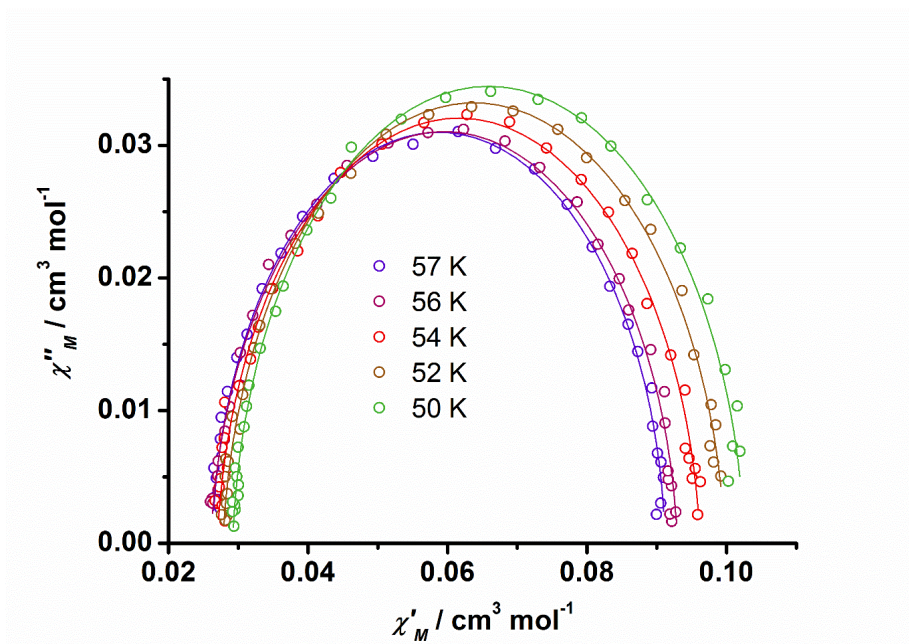


Figure 7.36 Cole-Cole plots for the AC susceptibilities in zero DC field for **[4.7][B(C₆F₅)₄]** from 50–57 K.

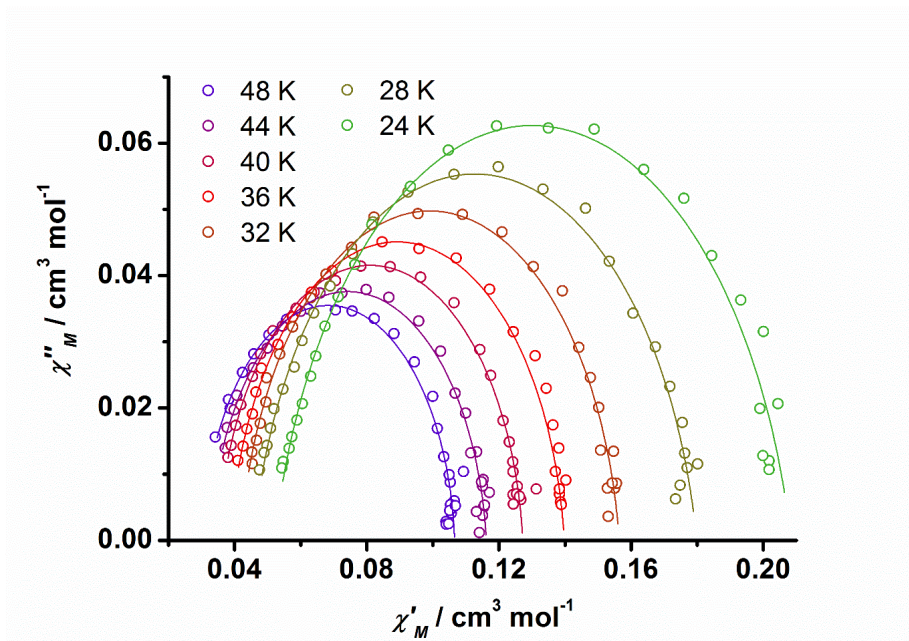


Figure 7.37 Cole-Cole plots for the AC susceptibilities in zero DC field for **[4.7][B(C₆F₅)₄]** from 24–48 K.

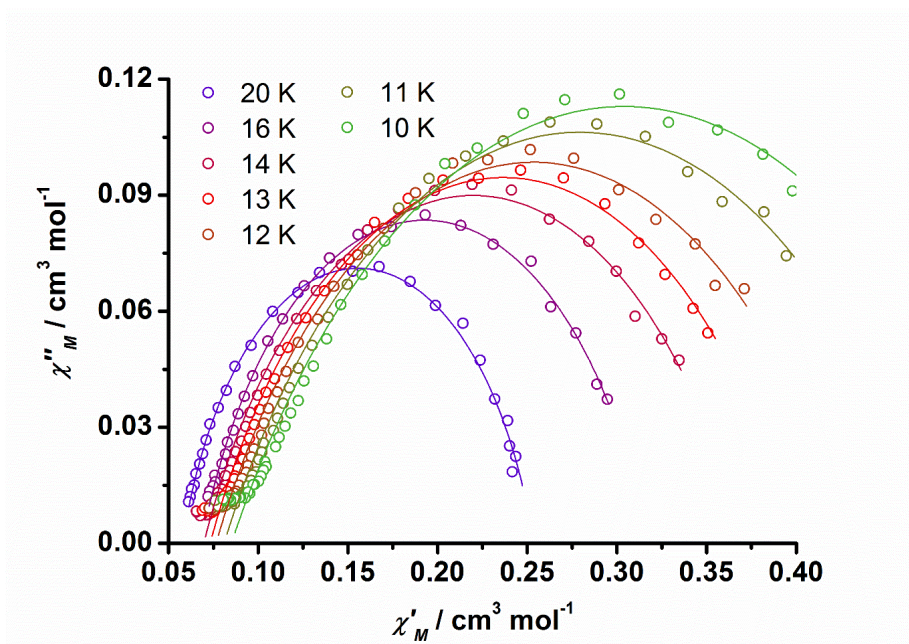


Figure 7.38 Cole-Cole plots for the AC susceptibilities in zero DC field for **[4.7][B(C₆F₅)₄]** from 10–20 K.

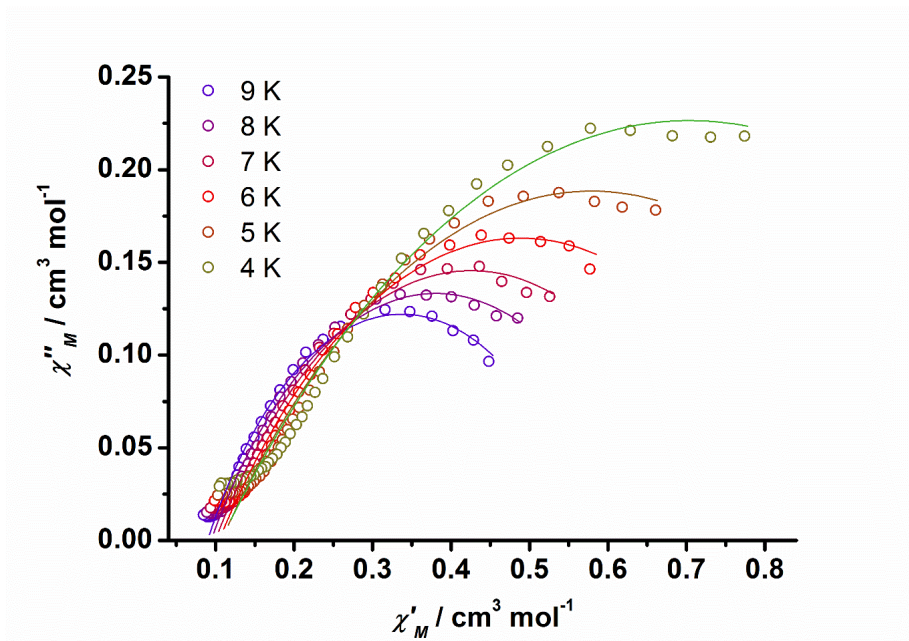


Figure 7.39 Cole-Cole plots for the AC susceptibilities in zero DC field for **[4.7][B(C₆F₅)₄]** from 4–9 K.

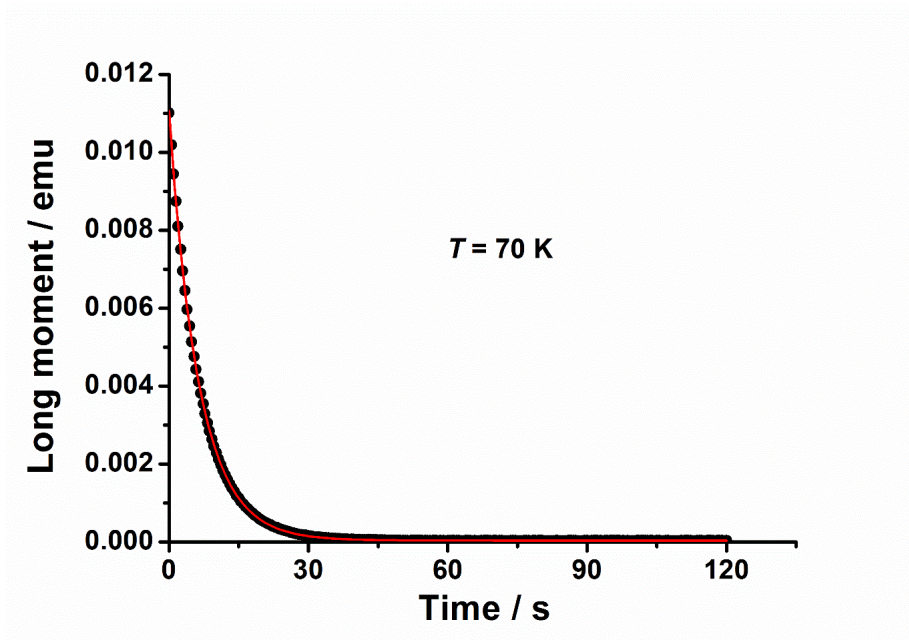


Figure 7.40 Plots of magnetization decay vs. time used to derive relaxation times for **[4.7][B(C₆F₅)₄]** at 70 K.

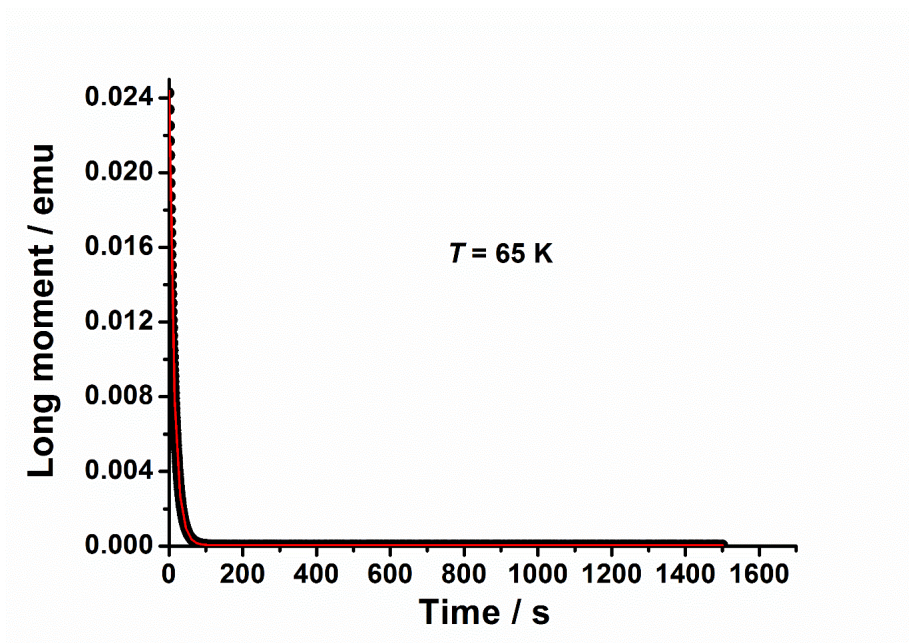


Figure 7.41 Plots of magnetization decay vs. time used to derive relaxation times for [4.7][B(C₆F₅)₄] at 65 K.

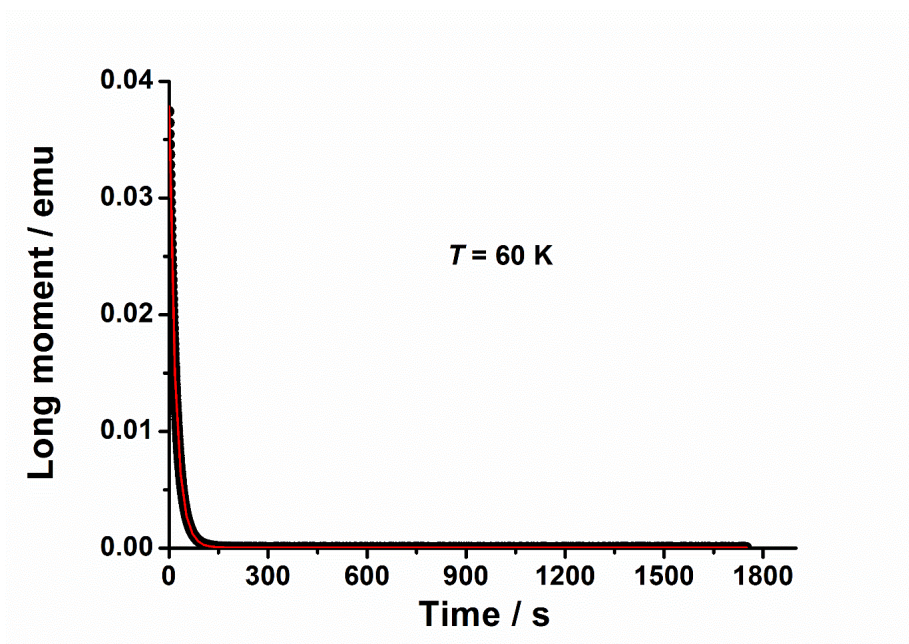


Figure 7.42 Plots of magnetization decay vs. time used to derive relaxation times for [4.7][B(C₆F₅)₄] at 60 K.

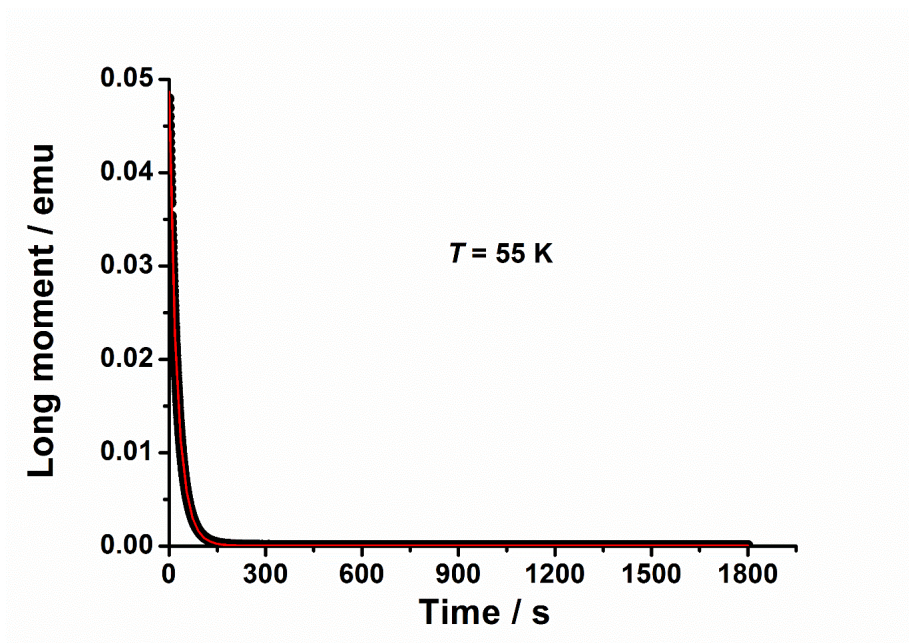


Figure 7.43 Plots of magnetization decay vs. time used to derive relaxation times for [4.7][B(C₆F₅)₄] at 55 K.

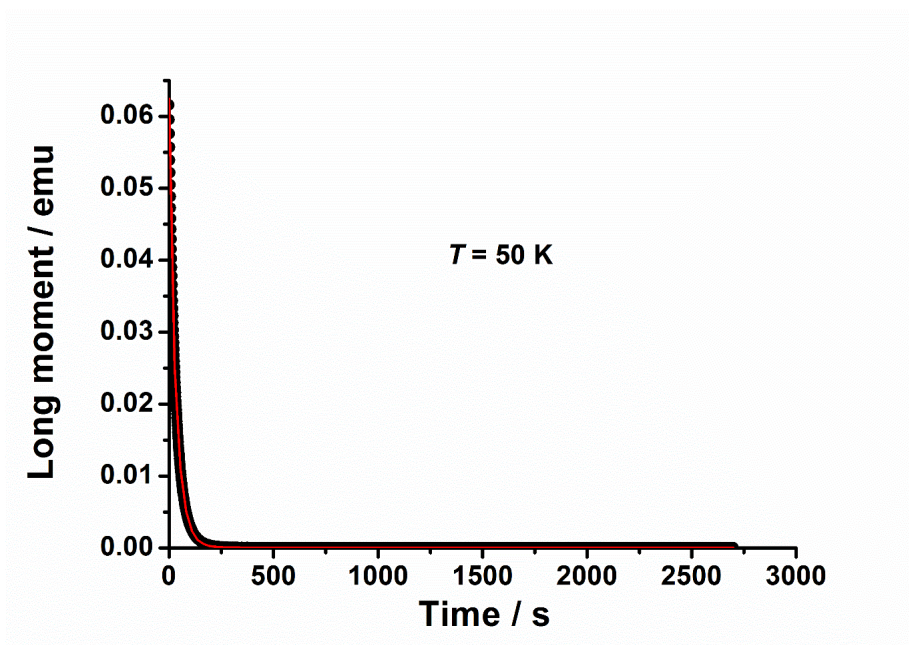


Figure 7.44 Plots of magnetization decay vs. time used to derive relaxation times for [4.7][B(C₆F₅)₄] at 50 K.

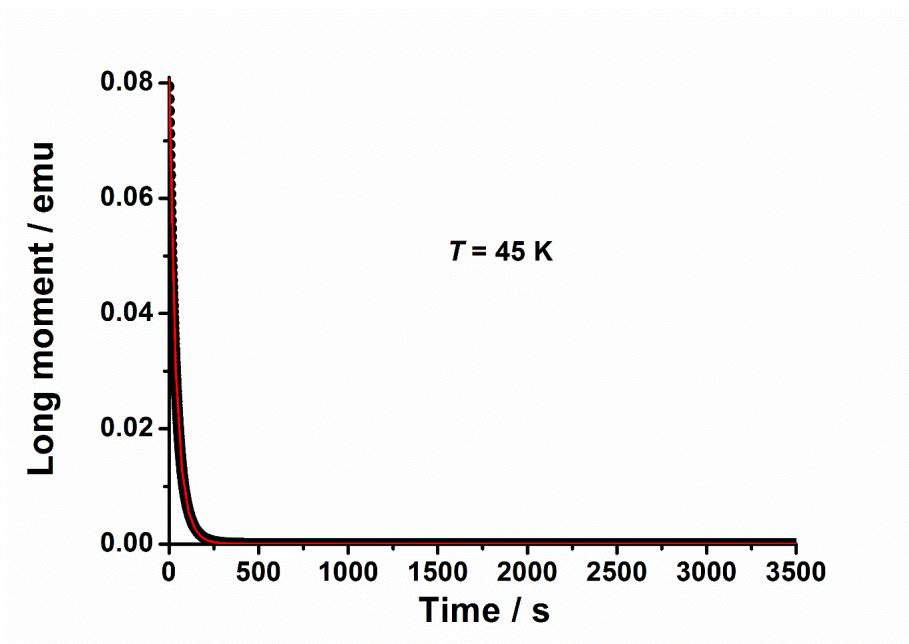


Figure 7.45 Plots of magnetization decay vs. time used to derive relaxation times for $[4.7][B(C_6F_5)_4]$ at 45 K.

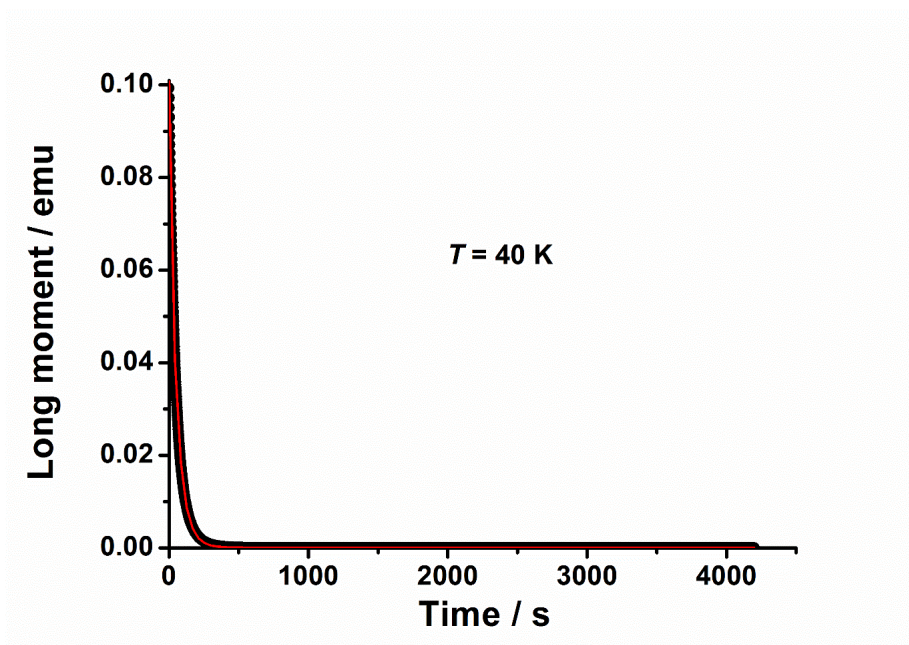


Figure 7.46 Plots of magnetization decay vs. time used to derive relaxation times for $[4.7][B(C_6F_5)_4]$ at 40 K.

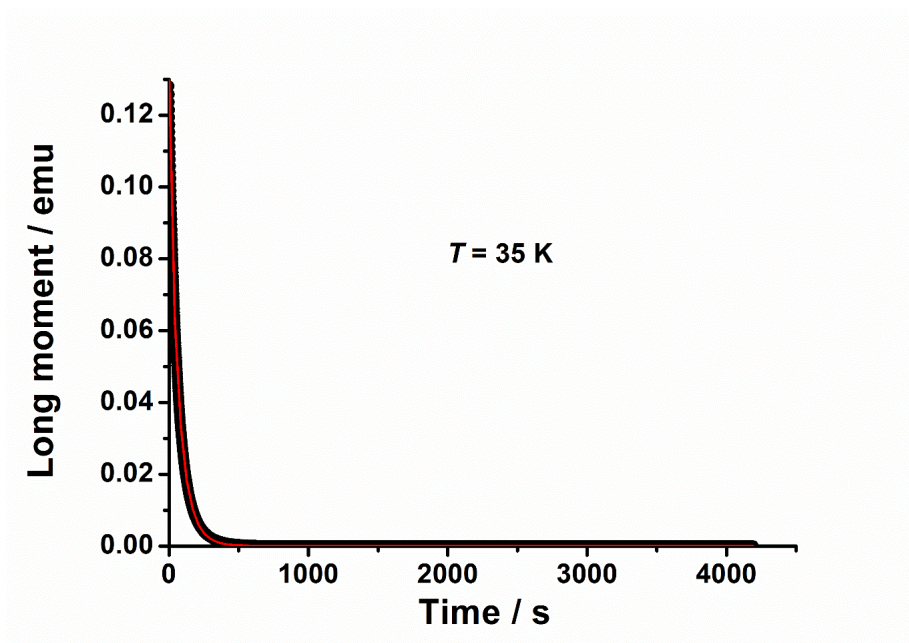


Figure 7.47 Plots of magnetization decay vs. time used to derive relaxation times for [4.7][B(C₆F₅)₄] at 35 K.

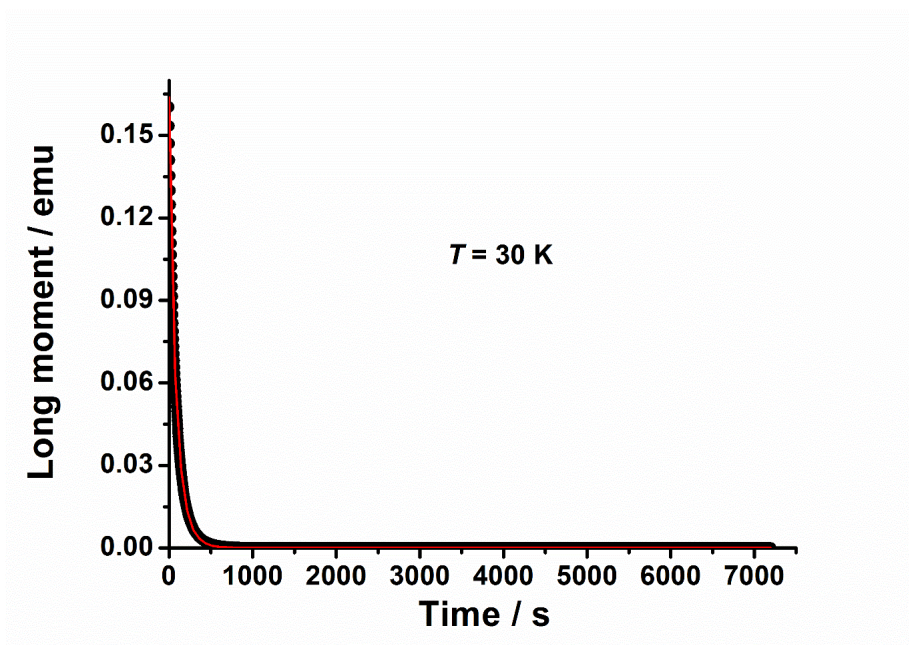


Figure 7.48 Plots of magnetization decay vs. time used to derive relaxation times for [4.7][B(C₆F₅)₄] at 30 K.

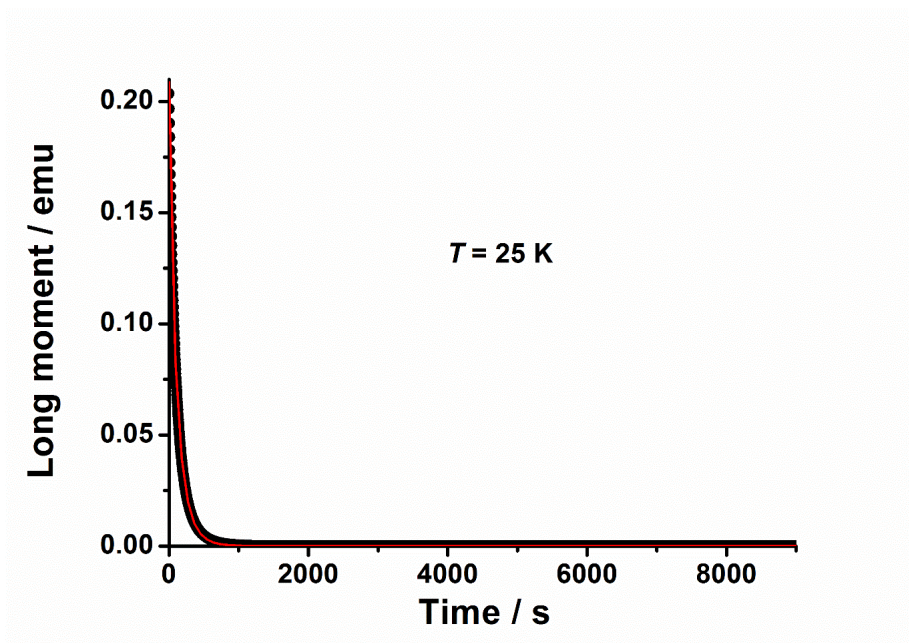


Figure 7.49 Plots of magnetization decay vs. time used to derive relaxation times for $[4.7][B(C_6F_5)_4]$ at 25 K.

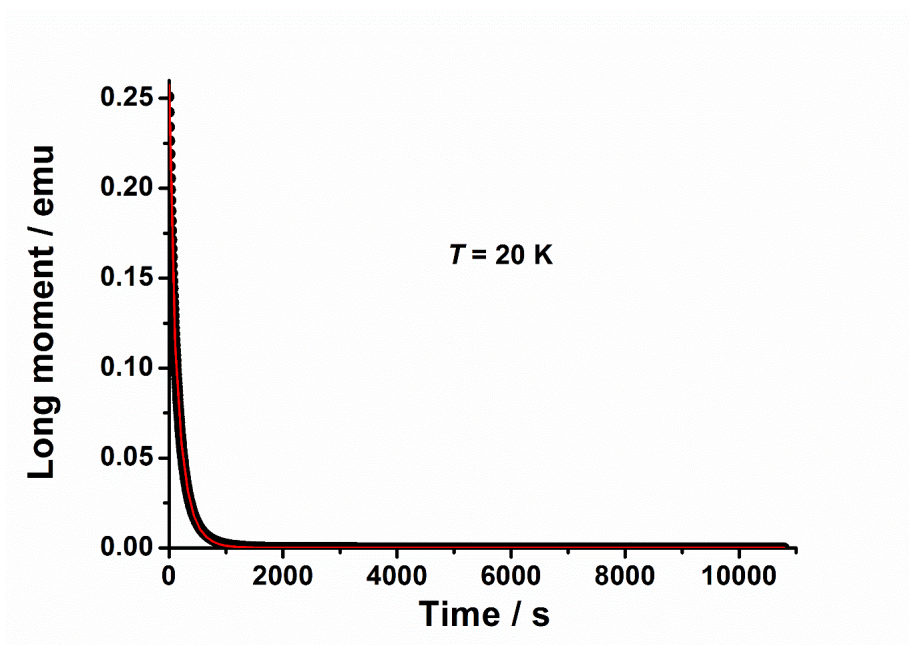


Figure 7.50 Plots of magnetization decay vs. time used to derive relaxation times for $[4.7][B(C_6F_5)_4]$ at 20 K.

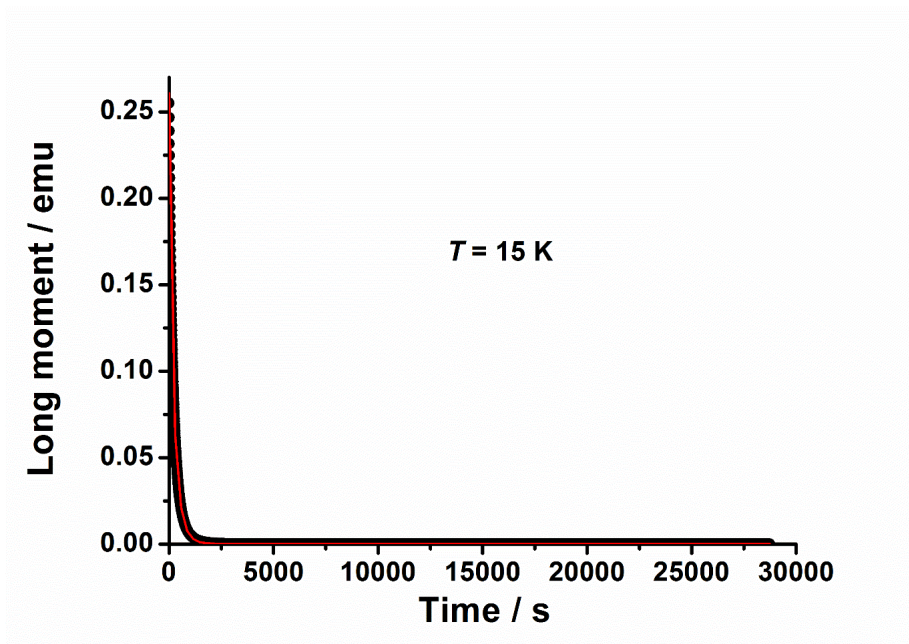


Figure 7.51 Plots of magnetization decay vs. time used to derive relaxation times for [4.7][B(C₆F₅)₄] at 15 K.

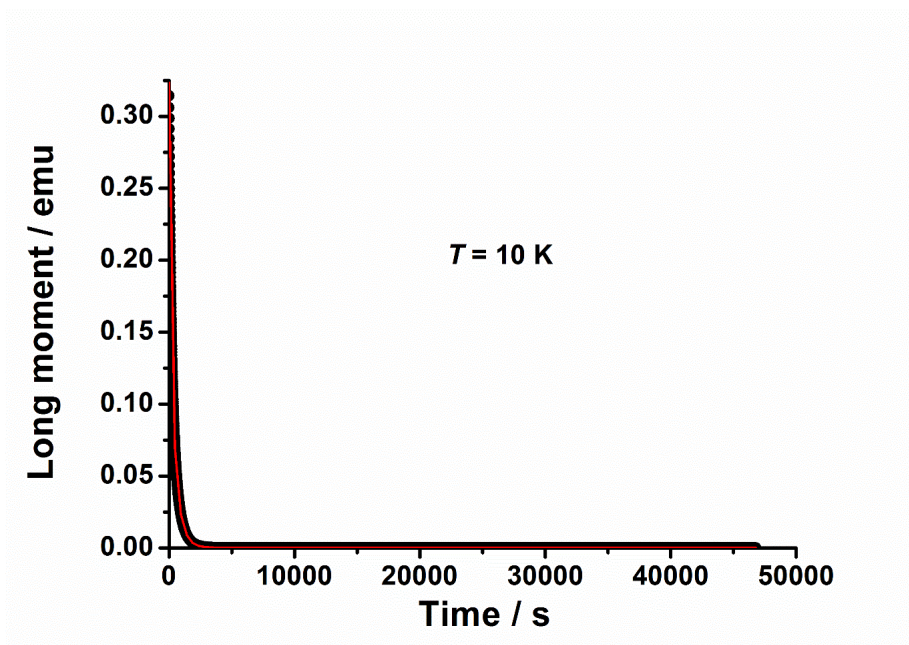


Figure 7.52 Plots of magnetization decay vs. time used to derive relaxation times for [4.7][B(C₆F₅)₄] at 10 K.

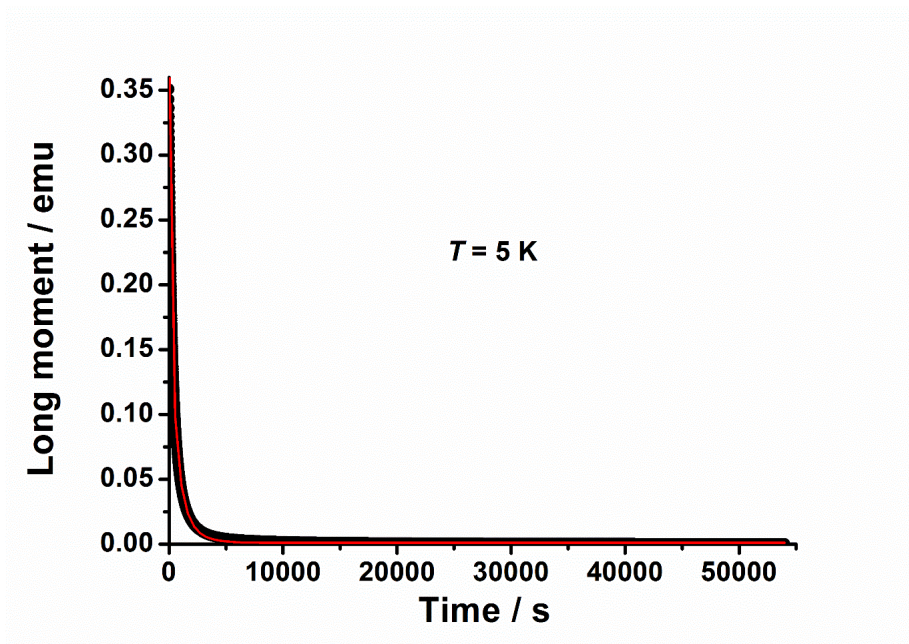


Figure 7.53 Plots of magnetization decay vs. time used to derive relaxation times for [4.7][B(C₆F₅)₄] at 5 K.

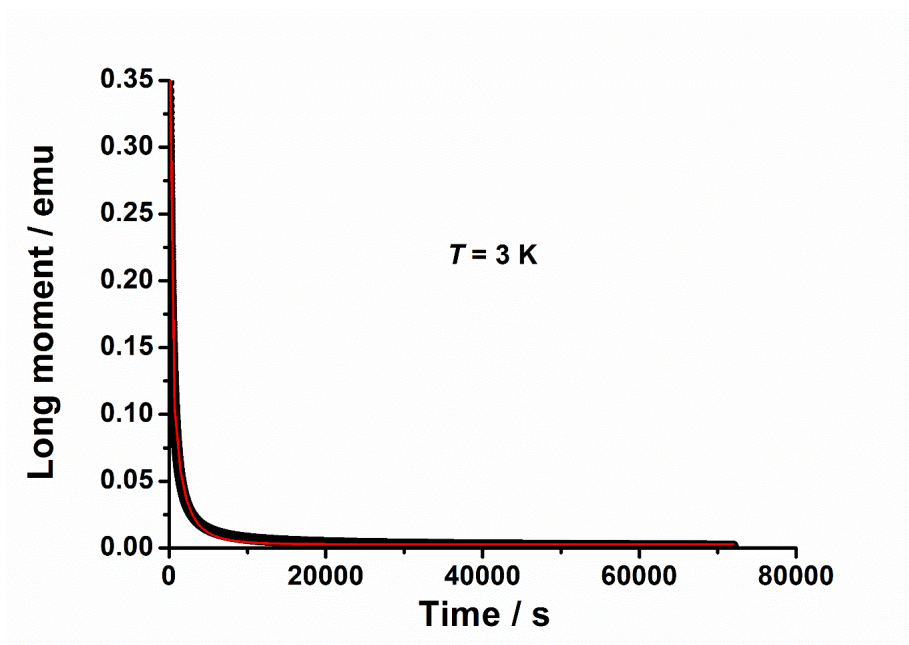


Figure 7.54 Plots of magnetization decay vs. time used to derive relaxation times for [4.7][B(C₆F₅)₄] at 3 K.

Table 7.20 Fitting parameters (initial magnetization (M_0), final magnetization (M_f), relaxation time (τ), and generalized coefficient (β)) for **[4.7][B(C₆F₅)₄]** at different temperatures from the least-squares fitting to the exponential decay as $M(t) = M_f + (M_0 - M_f) \exp[-(t/\tau)^\beta]$, as shown in Figure 7.40–7.54 and Figure 4.9.

T / K	M_f	M_0	τ / s	β
75	3.55283E-5	0.0022	1.9752	0.99946
70	3.8408E-5	0.01106	6.37419	0.98226
65	4.48027E-5	0.02438	13.22759	0.95965
60	4.44546E-5	0.03785	19.06457	0.94417
55	5.49101E-5	0.04865	24.236	0.93246
50	5.98953E-5	0.06243	30.10814	0.92496
45	6.71075E-5	0.08074	37.30459	0.9136
40	8.346E-5	0.10137	46.68922	0.90044
35	5.12631E-5	0.13095	58.98712	0.88591
30	6.23018E-5	0.16378	76.39537	0.87384
25	8.52658E-5	0.20873	100.03107	0.85543
20	1.03671E-4	0.25732	136.58272	0.84349
15	1.58857E-4	0.26074	190.96602	0.83432
10	7.09997E-5	0.3233	272.28663	0.77929
5	9.97628E-4	0.38353	338.14462	0.65582
3	0.00276	0.41586	384.68607	0.52618
2	0.00505	0.45148	412.43879	0.44874

Reference

1. P.-H. Guo, Y. Meng, Y.-C. Chen, Q.-W. Li, B.-Y. Wang, J.-D. Leng, D.-H. Bao, J.-H. Jia and M.-L. Tong, *J. Mater. Chem. C*, 2014, **2**, 8858-8864.
2. D. Pinkowicz, M. Ren, L. M. Zheng, S. Sato, M. Hasegawa, M. Morimoto, M. Irie, B. K. Breedlove, G. Cosquer and K. Katoh, *Chem. Eur. J.*, 2014, **20**, 12502-12513.
3. J. Wang, S. Chorazy, K. Nakabayashi, B. Sieklucka and S.-i. Ohkoshi, *J. Mater. Chem. C*, 2018, **6**, 473-481.
4. S. Sanvito, *Chem. Soc. Rev.*, 2011, **40**, 3336-3355.
5. F. S. Guo, B. M. Day, Y. C. Chen, M. L. Tong, A. Mansikkamaki and R. A. Layfield, *Science*, 2018, **362**, 1400-1403.
6. J. Tang and P. Zhang, *Lanthanide Single Molecule Magnets*, Springer Berlin Heidelberg, 2015.
7. C. H. Huang, *Rare Earth Coordination Chemistry: Fundamentals and Applications*, Wiley, 2011.
8. Z. B. Goldschmidt, *Handbook on the physics and chemistry of rare earths*, 1978, **1**, 1-171.
9. J. D. Rinehart and J. R. Long, *Chem. Sci.*, 2011, **2**, 2078-2085.
10. S.-D. Jiang and S.-X. Qin, *Inorg. Chem. Front.*, 2015, **2**, 613-619.
11. F. S. Guo, B. M. Day, Y. C. Chen, M. L. Tong, A. Mansikkamaki and R. A. Layfield, *Angew. Chem. Int. Ed.*, 2017, **56**, 11445-11449.
12. C. A. P. Goodwin, F. Ortu, D. Reta, N. F. Chilton and D. P. Mills, *Nature*, 2017, **548**, 439-442.
13. P. Zhang, L. Zhang, C. Wang, S. Xue, S.-Y. Lin and J. Tang, *J. Am. Chem. Soc.*, 2014, **136**, 4484-4487.
14. J. J. Le Roy, I. Korobkov and M. Murugesu, *Chem. Commun.*, 2014, **50**, 1602-1604.
15. R. Sessoli, D. Gatteschi, A. Caneschi and M. Novak, *Nature*, 1993, **365**, 141-143.
16. A. Caneschi, D. Gatteschi, R. Sessoli, A. L. Barra, L. C. Brunel and M. Guillot, *J. Am. Chem. Soc.*, 1991, **113**, 5873-5874.
17. R. Sessoli, H. L. Tsai, A. R. Schake, S. Wang, J. B. Vincent, K. Folting, D. Gatteschi, G. Christou and D. N. Hendrickson, *J. Am. Chem. Soc.*, 1993, **115**, 1804-1816.
18. T. Lis, *Acta Cryst.*, 1980, **B36**, 2042-2046.

19. L. Escalera-Moreno, J. J. Baldoví, A. Gaita-Ariño and E. Coronado, *Chem. Sci.*, 2018, **9**, 3265-3275.
20. L. Thomas, A. Caneschi and B. Barbara, *Phys. Rev. Lett.*, 1999, **83**, 2398.
21. D. Gatteschi and R. Sessoli, *Angew. Chem. Int. Ed.*, 2003, **42**, 268-297.
22. N. Shibata, Y. Kohno, A. Nakamura, S. Morishita, T. Seki, A. Kumamoto, H. Sawada, T. Matsumoto, S. D. Findlay and Y. Ikuhara, *Nat. Commun.*, 2019, **10**, 2308.
23. R. Min and Z. Li-Min, *Acta Chim. Sinica*, 2015, **73**, 1091-1113.
24. R. A. Layfield and M. Murugesu, *Lanthanides and actinides in molecular magnetism*, John Wiley & Sons, 2015.
25. M. He, F. S. Guo, J. Tang, A. Mansikkamaki and R. A. Layfield, *Chem. Sci.*, 2020, **11**, 5745-5752.
26. P. Zhang, Y.-N. Guo and J. Tang, *Coord. Chem. Rev.*, 2013, **257**, 1728-1763.
27. K. R. Meihaus, M. E. Fieser, J. F. Corbey, W. J. Evans and J. R. Long, *J. Am. Chem. Soc.*, 2015, **137**, 9855-9860.
28. J. An, Z.-D. Chen, X.-X. Zhang, H. G. Raubenheimer, C. Esterhuysen, S. Gao and G.-X. Xu, *J. Chem. Soc., Dalton Trans.*, 2001, 3352-3356.
29. G. Christou, *Polyhedron*, 2005, **24**, 2065-2075.
30. M. Feng and M. L. Tong, *Chem. Eur. J.*, 2018, **24**, 7574-7594.
31. A. J. Tasiopoulos, A. Vinslava, W. Wernsdorfer, K. A. Abboud and G. Christou, *Angew. Chem. Int. Ed.*, 2004, **43**, 2117-2121.
32. A. M. Ako, I. J. Hewitt, V. Mereacre, R. Clerac, W. Wernsdorfer, C. E. Anson and A. K. Powell, *Angew. Chem. Int. Ed.*, 2006, **45**, 4926-4929.
33. S. M. Aubin, M. W. Wemple, D. M. Adams, H.-L. Tsai, G. Christou and D. N. Hendrickson, *J. Am. Chem. Soc.*, 1996, **118**, 7746-7754.
34. C. J. Milios, A. Vinslava, W. Wernsdorfer, A. Prescimone, P. A. Wood, S. Parsons, S. P. Perlepes, G. Christou and E. K. Brechin, *J. Am. Chem. Soc.*, 2007, **129**, 6547-6561.
35. S. Realista, A. Fitzpatrick, G. Santos, L. Ferreira, S. Barroso, L. Pereira, N. Bandeira, P. Neugebauer, J. Hrubý and G. Morgan, *Dalton Trans.*, 2016, **45**, 12301-12307.
36. G. A. Craig, J. J. Marbey, S. Hill, O. Roubeau, S. Parsons and M. Murrie, *Inorg. Chem.*, 2015, **54**, 13-15.

37. J. Vallejo, A. Pascual-Alvarez, J. Cano, I. Castro, M. Julve, F. Lloret, J. Krzystek, G. De Munno, D. Armentano, W. Wernsdorfer, R. Ruiz-Garcia and E. Pardo, *Angew. Chem. Int. Ed.*, 2013, **52**, 14075-14079.
38. Y.-M. Liu, Z.-Y. Liu, E.-C. Yang and X.-J. Zhao, *Inorg. Chem. Commun.*, 2017, **77**, 27-30.
39. A. Pascual - Álvarez, J. Vallejo, E. Pardo, M. Julve, F. Lloret, J. Krzystek, D. Armentano, W. Wernsdorfer and J. Cano, *Chem. Eur. J.*, 2015, **21**, 17299-17307.
40. L. Chen, J. Wang, Y. Z. Liu, Y. Song, X. T. Chen, Y. Q. Zhang and Z. L. Xue, *Eur. J. Inorg. Chem.*, 2015, **2015**, 271-278.
41. M. Ding, G. E. Cutsail III, D. Aravena, M. Amoza, M. Rouziers, P. Dechambenoit, Y. Losovyj, M. Pink, E. Ruiz, R. Clerac and J. M. Smith, *Chem. Sci.*, 2016, **7**, 6132-6140.
42. C. Sangregorio, T. Ohm, C. Paulsen, R. Sessoli and D. Gatteschi, *Phys. Rev. Lett.*, 1997, **78**, 4645.
43. A. K. Bar, C. Pichon and J.-P. Sutter, *Coord. Chem. Rev.*, 2016, **308**, 346-380.
44. J. M. Frost, K. L. Harriman and M. Murugesu, *Chem. Sci.*, 2016, **7**, 2470-2491.
45. J. M. Zadrozny, D. J. Xiao, M. Atanasov, G. J. Long, F. Grandjean, F. Neese and J. R. Long, *Nat. Chem.*, 2013, **5**, 577-581.
46. C. G. Werncke, P. C. Bunting, C. Duhayon, J. R. Long, S. Bontemps and S. Sabo-Etienne, *Angew. Chem. Int. Ed.*, 2015, **54**, 245-248.
47. J. M. Zadrozny, M. Atanasov, A. M. Bryan, C.-Y. Lin, B. D. Rekker, P. P. Power, F. Neese and J. R. Long, *Chem. Sci.*, 2013, **4**, 125-138.
48. E.-C. Yang, D. N. Hendrickson, W. Wernsdorfer, M. Nakano, L. N. Zakharov, R. D. Sommer, A. L. Rheingold, M. Ledezma-Gairaud and G. Christou, *J. Appl. Phys.*, 2002, **91**, 7382-7384.
49. M. Murrie, *Chem. Soc. Rev.*, 2010, **39**, 1986-1995.
50. J. M. Zadrozny and J. R. Long, *J. Am. Chem. Soc.*, 2011, **133**, 20732-20734.
51. X.-N. Yao, J.-Z. Du, Y.-Q. Zhang, X.-B. Leng, M.-W. Yang, S.-D. Jiang, Z.-X. Wang, Z.-W. Ouyang, L. Deng and B.-W. Wang, *J. Am. Chem. Soc.*, 2017, **139**, 373-380.
52. N. Ishikawa, M. Sugita, T. Ishikawa, S.-y. Koshihara and Y. Kaizu, *J. Am. Chem. Soc.*, 2003, **125**, 8694-8695.

53. N. Ishikawa, M. Sugita, T. Okubo, N. Tanaka, T. Iino and Y. Kaizu, *Inorg. Chem.*, 2003, **42**, 2440-2446.
54. N. Ishikawa, M. Sugita, N. Tanaka, T. Ishikawa, S.-y. Koshihara and Y. Kaizu, *Inorg. Chem.*, 2004, **43**, 5498-5500.
55. S. Takamatsu, T. Ishikawa, S.-y. Koshihara and N. Ishikawa, *Inorg. Chem.*, 2007, **46**, 7250-7252.
56. N. Ishikawa, Y. Mizuno, S. Takamatsu, T. Ishikawa and S.-y. Koshihara, *Inorg. Chem.*, 2008, **47**, 10217-10219.
57. C. R. Ganivet, B. Ballesteros, G. de la Torre, J. M. Clemente-Juan, E. Coronado and T. Torres, *Chem. Eur. J.*, 2013, **19**, 1457-1465.
58. M. A. AlDamen, J. M. Clemente-Juan, E. Coronado, C. Martí-Gastaldo and A. Gaita-Ariño, *J. Am. Chem. Soc.*, 2008, **130**, 8874-8875.
59. J. J. Baldoví, J. M. Clemente-Juan, E. Coronado, Y. Duan, A. Gaita-Ariño and C. Giménez-Saiz, *Inorg. Chem.*, 2014, **53**, 9976-9980.
60. S. D. Jiang, B. W. Wang, H. L. Sun, Z. M. Wang and S. Gao, *J. Am. Chem. Soc.*, 2011, **133**, 4730-4733.
61. K. R. Meihaus and J. R. Long, *J. Am. Chem. Soc.*, 2013, **135**, 17952-17957.
62. L. Ungur, J. J. Le Roy, I. Korobkov, M. Murugesu and L. F. Chibotaru, *Angew. Chem. Int. Ed.*, 2014, **53**, 4413-4417.
63. Y.-S. Meng, C.-H. Wang, Y.-Q. Zhang, X.-B. Leng, B.-W. Wang, Y.-F. Chen and S. Gao, *Inorg. Chem. Front.*, 2016, **3**, 828-835.
64. J. Tang, I. Hewitt, N. Madhu, G. Chastanet, W. Wernsdorfer, C. Anson, C. Benelli, R. Sessoli and A. Powell, *Angew. Chem. Int. Ed.*, 2006, **45**, 1729-1733.
65. P. H. Lin, T. J. Burchell, R. Clerac and M. Murugesu, *Angew. Chem. Int. Ed.*, 2008, **47**, 8848-8851.
66. G.-F. Xu, Q.-L. Wang, P. Gamez, Y. Ma, R. Clérac, J. Tang, S.-P. Yan, P. Cheng and D.-Z. Liao, *Chem. Commun.*, 2010, **46**, 1506-1508.
67. Y. Ma, G.-F. Xu, X. Yang, L.-C. Li, J. Tang, S.-P. Yan, P. Cheng and D.-Z. Liao, *Chem. Commun.*, 2010, **46**, 8264-8266.
68. R. A. Layfield, J. J. McDouall, S. A. Sulway, F. Tuna, D. Collison and R. E. Winpenny, *Chem. Eur. J.*, 2010, **16**, 4442-4446.

69. J. Long, F. Habib, P.-H. Lin, I. Korobkov, G. Enright, L. Ungur, W. Wernsdorfer, L. F. Chibotaru and M. Murugesu, *J. Am. Chem. Soc.*, 2011, **133**, 5319-5328.
70. F. Habib, P.-H. Lin, J. Long, I. Korobkov, W. Wernsdorfer and M. Murugesu, *J. Am. Chem. Soc.*, 2011, **133**, 8830-8833.
71. J. D. Rinehart, M. Fang, W. J. Evans and J. R. Long, *Nat. Chem.*, 2011, **3**, 538-542.
72. P.-H. Lin, W.-B. Sun, M.-F. Yu, G.-M. Li, P.-F. Yan and M. Murugesu, *Chem. Commun.*, 2011, **47**, 10993-10995.
73. S. A. Sulway, R. A. Layfield, F. Tuna, W. Wernsdorfer and R. E. Winpenny, *Chem. Commun.*, 2012, **48**, 1508-1510.
74. Y.-N. Guo, G.-F. Xu, W. Wernsdorfer, L. Ungur, Y. Guo, J. Tang, H.-J. Zhang, L. F. Chibotaru and A. K. Powell, *J. Am. Chem. Soc.*, 2011, **133**, 11948-11951.
75. Y.-N. Guo, X.-H. Chen, S. Xue and J. Tang, *Inorg. Chem.*, 2011, **50**, 9705-9713.
76. F. Tuna, C. A. Smith, M. Bodensteiner, L. Ungur, L. F. Chibotaru, E. J. McInnes, R. E. Winpenny, D. Collison and R. A. Layfield, *Angew. Chem. Int. Ed.*, 2012, **51**, 6976-6980.
77. S. Demir, J. M. Zadrozny, M. Nippe and J. R. Long, *J. Am. Chem. Soc.*, 2012, **134**, 18546-18549.
78. Y. M. Song, F. Luo, M. B. Luo, Z. W. Liao, G. M. Sun, X. Z. Tian, Y. Zhu, Z. J. Yuan, S. J. Liu, W. Y. Xu and X. F. Feng, *Chem. Commun.*, 2012, **48**, 1006-1008.
79. I. J. Hewitt, Y. Lan, C. E. Anson, J. Luzon, R. Sessoli and A. K. Powell, *Chem. Commun.*, 2009, 6765-6767.
80. C.-S. Liu, M. Du, E. C. Sañudo, J. Echeverria, M. Hu, Q. Zhang, L.-M. Zhou and S.-M. Fang, *Dalton Trans.*, 2011, **40**, 9366-9369.
81. S.-Y. Lin, L. Zhao, Y.-N. Guo, P. Zhang, Y. Guo and J. Tang, *Inorg. Chem.*, 2012, **51**, 10522-10528.
82. S.-Y. Lin, Y.-N. Guo, Y. Guo, L. Zhao, P. Zhang, H. Ke and J. Tang, *Chem. Commun.*, 2012, **48**, 6924-6926.
83. P. H. Lin, T. J. Burchell, L. Ungur, L. F. Chibotaru, W. Wernsdorfer and M. Murugesu, *Angew. Chem. Int. Ed.*, 2009, **48**, 9489-9492.
84. Y.-N. Guo, G.-F. Xu, P. Gamez, L. Zhao, S.-Y. Lin, R. Deng, J. Tang and H.-J. Zhang, *J. Am. Chem. Soc.*, 2010, **132**, 8538-8539.
85. H. Ke, G.-F. Xu, Y.-N. Guo, P. Gamez, C. M. Beavers, S. J. Teat and J. Tang, *Chem. Commun.*, 2010, **46**, 6057-6059.

86. M. U. Anwar, L. K. Thompson, L. N. Dawe, F. Habib and M. Murugesu, *Chem. Commun.*, 2012, **48**, 4576-4578.
87. S. Xue, L. Zhao, Y.-N. Guo, X.-H. Chen and J. Tang, *Chem. Commun.*, 2012, **48**, 7031-7033.
88. R. J. Blagg, L. Ungur, F. Tuna, J. Speak, P. Comar, D. Collison, W. Wernsdorfer, E. J. McInnes, L. F. Chibotaru and R. E. Winpenny, *Nat. Chem.*, 2013, **5**, 673-678.
89. B. Hussain, D. Savard, T. J. Burchell, W. Wernsdorfer and M. Murugesu, *Chem. Commun.*, 2009, 1100-1102.
90. I. J. Hewitt, J. Tang, N. Madhu, C. E. Anson, Y. Lan, J. Luzon, M. Etienne, R. Sessoli and A. K. Powell, *Angew. Chem. Int. Ed.*, 2010, **49**, 6352-6356.
91. S. K. Langley, B. Moubaraki, C. M. Forsyth, I. A. Gass and K. S. Murray, *Dalton Trans.*, 2010, **39**, 1705-1708.
92. S. Sanz, R. D. McIntosh, C. M. Beavers, S. J. Teat, M. Evangelisti, E. K. Brechin and S. J. Dalgarno, *Chem. Commun.*, 2012, **48**, 1449-1451.
93. H. Tian, M. Wang, L. Zhao, Y. N. Guo, Y. Guo, J. Tang and Z. Liu, *Chem. Eur. J.*, 2012, **18**, 442-445.
94. S. Y. Lin, W. Wernsdorfer, L. Ungur, A. K. Powell, Y. N. Guo, J. Tang, L. Zhao, L. F. Chibotaru and H. J. Zhang, *Angew. Chem. Int. Ed.*, 2012, **51**, 12767-12771.
95. Y.-N. Guo, X.-H. Chen, S. Xue and J. Tang, *Inorg. Chem.*, 2012, **51**, 4035-4042.
96. Y. Z. Zheng, Y. Lan, W. Wernsdorfer, C. E. Anson and A. K. Powell, *Chem. Eur. J.*, 2009, **15**, 12566-12570.
97. X. Gu and D. Xue, *Inorg. Chem.*, 2007, **46**, 3212-3216.
98. J.-L. Liu, Y.-C. Chen, Y.-Z. Zheng, W.-Q. Lin, L. Ungur, W. Wernsdorfer, L. F. Chibotaru and M.-L. Tong, *Chem. Sci.*, 2013, **4**, 3310-3316.
99. J. Liu, Y.-C. Chen, J.-L. Liu, V. Vieru, L. Ungur, J.-H. Jia, L. F. Chibotaru, Y. Lan, W. Wernsdorfer and S. Gao, *J. Am. Chem. Soc.*, 2016, **138**, 5441-5450.
100. Y. S. Ding, N. F. Chilton, R. E. Winpenny and Y. Z. Zheng, *Angew. Chem. Int. Ed.*, 2016, **55**, 16071-16074.
101. R. Sessoli, *Nature*, 2017, **548**, 400-401.
102. J. Vallejo, J. Cano, I. Castro, M. Julve, F. Lloret, O. Fabelo, L. Cañadillas-Delgado and E. Pardo, *Chem. Commun.*, 2012, **48**, 7726-7728.

103. J. J. Le Roy, I. Korobkov, J. E. Kim, E. J. Schelter and M. Murugesu, *Dalton Trans.*, 2014, **43**, 2737-2740.
104. J. J. Le Roy, S. I. Gorelsky, I. Korobkov and M. Murugesu, *Organometallics*, 2015, **34**, 1415-1418.
105. Y.-S. Meng, Y.-S. Qiao, Y.-Q. Zhang, S.-D. Jiang, Z.-S. Meng, B.-W. Wang, Z.-M. Wang and S. Gao, *Chem. Eur. J.*, 2016, **22**, 4704-4708.
106. K. S. Pedersen, J. Dreiser, H. Weihe, R. Sibille, H. V. Johannesen, M. A. Sørensen, B. E. Nielsen, M. Sigrist, H. Mutka, S. Rols, J. Bendix and S. Piligkos, *Inorg. Chem.*, 2015, **54**, 7600-7606.
107. N. Magnani, C. Apostolidis, A. Morgenstern, E. Colineau, J. C. Griveau, H. Bolvin, O. Walter and R. Caciuffo, *Angew. Chem. Int. Ed.*, 2011, **50**, 1696-1698.
108. N. Magnani, E. Colineau, J.-C. Griveau, C. Apostolidis, O. Walter and R. Caciuffo, *Chem. Commun.*, 2014, **50**, 8171-8173.
109. S. A. Kozimor, B. M. Bartlett, J. D. Rinehart and J. R. Long, *J. Am. Chem. Soc.*, 2007, **129**, 10672-10674.
110. B. M. Gardner, C. E. Kefalidis, E. Lu, D. Patel, E. J. L. McInnes, F. Tuna, A. J. Wooles, L. Maron and S. T. Liddle, *Nat. Commun.*, 2017, **8**, 1898.
111. C. Camp, V. Mougel, J. Pécaut, L. Maron and M. Mazzanti, *Chem. Eur. J.*, 2013, **19**, 17528-17540.
112. C. T. Palumbo, L. Barluzzi, R. Scopelliti, I. Zivkovic, A. Fabrizio, C. Corminboeuf and M. Mazzanti, *Chem. Sci.*, 2019, **10**, 8840-8849.
113. J. D. Rinehart and J. R. Long, *J. Am. Chem. Soc.*, 2009, **131**, 12558-12559.
114. D. M. King, F. Tuna, J. McMaster, W. Lewis, A. J. Blake, E. J. McInnes and S. T. Liddle, *Angew. Chem. Int. Ed.*, 2013, **52**, 4921-4924.
115. L. C. Pereira, C. m. Camp, J. T. Coutinho, L. Chatelain, P. Maldivi, M. Almeida and M. Mazzanti, *Inorg. Chem.*, 2014, **53**, 11809-11811.
116. J. D. Rinehart, K. R. Meihaus and J. R. Long, *J. Am. Chem. Soc.*, 2010, **132**, 7572-7573.
117. J. T. Coutinho, M. Perfetti, J. J. Baldoví, M. A. Antunes, P. P. Hallmen, H. Bamberger, I. Crassee, M. Orlita, M. Almeida and J. Van Slageren, *Chem. Eur. J.*, 2019, **25**, 1758-1766.

118. K. R. Meihaus, S. G. Minasian, W. W. Lukens Jr, S. A. Kozimor, D. K. Shuh, T. Tyliczszak and J. R. Long, *J. Am. Chem. Soc.*, 2014, **136**, 6056-6068.
119. J. J. Le Roy, S. I. Gorelsky, I. Korobkov and M. Murugesu, *Organometallics*, 2015, **34**, 1415-1418.
120. F. S. Guo, Y. C. Chen, M. L. Tong, A. Mansikkamäki and R. A. Layfield, *Angew. Chem. Int. Ed.*, 2019, **58**, 10163-10167.
121. F. S. Guo, N. Tsoureas, G. Z. Huang, M. L. Tong, A. Mansikkamäki and R. A. Layfield, *Angew. Chem. Int. Ed.*, 2020, **59**, 2299-2303.
122. L. Escalera-Moreno, J. J. Baldoví, A. Gaita-Ariño and E. Coronado, *Inorg. Chem.*, 2019, **58**, 11883-11892.
123. X. L. Ding, Y. Q. Zhai, T. Han, W. P. Chen, Y. S. Ding and Y. Z. Zheng, *Chem. Eur. J.*, 2021, **27**, 2623-2627.
124. G. Wilkinson and J. M. Birmingham, *J. Am. Chem. Soc.*, 1954, **76**, 6210-6210.
125. J. M. Birmingham and G. Wilkinson, *J. Am. Chem. Soc.*, 1956, **78**, 42-44.
126. H.-L. Teng, Y. Luo, M. Nishiura and Z. Hou, *J. Am. Chem. Soc.*, 2017, **139**, 16506-16509.
127. K. R. Meihaus, M. E. Fieser, J. F. Corbey, W. J. Evans and J. R. Long, *J. Am. Chem. Soc.*, 2015, **137**, 9855-9860.
128. S. Demir, M. D. Boshart, J. F. Corbey, D. H. Woen, M. I. Gonzalez, J. W. Ziller, K. R. Meihaus, J. R. Long and W. J. Evans, *Inorg. Chem.*, 2017, **56**, 15049-15056.
129. W. J. Evans, C. A. Seibel and J. W. Ziller, *J. Am. Chem. Soc.*, 1998, **120**, 6745-6752.
130. W. J. Evans, B. L. Davis, T. M. Champagne and J. W. Ziller, *PNAS*, 2006, **103**, 12678-12683.
131. S. Demir, J. M. Zadrozny and J. R. Long, *Chem. Eur. J.*, 2014, **20**, 9524-9529.
132. K. Randall McClain, C. A. Gould, K. Chakarawet, S. J. Teat, T. J. Groshens, J. R. Long and B. G. Harvey, *Chem. Sci.*, 2018, **9**, 8492-8503.
133. D. N. Woodruff, R. E. P. Winpenny and R. A. Layfield, *Chem. Rev.*, 2013, **113**, 5110-5148.
134. J. Wang, Q.-W. Li, S.-G. Wu, Y.-C. Chen, R.-C. Wan, G.-Z. Huang, Y. Liu, J.-L. Liu, D. Reta, M. J. Giansiracusa, Z.-X. Wang, N. F. Chilton and M.-L. Tong, *Angew. Chem. Int. Ed.*, 2021, **60**, 5299-5306.

135. S. Sakaue, A. Fuyuhiko, T. Fukuda and N. Ishikawa, *Chem. Commun.*, 2012, **48**, 5337-5339.
136. K. Katoh, T. Kajiwara, M. Nakano, Y. Nakazawa, W. Wernsdorfer, N. Ishikawa, B. K. Breedlove and M. Yamashita, *Chem. Eur. J.*, 2011, **17**, 117-122.
137. T. Morita, K. Katoh, B. K. Breedlove and M. Yamashita, *Inorg. Chem.*, 2013, **52**, 13555-13561.
138. T. Morita, M. Damjanović, K. Katoh, Y. Kitagawa, N. Yasuda, Y. Lan, W. Wernsdorfer, B. K. Breedlove, M. Enders and M. Yamashita, *J. Am. Chem. Soc.*, 2018, **140**, 2995-3007.
139. J. J. Le Roy, M. Jeletic, S. I. Gorelsky, I. Korobkov, L. Ungur, L. F. Chibotaru and M. Murugesu, *J. Am. Chem. Soc.*, 2013, **135**, 3502-3510.
140. B. M. Day, F.-S. Guo and R. A. Layfield, *Acc. Chem. Res.*, 2018, **51**, 1880-1889.
141. T. Pugh, F. Tuna, L. Ungur, D. Collison, E. J. L. McInnes, L. F. Chibotaru and R. A. Layfield, *Nat. Commun.*, 2015, **6**, 7492.
142. C. A. Gould, L. E. Darago, M. I. Gonzalez, S. Demir and J. R. Long, *Angew. Chem. Int. Ed.*, 2017, **56**, 10103-10107.
143. F.-S. Guo and R. A. Layfield, *Chem. Commun.*, 2017, **53**, 3130-3133.
144. P. Scott, U. Rief, J. Diebold and H. H. Brintzinger, *Organometallics*, 1993, **12**, 3094-3101.
145. P. Jutzi, J. Schnittger, W. Wieland, B. Neumann and H.-G. Stammer, *J. Organomet. Chem.*, 1991, **415**, 425-434.
146. F. Nief and L. Ricard, *J. Organomet. Chem.*, 1998, **553**, 503-506.
147. R. Brand, H.-P. Krimmer, H.-J. Lindner, V. Sturm and K. Hafner, *Tetrahedron Lett.*, 1982, **23**, 5131-5134.
148. H. Sitzmann, C. Bollmann and E. V. Dehmlow, *Tetrahedron Lett.*, 1994, **35**, 5619-5620.
149. C. Benelli and D. Gatteschi, *Chem. Rev.*, 2002, **102**, 2369-2388.
150. X. Zhang, N. Xu, W. Shi, B.-W. Wang and P. Cheng, *Inorg. Chem. Front.*, 2018, **5**, 432-437.
151. M. Lines, *J. Chem. Phys.*, 1971, **55**, 2977-2984.
152. M. A. Bau, S. Wiesler, S. L. Younas and J. Streuff, *Chem. Eur. J.*, 2019, **25**, 10531-10545.

153. L. Ungur, W. Van den Heuvel and L. F. Chibotaru, *New J. Chem.*, 2009, **33**, 1224-1230.
154. T. Pugh, V. Vieru, L. F. Chibotaru and R. A. Layfield, *Chem. Sci.*, 2016, **7**, 2128-2137.
155. T. Pugh, N. F. Chilton and R. A. Layfield, *Chem. Sci.*, 2017, **8**, 2073-2080.
156. F.-S. Guo, A. K. Bar and R. A. Layfield, *Chem. Rev.*, 2019, **119**, 8479-8505.
157. S.-M. Chen, J. Xiong, Y.-Q. Zhang, Q. Yuan, B.-W. Wang and S. Gao, *Chem. Sci.*, 2018, **9**, 7540-7545.
158. P. Evans, D. Reta, G. F. S. Whitehead, N. F. Chilton and D. P. Mills, *J. Am. Chem. Soc.*, 2019, **141**, 19935-19940.
159. D. Turcitu, F. Nief and L. Ricard, *Chem. Eur. J.*, 2003, **9**, 4916-4923.
160. K. R. Meihaus and J. R. Long, *Dalton Trans.*, 2015, **44**, 2517-2528.
161. L. Barluzzi, L. Chatelain, F. Fadaei-Tirani, I. Zivkovic and M. Mazzanti, *Chem. Sci.*, 2019, **10**, 3543-3555.
162. D. P. Mills, F. Moro, J. McMaster, J. Van Slageren, W. Lewis, A. J. Blake and S. T. Liddle, *Nat. Chem.*, 2011, **3**, 454-460.
163. P. L. Arnold, T. Ochiai, F. Y. T. Lam, R. P. Kelly, M. L. Seymour and L. Maron, *Nat. Chem.*, 2020, **12**, 654-659.
164. V. Mougel, L. Chatelain, J. Pécaut, R. Caciuffo, E. Colineau, J.-C. Griveau and M. Mazzanti, *Nat. Chem.*, 2012, **4**, 1011-1017.
165. S. M. Cendrowski-Guillaume, G. Le Gland, M. Nierlich and M. Ephritikhine, *Organometallics*, 2000, **19**, 5654-5660.
166. S. J. Connelly, W. Kaminsky and D. M. Heinekey, *Organometallics*, 2013, **32**, 7478-7481.
167. M. D. Walter, C. D. Sofield, C. H. Booth and R. A. Andersen, *Organometallics*, 2009, **28**, 2005-2019.
168. B. Zhu, O. Š. Miljanić, K. P. C. Vollhardt and M. J. West, *Synthesis*, 2005, **2005**, 3373-3379.
169. O. V. Dolomanov, L. J. Bourhis, R. J. Gildea, J. A. Howard and H. Puschmann, *J. Appl. Crystallogr.*, 2009, **42**, 339-341.
170. G. M. Sheldrick, *Acta Cryst.*, 2015, **C71**, 3-8.
171. G. M. Sheldrick, *Acta Cryst.*, 2008, **A64**, 112-122.